Experimental Studies of Interactions in Ytterbium Fermi Gases and Quantum Hall Ladder Systems

Dissertation
zur Erlangung des Doktorgrades
an der Fakultät für Mathematik, Informatik und Naturwissenschaften
Fachbereich Physik
der Universität Hamburg

vorgelegt von

Marcel Friedrich Georg Diem

Hamburg

2024

Gutachter/innen der Dissertation:	Prof. Dr. Klaus Sengstock Prof. Dr. Henning Moritz
Zusammensetzung der Prüfungskommission:	Prof. Dr. Klaus Sengstock Prof. Dr. Henning Moritz Prof. Dr. Michael Potthoff Prof. Dr. Dieter Hans Jaksch Dr. Juliette Simonet
Vorsitzende/r der Prüfungskommission:	Prof. Dr. Michael Potthoff
Datum der Disputation:	03.04.2025
Vorsitzender des Fach-Promotionsausschusses PHYSIK:	Prof. Dr. Wolfgang J. Parak
Leiter des Fachbereichs PHYSIK	Prof. Dr. Markus Drescher
Dekan der Fakultät MIN	Prof. Dr.-Ing. Norbert Ritter

Abstract

This thesis is based in the research field of quantum simulation, particularly in the investigation of quantum phenomena with cold ytterbium atoms. Based on Richard Feynman's vision, the work employs experimental techniques for the creation and manipulation of cold atoms to simulate specific quantum scenarios.

In the first part, we investigate, on the one hand, interisotope interorbital interactions in mixtures of ^{171}Yb and ^{173}Yb and, on the other hand, spin-exchange interactions of ^{171}Yb using clock spectroscopy. We characterize the elastic scattering lengths as ${}^{171}_{173}a_{\mathrm{eg}} = 497.4(8)a_0$ and ${}^{171}_{173}a_{\mathrm{ge}} = 482(1)a_0$ and proof their SU(2) $\otimes$ SU(6) symmetry. The measured decay coefficients for inelastic interactions reveal that ${}^{171}_{173}\beta_{\mathrm{eg}}$ is approximately 400 times stronger than ${}^{171}_{173}\beta_{\mathrm{ge}}$, indicating that $^{171}\mathrm{Yb_g}$-$^{173}\mathrm{Yb_e}$ mixtures are more suited for quantum simulations. For the spin-exchange interactions of ^{171}Yb, we find scattering lengths of $a_{\mathrm{eg}^+} = 203(5)a_0$ and $a_{\mathrm{eg}^-} = 308(6)a_0$. The negative value of the spin-exchange interaction V_{ex} confirms its antiferromagnetic nature, making ^{171}Yb a promising candidate for simulating the Kondo lattice model [1, 2].

In the more comprehensive second part, we investigate the influence of inter-particle interactions on the emergence of chiral edge currents in quantum Hall systems. We provide a detailed report on the experimental realization of a quantum Hall ladder system, beginning with the theoretical foundations of the Harper-Hofstadter model and its implementation in cold atom systems through artificial gauge fields. We outline the essential steps for preparing and implementing quantum Hall ladders, confirming the successful realization of the system through precise measurements of chiral edge currents. Additionally, this work provides valuable insights into practical challenges and optimization strategies for experimental data. We describe previously unreported dynamics during bandmapping and, more importantly, during the eigenstate preparation, which significantly impact the measurement of chiral currents. We observe prominent chiral currents, which exceed those reported in comparable experimental studies (see Ref. [3–7]) and exhibit momentum distributions closely aligning with theoretical predictions. Finally, we examine how inter-particle interactions, which are infinitely long-ranged along a synthetic dimension and localized to a single lattice site along a shallow optical lattice, affect the topologically protected chiral edge currents. In the strongly interacting regime, we find a suppression of chiral currents. Our data is consistent with two distinct interaction behaviors: a linear differential response and a constant relative suppression of the currents within the explored interaction regime. Furthermore, our findings suggest the possibility of a dynamic area in the weakly repulsive regime.

This thesis advances the field of quantum simulation by enhancing our understanding of interactions and topological properties in cold atom systems. Our results deepen the comprehension of interaction effects in different scenarios, and may contribute to the exploration of *fractional* quantum Hall states [8–13]. In this context, a deeper understanding of interactions could pave the way for the development of robust quantum information protocols [14].

Zusammenfassung

Diese Dissertation ist im Forschungsbereich der Quanten-Simulation angesiedelt, insbesondere in der Untersuchung von Quantenphänomenen mit kalten Ytterbiumatomen. Basierend auf Richard Feynmans Vision werden experimentelle Techniken zur Erzeugung und Manipulation kalter Atome eingesetzt, um spezifische Quantenszenarien zu simulieren.

Im ersten Teil untersuchen wir einerseits interisotopische interorbitale Wechselwirkungen in Mischungen von ^{171}Yb und ^{173}Yb und andererseits Spin-Austausch-Wechselwirkungen von ^{171}Yb mittels Uhrenspektroskopie. Wir charakterisieren die elastischen Streulängen als ${}^{171}_{173}a_{\mathrm{eg}} = 497.4(8)a_0$ und ${}^{171}_{173}a_{\mathrm{ge}} = 482(1)a_0$ und bestätigen deren SU(2) $\otimes$ SU(6)-Symmetrie. Die gemessenen Zerfallskoeffizienten für inelastische Wechselwirkungen zeigen, dass ${}^{171}_{173}\beta_{\mathrm{eg}}$ etwa 400-mal stärker ist als ${}^{171}_{173}\beta_{\mathrm{ge}}$, was darauf hinweist, dass Mischungen aus $^{171}\mathrm{Yb_g}$-$^{173}\mathrm{Yb_e}$ besser für Quanten-Simulationen geeignet sind. Für die Spin-Austausch-Wechselwirkungen von ^{171}Yb ermitteln wir Streulängen von $a_{\mathrm{eg}^+} = 203(5)a_0$ und $a_{\mathrm{eg}^-} = 308(6)a_0$. Der negative Wert der Spin-Austausch-Wechselwirkung V_{ex} bestätigt deren antiferromagnetische Natur, was ^{171}Yb zu einem vielversprechenden Kandidaten für die Simulation des Kondo-Gittermodells [1, 2] macht.

Im umfassenderen zweiten Teil untersuchen wir den Einfluss von Teilchenwechselwirkungen auf das Auftreten chiraler Randströme in Quanten-Hall-Systemen. Wir berichten detailliert über die experimentelle Realisierung eines Quanten-Hall-Leitersystems, ausgehend von den theoretischen Grundlagen des Harper-Hofstadter-Modells und dessen Implementierung in kalten Atomen mittels künstlicher Eichfelder. Wir skizzieren die wesentlichen Schritte zur Vorbereitung und Implementierung von Quanten-Hall-Leitern und bestätigen die erfolgreiche Realisierung des Systems durch präzise Messungen chiraler Randströme. Darüber hinaus bietet diese Arbeit wertvolle Einblicke in praktische Herausforderungen und Optimierungsstrategien für experimentelle Daten. Wir beschreiben bisher nicht berichtete Dynamiken während des Bandmappings und noch wichtiger während der Eigenzustandspräparation, die die Messung chiraler Ströme erheblich beeinflussen. Es werden ausgeprägte chirale Ströme beobachtet, die die in vergleichbaren experimentellen Studien (siehe Ref. [3–7]) berichteten Werte übertreffen und Impulsverteilungen aufweisen, die eng mit den theoretischen Vorhersagen übereinstimmen. Schließlich untersuchen wir, wie Teilchenwechselwirkungen, die entlang einer synthetischen Dimension unendlich langreichend und entlang eines flachen optischen Gitters auf eine einzelne Gitterstelle lokalisiert sind, die topologisch geschützten chiralen Randströme beeinflussen. Im stark wechselwirkenden Regime stellen wir eine Unterdrückung der chiralen Ströme fest. Unsere Daten sind mit zwei unterschiedlichen Wechselwirkungsverhalten konsistent: einer linearen differentiellen Wechselwirkungsantwort und einer konstanten relativen Unterdrückung der Ströme innerhalb des untersuchten Wechselwirkungsbereichs. Darüber hinaus deuten unsere Ergebnisse auf die Möglichkeit eines dynamischen Bereichs im schwach repulsiven Regime hin.

Diese Dissertation trägt zur Weiterentwicklung des Forschungsfeldes der Quanten-Simulation bei, indem sie unser Verständnis von Wechselwirkungen und topologischen Eigenschaften in kalten Atom-Systemen vertieft. Unsere Ergebnisse erweitern das Verständnis von Wechselwirkungseffekten in verschiedenen Szenarien und könnten zur Erforschung von *fraktionierten* Quanten-Hall-Zuständen beitragen [8–13]. In diesem Zusammenhang könnte ein tieferes Verständnis von Wechselwirkungen den Weg für die Entwicklung robuster Quanteninformationsprotokolle ebnen [14].

Publikationen

Im Rahmen der vorliegenden Arbeit sind die folgenden wissenschaftlichen Veröffentlichungen entstanden.

Publications

The following research articles have been published in the course of this thesis.

[15] K. Sponselee, L. Freystatzky, B. Abeln, M. Diem, B. Hundt, A. Kochanke, T. Ponath, B. Santra, L. Mathey, K. Sengstock and C. Becker, *"Dynamics of ultracold quantum gases in the dissipative Fermi-Hubbard model"*, Quantum Science and Technology **4** 014002 (2018).

[16] B. Abeln, K. Sponselee, M. Diem, N. Pintul, K. Sengstock and C. Becker, *"Interorbital interactions in an $SU(2) \otimes SU(6)$-symmetric Fermi-Fermi mixture"*, Phys. Rev. A **103** 033315 (2021)

Contents

List of Figures

List of Tables

Introduction

Quantum simulation, according to Richard Feynman's vision, overcomes the limitations of analytical calculations and computational power in the field of quantum physics by creating and manipulating real quantum systems to replicate and simulate specific scenarios in quantum physics. In the ideal scenario, properties of these quantum systems can be directly investigated and measured. Such quantum systems can, in principle, be based on various fundamental physical platforms, such as cold and ultracold molecules, color centers, dopants in semiconductors, gate-defined quantum dots, photons in nanostructures, photons and atoms in cavities, Rydberg atom arrays, superconducting quantum circuits, trapped atomic ions, ultracold neutral atoms, van der Waals heterostructures, Moiré materials, and excitons [17]. We will further focus on the platform of ultracold neutral atoms, which was utilized for this thesis. For cold atoms, the first major difficulty for the realization of quantum simulators was overcome by the development of methods for cooling and trapping atoms using laser light. This achievement was awarded with the Nobel prize in physics for Steven Chu, Claude Cohen-Tannoudji and William Daniel Phillips in 1997 [18]. With the help of these methods, it became possible to transfer atoms from the regime of classical physics into the realm of quantum statistics. Depending on the total spin of the atoms, they can be transformed into a Bose-Einstein condensate (BEC) [19, 20] or a degenerate Fermi gas [21]. Due to the versatile capabilities of manipulating atoms with laser light, cold atoms provide an excellent platform to realize a wide variety of very different quantum systems. This enables the observation of how the system behaves, when specific physical parameters are altered in an otherwise identical system. The tunability of the following parameters among others has been demonstrated, and many of these capabilities are now standard in modern cold atom laboratories: confining potentials, particle density, effective dimensionality [22], and interactions using Feshbach resonances [23]. Additionally, other parameters such as optical lattice potentials, lattice geometry, and external fields can be manipulated with high precision. To the most outstanding achievements with quantum gases belong the bosonic superfluid to Mott insulator transition [24–26], the exploration of the Bardeen-Cooper-Schrieffer (BCS)-BEC crossover with degenerate Fermi gases [27–31] and the creation of artificial gauge fields [32–41]. Initially, observations were limited to momentum space through time of flight methods. However, advancements in technology enabled the creation of quantum gas microscopes. These microscopes can pinpoint individual atoms within a two-dimensional optical lattice. This innovation enables the direct measurement of correlations. A significant milestone was achieved with the direct detection of antiferromagnetic order within an ultracold fermionic system confined to an optical lattice [42]. Furthermore, the recent development of a quantum gas magnifier for sub-lattice-resolved imaging of 3D quantum systems opens the path for spatially resolved studies of new quantum many-body regimes and paves the way for single-atom-resolved imaging of atomic species, where efficient laser cooling or deep optical traps are not available [43]. Another advancement involves micro-trap arrays, which enable the trapping, detection, and manipulation of individual atoms. These arrays facilitate the creation of defect-free atomic geometries atom by atom [44, 45]. Utilizing Rydberg excitation and blockade techniques, these systems have demonstrated the entanglement of numerous particles [46] and have been utilized to investigate phenomena such as the SSH model [47] and spin liquids [48].

The research field of quantum simulation, strives to increase possibilities to manipulate and tune system parameters, increase accuracy and precision of measurements and increase the range of quantum systems, which can be emulated. Two remarkable achievements in this direction, which are relevant for the work in this thesis, are the utilization of alkaline earth (like) elements such as strontium and ytterbium and the

implementation of artificial gauge fields for neutral atoms. Alkaline earth (like) elements feature optical transitions with linewidths below one Hz [49] and are, thus, much narrower than typical linewidths in alkaline elements, which are in the order of several MHz. One particularly narrow transition, is used in optical lattice clocks [50] as a frequency reference and by employing state-of-the-art technology, such as an optical frequency comb, they surpass existing frequency standards [51, 52]. In optical lattice clocks the combination of precise spectroscopy and ultracold quantum gases composed of alkaline earth elements yield new applications for quantum simulation. On the one hand, precise spectroscopy provides for example a robust tool for analyzing interaction-induced energy shifts in optical lattices [16, 53–60]. On the other hand, the extended lifetime of the long-lived metastable clock state surpasses typical experimental timescales, offering an additional degree of freedom for quantum simulation purposes [1, 2]. This orbital degree of freedom can, for example, induce particle losses, which result from inelastic collisions between excited-state atoms. These losses can be used to engineer dissipative Hubbard systems [15, 61], which hold potential for preparing highly entangled quantum states [15, 62].

The second remarkable achievement, the implementation of artificial gauge fields for neutral atoms, led to the possibility to mimic the behavior of charged particles in strong magnetic fields. The reachable magnetic fields are extraordinarily high and unattainable in conventional solid-state setups. Consequently, they open avenues for observing new phases of matter. Various schemes have been developed to implement artificial gauge fields, such as laser-assisted tunneling [36, 37], lattice shaking [38–41, 63, 64] or synthetic dimensions [3, 4, 65–67]. These techniques enable the creation of quantum Hall structures with quantum gases, as it was realized for bosons in Ref. [36, 66, 68–70] and for fermions in Ref. [3, 4, 7, 67, 71]. Prior to the discovery of the integer quantum Hall effect, quantum states were categorized based on spontaneous symmetry breaking, marking a significant milestone in condensed matter physics in the previous century [72]. However, the integer quantum Hall state cannot be characterized in this way, leading to the formulation of a new classification scheme based on topology. This classification of phases of matter such as topological insulators [73] exhibit an interplay between magnetic fields, spin-orbit coupling and particle interactions and evoke a spectrum of captivating effects [74–76]. In this thesis, we exploit the synthetic dimensions approach to realize quantum Hall states. This approach was first proposed in Ref. [65]. In this paper, the authors state, that an internal degree of freedom of atoms could be seen as a synthetic dimension, where different quantum states represent synthetic lattice sites. Possible internal states are, for example, momentum states [77], harmonic oscillator eigenstates [78], orbital states of an optical lattice [7, 79–81], electronic states [4, 67, 82] or spin states [3, 66]. Synthetic dimensions can be exploited to create exotic (lattice) structures [83] and increase the dimensionality of a system to accomplish, for example, a four-dimensional quantum Hall effect [70, 84]. Beyond this, synthetic dimensions can feature different interaction ranges. In this thesis, we realize a system, with long-range interactions along the synthetic dimension [85]. This is interesting, as the Coulomb interaction found in electron systems is long-ranged. Since the van der Waals force observed in ultracold gases typically behaves as a short-range interaction, which is often simplified as a contact interaction, various experimental methods are being explored to extend the interaction range. Some examples are the utilization of polar molecules [86] or elements possessing large magnetic moments like chromium [87], dysprosium [88], or erbium [89].

The content of this thesis is structured as follows:

- In chapter 1, we present our experimental methods for the creation and manipulation of degenerate Fermi gases. We introduce relevant properties of ytterbium, explain our setup to trap gaseous atoms and cool them down to quantum degeneracy, discuss our capabilities to engineer different

quantum systems and address our techniques for the detection of atoms and their internal and external states.

- Chapter 2 is about probing interactions with clock spectroscopy. In the first part of this chapter, we present results on interorbital interisotope interactions in Fermi-Fermi mixtures of ^{171}Yb and ^{173}Yb. We measure the elastic and inelastic part of the interactions and directly show the SU(2) $\otimes$ SU(6) symmetry of the elastic scattering lengths. In the second part, we report on interorbital interactions in a spin-balanced ^{171}Yb gas, where we determine the direct and spin-exchange interactions.

- In chapter 3, we present and discuss the realization of quantum Hall systems. We begin by introducing the theoretical framework, including an in-depth discussion of the Harper-Hofstadter model and its single-particle solutions. We then explain how this model can be realized in cold atom systems through the creation of artificial gauge fields. Furthermore, we provide a detailed explanation of our method for generating artificial magnetic fields, which employs stimulated Raman transitions.

- Chapter 4 focuses on the practical implementation and preparation of quantum Hall states, providing a comprehensive overview of the experimental setup and preparation techniques. We outline the design considerations and the selected parameter space with an emphasis on measurement capabilities. Moreover, we address the preparation of eigenstates for the Harper-Hofstadter Hamiltonian. Core measurements of Raman resonances, Raman-Rabi oscillations and chiral edge currents are thoroughly examined, as they characterize the system. In addition, this chapter provides valuable insights into practical challenges and optimization strategies for experimental data.

- In chapter 5, we present our results of interaction effects in quantum Hall ladders. In particular, we investigate how inter-particle interactions, which are infinitely long-ranged along a synthetic dimension and localized to a single lattice site along a shallow optical lattice, affect the topologically protected chiral edge currents.

1 Experimental Methods

This chapter provides information on the basic theoretical models and experimental methods used in this thesis. Most of this knowledge is required to understand the conducted research. First, we introduce relevant properties of ytterbium, which is the element used in our quantum gas machine. Second, we explain our setup to trap gaseous atoms and cool them down to quantum degeneracy. Third, we discuss our capabilities to engineer different quantum systems by selecting isotopes and manipulating internal atomic states. Fourth, we present another method for engineering trapped quantum systems by applying optical lattices. Fifth, we cover our techniques for the detection of atoms and their internal and external states. General information on the introduced theoretical models and applied experimental methods in quantum gas machines can be found in Ref. [90–93]. Specific information on our experimental setup is described in Ref. [94–100].

1.1 Ytterbium Properties

In this section, we introduce some basic properties of ytterbium, which are relevant for using it in quantum gas experiments. We provide the information needed to understand the behavior of ytterbium in our experimental setup. We describe its isotopes, electronic configuration, energy level structure and transitions. Furthermore, we discuss its interaction behavior and the consequences of its purely nuclear spin in its ground and clock state. Further information on ytterbium properties in the context of quantum gas machines can be found in Ref. [94].

Ytterbium is a lanthanide and has the atomic number 70. Because of its high atomic number, it has several stable isotopes in different natural abundances [101] as shown in Table 1.1. We use the two fermionic isotopes ^{171}Yb and ^{173}Yb in the measurements presented in this thesis. The electronic configuration of ytterbium in its ground state is [Xe]$4f^{14}6s^2$. The two valence electrons in the 6s-orbital make ytterbium behave like an alkaline earth element. As characteristic for alkaline earth elements, ytterbium features an energy level structure of singlet ($S = 0$) and triplet ($S = 1$) states, which are classified by the total electronic spin S. The energy level structure is depicted in Fig. 1.1.

Table 1.1: Ytterbium isotopes. The table lists ytterbium isotopes with their natural abundance (according to Ref. [101]), nuclear spin and statistical behavior.

Isotope	Natural abundance (%)	Nuclear spin	Statistical behavior
^{168}Yb	0.1	0	bosonic
^{170}Yb	3.0	0	bosonic
^{171}Yb	14.1	1/2	fermionic
^{172}Yb	21.7	0	bosonic
^{173}Yb	16.1	5/2	fermionic
^{174}Yb	32.0	0	bosonic
^{176}Yb	13.0	0	bosonic

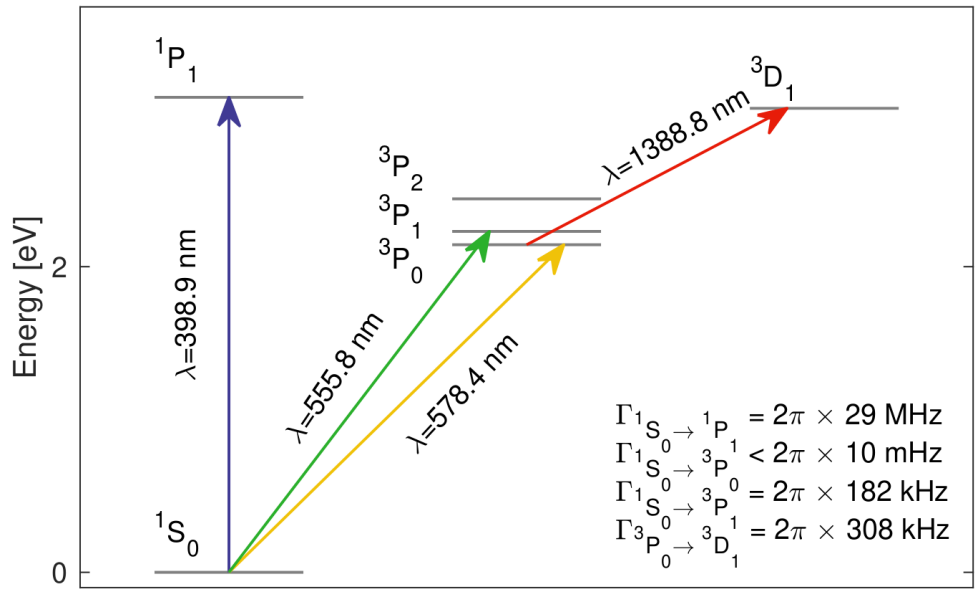

Figure 1.1: Ytterbium's reduced energy level scheme. The figure displays the fundamental atomic states and state transitions exploited in this thesis. In addition, the wavelengths λ and natural linewidths Γ of the transitions are listed. Taken from Ref. [100].

Ytterbium's ground state is the $^1S_0$ state. In this thesis, we exploit the transitions from this ground state to the states $^1P_1$, $^3P_1$ and $^3P_0$. While the transition to the $^1P_1$ state is a regular dipole transition, the $^3P_1$ and $^3P_0$ state transitions are intercombination transitions from a singlet to a triplet state. These intercombination transitions are only accessible by dipole radiation, because both states, $^3P_1$ and $^3P_0$, mix with the $^1P_1$ state (with different strengths) and, thus, are actually state mixtures [102]. Because of the state mixing, the linewidths of the intercombination transitions are narrower than the $^1S_0 \rightarrow {}^1P_1$ transition. The transition $^1S_0 \rightarrow {}^3P_0$ is particularly narrow and, thus, exploited by atomic lattice clocks [51, 103]. Therefore, this transition is often called clock transition and the $^3P_0$ state is referred to as the clock state.

We exploit the transitions shown in Fig. 1.1 for the following purposes. We use the $^1S_0 \rightarrow {}^1P_1$ transition for cooling and imaging and the $^1S_0 \rightarrow {}^3P_0$ transition for cooling, spin manipulation and Raman transitions. The clock transition is used to explore orbital physics and to measure frequency shifts as caused by interactions for example. With the transition $^3P_0 \rightarrow {}^3D_1$, we can repump atoms from the clock state to the ground state on experimental time scales, which is useful because of the long natural lifetime of ytterbium's clock state.

After the 3D-MOT cooling phase (see Sec. 1.2.1) at our quantum gas machine, ytterbium's atomic interactions are reduced to s-wave scattering processes [104]. For this kind of scattering, the interactions are characterized by a single number: the scattering length a. The inter- and intraisotope s-wave scattering lengths for ytterbium ground state atoms are listed in Table 1.2. The interaction strengths are relevant for the measurements in chapter 2 and are exploited for the chapter 5.

The interactions in ytterbium's ground state $^1S_0$ and in its clock state $^3P_0$ are special, as they are SU($\mathcal{N}$) symmetric and spin-conserving [1, 106, 107]. This is a result of the fact, that the total electronic angular momentum in these states is zero, $J = 0$, which means, that the total atomic angular momentum has no electronic part and is determined by the nuclear spin I, $F = I + J = I$. In addition, the nuclear

Table 1.2: Ytterbium's scattering lengths. The table lists the inter- and intraisotope s-wave scattering lengths of ytterbium isotopes in units of the Bohr radius $a_0 = 5.29177210903(80) \cdot 10^{-11}$ m. Adapted from Ref. [105].

	^{168}Yb	^{170}Yb	^{171}Yb	^{172}Yb	^{173}Yb	^{174}Yb	^{176}Yb
^{168}Yb	**251.9(34)**	117.0(15)	89.2(17)	65.0(19)	38.6(25)	2.5(34)	-359(30)
^{170}Yb		**63.9(21)**	36.5(25)	-2.1(36)	-81.3(68)	-518(51)	209.4(23)
^{171}Yb			**-2.8(36)**	-84.3(68)	-578(60)	429(13)	141.5(15)
^{172}Yb				**-599(64)**	418(13)	200.5(23)	106.2(15)
^{173}Yb					**199.4(21)**	138.7(15)	79.7(19)
^{174}Yb						**104.9(15)**	54.4(23)
^{176}Yb							**-24.2(43)**

magnetic moment is weaker with respect to an electronic magnetic moment by approximately the ratio of proton to electron mass $m_p/m_e \approx 1836$. Thus, the ground and clock state are not as sensitive to magnetic fields as states with $J \neq 0$, which includes for example ytterbium's $^1P_1$ and $^3P_1$ state or the ground states of alkaline atoms. This is an additional reason, why ytterbium and other alkaline earth (like) elements are well suited for atomic lattice clocks. However, another consequence is, that ytterbium does not possess magnetic Feshbach resonances, but only orbital Feshbach resonances [108–110] to tune its interactions.

This section provided the knowledge about ytterbium properties, which are needed to understand its behavior in the experimental context of this thesis. We presented its stable isotopes, its main energy level structure and transitions. We discussed its interaction behavior and the results of the purely nuclear total atomic angular momentum in its ground and clock state.

1.2 Atomic Trapping and Cooling

After introducing the atomic element of our quantum gas machine and its properties, we describe the methods used to trap ytterbium atoms and cool them down to quantum degeneracy for the measurements in this thesis. We focus on describing the functionality of the methods and disregard details of the building or preparation process. This section provides the information needed to understand the starting point for further manipulation and preparation of the atoms. The atoms are first trapped and cooled in a two-dimensional Magneto-Optical Trap (2D MOT) and 3D MOT setup. Afterwards, they are trapped in an all optical dipole trap, where they can reach quantum degeneracy through evaporative cooling. A schematic of the different cooling stages for a typical cooling sequence is displayed in Fig. 1.2. The planning, building and performance testing of the experimental setups in this section was mainly conducted by former PhD students and details about it can be found in Ref. [94–98].

1.2.1 Magneto-Optical Traps

The source of ytterbium atoms in our experiment are dispensers in the corners of a glass cell under a vacuum of $\leq 10^{-9}$ mbar. A dispenser is heated up by electric currents in the order of 5 to 6.5 A

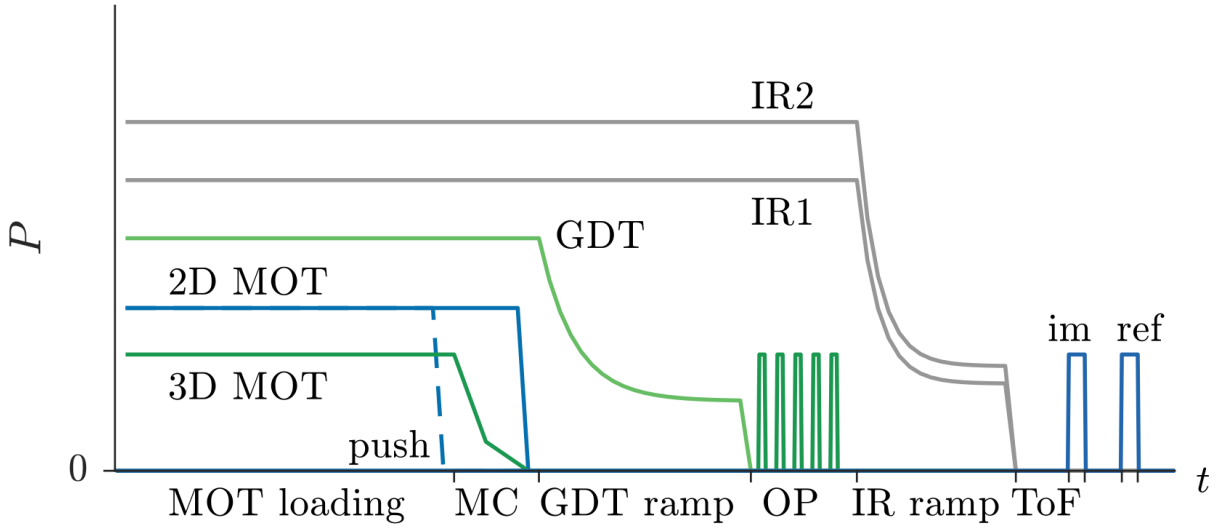

Figure 1.2: Schematic of a typical cooling sequence. The scheme shows a typical arrangement of the different stages in a cooling sequence. This is illustrated by relevant laser powers as a function of time. Different stages are labeled below the horizontal axis. The stages are: MOT loading, MOT compression (MC), green dipole trap ramp (GDT ramp), optical pumping (OP; see Sec. 1.3.2), crossed dipole trap ramp (IR ramp), time of flight (TOF). Different lines show the power of different laser beams and are labeled directly next to the respective line. The laser beams are: 2D MOT beams (2D MOT), 3D MOT beams (3D MOT), pushing beam (push), green dipole trap (GDT), crossed dipole trap beam one (IR1), crossed dipole trap beam two (IR2), first imaging beam (im; see Sec. 1.5.1), reference imaging beam (ref; see Sec. 1.5.1). Taken from Ref. [99].

and emits gaseous atoms through a small slit. The slit is directed at the horizontal center of our two-dimensional magneto-optical trap (2D MOT), which is also the horizontal center of the glass cell. The 2D MOT consists of a gradient magnetic field induced by magnetic coils and of two retro-reflected laser beams from orthogonal directions in the horizontal plane. The light is circularly polarized and drives the transition $^1S_0 \rightarrow {}^1P_1$ with a wavelength of 399 nm. The atoms are slowed down through absorption processes of the laser light (for details on the functionality of a magneto-optical trap see Ref. [91]). When atoms are sufficiently slowed down, they are horizontally trapped in the 2D MOT.

After the trapping in the 2D-MOT, the atoms are falling down by gravity and additionally are pushed downwards with a pushing beam coming from the top of the glass cell. The pushing beam is also operated at a wavelength of 399 nm. At the bottom of the 2D MOT glass cell, the atoms reach a differential pumping stage, pass through it and reach the 3D MOT glass cell on the other end, which is under a pressure of $\leq 2 \cdot 10^{-10}$ mbar. The 3D MOT is similarly constructed as the 2D MOT with a gradient magnetic field and circularly polarized laser beams. However, the 3D MOT features counter-propagating laser beams in all three spacial dimensions, such that cooling and trapping can be achieved in the gravity direction as well. Moreover, the beams have a wavelength of 556 nm and drive the intercombination transition $^1S_0 \rightarrow {}^3P_1$. Because this transition has a lower Doppler temperature (see Ref. [91]), the 3D MOT can cool the atoms further down and reach lower temperatures than the 2D MOT. Typical temperatures are 17(2) µK and 15(2) µK for ^{171}Yb and ^{173}Yb, respectively (for the temperature measurements see Ref. [99]). However, because of the narrow natural linewidth of the transition, the beams are frequency broadened to address a broader range of velocity classes (for details see Ref. [100]).

After a loading time of typically 18 s, during which atoms are accumulated in the 3D MOT, the MOT is

compressed in two stages and slightly shifted, if necessary, to maximize the loading of atoms into the combined dipole traps. During the two stages, which last about 200 ms each, the frequency broadening and the power of the MOT beams are reduced. At the same time the center frequency of the 3D MOT beams are shifted closer to resonance. The compressed 3D-MOT has a larger overlap with the combined dipole traps. After the atoms are transferred to the dipole traps, the beams of the 2D and 3D MOT are shuttered to avoid (near)-resonant stray light during the evaporative cooling and the experiments.

1.2.2 Evaporative Cooling

After the 3D MOT phase, the dipole traps are sufficient to trap the atoms and support them against gravity. The dipole traps consist of a crossed dipole trap in the horizontal plane and a third dipole beam, which is co-aligned onto one of the beams of the crossed dipole trap. The crossed dipole trap is operated at a wavelength of 1064 nm in the infrared regime, whereas the third beam is green with a wavelength of 532 nm. The confinement of the green beam is much stronger than the one of the crossed dipole trap. Therefore, it is used as the first evaporative cooling stage (for details on the functionality of evaporative cooling see Ref. [91]). After the exponential-like ramp for the cooling, the green beam is switched off and the atoms are only held against gravity by the crossed dipole trap. In a second evaporative cooling stage, the two beams of the crossed dipole trap are ramped down to a power, where the atomic sample has the desired temperature. We accomplish typically 10^5 atoms at temperatures of 25 % T_{Fermi} for ^{171}Yb and 1.5×10^5 atoms at temperatures of 20 % T_{Fermi} for ^{173}Yb, where T_{Fermi} is the Fermi temperature. The atoms have reached quantum degeneracy and can now be used as a quantum gas for experiments.

While the dipole trap beams can be operated with free running lasers, the MOT beams need a frequency stabilization in order to be functional. In general at our experiment, laser frequency stabilization is achieved by coupling a small amount of light (in the order of 1 to 10 µW) into a cavity and using the Pound-Drever-Hall locking technique (see Ref. [111]). Moreover, we have several lasers at the same wavelength, for which we use offset locks. While one laser is locked to a cavity, others can be locked on the first one, if the frequency difference is in the GHz regime or lower. These offset locks are either based on a digital phase detector (see Ref. [112]) or on the locking technique described in Ref. [113]. For details on our different locking schemes see Ref. [100].

In this section, we described the cooling and trapping methods used in our quantum gas machine. We explained our 2D and 3D MOT setup and our evaporative cooling procedure. At the end, the atoms have reached quantum degeneracy.

1.3 Selection of Isotopes and Internal Atomic States

In the last section, we explored how quantum degeneracy can be reached in our setup. Here, we specify what kind of quantum gases we can prepare by presenting the possibilities of our quantum gas machine to select different ytterbium isotopes and manipulate atomic states. The atomic samples, which can be prepared, are various and have an influence on the fundamental physics, which can be observed. First, we discuss single isotopes and mixtures of isotopes. Second, we address m_{F} state manipulation and, third, we cover the clock state addressing.

1.3.1 Selection of Isotopes

As mentioned in Sec. 1.1, ytterbium possesses several stable isotopes with different statistical behavior and interactions. The measurements described in this thesis were conducted either with ^{171}Yb atoms, with ^{173}Yb atoms or with a mixture of these two isotopes. The preparation of single isotopes and of mixtures is described in the following.

Ytterbium's isotopes have different resonance frequencies for the transitions addressed by the MOTs (see Sec. 1.2.1). Therefore, for cooling different isotopes or mixtures to quantum degeneracy, we need to adjust the frequencies of the MOT beams accordingly. For optimal MOT loading efficiencies, we adjust also the alignment and polarization of the MOT beams slightly. For isotope mixtures, we use a compromise between the optimal settings for the single isotopes. The frequency adjustment is performed through changing the locking point of the frequency stabilization (see Sec. 1.2.2).

The cooling and trapping of isotope mixtures requires, that the 2D and 3D MOT are operated for both isotopes in the same measurement cycle. We operate the 2D-MOT such, that we first load one isotope, shift the frequency of the MOT beams and, then, load the other isotope. Whereas the 3D-MOT is operated bicolor to trap both isotopes at the same time. For this purpose, we use two lasers at different frequencies, whose beams are overlapped for the MOT. For details on the exact implementation see Ref. [114].

For a degenerate gas of ^{171}Yb, the cooling procedure is more complex than for ^{173}Yb and ^{174}Yb because the ^{171}Yb atoms do not thermalize on experimental timescales, as the intraisotope s-wave scattering length is too weak with $a = -3(4)\ a_0$. Thus, this isotope requires sympathetic cooling (for details on this concept see Ref. [91]). For this purpose, we use a mixture of ^{171}Yb and ^{173}Yb during the evaporative cooling. Depending on the atom numbers of both isotopes before the evaporation, we can create either a degenerate gas of ^{171}Yb atoms alone or a mixture of ^{171}Yb and ^{173}Yb atoms with various atom number ratios. The initial atom numbers of the isotopes can be influenced by the respective 2D-MOT loading times.

1.3.2 Manipulation of Spin States

Once, the isotope or isotope mixture is selected, spin state manipulation delivers another choice for the preparation of quantum systems. The m_F state populations can influence the fundamental behavior of the system. The possibility to manipulate them is necessary for the observations in chapters 2, 3 and 5. In the following, we discuss our optical pumping procedure, the blasting of spin states and the stability of the m_F state populations.

After the atoms are transferred to the dipole traps (see Sec. 1.2.2), all available m_F states of the ground state(s) are equally populated, even though, not all of these states are initially trapped by the MOTs (see Ref. [94, 115]). Atoms can be pumped from one m_F state to another with resonant excitations by laser light. For this purpose, we use green light at a wavelength of 556 nm to address the transition $|^1S_0, F = 1/2, m_F\rangle \rightarrow |^3P_1, F' = 3/2, m_F \pm 1\rangle$ for ^{171}Yb and $|^1S_0, F = 5/2, m_F\rangle \rightarrow |^3P_1, F' = 7/2, m_F \pm 1\rangle$ for ^{173}Yb. The intercombination transition allows us to address single m_F states, if the transition frequencies are much more separated than the broadened linewidth of the transition. The transition is broadened, on the one hand, by the power of the laser beams (see Ref. [91]) and, on the other hand, by the beam profiles of the trapping beams, which can lead to inhomogeneous AC Stark shifts for the atoms. In our setup, the separation of the transitions is dominated by the differential Zeeman splitting between $^1S_0$ and

$^3P_1$ for $|\Delta m_F| := |m'_F - m_F| = 1$, which is $\Delta E_{Zeeman} = 1.4$ MHz / G for ^{171}Yb and $\Delta E_{Zeeman} = 597$ kHz / G for ^{173}Yb. With an external magnetic field of about 18 G, the transitions are split by 10.7 MHz. On the one hand, this is far enough separated to address the transitions individually with reasonable power (to have enough absorption processes for a good depletion) and, on the other hand, the energy differences are manageable with frequency changes of a double-pass acousto-optic modulator (AOM). For ^{171}Yb, it is much simpler to address the states individually, since there are only two different nuclear spins. Thus, the separation of the two transitions can take up the full operation range of an AOM.

We perform the optical pumping in between the two evaporation stages. At this point of the cooling, the confinement of the atoms is homogeneous enough, such that the linewidth broadening caused by the beam profiles of the trapping beams is weak enough to address the states individually for all atoms. At the same time, the confinement is still strong enough to keep the atoms trapped, when the optical pumping gives the atoms a momentum impact. We use the 3D MOT beams for the optical pumping since they are already aligned at the atoms and have a rather homogeneous intensity over the atomic sample. Depending on the desired final results of populated m_F states, we perform up to five pump pulses towards lower or higher states. A single pump pulse with a duration from 10 μs to 1 ms can depopulate a single m_F state to a great extent and pumps the atoms either to higher states $m_F \rightarrow m_F + \{1, 2\}$ or to lower states $m_F \rightarrow m_F - \{1, 2\}$. The repopulation after a single absorption process towards higher or lower states depends on the Clebsch-Gordan coefficients, which can be found in Ref. [115, 116] for the used transition.

For a clear depopulation of a spin state and without repopulation of others, blast pulses can be used. They can be either used before the main preparation of the measurement state for a cleaner preparation or directly before the imaging to image a single spin state for example. The blast pulses are done almost in the same way as the pump pulses. The differences between them are the following. The blast pulses are used, when the trapping confinement is weak enough to let the targeted atoms escape. Also, the pulse durations can be longer and the resonance frequencies are slightly different because of the reduced dipole potential. The population of the m_F states stays stable as long as the quantization axis is either not changed at all or only adiabatically, such that the spin orientation of the atoms can follow it. This stability of the spin state population results from the lack of spin-changing collisions (see section 1.1) for ytterbium's ground and clock state.

With an optical pumping sequence, we can produce atomic samples with different populations in the m_F states, from spin-polarized samples to samples with only one depopulated m_F state. We can also produce off-balanced samples with, for example 75 % of atoms in one m_F state and 25 % of atoms in another. In Fig. 1.3 an unperturbed, spin-balanced sample is shown together with spin-polarized samples for the six different spin states of ^{173}Yb. The spin states are separated before they are imaged using an optical Stern-Gerlach technique (see Sec. 1.5.2). Spin manipulation is used for all measurements described in this thesis.

1.3.3 Clock State Addressing

Another possible manipulation of atomic states is the addressing and preparation of ytterbium's clock state $^3P_0$. The clock state has a long lifetime, which we observed to be $\tau \approx 4$ s in our optical lattice (see Sec. 1.4), and, thus, can be treated as stable for the time scales of typical quantum gas experiments and for the measurements presented in this thesis. Here, we explain the requirements for exciting ground

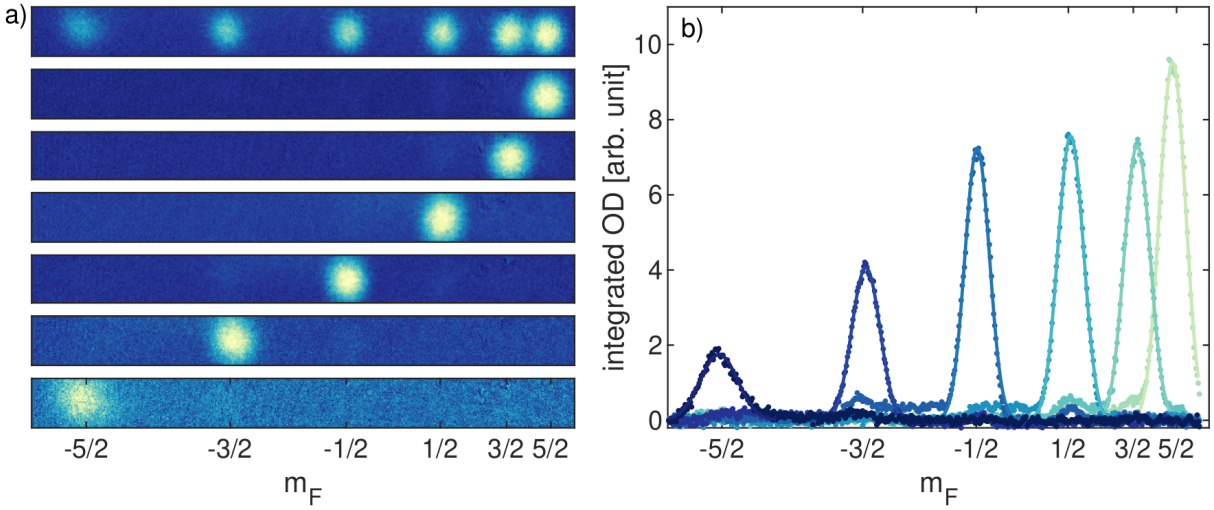

Figure 1.3: Spin state manipulation. The figures show the m_F states of 173Yb for an unperturbed spin distribution and for spin-polarized gases in different m_F states. The states are spatially separated on the images by applying an optical Stern-Gerlach technique (see Sec. 1.5.2). Figure a) shows the optical density images, while figure b) shows an integrated signal along the vertical direction of the images in figure a) for all spin-polarized cases. Taken from Ref. [100].

state atoms into the clock state. In this thesis, the meta-stable clock state is used to probe interaction strengths (see chapter 2).

The clock state has the same number of m_F states as the ground state and can be excited with different polarizations of a laser beam. We perform the excitation either with a π pulse on resonance or with a rapid adiabatic passage (RAP; see Ref. [90, 117]) over the resonance. As the natural linewidth of the clock transition is very narrow with $\Gamma < 2\pi \times 10$ mHz [118], we take several measures to avoid broadening the transition resonance. First, we trap the atoms only a three dimensional optical lattice (see Sec. 1.4) without additional dipole traps and operate the lattice beams at the magic wavelength (see Ref. [119]) of the desired clock transition. Second, we make the optical lattice deep enough to be in the Lamb-Dicke regime (see for example Ref. [120]). In addition to the efforts for keeping the transition linewidth narrow, we reduce the linewidth of our clock laser, which is used to address the transition. For the reduction of the linewidth, the laser is locked on an ultrastable cavity in a shielded housing. Furthermore, a fiber noise cancellation technique is applied. A detailed description of the experimental setup and challenges of the frequency stabilization can be found in Ref. [95, 98, 100]. The narrowest linewidth, we measured with this setup, is 26.7(2.4) Hz full width at half maximum (FWHM).

In this section, we described the basic addressing and preparation of different isotopes and states. The different techniques can be used in various combinations. Starting with the selection of the isotope or mixture, different possibilities for m_F states and clock state are available.

1.4 Atoms in Optical Lattices

After clarifying the internal degrees of freedom for the choice of the quantum gas with the isotope and atomic state selection, a common external degree of freedom is described in this section. Optical lattices are used to implement periodic potentials for quantum gases. This is often imposed with the aim, that

the atoms mimic the behavior of electrons in the atomic potential of solid state materials. All main measurements in this thesis are performed with atoms in optical lattices. First, we present the creation of optical lattices and introduce their mathematical description. Second, we give a background about the theories for describing particles in periodic potentials: Bloch's theorem and Wannier states. Third, we discuss a more specific model relevant for our system: the Fermi-Hubbard model.

1.4.1 Optical Lattices

Laser beams can be used to implement a periodic potential for atoms and, thus, realize an optical lattice. This requires, that the laser radiation imposes an AC Stark shift on the atoms and that the laser beams interfere, such that they form standing waves. A simple scenario to realize an optical lattice is to use two counter-propagating laser beams at the same wavelength λ_{lat}, with the same polarization and which are phase-locked to each other. This can be realized with a single beam, which is retro-reflected. The wave number of the beams is $k_{\mathrm{lat}} = 2\pi/\lambda_{\mathrm{lat}}$ and the propagation direction is along z. Then, the laser beams create the lattice potential [121]

$$V_{\mathrm{lat}} = V_0 \cos^2(k_{\mathrm{lat}} z), \tag{1.1}$$

where V_0 represents the depth of the lattice, which is commonly given in units of the recoil energy $E_{\mathrm{rec}} = \hbar^2 k_{\mathrm{lat}}^2/(2m)$.

In our experiment, we use a retro-reflected one-dimensional lattice (1D lattice) along z and a two-dimensional lattice (2D lattice) in the x-y plane, which is formed by three laser beams under an angle of 120 degrees. For the results in this thesis, the 2D lattice is operated as a triangular lattice with a linear polarization out of plane, but in general it can be used as a hexagonal lattice or other structures with different polarization (see Ref. [122]). The optical lattices used in this thesis are operated at the magic wavelength (see Ref. [119]) to enable narrow clock transitions (see subsection 1.3.3). However, we have an additional 1D lattice at a wavelength of $\lambda = 660$ nm, which is used to implement a state-dependent potential for the ground and clock state atoms (see Ref. [100]).

1.4.2 Bloch's Theorem and Wannier States

Particles in a periodic potential V_{periodic}, such as atoms in an optical lattice, can be described by Bloch waves according to the Bloch theorem [93]. The Bloch waves are the solution of the corresponding stationary Schrödinger equation

$$\mathcal{H}\psi = \left[\frac{p^2}{2m} + V_{\mathrm{periodic}}\right]\psi = E\psi. \tag{1.2}$$

For a single dimension z, a Bloch wave $\psi_{n,q}$ depends on the band index n and the quasimomentum q as follows [93]

$$\psi_{n,q}(z) = \mathrm{e}^{iqz} \cdot u_{n,q}(z), \tag{1.3}$$

where $u_{n,q}(z)$ has the same periodicity as V_{periodic}. The momentum is not a good quantum number in these systems and is replaced by the band index and the quasimomentum, which is reduced to the first Brillouin zone (see Ref. [93]).

In a periodic potential, particles can be either rather delocalized over many lattice sites or stronger confined to a single lattice site. In an optical lattice, this depends on the lattice depth V_0. For the delocalized

case, Bloch waves are a common description, but for localized particles a description in terms of Wannier states is more suited. The Wannier states can be expressed by Bloch waves as [121, 123]

$$w_{n,\vec{r}_i}(\vec{r}-\vec{r}_i) = \Theta^{-1/2} \sum_{\vec{q}} \mathrm{e}^{-i(\vec{q}\vec{r}_i)} \psi_{n,q}(\vec{r}), \tag{1.4}$$

where $\vec{r}_i$ is a lattice vector. The Wannier functions are a complete set of states for each band n [121].

1.4.3 Fermi-Hubbard Model

In the tight-binding approximation, particles in a lattice are localized to single lattice sites and only nearest neighbor tunneling is considered. Furthermore, interactions are limited to particles at the same lattice site (on-site interaction) [93]. This is a good approximation for deep enough lattices. Hubbard models can describe the dynamics of the particles in this approximation, if we assume that all particles are in the lowest Bloch band. The Fermi Hubbard Hamiltonian for fermions with spin σ is in second quantization [124]

$$\hat{\mathcal{H}}_{\text{Fermi-Hubbard}} = -t \sum_{<i,j>,\sigma} \left(\hat{c}^{\dagger}_{i,\sigma} \hat{c}_{j,\sigma} + \hat{c}^{\dagger}_{j,\sigma} \hat{c}_{i,\sigma} \right) + U_{\text{int}} \sum_{j,\sigma\neq\sigma'} \hat{n}_{j,\sigma} \hat{n}_{j,\sigma'}, \tag{1.5}$$

where $\hat{c}^{\dagger}_{j,\sigma}$ ($\hat{c}_{j,\sigma}$) creates (annihilates) a particle with spin m at lattice site $\vec{r}_j$, $\hat{n}_{j,\sigma} := \hat{c}^{\dagger}_{j,\sigma}\hat{c}_{j,\sigma}$ is the fermionic number operator and $<i, j>$ denotes, that the sum only considers nearest neighbor lattice sites. The tunneling matrix element t can be calculated as [121]

$$t = \int w^{*}_{\vec{r}_i}(\vec{r}) \left[\frac{p^2}{2m} + V_{\text{periodic}} \right] w_{\vec{r}_j}(\vec{r})\, \mathrm{d}\vec{r} \tag{1.6}$$

and the interaction potential U_{int} as [121]

$$U_{\text{int}} = g \int \left| w(\vec{r}) \right|^4 \mathrm{d}\vec{r}, \tag{1.7}$$

where we denoted the Wannier function for the lowest Bloch band as $w_{\vec{r}_i} := w_{0,\vec{r}_i}$. If interactions are limited to s-wave scattering (see Ref. [104]), the interaction strength g is given by [121]

$$g = \frac{4\pi\hbar^2 a}{m}, \tag{1.8}$$

where a is the s-wave scattering length and m is the mass of the interacting particle.

In this section, we introduced the description of physics in optical lattices. We explained how laser beams can create a periodic potential for atoms, presented the eigenstates of such a system and introduced the Fermi-Hubbard model. All the results in this thesis, where at least partially conducted in optical lattices.

1.5 Detection of Atomic States

So far in this chapter, we discussed our capabilities to prepare and manipulate different quantum systems with ytterbium atoms in our quantum gas machine. In this last section of the chapter, we cover our

methods to detect atoms and their internal and external quantum states. These techniques are essential for any measurements. First, we describe our basic absorption imaging of ground state atoms and the detection of the atoms' momentum state. Second, we discuss the detection of different nuclear spin states. Third, we report on the simultaneous imaging of different isotopes and the detection of clock state atoms.

1.5.1 Absorption Imaging and Momentum Detection

In our experiment, we use absorption imaging to image ground state atoms. For this purpose, we shine laser beams on the atoms, which are resonant with the blue transition $^1S_0 \rightarrow {}^1P_1$ of the desired ytterbium isotope. The atoms absorb the resonant photons and, thus, reduce the optical density of the imaging beam at their position. This difference in optical density is measured by taking two images; one with atoms and a second one without atoms as a reference. These two imaging pulses are displayed in the typical cooling sequence illustration in Fig. 1.2. In addition, we take two dark images without atoms and without imaging light to further improve the imaging quality in further processing (see Ref. [92]).

We use two different imaging axis and objectives. The main imaging is along the x direction, which is in the horizontal plane and perpendicular to the 1D lattice. It has a magnification of 4.7 and is used for all main results presented in this thesis. Images along this direction are taken with an EMCCD camera. The second imaging axis is along the z direction, which means along the 1D lattice and orthogonal to the 2D lattice. It has a magnification of 2.2 and is mainly used for 2D lattice alignment and calibration. Images along this direction are taken with a CCD camera. For further details on the imaging beam setup and the imaging procedure see Ref. [100, 125]. The absorption imaging is the basis of the atomic state detection and used in all other detection methods.

In most cases, we image the atomic cloud after a time of flight (TOF), in which the atoms fall towards gravity direction and additionally move according to their initial momentum. Typical TOFs of 16 to 19 ms long enough for the atoms to move far enough, such that their initial spatial position within the cloud can be neglected and their position at the moment of the imaging, resembles their momentum state. This allows us, to image the atoms in momentum space. Moreover, for atoms in optical lattices, we can image the quasimomentum state in different bands by applying a bandmapping technique (see Ref. [126]). For this purpose, the lattice power is ramped down quasi-exponentially, in such a way, that the quasimomentum of the atoms goes over into momentum in real space. This means, that the ramp needs to be non-adiabatic to avoid band transitions [126, 127]. Occupation of higher bands is mapped to the corresponding Brillouin zones.

1.5.2 Spin State Imaging

At our quantum gas machine, we use two different methods to detect population in single m_F states of ytterbium's ground state. The first method uses an optical Stern-Gerlach (OSG) technique (see Ref. [128, 129] and the second method relies on blast pulses, which are described in Sec. 1.3.2.

The OSG technique uses a spin state-dependent force to separate different spin states spatially. This force is realized with AC Stark shifts and an intensity gradient over the atomic sample. For small enough detunings from a resonance, the AC Stark shifts can be different for each m_F state. The intensity gradient can be provided by the slope of a laser beam profile, when the beam is not exactly centered on the atomic

Table 1.3: Comparison of spin-selective imaging via blast pulses and OSG. The table lists application advantages and disadvantages of two spin-selective imaging techniques described in the main text.

	OSG	**Blast pulses**
Advantages	• all spin states detected in same image	• momentum of atoms stays unperturbed
Disadvantages	• momentum of atoms is influenced	• only one spin state population imaged per cycle

cloud, but slightly displaced, such that the center of the beam does not hit the atoms. We implement this with a laser beam of σ^- polarized light at a detuning of 1.4 GHz above the $|^1S_0, F = 5/2\rangle \rightarrow |^3P_1, F' = 7/2\rangle$ transition of ^{173}Yb. We apply laser pulses with a power of 30 to 40 mW and durations of 200 to 800 μs right after the release of the atoms from their confinement and during TOF. After a reduced TOF of typically 13.5 ms, the different spin states are separated because of the additional momentum gained by the state-dependent force and can be detected individually in the same absorption image. We use the same OSG beam with the same parameters for ^{171}Yb and ^{173}Yb atoms. We can even image all different m_F states of both isotopes at the same time (see Sec. 1.5.3). A disadvantage of the OSG is, that the momentum of the atoms is influenced and, thus, that a simultaneous momentum imaging is not possible or at least has a higher uncertainty. For further details on the implementation and the optical setup see Ref. [95, 97, 114].

For the second method, blast pulses are used right before the imaging to depopulated targeted spin states. We can check the influence of the blast pulses with OSG images. If necessary, we can improve the blasting effect by adjusting AOM frequencies, pulse durations or the beam power. If the blast pulse sequence has the desired effect in the OSG images, we can use the sequence without the OSG to get the undisturbed momentum information, if combined with the momentum detection described above. Usually, we apply them to depopulated all states but one. This remaining state is then imaged alone with the absorption imaging described above. With this procedure, we can implement a spin-selective imaging. We can image, for example, the quasimomentum of a single m_F state in a system where several m_F states are present. This is exploited in chapters 3 and 5. However, for a single measurement cycle, we can only determine the individual population of a single spin state. A comparison of different spin state populations can only be achieved by performing several measurement cycles and taking the uncertainty of cycle-to-cycle fluctuations into account. An application comparison of our two spin-selective imaging methods is shown in Table 1.3.

1.5.3 Imaging of Isotope Mixtures and Clock State Atoms

The basic absorption imaging sequence as described above in subsection 1.5.1, can be altered in the following ways to allow double imaging methods. These methods enable, on the one hand, the detection of ^{171}Yb and ^{173}Yb ground state atoms in the same measurement cycle, and, on the other hand, the detection of ground state and clock state atoms of a single isotope.

For the detection of isotope mixtures, the imaging beams for ^{171}Yb and ^{173}Yb are overlapped and aligned along the main detection axis. The first absorption image is taken with imaging light, which is resonant for ^{171}Yb, whereas the reference image is taken with imaging light, which is resonant for ^{173}Yb. The

data and reference images are taken with a delay in between, such that the ^{173}Yb atoms experience a longer TOF (typically 19 ms) and are imaged at a different position than the ^{171}Yb atoms with a typical TOF of 16 ms. Because of the different positions, the reference image can still function as a reference for ^{171}Yb and the data image can be used as a reference for ^{173}Yb. The evaluation of the images needs to be adjusted accordingly. The imaging beams are overlapped and aligned along the main detection axis. Isotope double imaging is used in chapter 2. For details on the planning, implementation and imaging laser system see Ref. [100, 114].

For detecting atoms in the clock state, the atoms are first repumped into the ground state and, then, imaged with the ground state imaging light. For this purpose, a repumper with a wavelength of 1389 nm is used, which addresses the transition $^3P_0 \rightarrow {}^3D_1$. Atoms, which are excited to the $^3D_1$ state, decay either into the $^3P_2$, into the $^3P_1$ or back into the $^3P_0$ state. We drive the transition long enough, such that remaining clock state population can be neglected. Then, atoms have a theoretical probability of 97.5 % to decay back into the ground state via the $^3P_1$ state [97]. The remaining 2.5 % of atoms in the $^3P_2$ state are not imaged. This branching ratio is accounted for in the evaluation of the number of excited state atoms. The repumper can be used for ^{171}Yb and ^{173}Yb atoms.

For double imaging ground state and clock state atoms in the same image, the basic absorption imaging procedure is altered similarly as for the isotope double imaging. First, the absorption image of the ground state atoms is taken. Second, remaining ground state atoms are blasted away. Third, atoms in the clock state are repumped to the ground state. Fourth, the reference image is taken, which images the repumped atoms. The ground state atoms experience typically a TOF of 16 ms and the repumped atoms a TOF of 19 ms. Thus, as for the isotope double imaging, atoms of different initial states are imaged at different positions on the same image and and the reference image can function as a reference for the ground state atom detection and the first image can function as a reference for the excited state atom detection. As the repumping process is not spin-conserving, the detection of clock state atoms is not spin-resolved. However, first steps have been taken for the implementation of a spin-conserving repumping mechanism at our experiment (see Ref. [100, 130] for details). Clock state imaging is used in chapter 2.

In this section, we described our methods to detect atoms and their internal and external quantum states. We described the basic absorption imaging of ground state atoms and the detection of the atoms' momentum state. We discussed the detection of different nuclear spin states and we reported on the simultaneous imaging of different isotopes and the imaging of clock state atoms. We can combine the different detection methods to image for example all different m_F states of ^{171}Yb and ^{173}Yb atoms in a single image or the quasimomentum of a single spin state in a spin mixture.

This chapter introduced the general theoretical models and experimental methods used for the experimental results in this thesis. We introduced relevant properties of ytterbium and explained our setup to trap and cool atoms. Furthermore, we discussed our capabilities to engineer different quantum systems by selecting isotopes, manipulating internal and external atomic states and covered our techniques for the detection of atoms and their internal and external states. Moreover, we addressed the particularly relevant physics of stimulated Raman transitions, which are used to realize an artificial gauge field in chapters 3 and 5. This chapter provided the basic knowledge to understand the research described in the rest of this thesis.

2 Probing Interactions with Clock Spectroscopy

In the previous chapter, we introduced the basic theoretical models and experimental methods of our quantum gas machine. On this basis, we present results for probing interactions in Fermi gases and Fermi-Fermi isotope mixtures with clock spectroscopy in this chapter. We discuss the specific underlying theories and the experimental approaches to gain insight into the systems.

Because of its narrow natural linewidth, clock transitions in alkaline earth (like) atoms (see Sec. 1.1) are used for high precision spectroscopy measurements. In particular, the combination of narrow linewidths and the low temperatures of quantum gases enables the detection of interaction induced energy shifts. This concept was exploited to measure different kinds of interactions in Ref. [53–57, 60]. We use our high precision spectroscopy to detect energy shifts, which are induced by inter-orbital interactions of either distinguishable or indistinguishable particles. In the first part of this chapter, we present results from a set of measurements on interorbital interisotope interactions in Fermi-Fermi mixtures of ^{171}Yb and ^{173}Yb. We measure the elastic and inelastic part of the interactions and directly show the SU(2) $\otimes$ SU(6) symmetry of the elastic scattering lengths. In the second part, we report on another set of measurements on interorbital interactions in a spin-balanced ^{171}Yb gas, where we determine the direct and spin-exchange interactions. During our investigations, the latter interactions have also been characterized in Ref. [58, 59].

The work in this chapter was done under the project administration and supervision of C. Becker and K. Sengstock. First measurement series of the interorbital interisotope interactions were conducted by B. Abeln, K. Sponselee, N. Pintul and the author. The final measurements were taken and analyzed by B. Abeln and K. Sponselee. First measurement series of the spin-exchange interaction in ^{171}Yb were conducted and analyzed by B. Abeln, K. Sponselee and the author. The final measurements shown here were taken by B. Abeln, K. Sponselee and the author with help of N. Pintul. The final data analysis was performed by B. Abeln and K. Sponselee. The main results of this chapter are published in Ref. [16]. For details about high precision spectroscopy with our clock laser in general see Ref. [99, 100].

2.1 Interorbital Interactions of ^{171}Yb-^{173}Yb Mixtures

As introduced above, in this first section of the chapter, we present results on interorbital interisotope interactions in Fermi-Fermi mixtures of ^{171}Yb and ^{173}Yb, where we fully characterize the interactions. The isotope mixtures described here feature an SU(2) $\otimes$ SU(6) symmetry, which might enable quantum simulation of two-flavor superfluid symmetry-locking phases [131, 132]. Our measurements give insight into these exotic mixtures and generally extend the knowledge about Fermi-Fermi mixtures with SU(2) $\otimes$ SU($\mathcal{N} \geq 2$) symmetry. The section is structured as follows. First, we describe the theory of the elastic interactions in the Fermi-Fermi mixtures with possible scattering channels. Second, we present our measurements on interaction strength and interaction symmetry. Third, we address the inelastic interactions in the mixtures.

2.1.1 Theory of Elastic Interactions

Before we present our measurements on the interactions in Fermi-Fermi mixtures of ^{171}Yb and ^{173}Yb, we describe the theory of the elastic interactions and their properties in the following. The interactions in the mixtures are characterized by the Hubbard on-site interaction defined in Eq. 1.7. Furthermore, as we exclusively consider s-wave scattering, the interaction strength g is given by Eq. 1.8. We denote an interisotope quantity X in the form ${}^{171}_{173}X_{ij}$ for a ^{171}Yb atom in orbital state i and a ^{173}Yb atom in orbital state j. The Hubbard on-site interaction is adjusted for the case of interisotope interactions, such that the interaction potential is [16]

$$ {}^{171}_{173}U_{ij} = \frac{4\pi\, {}^{171}_{173}a_{ij}\,\hbar^2}{2\mu} \int \left|w_0(s_{1D}, s_{2D}, \vec{r})\right|^4 \, \mathrm{d}\vec{r}, \tag{2.1} $$

where ${}^{171}_{173}a_{ij}$ is the interisotope s-wave scattering length and w_0 the Wannier functions of the lowest band, which depend on the lattice depths s_{1D} and s_{2D} of our 1D and 2D lattice, respectively, and the lattice geometry. A particularly relevant feature of the on-site interactions discussed in this chapter is the SU($\mathcal{N}$) symmetry (see Sec. 1.1). It is characteristic for the ground and clock state of alkaline earth (like) atoms, which have a close-to-perfect decoupling of the nuclear spin and electronic angular momentum, which manifests in the fact, that the total electronic angular momentum $J = 0$. In the measurements presented in this section, we want to prove, that the interisotope interactions of the Fermi-Fermi mixture are in fact SU(2) $\otimes$ SU(6) symmetric, which would mean, that the interactions are independent of the spin projections of the atoms.

In the following, we demonstrate, that the twelve different possible spin projections of the two isotopes can only interact via two distinguishable scattering lengths (in different compositions). This means, that it is sufficient to show, that these two scattering lengths are equal to prove the full SU(2) $\otimes$ SU(6) symmetry. Since s-wave interactions are rotationally symmetric, the corresponding interaction Hamiltonian $\mathcal{H}_{\text{int, s-wave}}$ commutes with the square of the total spin operator $\hat{F}^2$. The total spin of the system is $\vec{F} = \vec{f}_{171} + \vec{f}_{173}$ and the total magnetization is $M = m_{171} + m_{173}$, where $\vec{f}_{171}$ ($\vec{f}_{173}$) is the total spin and m_{171} (m_{173}) is the magnetization along z of the ^{171}Yb (^{173}Yb) atom. Then, $\mathcal{H}_{\text{int, s-wave}}$ can be expressed in the eigenfunctions $|F, M\rangle$ of operator $\hat{F}^2$, such that [16]

$$ \mathcal{H}_{\text{int, s-wave}} = \frac{4\pi\hbar}{2\mu}\delta(\vec{r}_1 - \vec{r}_2) \sum_{F=|f_{171}-f_{173}|}^{F=f_{171}+f_{173}} \sum_{M=-F}^{F} a_F \, |F, M\rangle \langle F, M| \, . \tag{2.2} $$

In this equation, $\delta(\vec{r}_1 - \vec{r}_2)$ denotes the Dirac delta function for atoms at positions $\vec{r}_1$ and $\vec{r}_2$ and the summations go over all possible $|F, M\rangle$ states. The equation shows, that the scattering lengths a_F only depend on the total spin F. Our isotope mixtures have the spins $f_{171} = 1/2$ and $f_{173} = 5/2$. Therefore, the total spin can only reach the values $F = 2$ and $F = 3$. This means, that there are only two different scattering lengths in our system: a_2 and a_3. Thus, to prove SU(2) $\otimes$ SU(6) symmetry, it is sufficient to demonstrate, that $a_2 = a_3$.

In our measurements, we do not have direct access to these scattering lengths, as we operate in the magnetization basis $|m_{171}, m_{173}\rangle$. We use this basis, because we can experimentally control and observe the single magnetization of the particles, but not the total spin or the total magnetization. The transformation between the two bases is described by

$$ |m_{171}, m_{173}\rangle = \sum_{F=|f_{171}-f_{173}|}^{F=f_{171}+f_{173}} c^{F,M}_{m_{171},m_{173}} \, |F, M\rangle \, , \tag{2.3} $$

where $c^{F,M}_{m_{171},m_{173}}$ denote the Clebsch-Gordan coefficients and, for the case of ^{171}Yb-^{173}Yb Fermi-Fermi mixtures, the summation is carried out from $F = 2$ to $F = 3$. Using this basis transformation, we can extract the two a_F values, by measuring the interactions for only two different spin configurations in our magnetization basis.

2.1.2 Measurements of Elastic Interactions

After the theoretical description of the interorbital interactions and their properties, we describe measurements to determine the elastic scattering lengths for two different spin configurations of ^{171}Yb-^{173}Yb mixtures in the following. Furthermore, we proof the underlying SU(2) ⊗ SU(6) symmetry of the interactions. We prepare a degenerate Fermi-Fermi mixture of spin-polarized ^{171}Yb and ^{173}Yb atoms using the methods described in Sec. 1.2 and 1.3. We reach atom numbers of $N_{171,173} \approx 10$ to 40×10^3 atoms at $T_{171,173} \approx 0.25$ to $0.55\ T_\mathrm{F}$, where T_F is the Fermi temperature, and load the mixture into our magical optical 1D and 2D lattice (see Sec. 1.4). In the following, lattice depths are given in units of the recoil energy $E_\mathrm{r} = h \cdot 2.0\,\mathrm{kHz}$. Furthermore, we set a magnetic field of $B = 8.8\,\mathrm{G}$ in gravity direction. To this system, we apply π-polarized clock laser light co-propagating with our 1D lattice to excite ^{171}Yb or ^{173}Yb atoms from the ground state $^1\mathrm{S}_0$ to the excited state $^3\mathrm{P}_0$. The states are denoted as $|\mathrm{g}\rangle$ and $|\mathrm{e}\rangle$, respectively, in the following. For the excitation, we use rectangular π-pulses with a duration $t_\mathrm{pulse} = 1.6$ ms (1.55 ms) resulting in a Fourier-limited spectroscopic line width of $\Gamma_\mathrm{FWHM} \approx 500$ Hz (516 Hz). As the resonance frequencies of the two isotopes differ by approximately 20 GHz [115, 133], the locking point of our frequency stabilization (see Sec. 1.2) needs to be adjusted, when switching between the excitation of one isotope to another (see Ref. [100] for details). Consequently, we either excite ^{171}Yb or ^{173}Yb, but not both at the same time. After the excitation pulse, we detect the atom numbers of the ground and excited state with a double-imaging technique in the same image (see Sec. 1.5.3). The atom numbers are recorded for different laser frequencies around the clock transition resonance for single-particles to form a spectrum.

Moreover, we conduct auxiliary measurements to keep track of the linear drifts of our clock cavity, which is used for the frequency stabilization. In these auxiliary measurements, we record a spectrum of a single spin-polarized isotope and fit this data to extract the resonance position. Then, the linear drifts are continuously compensated afterwards. With these auxiliary measurements, we know the exact position of the single-particle resonances. Because of that, we can directly identify these resonances in the spectra recorded with isotope mixtures. As another auxiliary measurement, we record the blue sideband of our magic 1D lattice for each spectrum. This data provides a more accurate information on the 1D lattice depth than the momentum-resolved lattice modulation spectroscopy, which we typically use to calibrate the depth of our optical lattices (see Ref. [126]). As this data is only used for the 1D lattice calibration, we do not present it here. However, this data can be found in Ref. [100].

In Fig. 2.1, we present parts of our spectroscopic data for the excitation of either ^{171}Yb or ^{173}Yb. We plot the excited state fraction $n_\mathrm{e} = N_\mathrm{e}/(N_\mathrm{g} + N_\mathrm{e})$ as a function of the clock laser frequency detuning δ with respect to the single-particle resonance. Several spectra are shown for different 1D lattice depths as indicated by the legend. In each spectrum, we observe another spectroscopic feature despite the already identified single-particle resonance. We expect this feature to be the excitation of an atom at a doubly-occupied lattice site. With respect to the single-particle resonance, the peak of the $^{171}\mathrm{Yb}_\mathrm{e}$-$^{173}\mathrm{Yb}_\mathrm{g}$ or $^{171}\mathrm{Yb}_\mathrm{g}$-$^{173}\mathrm{Yb}_\mathrm{e}$ mixture would be displaced by the differential Hubbard on-site interaction $\Delta U_\mathrm{eg/ge} = {}^{171}_{173}U_\mathrm{eg/ge} - {}^{171}_{173}U_\mathrm{gg}$. Moreover, the interaction peak displacement would depend on the 1D lattice

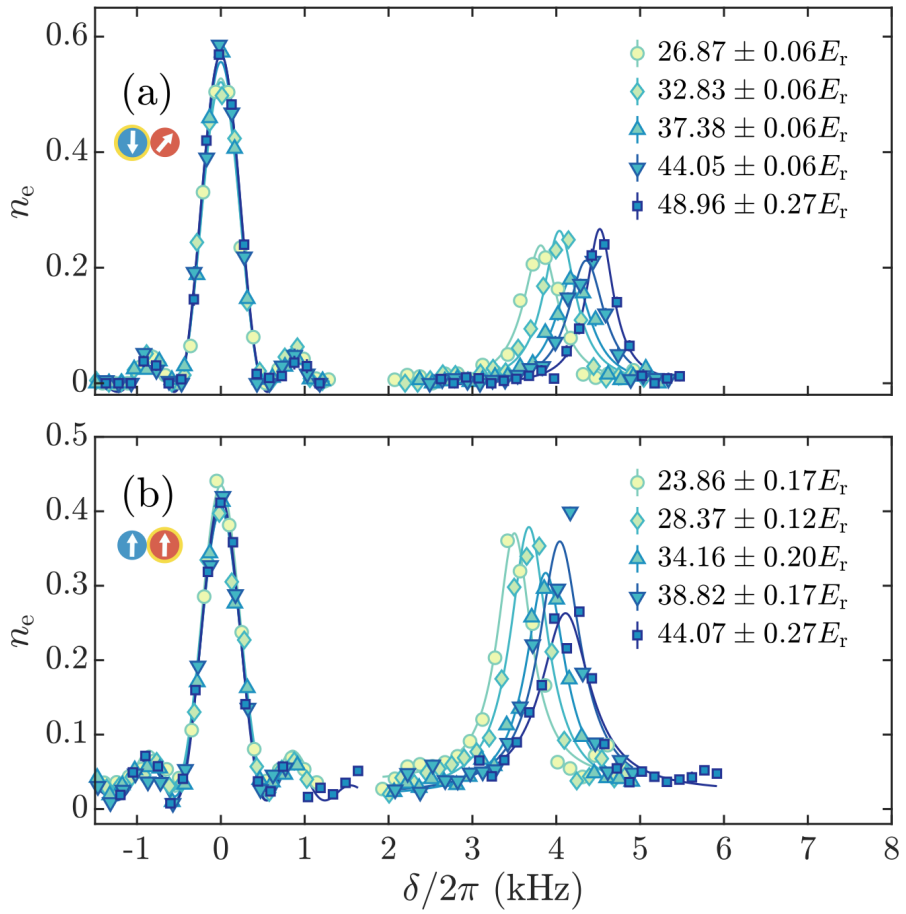

Figure 2.1: Spectroscopy of elastic interactions. The figure shows the excited state fraction n_e as a function of the clock laser frequency detuning with respect to the single-particle resonance. Spectroscopy for the excitation of ^{171}Yb is presented in (a), while spectroscopy for the excitation of ^{173}Yb is presented in (b). Data points represent single measurements of n_e. Lines show a fit with a sinc^2 function for the peaks at $\delta = 0$ and a fit with a Lorentzian for the remaining peaks. Different markers and colors denote different 1D lattice depths s_{1D} as listed in the legends, whereas the 2D lattice depths is fixed at $s_{2D} = 16.971(15)\, E_r$. Reprinted figure with permission from Ref. [16]. Copyright 2021 by the American Physical Society.

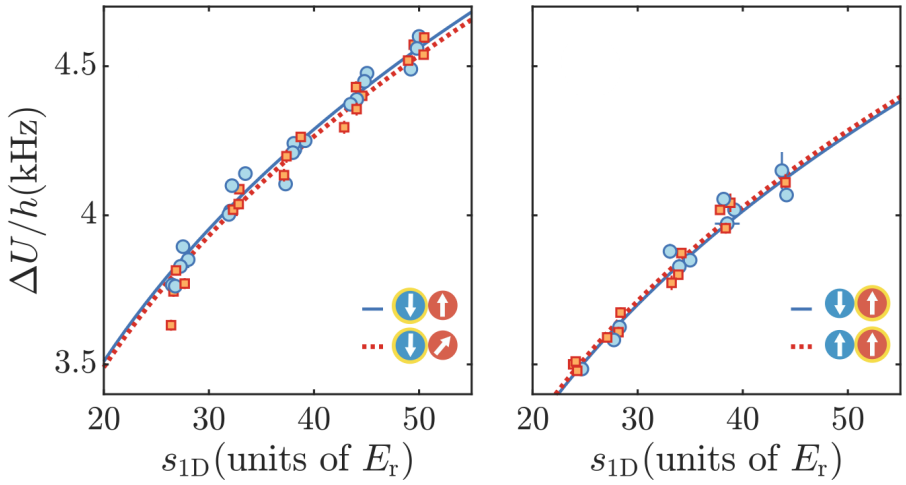

Figure 2.2: Elastic interactions in lattice depth dependence. The figure shows the differential interisotope interorbital interactions ΔU as a function of the 1D lattice depth s_{1D} for the the excitation of ^{171}Yb on the left and for the excitation of ^{173}Yb on the right. ΔU is obtained by the frequency difference between single-particle and interaction peaks for spectra as shown in Fig. 2.1, while s_{1D} is determined from auxiliary measurements as described in the main text. Each data point is extracted from a single spectrum and error bars represent the peak fit uncertainty. For each excitation, data is presented for several measurements and two different spin configurations, which are denoted by different markers and colors as illustrated in the legends. The spin configurations are $|m_{171} = -1/2; m_{173} = 5/2\rangle$ and $|-1/2; 3/2\rangle$ in the figure on the left and $|-1/2; 5/2\rangle$ and $|1/2; 5/2\rangle$ in the figure on the right. For each excitation and spin configuration, the data is fitted using Eq. 2.1 with the differential scattering length $\Delta a_{\mathrm{eg/ge}} = {}^{171}_{173}a_{\mathrm{eg/ge}} - {}^{171}_{173}a_{\mathrm{gg}}$ as a free parameter. The fits are plotted as solid and dashed lines in the colors of the respective data points. Reprinted figure with permission from Ref. [16]. Copyright 2021 by the American Physical Society.

depth because of the Wannier functions, as it can be seen in Eq. 2.1. In the spectra, we can observe a monotonic increase of the frequency difference between the single-particle peak and the interaction peak candidate for increasing lattice depth. This behavior matches the expectations from the Wannier integrals, thus, we claim, that the second spectroscopic feature is in fact the interaction peak. We fit the single-particle resonances in the spectra with a sinc^2 function and the interaction peak with a Lorentzian. Then, we extract the difference between the two peak positions, which is identical to ΔU (denotes either ΔU_{eg} or ΔU_{ge}). We plot ΔU as a function of the 1D lattice depth s_{1D} in Fig. 2.2. In addition to the data displayed in Fig. 2.1, we include data of two different spin configurations for each isotope excitation, namely $|m_{171} = -1/2; m_{173} = 5/2\rangle$ and $|-1/2; 3/2\rangle$ for the excitation of ^{171}Yb and $|-1/2; 5/2\rangle$ and $|1/2; 5/2\rangle$ for the excitation of ^{173}Yb. We fit this data with $\Delta U_{\mathrm{eg/ge}}$ using Eq. 2.1, where we use the differential scattering length $\Delta a_{\mathrm{eg/ge}} = {}^{171}_{173}a_{\mathrm{eg/ge}} - {}^{171}_{173}a_{\mathrm{gg}}$ as a free parameter. The result of the fit is plotted as a blue solid line (red dotted line) for the first (second) spin configuration in Fig. 2.2. The good agreement of the fit with the data confirms the underlying theory. From the fit, we obtain the lattice independent observable $\Delta a_{\mathrm{eg/ge}}$ for each data set.

The differential scattering lengths $\Delta a_{\mathrm{eg/ge}}$ can be expressed in the two fundamental scattering lengths $\Delta a_2 = a_2 - {}^{171}_{173}a_{\mathrm{gg}}$ and $\Delta a_3 = a_3 - {}^{171}_{173}a_{\mathrm{gg}}$ by exploiting Eq. 2.2 and 2.3. For ΔU_{eg} the basis transformations

Table 2.1: Scattering length results. The table lists the results for the measurements of the differential scattering lengths for elastic interactions in ^{171}Yb-^{173}Yb mixtures.

Quantity	$^{171}\mathrm{Yb_e}$-$^{173}\mathrm{Yb_g}$	$^{171}\mathrm{Yb_g}$-$^{173}\mathrm{Yb_e}$
$\Delta a_{-1/2,5/2}$	498(1)	481.3(18)
$\Delta a_{-1/2,3/2}$	495.7(13)	-
$\Delta a_{1/2,5/2}$	-	482.9(13)
Δa_2	501.2(25)	481(2)
Δa_3	485(8)	482.9(13)
$\Delta\overline{a}$	497.4(8)	482(1)

are [16]

$$\Delta a_{-1/2,5/2;\mathrm{eg}}\,|-1/2;5/2\rangle = \sqrt{\frac{1}{6}}\Delta a_{3;\mathrm{eg}}\,|3,2\rangle - \sqrt{\frac{5}{6}}\Delta a_{2;\mathrm{eg}}\,|2,2\rangle \tag{2.4}$$

$$\Delta a_{-1/2,3/2;\mathrm{eg}}\,|-1/2;3/2\rangle = \sqrt{\frac{1}{3}}\Delta a_{3;\mathrm{eg}}\,|3,1\rangle - \sqrt{\frac{2}{3}}\Delta a_{2;\mathrm{eg}}\,|2,1\rangle \tag{2.5}$$

and for ΔU_{ge} the transformations are [16]

$$\Delta a_{-1/2,5/2;\mathrm{ge}}\,|-1/2;5/2\rangle = \sqrt{\frac{1}{6}}\Delta a_{3;\mathrm{ge}}\,|3,2\rangle - \sqrt{\frac{5}{6}}\Delta a_{2;\mathrm{ge}}\,|2,2\rangle \tag{2.6}$$

$$\Delta a_{1/2,5/2;\mathrm{ge}}\,|1/2;5/2\rangle = \Delta a_{3;\mathrm{ge}}\,|3,3\rangle\,. \tag{2.7}$$

We calculate Δa_2 and Δa_3 and determine the average $\Delta\overline{a}$ from the measured scattering lengths $\Delta a_{m_{171},m_{173}}$ of the two spin configurations for both interactions ΔU_{eg} and ΔU_{ge}. The results for the differential scattering lengths are listed in Table 2.1. The fundamental scattering lengths Δa_2 and Δa_3 do not differ significantly for both interactions ΔU_{eg} and ΔU_{ge}. This proofs the underlying SU(2) $\otimes$ SU(6) symmetry. Furthermore, the interactions for the two scenarios $^{171}\mathrm{Yb_e}$-$^{173}\mathrm{Yb_g}$ and $^{171}\mathrm{Yb_g}$-$^{173}\mathrm{Yb_e}$ are significantly different in their absolute values. This difference is unexpected, as the reduced mass is the same for both scenarios. Therefore, this could be interesting for theoretical studies of interactions, which go beyond mass scaling.

2.1.3 Inelastic Interactions

The measurements of the elastic interisotope interorbital interactions in the last section characterizes only one part of the interactions. For a full characterization, also the inelastic part of the interactions is required. Here, we conduct loss measurements on the $^{171}\mathrm{Yb_e}$-$^{173}\mathrm{Yb_g}$ and $^{171}\mathrm{Yb_g}$-$^{173}\mathrm{Yb_e}$ mixtures to extract the inelastic interactions and complete the interaction information for two different spin configurations for each mixture. Similar to the elastic interactions in Eq. 2.1, the inelastic part of the interactions ${}^{171}_{173}\Gamma_{ij}$ can be expressed by a lattice independent parameter ${}^{171}_{173}\beta_{ij}$ and a Wannier integral as [57]

$${}^{171}_{173}\Gamma_{ij} = {}^{171}_{173}\beta_{ij}\int \left|w_0(s_{1D}, s_{2D}, \vec{r})\right|^4 \mathrm{d}\vec{r}. \tag{2.8}$$

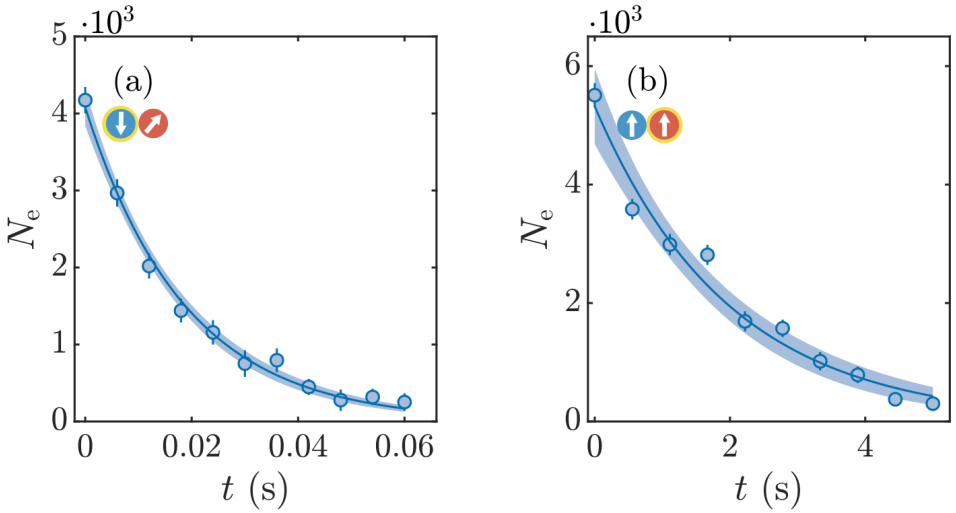

Figure 2.3: Typical loss measurements of ^{171}Yb$_e$-^{173}Yb$_g$ and ^{171}Yb$_e$-^{173}Yb$_g$ mixtures. The figure shows the number of excited atoms N_e as a function of holding time t in the optical lattice. Data for $|e, m_{171} = -1/2; g, m_{173} = 3/2\rangle$ is presented in (a), while data for $|g, 1/2; e, 5/2\rangle$ is presented in (b). Data points show the atom number determined by a single measurement and error bars the uncertainty in the determination. Solid curves show an exponential fit (see Eq. 2.10) and the shaded area around it the 95 % confidence interval of the fit. Lattice depths for the data in (a) are $s_{1D} = 24.0(2)\,E_r$ and $s_{2D} = 16.0(1)\,E_r$ and for the data in (b) $s_{1D} = 34.7(6)\,E_r$ and $s_{2D} = 17.0(4)\,E_r$. Reprinted figure with permission from Ref. [16]. Copyright 2021 by the American Physical Society.

For the measurement of the inelastic interactions ${}^{171}_{173}\Gamma_{ij}$ of the Fermi-Fermi mixtures, we prepare and excite the atoms in the same way as for the elastic interaction measurements. However, this time, we do not take spectra, but excite the atoms on resonance to the interaction states $|e, m_{171}; g, m_{173}\rangle$ and $|g, m_{171}; e, m_{173}\rangle$. Then, we measure the number of excited atoms N_e, which is equivalent to the number of excited doublons, for various holding times t in the lattice after the excitation pulse. The number of excited atoms is expected to decrease with time due to the inelastic interactions, however, despite the decay rate Γ_{int} caused by these two-body losses, the excited state fraction can also decrease via one-body losses. To distinguish between these two processes, we characterize the one-body losses separately and subtract them from the total losses. We obtain the decay rate via one-body losses Γ_0 by additionally measuring the losses in the number of excited atoms of the single-particle resonances for various holding times in the lattice. The decay rates are determined in the same way as for the two-body decay rates described below, but the data is not shown here. Then, the decay rate caused by inelastic collisions is

$$ {}^{171}_{173}\Gamma_{eg/ge} = \Gamma_{int} - \Gamma_0. \tag{2.9} $$

In Fig. 2.3 one example of the interaction state decay measurements for each interaction is shown, where the number of excited atoms N_e is plotted as a function of the holding time t. We expect an exponential decay (see Ref. [57]) and fit the data with the function [16]

$$ N_e(t) = N_d \exp(-t \cdot \Gamma_{int}), \tag{2.10} $$

where $N_d = N_e(t = 0)$ is the initial number of doublons. The fit with N_d and Γ_{int} as free parameters is displayed as a solid blue line and the shaded area around it shows the 95% confidence interval. These measurements are conducted for the same spin configurations as for the elastic interaction measurements

Table 2.2: Inelastic decay coefficients. The table lists the results for the determination of the decay coefficients for inelastic interactions.

Quantity	^{171}Yb$_e$-^{173}Yb$_g$	^{171}Yb$_g$-^{173}Yb$_e$
$\beta_{-1/2,5/2}$	$1.69(7) \times 10^{-12}$ cm^3 s^{-1}	$4.6(17) \times 10^{-15}$ cm^3 s^{-1}
$\beta_{-1/2,3/2}$	$1.79(5) \times 10^{-12}$ cm^3 s^{-1}	-
$\beta_{1/2,5/2}$	-	$3(1) \times 10^{-15}$ cm^3 s^{-1}

and for each spin configuration the decay rates are recorded for various 1D lattice depths s_{1D}. The data for further lattice depths can be found in Ref. [99]. For all data sets, N_e decreases monotonically with increasing holding time t and seems to vanish for long enough times. The behavior is in good agreement with the assumed exponential decay.

We extract the decay rates for the interaction states and the single-particle excitations and calculate ${}^{171}_{173}\Gamma_{eg/ge}$ using Eq. 2.9. The results are plotted as data points in dependence of the 1D lattice depth s_{1D} in Fig. 2.4. From this data, we determine the lattice independent parameters β for each interaction and spin configuration using Eq. 2.8. The values are $\beta_{-1/2,5/2} = 1.69(7) \times 10^{-12}$ cm^3 s^{-1} and $\beta_{-1/2,3/2} = 1.79(5) \times 10^{-12}$ cm^3 s^{-1} for ^{171}Yb$_e$-^{173}Yb$_g$ and $\beta_{-1/2,5/2} = 4.6(17) \times 10^{-15}$ cm^3 s^{-1} and $\beta_{1/2,5/2} = 3(1) \times 10^{-15}$ cm^3 s^{-1} for ^{171}Yb$_g$-^{173}Yb$_e$. The results are also listed in Table 2.2. Furthermore, we use the results of β to calculate ${}^{171}_{173}\Gamma_{eg/ge}(s_{1D})$ and plot it as solid lines in Fig. 2.4. The shaded area around the lines represents the 95 % confidence interval. These calculations agree well with the data points with only one exception and, thus, confirm the underlying theory.

For each interaction, the decay coefficients of the two spin configurations are equal within experimental uncertainties. However, in contrast to the elastic interactions, the inelastic interactions cannot be reduced to two fundamental scattering channels. Hence, it is not sufficient to prove the equality of two spin configurations to demonstrate a possible SU(2) $\otimes$ SU(6) symmetry. This proof, would require a measurement of the decay coefficients of all twelve spin configurations. The decay coefficients of the ^{171}Yb$_e$-^{173}Yb$_g$ mixtures are approximately 400 times stronger than the ones of the ^{171}Yb$_g$-^{173}Yb$_e$ mixtures, whereas the elastic interactions only slightly differ from each other (see Table 2.1). The origin of this difference is unclear. Possible reasons could be laser-assisted losses or photo-association to a molecular state in a similar way to the measurements in Ref. [105]. A source for these processes could be our 1D and 2D lattice, which are detuned with respect to each other by 160 kHz to prevent interferences.

In this section, we fully characterized the interisotope interorbital interactions of ^{171}Yb-^{173}Yb mixtures for two spin configurations. We determined the elastic scattering lengths ${}^{171}_{173}a_{eg}$ and ${}^{171}_{173}a_{ge}$ and proofed their SU(2) $\otimes$ SU(6) symmetry. Furthermore, we measured the decay coefficients ${}^{171}_{173}\beta_{eg}$ and ${}^{171}_{173}\beta_{ge}$ of the inelastic part of the interactions for two spin configurations. The values of ${}^{171}_{173}a_{eg}$ and ${}^{171}_{173}a_{ge}$ are similar, but differ significantly, which might be interesting for theoretical studies, as this difference cannot be explained by mass scaling. In contrast to the similar elastic interactions, the decay coefficients ${}^{171}_{173}\beta_{eg}$ are approximately 400 times stronger than ${}^{171}_{173}\beta_{ge}$, which makes ^{171}Yb$_g$-^{173}Yb$_e$ mixtures more suited for quantum simulations.

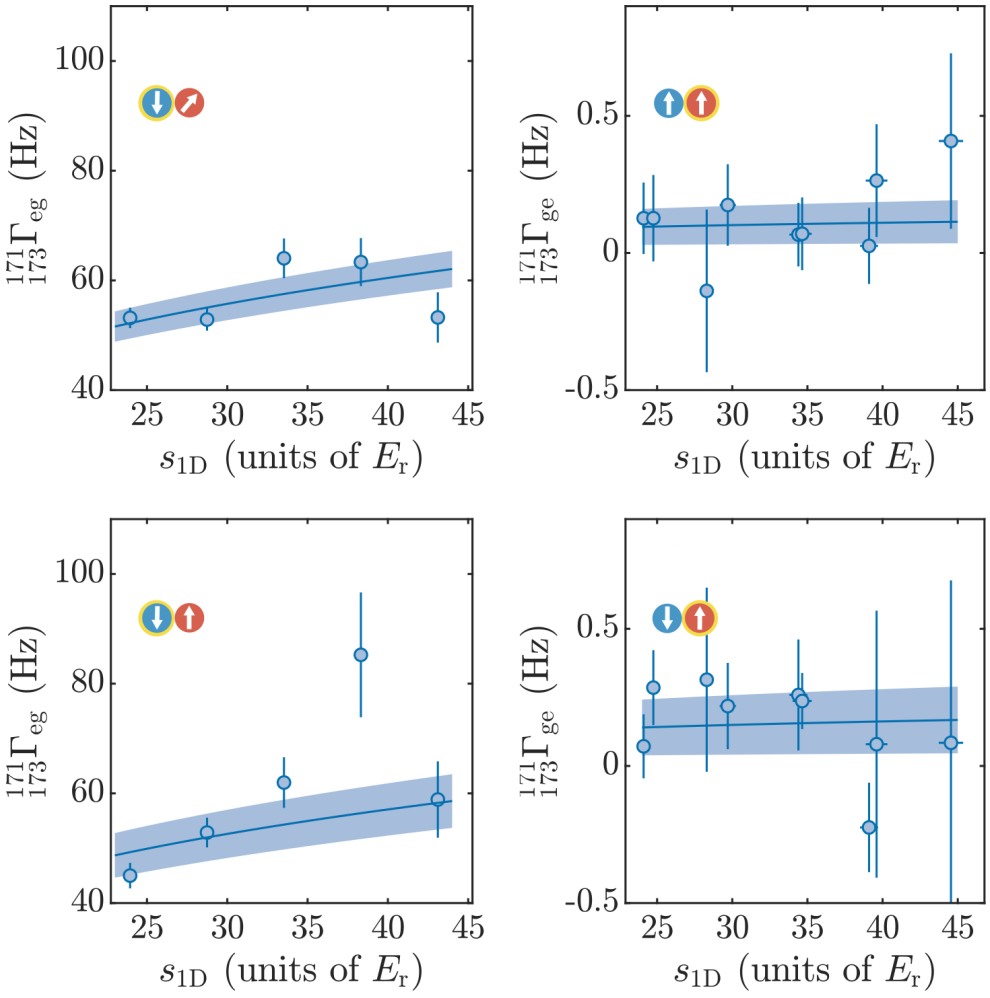

Figure 2.4: Inelastic decay rates in dependence of lattice depth. The figures show different decay rates as a function of the 1D lattice depth $s_{1\mathrm{D}}$. The decay rate $^{171}_{173}\Gamma_{\mathrm{eg}}$ is displayed on the left for the states $|\mathrm{e}, -1/2; \mathrm{g}, 3/2\rangle$ (top) and $|\mathrm{e}, -1/2; \mathrm{g}, 5/2\rangle$ (bottom), while $^{171}_{173}\Gamma_{\mathrm{ge}}$ is displayed on the right for the states $|\mathrm{g}, 1/2; \mathrm{e}, 5/2\rangle$ (top) and $|\mathrm{g}, -1/2; \mathrm{e}, 5/2\rangle$ (bottom). The decay rates are extracted from the exponential fit of loss measurements as the ones presented in Fig. 2.3. Each data point is averaged several times and the error bars represent the fit uncertainties. To this data, we fit Eq. 2.8 with $^{171}_{173}\beta_{\mathrm{eg/ge}}$ as a free parameter. The fit is shown as a solid line and the shaded area around it represents the 95% confidence interval. Reprinted figure with permission from Ref. [16]. Copyright 2021 by the American Physical Society.

2.2 Interorbital Spin-Exchange Interactions of ^{171}Yb

While in the last section, we investigated the interactions between different orbitals and isotopes, in this section, we explore the interactions between different orbitals of the same isotope. The fundamental difference between the two systems is, that the former dealt with distinguishable particles, whereas the particles, underlying the interactions in this section, are indistinguishable. Because of that, the particles experience spin-exchange dynamics, which could be used for simulating orbital magnetism or the Kondo lattice model [1, 2]. Spin exchange interactions were already measured for ^{173}Yb and ^{87}Sr in Ref. [53–55]. For example, the interorbital spin-exchange interaction of ^{173}Yb was found to be ferromagnetic and exceptionally large [53, 54]. However, for the simulation of the Kondo lattice model, the spin-exchange interaction needs to be antiferromagnetic and the ground state interactions of the system need to be negligible [2]. In this section, we characterize the spin-exchange interactions of ^{171}Yb, which has an exceptionally small ground state interaction with $a_{gg} = -3(4)a_0$ [105]. At first, we derive the Hamiltonian, which describes the atomic system and the possible clock excitations. Afterwards, we present our experimental characterization of the spin-exchange interactions. During our investigations, these spin-exchange interactions were also characterized in Ref. [58, 59].

2.2.1 Spectroscopy Hamiltonian

In the following, we derive the spectroscopy Hamiltonian of our clock excitation for a spin-balanced ^{171}Yb gas. This derivation is based on Ref. [95, 100, 115]. We consider a degenerate Fermi gas of ^{171}Yb atoms with $m_F = \pm 1/2$ in a deep optical lattice, where the tight-binding approximation is valid (see Sec. 1.4.3). This system is described by the Fermi-Hubbard model (see Sec. 1.4.3) for indistinguishable particles with spin $\pm 1/2$. The lattice sites of this model can be empty, singly occupied or doubly occupied. For singly occupied lattice sites, the particle wave function is the same as for a spin-polarized gas, whereas, for doubly occupied sites, the two particles become part of a two-body wave function. As the two particles are at the same lattice site, the spatial wave function is symmetric and neglected in the following considerations. We extend the model by the metastable clock state $^3P_0$, which we denote as $|e\rangle$, while the ground state ($^1S_0$) is $|g\rangle$. Then, the two-body wave function is a product state of an orbital wave function and a spin wave function. Since fermions are considered, the total wave function is required to be antisymmetric. This can either be achieved by a symmetric orbital wave function and antisymmetric spin wave function or vice versa. In total, there are six different ways to form the two-body wave function for two particles at the same lattice site. The wave functions are as follows.

If both atoms are simultaneously either in the ground or in the excited state, the Pauli principle dictates an antisymmetric spin wave function. The resulting states are

$$|gg\rangle = |g,g\rangle \otimes \frac{1}{\sqrt{2}} (|\uparrow\downarrow\rangle - |\downarrow\uparrow\rangle) \quad \text{and} \tag{2.11}$$

$$|ee\rangle = |e,e\rangle \otimes \frac{1}{\sqrt{2}} (|\uparrow\downarrow\rangle - |\downarrow\uparrow\rangle) . \tag{2.12}$$

For one particle in the ground and one particle in the excited state, four states can be formed with either an antisymmetric spin singlet (and accordingly a symmetric orbital state) or a symmetric spin triplet (and

accordingly an antisymmetric orbital state). The four states are

$$|\mathrm{eg}^+\rangle = \frac{1}{\sqrt{2}}\left(|\mathrm{e,g}\rangle + |\mathrm{g,e}\rangle\right) \otimes \frac{1}{\sqrt{2}}\left(|\uparrow\downarrow\rangle - |\downarrow\uparrow\rangle\right), \tag{2.13}$$

$$|\mathrm{eg}^-\rangle = \frac{1}{\sqrt{2}}\left(|\mathrm{e,g}\rangle - |\mathrm{g,e}\rangle\right) \otimes \frac{1}{\sqrt{2}}\left(|\uparrow\downarrow\rangle + |\downarrow\uparrow\rangle\right), \tag{2.14}$$

$$|\mathrm{eg}^\uparrow\rangle = \frac{1}{\sqrt{2}}\left(|\mathrm{e,g}\rangle - |\mathrm{g,e}\rangle\right) \otimes |\uparrow\uparrow\rangle \quad \text{and} \tag{2.15}$$

$$|\mathrm{eg}^\downarrow\rangle = \frac{1}{\sqrt{2}}\left(|\mathrm{e,g}\rangle - |\mathrm{g,e}\rangle\right) \otimes |\downarrow\downarrow\rangle\,. \tag{2.16}$$

Since we are interested in spin-exchange dynamics, we disregard the latter two states, $|\mathrm{eg}^\uparrow\rangle$ and $|\mathrm{eg}^\downarrow\rangle$, where both particles have the same spin. This negligence is also reasonable, as these states are not accessible in the measurements described below, because of the π-polarization of the excitation pulse (see below for details). The four remaining states form a two-body interaction basis, where the two states with one ground state and one excited state atom, $|\mathrm{eg}^+\rangle$ and $|\mathrm{eg}^-\rangle$, experience the spin-exchange interactions, which we want to investigate.

The total atomic Hamiltonian $\mathcal{H}_{\mathrm{atom}}$ of this system is the sum of three parts: the electronic state Hamiltonian $\mathcal{H}_{\mathrm{el}}$, the atomic interaction Hamiltonian $\mathcal{H}_{\mathrm{int}}$, and the Zeeman Hamiltonian $\mathcal{H}_{\mathrm{Z}}$. Thus, the atomic Hamiltonian can be written as

$$\mathcal{H}_{\mathrm{atom}} = \mathcal{H}_{\mathrm{el}} + \mathcal{H}_{\mathrm{int}} + \mathcal{H}_{\mathrm{Z}} \tag{2.17}$$

and the individual Hamiltonians are given as follows. First, if only the ground and clock state are considered and if the system is transformed into the rotating frame of the clock laser, the electronic state Hamiltonian is

$$\mathcal{H}_{\mathrm{el}} = \hbar\Delta\left(|\mathrm{gg}\rangle\langle\mathrm{gg}| - |\mathrm{ee}\rangle\langle\mathrm{ee}|\right), \tag{2.18}$$

where Δ is the detuning of the clock laser with respect to the atomic resonance. Second, the atomic interaction Hamiltonian can be expressed by the respective Hubbard on-site interaction U_{ij} of state $|ij\rangle$:

$$\mathcal{H}_{\mathrm{int}} = U_{\mathrm{gg}}|\mathrm{gg}\rangle\langle\mathrm{gg}| + U_{\mathrm{ee}}|\mathrm{ee}\rangle\langle\mathrm{ee}| + U_{\mathrm{eg}^+}|\mathrm{eg}^+\rangle\langle\mathrm{eg}^+| + U_{\mathrm{eg}^-}|\mathrm{eg}^-\rangle\langle\mathrm{eg}^-|\,. \tag{2.19}$$

Third, the Zeeman Hamiltonian is [100]

$$\mathcal{H}_{\mathrm{Z}} = E_{\mathrm{Z}}(B)\left(|\mathrm{eg}^-\rangle\langle\mathrm{eg}^+| + |\mathrm{eg}^+\rangle\langle\mathrm{eg}^-|\right), \tag{2.20}$$

where the differential Zeeman energy $E_{\mathrm{Z}}(B) = \delta g B m_F$. δg is the differential Landé factor. Then, the total atomic Hamiltonian $\mathcal{H}_{\mathrm{atom}}$ in the interaction basis (Eq. 2.11, 2.12, 2.13 and 2.14) is

$$\mathcal{H}_{\mathrm{atom}} = \begin{pmatrix} U_{\mathrm{gg}} + \hbar\Delta & 0 & 0 & 0 \\ 0 & U_{\mathrm{eg}^+} & E_{\mathrm{Z}}(B) & 0 \\ 0 & E_{\mathrm{Z}}(B) & U_{\mathrm{eg}^-} & 0 \\ 0 & 0 & 0 & U_{\mathrm{ee}} - \hbar\Delta \end{pmatrix} \tag{2.21}$$

Since the Zeeman energy mixes the states $|\mathrm{eg}^+\rangle$ and $|\mathrm{eg}^-\rangle$, the atomic Hamiltonian is not diagonal and $|\mathrm{eg}^+\rangle$ and $|\mathrm{eg}^-\rangle$ are not eigenstates of the Hamiltonian. Therefore, the eigenstates are calculated and

denoted as [16]

$$|+\rangle = c_1(B)\,|\mathrm{eg}^+\rangle + c_2(B)\,|\mathrm{eg}^-\rangle \quad \text{and} \tag{2.22}$$

$$|-\rangle = c_1(B)\,|\mathrm{eg}^-\rangle + c_2(B)\,|\mathrm{eg}^+\rangle\,, \tag{2.23}$$

where $|\mathrm{gg}\rangle$ and $|\mathrm{ee}\rangle$ are already eigenstates and complete the new basis. The $|\pm\rangle$ states are mixtures of the $|\mathrm{eg}^+\rangle$ and $|\mathrm{eg}^-\rangle$ states with the mixing coefficients [16]:

$$c_1(B) = \frac{|V_{\mathrm{ex}}| + \sqrt{V_{\mathrm{ex}}^2 + E_{\mathrm{Z}}^2(B)}}{\sqrt{2V_{\mathrm{ex}}^2 + 2E_{\mathrm{Z}}^2(B) + 2|V_{\mathrm{ex}}|\sqrt{V_{\mathrm{ex}}^2 + E_{\mathrm{Z}}^2(B)}}} \quad \text{and} \tag{2.24}$$

$$c_2(B) = \frac{|E_{\mathrm{Z}}(B)|}{\sqrt{2V_{\mathrm{ex}}^2 + 2E_{\mathrm{Z}}^2(B) + 2|V_{\mathrm{ex}}|\sqrt{V_{\mathrm{ex}}^2 + E_{\mathrm{Z}}^2(B)}}}. \tag{2.25}$$

$$\tag{2.26}$$

At $B = 0$ and consequently $E_{\mathrm{Z}}(B = 0) = 0$, the coefficients are $c_1(B = 0) = 1$ and $c_2(B = 0) = 0$ and the eigenstates automatically reduce to the interaction basis. The eigenenergies $E_\pm$ of the atomic Hamiltonian are [16]

$$E_\pm = V \pm V_{\mathrm{ex}}\sqrt{1 + \left(\frac{E_{\mathrm{Z}}(B)}{V_{\mathrm{ex}}}\right)^2}, \tag{2.27}$$

where the direct interaction V and spin-exchange interaction V_{ex} are [16]

$$V = \frac{U_{\mathrm{eg}^+} + U_{\mathrm{eg}^-}}{2} \quad \text{and} \tag{2.28}$$

$$V_{\mathrm{ex}} = \frac{U_{\mathrm{eg}^+} - U_{\mathrm{eg}^-}}{2}. \tag{2.29}$$

In addition to the atomic Hamiltonian, we consider the coupling of its eigenstates by π-polarized light, which is used in the measurements. At vanishing magnetic field, the atom-field Hamiltonian $\mathcal{H}_{\text{atom-field}}$ has only two non-vanishing matrix elements and, thus, can be expressed as [100]

$$\mathcal{H}_{\text{atom-field}} = \frac{\hbar\Omega}{\sqrt{2}}\left(|\mathrm{eg}^-\rangle\langle\mathrm{gg}| - |\mathrm{ee}\rangle\langle\mathrm{eg}^-| + \mathrm{h.c.}\right), \tag{2.30}$$

where Ω is the Rabi frequency and h.c. denotes the hermitian conjugate. Because of opposite signs in the Clebsch-Gordan coefficients, the Hamiltonian does not couple to the spin singlet state $|\mathrm{eg}^+\rangle$ [100, 115]. For a finite magnetic field, the couplings are [100]

$$\mathcal{H}_{\text{atom-field}} = \sqrt{2}c_2(B)\frac{\hbar\Omega}{2}\left(|+\rangle\langle\mathrm{gg}| + |\mathrm{ee}\rangle\langle+| + \mathrm{h.c.}\right) \tag{2.31}$$

$$+ \sqrt{2}c_1(B)\frac{\hbar\Omega}{2}\left(|-\rangle\langle\mathrm{gg}| + |\mathrm{ee}\rangle\langle-| + \mathrm{h.c.}\right) \tag{2.32}$$

$$= \frac{\hbar\Omega_+}{2}\left(|+\rangle\langle\mathrm{gg}| + |\mathrm{ee}\rangle\langle+| + \mathrm{h.c.}\right) \tag{2.33}$$

$$+ \frac{\hbar\Omega_-}{2}\left(|-\rangle\langle\mathrm{gg}| + \langle\mathrm{ee}|\langle-| + \mathrm{h.c.}\right), \tag{2.34}$$

where the effective Rabi frequencies $\Omega_\pm$ of the $|\pm\rangle$ states depend on the magnetic field and are

$$\Omega_\pm = \sqrt{2}\, c_{2/1}(B)\, \Omega. \tag{2.35}$$

This completes the theoretical description of the atomic system for two particles at the same lattice site with the four two-body wave functions $|gg\rangle$, $|ee\rangle$ and $|\pm\rangle$ and their spectroscopic coupling by $\mathcal{H}_{\text{atom-field}}$.

2.2.2 Spectroscopic Characterization of Spin-Exchange Interactions

After the theoretical description of the atomic system and its possible excitations above, here, we present our experimental characterization of the direct and spin-exchange interactions. We prepare a spin-balanced degenerate Fermi gas of ^{171}Yb atoms (see Sec. 1.2). We reach atom numbers of $N_{171} \approx (15 \text{ to } 35) \times 10^3$ atoms and load them into a magical optical lattice (see Sec. 1.4) with $s_{1D} = 50(2)\ E_{\text{recoil}}$ and $s_{2D} \approx 25.0(3)\ E_{\text{recoil}}$. To this system, we apply π-polarized clock laser light co-propagating with our 1D lattice to excite ^{171}Yb atoms from the ground state $^1S_0$ to the excited state $^3P_0$. For the excitation, we use rectangular π-pulses with a Rabi frequency of $\Omega = 2\pi \times 345(2)$ Hz for the single-particle transition. We adapt the length of the clock pulse to account for different Rabi frequencies and to fulfill the π-pulse condition for excitations, which we expect to correspond to the $|\pm\rangle$ states. After the excitation pulse, we detect the atom numbers of the ground and excited state N_g and N_e, respectively, in the same image (see Sec. 1.5.3). The atom numbers are recorded for different laser frequencies around the clock transition resonances to form a spectrum. Furthermore, we take spectra at various magnetic field strengths in gravity direction. An example of such a spectrum is shown in Fig. 2.5 for $B = 13.1$ G, where the excited state fraction $n_e = N_e/(N_g + N_e)$ is plotted as a function of the clock laser detuning Δ with respect to the single-particle resonance at $B = 0$.

We observe four spectroscopic features and fit them with a multi-peak function consisting of four sinc^2-functions. We can directly identify two peaks as the single-particle excitations $|g,\uparrow\rangle \rightarrow |e,\uparrow\rangle$ and $|g,\downarrow\rangle \rightarrow |e,\downarrow\rangle$, because the single-particle resonance is determined with a spin-polarized sample in auxiliary measurements. We denote these excitation peaks as $|\uparrow\rangle$ and $|\downarrow\rangle$. The remaining two spectroscopy features are expected to be the excitations of the $|\pm\rangle$ states (Eq. 2.22 and 2.23) from the theoretical considerations in Sec. 2.2.1. To distinguish between the $|+\rangle$ and $|-\rangle$ state, we record the Rabi frequencies of their excitation for various magnetic fields, which is further described below.

We take such a spectrum for six different magnetic field strengths and display them in Fig. 2.6. In addition, the centers of the spectroscopy peaks are extracted from the fits for each spectrum and are also plotted in Fig. 2.6 as data points with their detuning Δ as a function of the magnetic field strength B. Each spectrum exhibits four peaks, except for the measurement at the lowest magnetic field with $B = 0.9$ G, which shows only three features. We notice, that the energy difference between $|\uparrow\rangle$ and $|\downarrow\rangle$ increases monotonically and linearly for increasing magnetic field strength, which is expected from the linear Zeeman shift. Whereas, the energy difference between $|+\rangle$ and $|-\rangle$ increases also monotonically, but only roughly linearly for $B \geq 8.8$ G. For smaller magnetic field strengths, the energy difference deviates from the linearity. This behavior is expected, since, for $E_Z(B) \gg V_{\text{ex}}$, the eigenenergies in Eq. 2.27 are proportional to the differential Zeeman shift: $E_\pm \propto E_Z(B)$, but, for $E_Z(B) \ll V_{\text{ex}}$, the eigenenergies are: $E_\pm = V \pm V_{\text{ex}}$ and, thus, independent of the magnetic field.

To further analyze the data, we fit the resonance positions of $|\uparrow\rangle$ and $|\downarrow\rangle$ with $E_{\uparrow\downarrow} = \pm E_Z(B)$, where $E_Z(B) = -399.0(1)\,\text{Hz/G} \times B\, m_F$ for ^{171}Yb [59]. As the Zeeman shift is known, the fit is used to determine the magnetic field strength. For the two-body states, we only have direct access to the differential

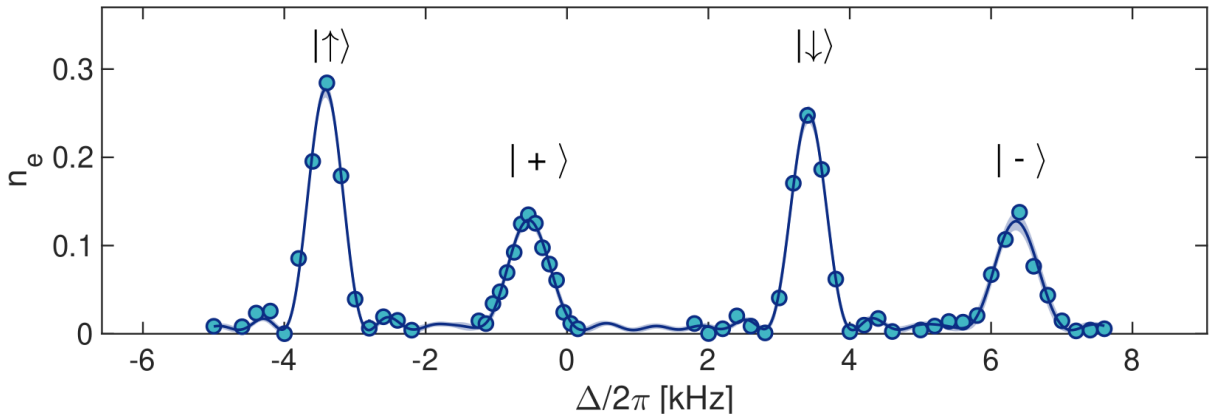

Figure 2.5: Typical clock spectrum of spin-balanced ^{171}Yb. The figure shows the excited state fraction n_e of a spin-balanced degenerate ^{171}Yb gas after a π-pulse excitation. n_e is plotted as a function of the clock laser frequency detuning Δ with respect to the center of the single-particle resonances. Data points are averages over three individual measurements. Error bars display one standard deviation, but are typically smaller than the size of the data points. The solid line represents a fit of the data with a multi-peak function consisting of four sinc^2 functions. The shaded area around the line indicates the 95 % confidence interval of the fit. The data is recorded at a magnetic field strength of $B = 13.1$ G. Peaks are labeled after the expected excited state. For the single-particle excitations the used pulse time is $t_{\text{pulse}} = 1.45$ ms, which corresponds to a Rabi frequency $\Omega_0 = 2\pi \times 345(2)$ Hz. Whereas, for the peaks labeled with $|+\rangle$ and $|-\rangle$, the pulse duration was adapted to achieve the highest excited state fraction. Figure adapted with permission from Ref. [16]. Copyrighted by the American Physical Society.

quantities, which take the ground state interactions U_{gg} into account. Therefore, with the magnetic field strength information, we calculate the differential interactions $\Delta U_{\text{eg}^\pm} = U_{\text{eg}^\pm} - U_{\text{gg}}$ for each spectrum in Fig. 2.6 and average the results. We find $\Delta U_{\text{eg}^+}/h = 3.53(4)$ kHz and $\Delta U_{\text{eg}^-}/h = 2.32(3)$ kHz, which correspond to $\Delta V/h = (V - U_{\text{gg}})/h = 2.896(11)$ kHz and $\Delta V_{\text{ex}}/h = (V_{\text{ex}} - U_{\text{gg}})/h = -0.60(2)$ kHz. Furthermore, we compute the Wannier integrals and use Eq. 1.7 and 1.8 to determine the s-wave scattering lengths, which are lattice-independent parameters. The results are $a_{\text{eg}^+} = 203(5)a_0$ and $a_{\text{eg}^-} = 308(6)a_0$, where we used $a_{\text{gg}} = -3(4)a_0$ from Ref. [105]. Using these results, we calculate $\Delta E_\pm(B) = E_\pm(B) - U_{\text{gg}}$ with Eq. 2.27 and plot them in dependence of the magnetic field as solid lines in Fig. 2.6. The lines are in good agreement with the data points for $|\pm\rangle$ and, hence, confirm the theoretical model.

In addition to the measurements above, we measure the magnetic field dependence of the Rabi frequencies $\Omega_\pm$ for the excitation of the $|\pm\rangle$ states. For this purpose, we record the excited state fraction n_e at the $|+\rangle$ and $|-\rangle$ resonance for various durations t_{pulse} of the excitation pulse. Subsequently, we fit n_e as a function of t_{pulse} with solutions of the optical Bloch equations and extract the Rabi frequencies. More details on this topic and the single measurements of the Rabi oscillations can be found in Ref. [99, 100]. Here, we present the results for $\Omega_\pm$ as a function of the magnetic field in the lower right of Fig. 2.6. Moreover, we calculate $\Omega_\pm$ using Eq. 2.35, 2.24 and 2.25 and the found result of V_{ex}. We plot $\Omega_\pm(B)$ in dependence of the magnetic field in the lower right of Fig. 2.6 as solid lines. The data points agree well with the calculations and, thus, confirm the underlying theory.

In this section, we characterized the scattering lengths a_{eg^+} and a_{eg^-}. We found V_{ex} to have a negative sign and, thus, to be antiferromagnetic. The interorbital spin-exchange interaction in ^{171}Yb was also characterized in Ref. [58, 59]. The results of the different groups for the interaction parameters are listed in Table 2.3. The results of all three measurements correspond to an antiferromagnetic spin-

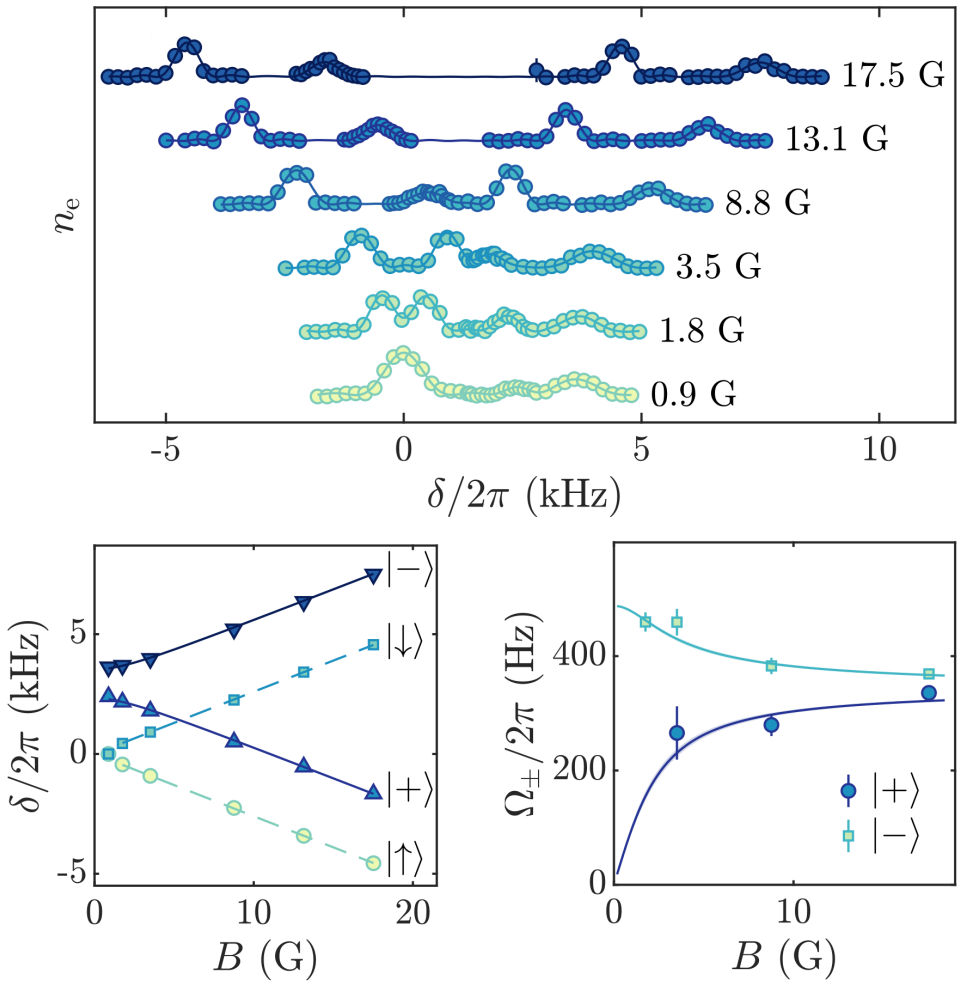

Figure 2.6: Clock spectra of spin-balanced ^{171}Yb at different magnetic field strengths. The upper figure shows the spectroscopy signals at various magnetic field strengths in the range $B \in [0.9, 17.5]\,\mathrm{G}$. The indications of data points and solid lines are analogous to the ones in Fig. 2.5. The individual spectra are displaced vertically with respect to each other for clarity and each spectrum is labeled by the magnetic field strength, at which it is recorded. Within each spectrum the vertical direction reflects the excited state fraction n_e. The data points in the lower left figure illustrate the detuning frequency δ of each peak center from the spectroscopy measurements as a function of the magnetic field strength B. The color of the data points reflects the corresponding excited state as labeled on the right. The dashed lines display calculations of $E_{\uparrow\downarrow} = \pm E_Z(B)$, while the solid lines display calculations of $\Delta E_\pm$. All lines are in the color of the respective data points. The figure in the lower right displays the Rabi frequencies $\Omega_\pm$ as a function of the magnetic field strength B. Data points are the fit results of Rabi oscillation measurements and the error bars indicate the uncertainty of the respective fit. The color of the data points reflects the state correspondence as specified in the legend. Lines are calculations of $\Omega_\pm(B)$ using Eq. 2.35, 2.24 and 2.25 with the found result of V_{ex}. The lines are displayed in the color of the respective data points. Reprinted figure with permission from Ref. [16]. Copyright 2021 by the American Physical Society.

Table 2.3: Spin-exchange scattering length results. The table lists the results from different references for the measurements of the spin-exchange scattering lengths of ^{171}Yb.

a_{eg^+} (a_0)	a_{eg^-} (a_0)	Reference
203(5)	308(6)	[16] (this work)
225(13)	355(6)	[58]
240(4)	389(4)	[59]

exchange interaction with $V_{\mathrm{ex}} < 0$ and agree qualitatively as all values lay within the same order of magnitude. However, quantitatively all results differ significantly with the exception of the result of a_{eg^+} in Ref. [58] which has the largest uncertainty and agrees with the results of Ref. [59] and this work. An experimental difference between the setup of this work and the other two setups is the lattice geometry. Both references use simple cubic lattices, whereas we work with a triangular 2D lattice in combination with a 1D lattice. However, the determined scattering lengths are independent of the lattice geometry. Hence, the origin of the different results remains unclear. The found results of moderate antiferromagnetic spin-exchange interactions and the very weak ground state interactions make ^{171}Yb a promising candidate for the simulation of the Kondo lattice model [1, 2]. Furthermore, our high-precision clock spectroscopy of interorbital interactions in ^{171}Yb gases and ^{171}Yb-^{173}Yb mixtures enriches the knowledge about interorbital scattering behavior of particles and provides a basis for further studies.

3 Realization of Quantum Hall States

In the previous chapter, we reported on measurements on Fermi gases and Fermi-Fermi mixtures in a zero-dimensional system. There, any motion was frozen in a deep three dimensional lattice, which inhibited tunneling processes in every direction. In this chapter and following chapters, we work in a different system, where tunneling is possible in a single real space dimension and, moreover, in a synthetic dimension, realizing a two dimensional system. Furthermore, we implement an artificial gauge field in this system to mimic the behavior of charged particles in a strong magnetic field. These two ingredients let us create a quantum Hall structure with quantum gases. Similar systems have already been realized for bosons in Ref. [36, 66, 68–70] and for fermions in Ref. [3, 4, 7, 67, 71]. We want to realize it for further in depth studies, which are reported in the following chapters. Here, we describe and discuss our realization of quantum Hall systems. In Sec. 3.1, we introduce the basic model and the theoretical background. We go into the description of the Harper-Hofstadter model and discuss the single particle solutions, i.e. without inter-particle interactions. In Sec. 3.2, we explain how this model can be implemented in cold atom systems by creating artificial gauge fields. In addition, we detail our specific method for generating an artificial magnetic field by exploiting stimulated Raman transitions.

Calculations on the properties of the Harper-Hofstadter Model in Sec. 3.1.3 were carried out by L. Hilbig under the author's supervision (see Ref. [116] for details). All other aspects of this chapter were completed by the author.

3.1 Theory of Quantum Hall States

As a first step towards the realization of quantum Hall systems in quantum gases, we present the theoretical description of the system to gain insight into the system properties. This section is organized as follows. In the first part, we give a brief overview of the concept of topological matter. In the second part, we examine the theoretical model of the system: the Harper-Hofstadter model. In the third part, we analyze the properties of this model.

3.1.1 Integer Quantum Hall Effect and Topological Matter

In the following, we place our work in the context of the research field by introducing two fundamental concepts: the integer quantum Hall effect and topological matter. We begin with an explanation of the integer quantum Hall effect and, subsequently, provide a concise overview of the theory of topological states. Detailed descriptions and explanation of the quantum Hall effect and topological classification of matter can be found in Ref. [74, 75, 134–136].

The integer quantum Hall effect was first observed by von Klitzing in 1980 in a two-dimensional semiconductor at a temperature of $T = 1.5\,\mathrm{K}$ and a magnetic field of $B = 18\,\mathrm{T}$ normal to the semiconductor plane [137]. In the semiconductor, which is insulating in its bulk, a Hall conductance σ was observed. This Hall conductance was strictly quantized in the following way

$$\sigma = n \cdot \frac{e^2}{h}, \tag{3.1}$$

where n is a positive integer, h is the Planck constant and e is the elementary charge. The measured conductance comes from states, which are localized at the edges of the sample and, thus, are called edge states. When electrons populate these states, they can move along the edge, where they travel in opposite directions for opposite edges. Therefore, the total motion is chiral. In a semiclassical approach, this can be thought of as follows. The electrons in the semiconductor perform cyclotron orbits because of the magnetic field. In the bulk of the sample, these orbits are closed, but at the edges, the electrons cannot complete the whole orbit, instead they bounce off the edge and continue with a new orbit until they reach the edge again. As a result, they move in half circles along the edge. By performing these skipping orbits [138], they move forward, instead of staying localized in a single orbit. In this picture, it is also clear, why the electrons move in a chiral way: the performed half circles are complementary for opposite edges. Whether the electrons circle the cyclotron orbits clockwise or anticlockwise depends on the magnetic field direction. Hence, the chirality of the edge currents depends also on the magnetic field direction.

Until the discovery of the integer quantum Hall effect, quantum states were classified in means of spontaneous symmetry breaking, which was one of the greatest achievements in condensed matter physics in the last century [72]. However, the integer quantum Hall state cannot be classified in this way. Thus, a new kind of state classification in terms of topology was formulated. Topology is a mathematical concept denoting specific characteristics, which are conserved during continuous deformations [138]. A typical example for topology is described in Ref. [138] and examines the number of twists in a buckled belt. The number of twists in the belt cannot be changed by a continuous deformation and partial twists are not possible. A possible deformation, which is not continuous and which can change the number of twists, needs to open and close the belt. In this example, one can think of the number of twists in the belt as a topological invariant, which characterizes different states. Analogously, in condensed matter physics, topological invariants are independent of continuous changes in a material. Here, a continuous change means, that energy gaps to other bands must not be closed [138].

In this framework, the integer quantum Hall effect can be explained as follows. The integer quantum Hall state and the vacuum are both insulating phases, which do not have the same topology. Therefore, the Hamiltonian must be gapless (deformation, which is not continuous) at the boundary and there must exist a conductive state: the edge state, which carries the Hall conductance. The integer quantum Hall effect was the first observation of a topologically nontrivial state [139]. It has a broken time-reversal symmetry because of the applied magnetic field. Hence, it belongs to a topological class, which breaks time-reversal symmetry explicitly [136]. In a different topological class, the class of 2D topological insulators or synonymously called quantum spin Hall insulators, the time-reversal symmetry remains intact and strong spin-orbit coupling plays an essential role [136, 139]. Therefore, time-reversal symmetry breaking is not a requirement for topological non-trivial phases.

The quantum Hall and the quantum spin Hall state both feature an insulating bulk and conducting edge states. The edge states and, therefore, the chiral currents are very robust against impurities [136]. This is a result of the fact, that they are squeezed in between two vacua, which belong to different topological classes [139]. This robustness of the currents makes these states highly interesting research subjects with astonishing possible applications [14]. The fundamental relevance of topology was acknowledged by the Nobel Prize in Physics to David J. Thouless, F. Duncan M. Haldane and J. Michael Kosterlitz "for theoretical discoveries of topological phase transitions and topological phases of matter" [18]. In this work, we want to explore the robustness of chiral edge currents under interactions between the (effectively) charge carrying particles and investigate the general behavior under these interactions. Our

findings may contribute to advancing the understanding of *fractional* quantum Hall (FQH) states [9]. FQH states can arise in a quantum Hall system with strong interactions. In the FQH effect, the Hall conductance is quantized at fractional values of e^2/h, rather than at exact integer multiples. As the FQH effect is not yet fully understood theoretically and is believed to involve phenomena such as non-Abelian anyonic excitations, it remains a highly promising area of research. The scientific significance of the FQH state was recognized in 1998 when Robert B. Laughlin, Horst L. Störmer, and Daniel C. Tsui were awarded the Nobel Prize in Physics "for their discovery of a new form of quantum fluid with fractionally charged excitations" [18]. Several proposals suggest the potential for using ultracold atomic gases as quantum emulators for FQH states [8–13]. The synthetic dimensions approach explored in this thesis (see Sec. 3.2.1) appears particularly well-suited for this purpose, due to the long-range interactions present in the synthetic dimension [8]. In this context, enhancing our understanding of interaction dynamics could also pave the way for the development of robust quantum information protocols [14]. The interaction regime is particularly hard to access with computations because, when the particles interact, the single particle solution ansatz (see Eq. 3.10) discussed below breaks down. Therefore, we use our quantum gas machine to probe the influence of repulsive interparticle interactions on chiral edge currents.

3.1.2 Harper-Hofstadter Model

Following the introduction of the integer quantum Hall effect and its profound connection to topological matter, we aim to establish the theoretical framework for the integer quantum Hall state. For this purpose, we use the Peierls substitution to derive the Harper-Hofstadter Hamiltonian, which generally describes the behavior of charged particles in two-dimensional lattice systems with uniform magnetic field [135]. We restrict our considerations to non-interacting particles.

To understand the effect of a magnetic vector potential $\vec{A}$ on charged particles, we explore the case of charged particles in free space. When particles with charge q move around in this system, they accumulate a phase $\Phi_{\text{Aharanov-Bohm}}$ along their path $\mathcal{P}$ according to the Aharanov-Bohm effect (see Ref. [140]):

$$\Phi_{\text{Aharanov-Bohm}} = \frac{q}{\hbar} \int_{\mathcal{P}} \vec{A} \cdot d\vec{r}. \tag{3.2}$$

We proceed by switching from free space to a two-dimensional lattice system, where the motion of particles is limited to tunneling from one lattice site to an adjacent lattice site. This system is realized, when the tight-binding approximation is valid (see Sec. 1.4.3). In addition, we consider the particles to be fermions and restrict the dynamics to the lowest lattice band. Then, the describing Hamiltonian is the Fermi-Hubbard Hamiltonian (see Eq. 1.5). Analogous to the free space case, if a vector potential $\vec{A}$ is added to this system, charged particles acquire a phase, when they tunnel from one lattice site to the next. This Peierls phase $\phi^i_{m,n}$ (see Ref. [141]) depends on the position of the particle in the lattice (lattice site) and the tunnel direction. It can be calculated as [141]

$$\phi^i_{m,n} = -qA^i_{m,n}/h, \tag{3.3}$$

where i is a placeholder for one of the dimensions $\{x, y\}$ and m (n) is the number of the lattice site in direction x (y). To implement this phase factor in the Fermi-Hubbard Hamiltonian (Eq. 1.5), we substitute the real tunneling matrix elements with complex ones, which include the Peierls phase. This process is the Peierls substitution [34]. Then, the Hamiltonian reads [142]

$$\mathcal{H} = \sum_{<m,n>} \left(-t_x e^{i\phi^x_{m,n}} \hat{c}^\dagger_{m+1,n} \hat{c}_{m,n} - t_y e^{i\phi^y_{m,n}} \hat{c}^\dagger_{m,n+1} \hat{c}_{m,n} + \text{h.c.} \right). \tag{3.4}$$

This Hamiltonian already describes the desired system: non-interacting charged particles on a two dimensional lattice with a magnetic vector potential. However, this Hamiltonian can be adjusted for an easier theoretical description in the case of a uniform magnetic field, which is our experimental scenario. For this purpose, we define the magnetic flux per lattice unit cell ϕ. It represents the accumulated flux for the motion around a single plaquette and can be calculated as follows [142]

$$\phi = \phi^x_{m,n} + \phi^y_{m+1,n} - \phi^x_{m,n+1} - \phi^y_{m,n}. \tag{3.5}$$

This is analogous to the Aharonov-Bohm effect, where for a closed path C, the acquired phase is exactly the magnetic flux enclosed by the path [140]:

$$\Phi_{\text{Aharonov-Bohm}} = \frac{q}{\hbar} \oint_C \vec{A} \cdot d\vec{r} = \frac{q \cdot \Phi_B}{\hbar}, \tag{3.6}$$

where Φ_B is the magnetic flux through the area enclosed by the particle's trajectory. As an additional step for the simplification of the theoretical computations, we perform a gauge transformation, that shifts the acquired phase to only one dimension. In this Landau gauge the phase factors are $\phi^x_{m,n} = -n \cdot \phi$ and $\phi^y_{m,n} = 0$ [138, 143]. The gauge modification does not change the values of the physical observables, even though, the Landau gauge is not the gauge of the implemented system (see Ref. [5], Fig. 3.6 and Sec. 3.2.3 for details). We apply this gauge to our Hamiltonian and get the Harper-Hofstadter Hamiltonian (see Ref. [144, 145])

$$\mathcal{H}_{\text{Harper-Hofstadter}} = \sum_{<m,n>} \left(-t_x e^{in\phi} \hat{c}^\dagger_{m+1,n} \hat{c}_{m,n} - t_y \hat{c}^\dagger_{m,n+1} \hat{c}_{m,n} + \text{h.c.} \right). \tag{3.7}$$

If the tunneling matrix elements in the Hamiltonian are complex with a phase $\phi \neq 0 \bmod 2\pi$, they break time-reversal symmetry and enable non-trivial topological states [138]. It is the theoretical fundament of the physics in this chapter and following chapters.

3.1.3 Properties of the Harper-Hofstadter Model

In addition to the derivation of the Harper-Hofstadter model above, we explore some relevant properties for our experimental studies. In the Harper-Hofstadter model, the behavior of particles in real space is described above: Particles can tunnel along two directions to adjacent lattice sites and, in the y direction (for the Landau gauge), they additionally acquire a phase factor each time they tunnel. Here, we take a look at, how the eigenenergies of this model dictate the behavior. For this purpose, we switch from the real space representation to the momentum space representation for the x direction, while leaving the other direction unaltered. The Harper-Hofstadter Hamiltonian takes the form [116]

$$\mathcal{H}_{\text{Harper-Hofstadter}} = \int_{-\pi}^{\pi} \frac{dk_x}{2\pi} \mathcal{H}(k_x) = \int_{-\pi}^{\pi} \frac{dk_x}{2\pi} \sum_n -2t_x \cos(k_x + n\phi) \hat{c}^\dagger_{k_x,n} \hat{c}_{k_x,n} - \left(t_y \hat{c}^\dagger_{k_x,n+1} \hat{c}_{k_x,n} + \text{h.c.} \right). \tag{3.8}$$

As this Hamiltonian is time independent, the eigenenergy problem is described by the stationary Schrödinger equation:

$$\mathcal{H}(k_x) |\psi\rangle = E(k_x) |\psi\rangle, \tag{3.9}$$

where $|\psi\rangle$ is the wavefunction of the system and $E(k_x)$ are the eigenenergies. To solve the Schrödinger equation, we use the ansatz [34]:

$$|\psi\rangle = \sum_{n=0}^{N-1} a_n \hat{c}^\dagger_{k_x,n} |0\rangle. \tag{3.10}$$

This ansatz leads to the following eigenenergy equation [116]

$$E(k_x)a_n = -2t_x\cos(k_x + n\phi)a_n - t_y(a_{n-1} + a_{n+1}) = \nu_{n+1}a_n - t_y(a_{n-1} + a_{n+1}), \tag{3.11}$$

where

$$\nu_{n+1} = -2t_x\cos(k_x + n\phi). \tag{3.12}$$

The eigenenergy equation reveals insights, which become clearer when expressed as a matrix in the basis of Bloch bands:

$$\begin{pmatrix} \nu_1 - E_1(k_x) & -t_y & 0 & \dots & 0 & -t_y' \\ -t_y & \nu_2 - E_2(k_x) & -t_y & & & 0 \\ 0 & -t_y & \nu_3 - E_3(k_x) & & & \vdots \\ \vdots & & & \ddots & & 0 \\ 0 & & & & & -t_y \\ -t_y' & 0 & \dots & 0 & -t_y & \nu_{N-1} - E_{N-1}(k_x) \end{pmatrix} \begin{pmatrix} a_1 \\ a_2 \\ \\ \vdots \\ \\ a_{N-1} \end{pmatrix} = 0, \tag{3.13}$$

where

$$t_y' = \begin{cases} t_y & \text{for periodic boundary conditions.} \\ 0 & \text{for open boundary conditions.} \end{cases} \tag{3.14}$$

The diagonal elements show, that neighboring Bloch bands are displaced by ϕ with respect to each other. Two of these bare bands are plotted as dashed lines in Fig. 3.1. In addition, the off-diagonal elements show, that the Hamiltonian couples neighboring Bloch bands with the amplitude t_y. If this coupling is realized, the eigenstates of the Hamiltonian form dressed bands as plotted in Fig. 3.1 as solid lines.

The energy spectrum of the Harper-Hofstadter model is given by the solution of Eq. 3.11, that means the diagonalization of the matrix in Eq. 3.13. For $t_x = t_y$ and periodic boundary conditions along the y direction, this energy spectrum is known as the Hofstadter butterfly (see Ref. [145]). It can be seen in Fig. 3.2 on the upper left. The spectrum shows a fractal structure, which can be explained as follows. Without a magnetic field the Harper-Hofstadter Hamiltonian reduces to the non-interacting Fermi-Hubbard Hamiltonian (Eq. 1.5), which features translational invariance for multiples of one lattice spacing, i.e. for $n \cdot a$, where $n \in \mathbb{Z}$ and a is the lattice spacing. The presence of a magnetic field breaks this translational invariance in general [34]. However, the invariance can be restored for different translation operations in the following cases. If

$$\phi = 2\pi \cdot \frac{p}{q}, \tag{3.15}$$

with p and $q \in \mathbb{Z} \setminus 0$ and prime to each other, the Hamiltonian is invariant under translations of $n \cdot qa$, where $n \in \mathbb{Z}$. This means, that the unit cell of the Bravais lattice is enlarged by q with respect to the case of $\vec{B} = \vec{0}$ and consequently the Brillouin zone is shrunk by q. Thus, the lowest Bloch band splits into q subbands and possesses $q - 1$ band gaps [34]. The splitting of the bands is illustrated in Fig. 3.2 on the medium and lower left for the two different fluxes $\phi = 2\pi \cdot 1/3$ and $\phi = 2\pi \cdot 1/5$. This is characteristic of the Hofstadter butterfly and explains the fractal structure, when the energy of the states is plotted against the magnetic flux in the system.

The spectrum for open boundary conditions along y is shown in Fig. 3.2 on the right under the same conditions and for direct comparison to the case of closed boundary conditions on the left. The energy spectrum changes such, that it exhibits states, which energies lie in the band gaps and connect the bands.

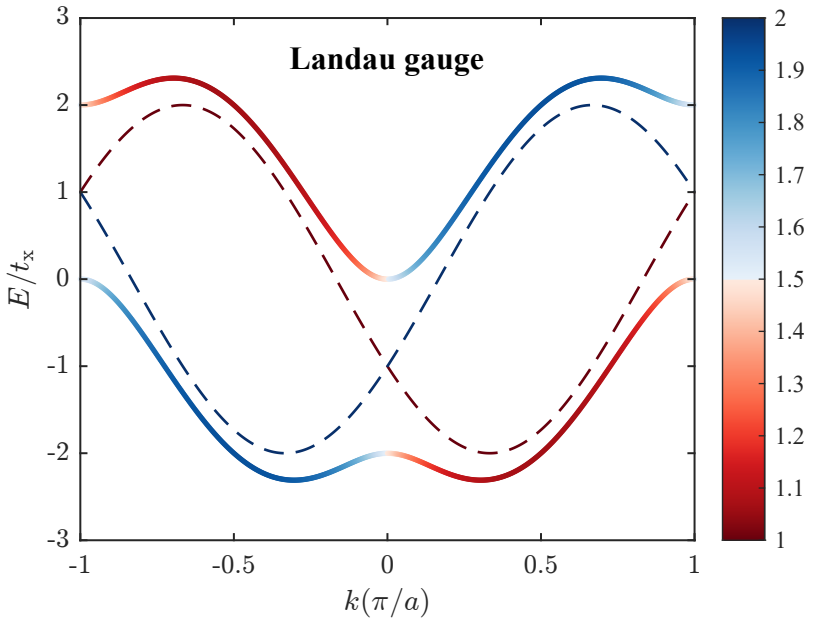

Figure 3.1: Bandstructure Harper-Hofstadter model. The figure depicts the bandstructure of two eigenstate bands in the Landau gauge and $\phi = 2\pi \cdot 1/3$. The vertical axis displays the energy in units of the tunneling energy t_x and the horizontal axis displays the quasimomentum k for the first Brillouin zone. Dashed lines show the unperturbed bandstructure of the bare bands with vanishing coupling, i.e. $t_y \to 0$. Whereas solid lines show the bandstructure of the eigenstate bands with $t_y = t_x$. The color of the solid lines express the state population as denoted in the color bars on the right. For the bandstructure in the laboratory gauge see Fig. 3.6. Figure adapted from Ref. [116].

In real space these states are located at the edge of the system and, thus, are called edge states. These edge states are integer quantum Hall phases [34]. This demonstrates the direct connection to the quantum Hall effect. Furthermore, the edge states are connected to the topology of the bulk of the system over the bulk-boundary correspondence (see Ref. [75]). This means, that the existence of the edge states is protected as long as the topology of the bulk does not change. For example, the size of the bulk, that means the number of lattice sites along y do not influence the edge states. Even a system without bulk, which consists solely of edges, features the same edge state energies, if the number of lattice sites along y are at least $n \cdot q - 1$, $n \in \mathbb{N} \setminus 0$ [146]. This is particularly interesting for ladder systems, which have only few lattice sites (typically less than 5) in one of the two directions. In Fig. 3.3 the energy bands for two different bulk sizes are compared. The figure displays the energy bands for a magnetic flux of $\phi = 2\pi \cdot 1/4$ as a function of the quasimomentum. The bands are plotted for a maximally reduced system (3 lattice sites along y) on the left and for a system with a larger bulk (11 lattice sites along y) on the right. The comparison demonstrates, that the edge states of both systems are identical. For the larger bulk additional energy bands appear, but these do not alter the bands of the edge states. In this thesis, we create a ladder system (see Sec. 3.2.3), which we use to observe edge state physics.

3.2 Harper-Hofstadter Hamiltonian in Quantum Gases

Above, we introduced the integer quantum Hall effect and topological matter and presented the system describing Hamiltonian with its properties. Here, we turn to methods to realize the Harper-Hofstadter

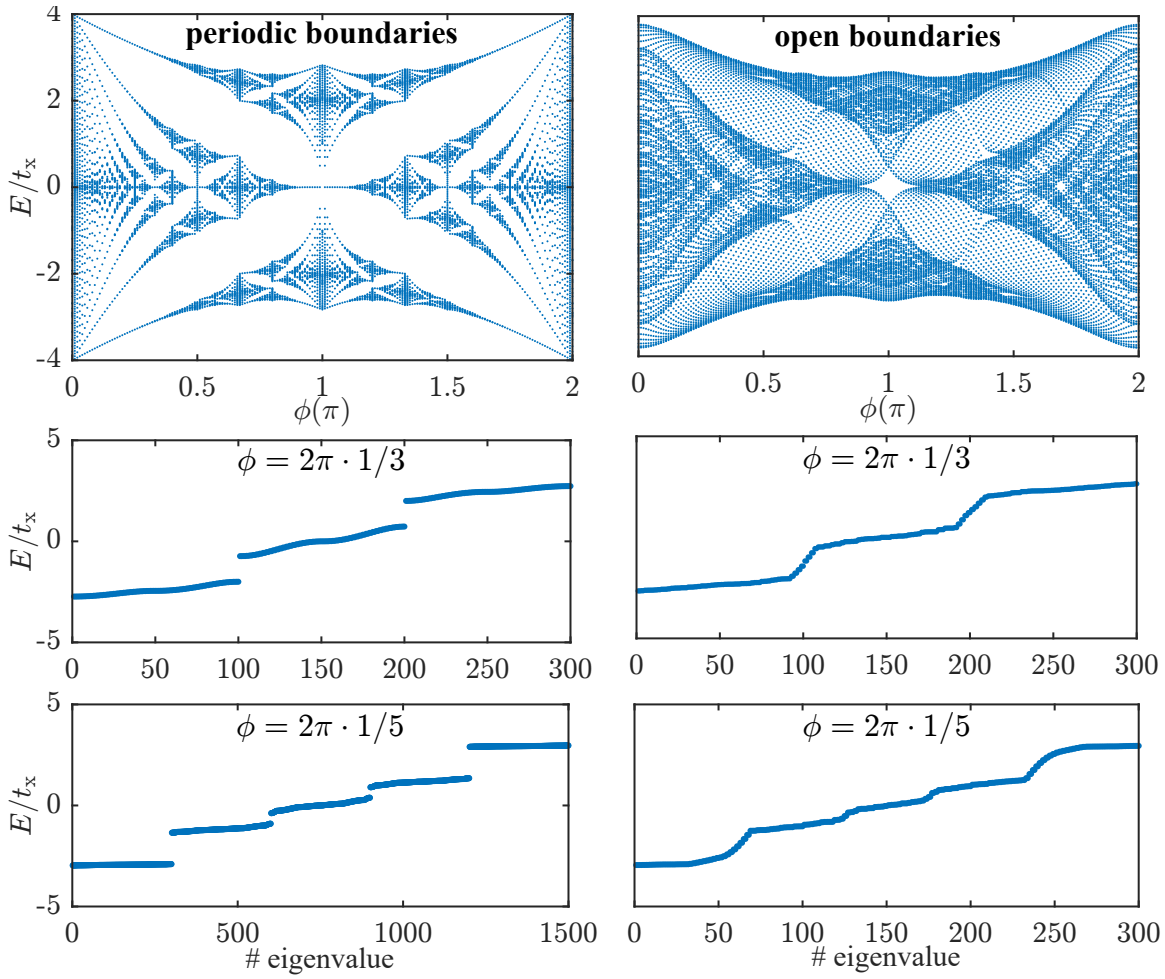

Figure 3.2: Energy spectrum of the Harper-Hofstadter Hamiltonian for periodic and open boundary conditions. The figure displays the energy spectrum of the Harper-Hofstadter Hamiltonian for periodic and open boundary conditions along the y direction. The spectrum is plotted for the energy range, which corresponds to the lowest Bloch band of the Fermi-Hubbard Hamiltonian (see Eq. 1.5). The data is computed for $t_x = t_y$ and 50×6 lattice sites. The left column presents data for periodic boundary conditions and the right column the same data for open boundary conditions. The first row displays the energy as a function of the magnetic flux ϕ. The second and third row illustrate all energy states for a specific flux of $\phi = 2\pi \cdot 1/3$ and $\phi = 2\pi \cdot 1/5$, respectively. Figure adapted from Ref. [116].

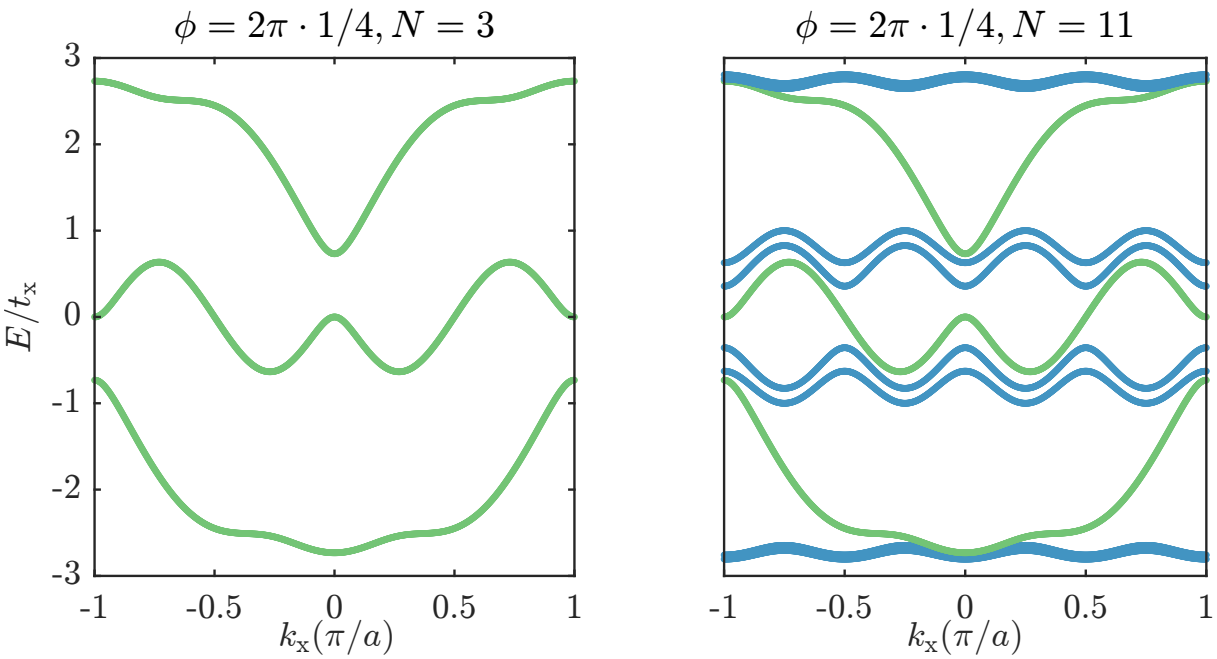

Figure 3.3: Comparison of different bulk sizes. The figure presents the energy bands for a magnetic flux of $\phi = 2\pi \cdot 1/4$ as a function of the quasimomentum. The bands are plotted for a maximally reduced system (3 lattice sites along y) on the left and for a system with a larger bulk (11 lattice sites along y) on the right. The energy bands of the edge states are displayed in red, whereas energy bands of the bulk are displayed in blue. The edge states of both systems are identical. Figure adapted from Ref. [116].

Hamiltonian in Eq. 3.7 in quantum gas systems and describe the experimental access to the model and its physics. In the first part, we start with a short argumentation why quantum gases are a good platform for the study of these physics. We continue with the description of how the realization works with artificial gauge fields and what different approaches are used for the realization. In the second part, we introduce our method of stimulated Raman transitions and, in the third part, we detail the realization of the Harper-Hofstadter Hamiltonian in our system.

3.2.1 Artificial Gauge Fields

The Harper-Hofstadter model describes charged particles in a two-dimensional lattice with a uniform magnetic field (see Sec. 3.1.3). Two-dimensional lattice systems can be routinely created in solid state materials and quantum gases. The part, that is harder to realize, is a magnetic field, that is strong enough to realize magnetic fluxes in the order of $\phi \approx 0.1\,\pi$. Only with magnetic fluxes in this order of magnitude, the model can be explored in a decent range with non-trivial physics to observe, since for $\phi = 0$ the model is reduced to the tight-binding model. With current technology, magnetic fields of about 50 T can be routinely applied to materials in laboratories. This field strength corresponds to $\phi \approx 10^{-4}\pi$, for typical lattice spacings of 10^{-10} m in condensed matter [143]. Therefore, the regime of the Harper-Hofstadter model accessible with condensed matter is strongly limited. Also for quantum gases, external magnetic fields are not strong enough to reach desired magnetic fluxes. In addition, neutral atoms are not charged and, thus, even with a strong magnetic field, the particles could not show Harper-Hofstadter physics. However, for quantum gases, there exists a solution to overcome these issues. With the creation of an artificial gauge field, the atoms behave as charged particles, on the one hand, and, on the other hand,

fluxes in the order of $\phi \approx \pi$ can be reached [32, 147–150]. Hence, the generation of artificial gauge fields generally enrich the physics, which can be simulated with cold atoms, and has gained a lot of interest in the last 25 years [34, 143, 151, 152].

Artificial gauge fields implement gauge field physics in quantum gases by realizing the Peierls substitution (see Sec. 3.1.3) in the Hamiltonian in the following way. We described in Sec. 3.1.3, that a magnetic vector potential can be accounted for in the Hamiltonian, when the tunneling becomes complex for at least one direction. It is also sufficient to show, that the Hamiltonian features non-trivial complex tunneling matrix elements, in order to prove, that the corresponding particles behave as charged particles in a magnetic field. The implementation of Peierls phases for artificial gauge fields can be done with different techniques. Many schemes first inhibit the common tunneling along one lattice direction and then recreate it with either laser-assisted tunneling [36, 37] or lattice shaking [38–41, 63, 64]. The common tunneling can be stopped, for example, by either tilting the lattice [36] or by creating a superlattice [153]. However, these schemes are not used in this thesis and are, therefore, not further discussed. The approach, we use for the results in this thesis, is the one of synthetic dimensions.

In the synthetic dimensions approach, physical systems are engineered so that various internal states (or other non-spatial degrees of freedom) of particles are reinterpreted as additional spatial dimensions. These synthetic dimensions are formed by coupling different internal states, with the couplings designed to mimic the behavior of particles hopping between sites in a lattice. The synthetic dimensions approach was first proposed in Ref. [65]. In this paper, the authors state, that an internal degree of freedom of atoms could be seen as a synthetic dimension, where different quantum states represent synthetic lattice sites. In comparison to lattice sites of an optical lattice, we highlight two advantages in the context of topological edge states and artificial gauge fields. The first advantage is, that the synthetic dimension naturally has sharp edges, because typically the coupling of the internal states can be controlled well. For an optical lattice, this is not the case for most implementations. Because of harmonic confinement, the coupling becomes rather weaker and weaker towards the edges until it is negligible. As a result of sharp edges, the observation of edge states is much simpler, because it is clear, where they are localized. In addition, if the edges are energy states, state-selective imaging techniques (see Sec. 1.5) can be used to image each edge individually. The second advantage of synthetic dimensions is, that the internal states are not naturally coupled, which means for the realization of Peierls phases, it is not necessary to inhibit normal tunneling, which is usually a first step. Without additional steps, the internal states or synthetic lattice sites can be coupled by laser fields to reach a non-trivial complex tunneling and create an artificial magnetic field.

The internal states of the atoms used as synthetic lattice sites are arbitrary, but there are two requirements to meet:

- The states need to be stable at least on the timescales of the measurements conducted on them. Otherwise, there can be atoms dissipating out of the system, which is typically unwanted, or the atoms stay in the system, but destroy the coherence of the system.
- In the context of artificial gauge field creation, there should be a coupling available, which can impose a non-trivial phase factor onto the atoms.

Possible internal states are, for example, momentum states [77], harmonic oscillator eigenstates [78], orbital states of an optical lattice [7, 79–81], electronic states [4, 67, 82] or spin states [3, 66]. The last approach is the one, we use and further present in this thesis.

The coupling of the synthetic lattice sites has one strict and one soft requirement, if it is supposed to implement an artificial magnetic field. The strict one is, as mentioned above, that it imposes a complex phase to the atoms with the coupling and that this phase should be at least in the order of $\phi = 0.1\pi$. The soft requirement is, that the coupling should not heat the sample or destroy coherence in a different way. This is desired for a robust experimental system. A low heating rate typically expands the range of accessible measurements in the setup. Already the strict requirement is an experimental challenge. Usually, the coupling of states is realized with dipole transitions. However, for typical optical lattice spacings the imposed phase is only large enough, if the dipole transition is energetically in the optical regime or higher. This is a challenge, since the lifetime of coupled excited states in the optical regime, which are accessible via dipole transition, is typically to short. The states are not stable, for typical measurement times in the range of 10 ms to 100 ms. There are two solutions for that. The first solution is, to use an intercombination transition (see Sec. 1.1), preferable a clock transition, which feature longer lifetimes than ordinary dipole transitions for the same energy difference. Such systems were realized in Ref. [4, 67]. The second solution is, to use stimulated two-photon Raman transitions (see Sec. 3.2.2). For such a transition, the laser fields can be in the optical regime, while the coupled states can have no energy difference at all. For the results in this thesis, we use the latter solution of stimulated Raman transitions.

In the following, we will point out the characteristics of our approach for the realization of artificial gauge fields. We use different nuclear spin states (m_F states) of ytterbium atoms as a synthetic dimension, which are coupled by two-photon Raman transitions. Some of these properties are not limited to our system and are typical for other schemes as well.

- As mentioned above, synthetic dimensions, feature sharp edges, which in the case of m_F states can be individually imaged with our spin-selective imaging (see Sec. 1.5.2).
- Interactions are in the real dimension strongly localized to a single lattice site, whereas in the synthetic dimension, they are infinitely long-ranged over all lattice sites.
- The induced heating by the Raman laser coupling on the intercombination transition $^1S_0 \rightarrow {}^3P_1$ is negligible on our experimental timescales as the ratio of coupling strength over scattering rate is 3.983×10^3 and higher.
- The implementation at a quantum gas experiment only requires the alignment of one (for direct clock transitions) or two (for Raman transitions) beams. In addition, for desired coupling strengths of $\Omega \approx 100 - 500$ Hz, the required intensities in the coupling beams is easily provided by modern lasers.
- The magnetic flux can be altered by changing the angle between the coupling beams and the lattice in real space.
- The induced magnetic flux is, by construction, uniform and orthogonal to the 2D system. This means that the Harper-Hofstadter model is directly realized.
- A clear drawback of the synthetic dimensions approach is, that the number of lattice sites is very limited in the synthetic dimension. For most schemes, as in this thesis, it is restricted to single digits. The highest number of coupled states was realized with 17 spin states of dysprosium in Ref. [69].

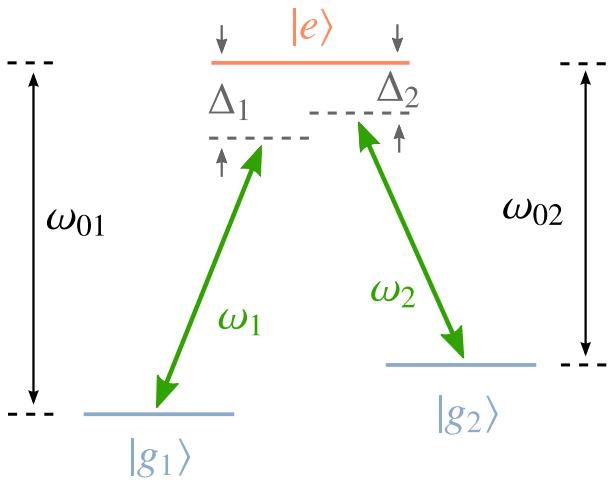

Figure 3.4: Schematic of stimulated Raman transitions. The figure illustrates the schematic of stimulated Raman transitions for a three-level atom in the Λ-configuration. A detailed description can be found in the main text. Figure inspired by Ref. [91, 117].

Our approach for the realization of an artificial gauge field automatically induces a significant spin-orbit coupling. This is a direct result of the fact, that the coupling of the m_F states needs to impart a significant momentum kick to the atoms for each spin transition. Otherwise, the magnetic flux of the system would be negligible (see Eq. 3.25 and Sec. 3.2.3 for details). Spin-orbit coupling naturally occurs in condensed matter, where it is a relativistic effect caused by the intrinsic high electric fields, which are present at the atomic scale [139]. It means a link between the spin and the momentum of particles, such that the quantities are not separated, but connected as such, that a certain spin is locked to a corresponding momentum and vice versa. Spin-orbit interactions can give rise to interesting classes of matter, such as topological insulators or topological superconductors [75]. Thorough proofs of the induced spin-orbit coupling of our synthetic dimensions approach can be found in Ref. [5, 139, 143, 154].

3.2.2 Stimulated Raman Transitions

Following the general realization of the Harper-Hofstadter model in cold atoms in the previous section, we now address the implementation of the synthetic dimension approach in our apparatus using stimulated Raman transitions. We apply them for all results presented in chapters 3 and 5. We present the mathematical terms for describing a stimulated Raman transition in atoms and its treatment as an effective two-level system. A thorough derivation of the presented results can be found in Ref. [91, 117].

Raman scattering describes the inelastic scattering of photons caused for example by multiple rotational and vibration sublevels of a molecule [91]. It was first discovered by Sir Chandrasekhara Venkata Raman and awarded with the Nobel Prize in Physics in 1930 [91]. While Raman scattering in general can be a spontaneous process and has various different applications, we focus on the case of stimulated Raman transitions in atoms.

At first, we consider a three-level atom in the Λ-configuration. In this configuration, which is illustrated in Fig. 3.4, there are two ground states $|g_1\rangle$ and $|g_2\rangle$ and one excited state $|e\rangle$. The energy difference between $|g_1\rangle$ and $|e\rangle$ is $\hbar\omega_{01}$ and the energy difference between $|g_2\rangle$ and $|e\rangle$ is $\hbar\omega_{02}$. To enable stimulated

Raman transitions in this atom, we add two light beams with the electric fields $\vec{E}_1(\vec{r}, t)$ and $\vec{E}_2(\vec{r}, t)$, where

$$\vec{E}_i(\vec{r}, t) = \hat{\epsilon}_i E_i \cos(\vec{k}_i \vec{r} - \omega_i t). \tag{3.16}$$

Furthermore, we define the energy differences $\Delta_1 = \omega_{01} - \omega_1$ and $\Delta_2 = \omega_{02} - \omega_2$. For this system, we make the following assumptions: $|\omega_{01} - \omega_{02}| \ll \omega_{0\alpha}$ and $|\Delta_1 - \Delta_2| \ll |\Delta_\alpha|$.

The system is described by an atom Hamiltonian $\mathcal{H}_{\text{atom}}$ and an atom-field interaction Hamiltonian $\mathcal{H}_{\text{atom-field}}$. The atom Hamiltonian can be expressed as [117]

$$\mathcal{H}_{\text{atom}} = \frac{p^2}{2m} - \hbar\omega_{01} |g_1\rangle\langle g_1| - \hbar\omega_{02} |g_2\rangle\langle g_2|, \tag{3.17}$$

where we set the energy of the excited state to be zero. If we apply the dipole and rotating wave approximation and perform the rotating frame transformation, the atom-field Hamiltonian is [117]

$$\mathcal{H}_{\text{atom-field}} = \frac{\hbar\Omega_1^{\text{Rabi}}}{2}\left(\sigma_1 e^{-i\vec{k}_1\cdot\vec{r}} e^{i\omega_1 t} + \sigma_1^\dagger e^{i\vec{k}_1\cdot\vec{r}} e^{-i\omega_1 t}\right) + \frac{\hbar\Omega_2^{\text{Rabi}}}{2}\left(\sigma_2 e^{-i\vec{k}_2\cdot\vec{r}} e^{i\omega_2 t} + \sigma_2^\dagger e^{i\vec{k}_2\cdot\vec{r}} e^{-i\omega_2 t}\right). \tag{3.18}$$

For $\mathcal{H}_{\text{atom-field}}$ we used $\sigma_\alpha := |g_\alpha\rangle\langle e|$ and the Rabi frequencies $\Omega_\alpha^{\text{Rabi}}$, which are defined as [91]

$$\Omega_\alpha^{\text{Rabi}} := \frac{-\langle g_\alpha | \vec{E}_\alpha \cdot \vec{d} | e\rangle}{\hbar}. \tag{3.19}$$

This system can be reduced to an effective two-level system (for details see Ref. [91, 117]). Then, the two-level system can be described by the effective Raman Hamiltonian [117]

$$\begin{aligned}\mathcal{H}_{\text{Raman}} = \frac{p^2}{2m} &+ \hbar(\Delta_1 + V_1) |g_1\rangle\langle g_1| + \hbar(\Delta_2 + V_2) |g_2\rangle\langle g_2| \\ &+ \frac{\hbar\Omega_{12}^{\text{Raman}}}{2}\left(\sigma_{\text{R}} e^{-i(\vec{k}_1 - \vec{k}_2)\cdot\vec{r}} + \sigma_{\text{R}}^\dagger e^{i(\vec{k}_1 - \vec{k}_2)\cdot\vec{r}}\right),\end{aligned} \tag{3.20}$$

where $\sigma_{\text{R}} := |g_1\rangle\langle g_2|$, Ω_{Raman} is the Raman Rabi frequency and V_α is the AC Stark shift induced by the two light beams. They can be calculated as [117]

$$\Omega_{12}^{\text{Raman}} := \frac{\Omega_1^{\text{Rabi}}\Omega_2^{\text{Rabi}}}{2\Delta_{\text{R}}}, \qquad V_\alpha := \frac{|\Omega_\alpha^{\text{Rabi}}|^2}{4\Delta_{\text{R}}}, \tag{3.21}$$

where Δ_{R} is the single-photon detuning, defined as $\Delta_{\text{R}} := (\Delta_1 + \Delta_2)/2$. Cross coupling effects from $\vec{E}_2$ on $|g_1\rangle$ and vice versa are assumed to be small and are neglected. In distinction to the single-photon detuning, we define the two-photon detuning $\delta_{\text{R}} := (\omega_2 - \omega_1) - (\omega_{02} - \omega_{01})$. The Raman Hamiltonian (equation 3.20) is equivalent to a two-level system, which is coupled by a single-photon transition with momentum $\vec{k}_{\text{R}} = \vec{k}_1 - \vec{k}_2$ and frequency $\Omega_{12}^{\text{Raman}}$.

The system can be extended to the case of multiple excited states $|e_n\rangle$, which are often present in real atomic systems, such as ytterbium. The states have the energies $\Delta_{\text{R}} - \delta_n$ with respect to the center of the ground states. Then, the equations for the Rabi frequency, the Raman-Rabi frequency and the light shifts are [117]

$$\Omega_{\alpha n}^{\text{Rabi}} := \frac{-\langle g_\alpha | \vec{E}_\alpha \cdot \vec{d} | e_n\rangle}{\hbar}, \tag{3.22}$$

$$\Omega_{12}^{\text{Raman}} = \sum_n \frac{\Omega_{1n}^{\text{Rabi}} \Omega_{2n}^{\text{Rabi}}}{2(\Delta_R - \delta_n)} \tag{3.23}$$

and

$$V_\alpha = \sum_n \frac{|\Omega_{\alpha n}^{\text{Rabi}}|^2}{4(\Delta_R - \delta_n)}. \tag{3.24}$$

In this section, we presented the initial conditions for stimulated Raman transitions and its reduction to an effective two-level system, which is even valid for multiple excited states. We introduced the terms for the calculation of the Raman-Rabi frequency and the expected AC Stark shifts, which are induced by the Raman beams.

3.2.3 Realization of the Harper-Hofstadter Hamiltonian

As mentioned in Sec. 3.2.1, we implement the Harper-Hofstadter Hamiltonian in this thesis by using a synthetic dimension to create an artificial magnetic field. There are different coupling methods for the implementation of a synthetic dimension in ytterbium atoms. The first successful method coupled different spin states of the ground state manifold with stimulated Raman transitions in Ref. [3]. The second successful method coupled the ground state to a metastable clock state with a clock transition in Ref. [4]. Another method realized in Ref. [7] used Raman transitions to couple orbital states of an optical lattice. In this thesis, we choose to work with different spin states, because we want to exploit the fact, that atoms in the ground state of ^{171}Yb are only weakly interacting. In addition, different orbital states of an optical lattice would have different interaction over tunneling ratios U_{int}/t_x because of the different tunneling rates in different bands. This would make the system more complex and is rather subject to possible future studies. Therefore, we use different m_F states of the ground state manifolds for the isotopes ^{171}Yb and ^{173}Yb to investigate their different interaction behavior. For this purpose, we implement the first realized technique, which uses stimulated Raman transitions. Furthermore, we prepare the following system. We use a degenerate Fermi gas of a single isotope and load it into a three-dimensional optical lattice (see Sec. 1.4). Along two dimensions, the lattice is deep and inhibits tunneling on experimental time scales. Only in the third dimension, the lattice is shallow enough to allow atom tunneling, yet still sufficiently deep to meet the requirements of the tight-binding approximation.

In the following, we demonstrate, that the Raman Hamiltonian in Eq. 3.20 can be transformed into the Harper-Hofstadter Hamiltonian for the prepared system. This will show, that stimulated Raman transitions can be used to realize the Harper-Hofstadter model, thereby enabling the realization of quantum Hall states. For this purpose, we bring the kinetic energy and the phase factor of the Raman Hamiltonian in different forms. First, we consider the kinetic energy term of the atomic motion in the Hamiltonian: $p^2/(2m)$. In the lattice system described above, this term transforms into a tunneling along the shallow lattice direction, as this is the only possible (real space) motion of the particles. The kinetic term becomes: $-t_x \sum_{<m,n>} \hat{c}^\dagger_{m+1,n} \hat{c}_{m,n}$, where t_x is the tunneling amplitude along the shallow lattice. Second, we express the phase factor associated with a state transition, $\exp(i(\vec{k}_2 - \vec{k}_1) \cdot \vec{r})$, in an alternative form. We define the momentum transfer Δk of the Raman beams along the shallow lattice, such that $(\vec{k}_2 - \vec{k}_1) \cdot \vec{r} = \Delta k \cdot x$. As we have a 1D lattice system, the position x is limited to lattice sites and can be expressed by the lattice spacing a and the lattice site m, such that $x = a \cdot m$. The lattice spacing, in turn, is

half the wavelength of the optical lattice laser: $a = \lambda_{\text{lat}}/2 = \pi/k_{\text{lat}}$. Altogether, the phase factor becomes $\exp(i(\vec{k}_2 - \vec{k}_1) \cdot \vec{r}) = \exp(im\pi\Delta k/k_{\text{lat}})$. Then, the Peierls phase induced by the Raman transition is

$$\phi = \pi \frac{\Delta k}{k_{\text{lat}}}. \tag{3.25}$$

The transferred momentum Δk of the Raman beams is the projection of the photon momentum vectors $\vec{k}_{\text{R}}$ on the shallow lattice direction. Because of the symmetry of our beams with respect to the lattice (see Fig. 4.1), it can be calculated as

$$\Delta k = \sin(\theta/2) \cdot 2\left|\vec{k}_{\text{R}}\right|, \tag{3.26}$$

where θ is the angle between the two Raman beams and $\left|\vec{k}_{\text{R}}\right|$ is the photon momentum of the Raman laser.

With the alterations of the kinetic term and the phase factor and Ω_{R} as the Raman-Rabi frequency of the coupling, which is assumed to be independent of the spin state n, the Raman Hamiltonian takes the form:

$$\mathcal{H} = \sum_{<m,n>} \hbar\delta_n \hat{c}^\dagger_{m,n}\hat{c}_{m,n} + \left(-t_x \sum_{<m,n>} \hat{c}^\dagger_{m+1,n}\hat{c}_{m,n} - \frac{\hbar\Omega_{\text{R}}}{2} \sum_{<m,n>} e^{im\phi}\hat{c}^\dagger_{m,n+1}\hat{c}_{m,n} + \text{h.c.}\right), \tag{3.27}$$

where $\delta_n = V_n - (n-1)\cdot\Delta\omega$. V_n is the AC Stark shift of the nth spin state (or equally: of the nth synthetic lattice site), which is induced by the Raman beams, as defined in Eq. 3.24. Moreover, $\Delta\omega$ is the frequency difference between the two Raman beams: $\Delta\omega = \omega_1 - \omega_2$. For $\delta_n = 0$, this is the Harper-Hofstadter Hamiltonian in a different gauge:

$$\mathcal{H}_{\text{Harper-Hofstadter}} = -t_{\text{x}} \sum_{<m,n>} \hat{c}^\dagger_{m+1,n}\hat{c}_{m,n} - \frac{\hbar\Omega_{\text{R}}}{2} \sum_{<m,n>} e^{im\phi}\hat{c}^\dagger_{m,n+1}\hat{c}_{m,n} + \text{h.c.} \tag{3.28}$$

The system described by this Hamiltonian is illustrated in position space in Fig. 3.5. In the synthetic dimension, displayed along the vertical axis, there are only two lattice sites or spin states: the (pseudo)spin-up, $|\uparrow\rangle$, and (pseudo)spin-down state, $|\downarrow\rangle$. This structure already reflects the specific realization of our system. In the real dimension x, the lattice consists of multiple sites labeled with $m-1$, m, $m+1$ and so forth. Atoms can tunnel along the real dimension with the amplitude t_{x} and along the synthetic dimension they tunnel with the amplitude $\hbar\Omega_{\text{R}}/2 \cdot e^{im\phi}$, which corresponds to a spin transition. The phase factor $e^{im\phi}$ leads to the magnetic flux ϕ, which pierces each plaquette of the two-dimensional system. For non-trivial cases of ϕ and $\Omega_{\text{R}}/t_{\text{x}}$, the system features chiral edge currents, which are indicated by the colored arrows, that illustrate the motion of atoms along the two legs.

This implementation of the Harper-Hofstadter model has a different gauge than the Landau gauge, which we introduced in Sec. 3.1.2 to simplify the theoretical calculations. The laboratory gauge differs by the fact, that the phase factor in the Hamiltonian is in the synthetic y direction instead of the real x direction. This gauge difference has direct consequences for the bandstructure, which are illustrated in Fig. 3.6. In the theory gauge (Fig. 3.1), the bare and dressed energy bands are axially symmetric with respect to the Brillouin zone center ($k = 0$). The bare Bloch bands of the two coupled states are shifted with their lowest energy from the center to $\phi/2$ and $-\phi/2$. In the laboratory gauge, the bare energy bands are the unshifted Bloch bands for both states with their lowest energy in the center of the Brillouin zone. The bare bands for both states are identical. While the state population in the dressed bands is complementary for the two different states in the theory gauge, this is not the case in the laboratory gauge. There, the areas

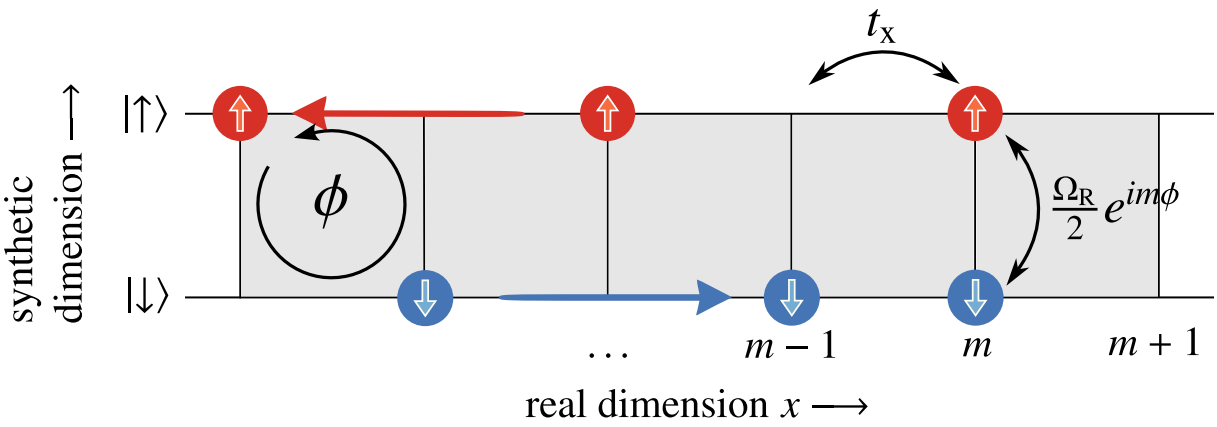

Figure 3.5: Two-leg quantum Hall ladder in position space. The figure presents a scheme of the realized two-leg quantum Hall ladder in position space. On the horizontal axis, the real dimension of the shallow optical lattice is shown. On the vertical axis, the synthetic dimension is shown with its two synthetic lattice sites $|\downarrow\rangle$ and $|\uparrow\rangle$. Along the real dimension the atoms can hop from lattice site m to $m+1$ with the tunneling amplitude t_x and along the synthetic dimension, atoms can hop at site m from $|\downarrow\rangle$ to $|\uparrow\rangle$ with the amplitude $(\Omega_R/2)\, e^{im\phi}$. This system is pierced by a uniform magnetic flux ϕ, which is the phase, that atoms acquire when they hop around a unit cell. For non-trivial cases of ϕ and Ω_R/t_x, the system features chiral edge currents, which are indicated by the colored arrows, that illustrate the motion of atoms along the two legs.

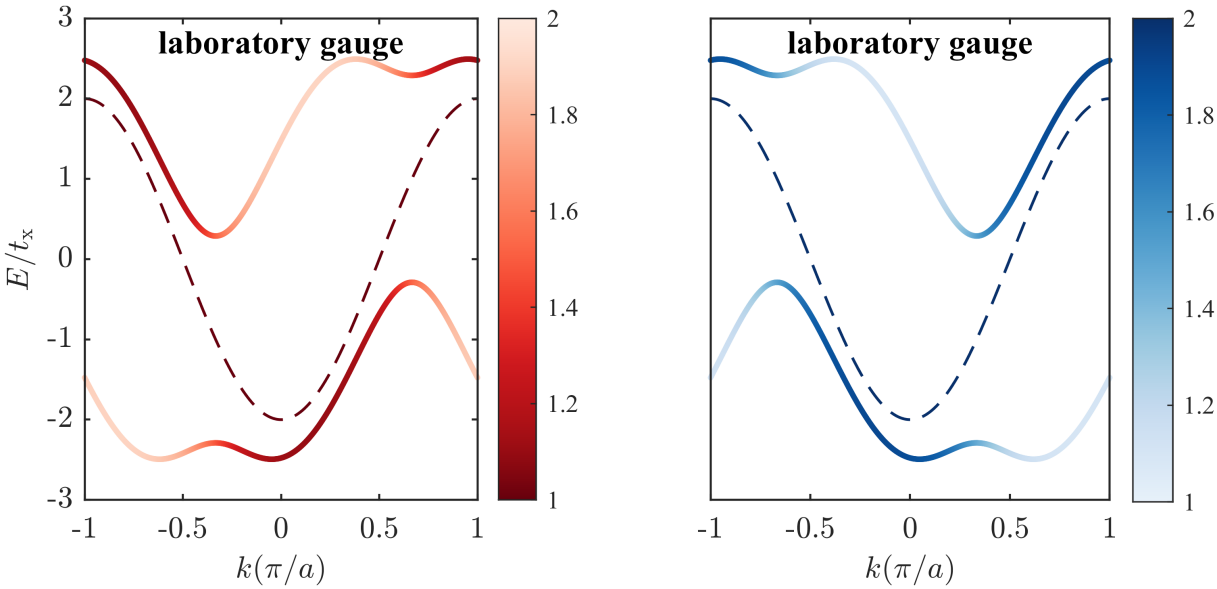

Figure 3.6: Bandstructure in the laboratory gauge. The figure depicts the bandstructure of the two lowest dressed bands in the laboratory gauge for a two-photon detuning $\delta_R = 0$ and $\phi = 2\pi \cdot 1/3$. The vertical axis displays the energy in units of the tunneling energy and the horizontal axis displays the quasimomentum k for the first Brillouin zone. Dashed lines show the unperturbed bandstructure of the bare bands with vanishing Raman coupling, i.e. $\Omega_R \to 0$. Whereas solid lines show the bandstructure of the dressed bands with $\Omega_R = 2t_x$. The color and opacity of the solid lines express the state population as denoted in the color bars on the right. For the bandstructure in the Landau gauge see Fig. 3.1. Figure adapted from Ref. [116].

with the highest populations in the center and at the boundaries of the Brillouin zone are overlapping for both states. In our measurements with quantum Hall ladders described below, we observe the state populations in the first Brillouin zone with our bandmapping technique (see Sec. 1.5.1). Hence, we only have access to the laboratory gauge and expect the populations to be as plotted in Fig. 3.6.

The depicted bandstructure in both gauges shows the bands of the edge states, which reside in the $q-1$ band gaps. We can identify two eigenstate bands, which correspond to the $q-1=2$ band gaps for the magnetic flux of $\phi = 2\pi \cdot 1/3$ (see Fig. 3.3 for comparison). However, because of the finite size of our system along the synthetic dimension (with only two legs), the bandstructure transforms smoothly for changes in ϕ. As a result, also for $\phi = 2\pi \cdot 1/4$, the bandstructure does not split into $q-1=3$ bands, but still features only 2 bands, with their form modified according to the different momentum transfer between the two bare bands. This finite size effect, makes the bandstructure - and, thus, the predictions on the chiral edge currents - robust against small variations in ϕ. This is despite the fact that, in principle, the bandstructure depends strongly on the precise value of ϕ, as demonstrated by the fractal structure displayed in the upper-right subfigure in Fig. 3.2.

In this chapter, we have detailed the realization of quantum Hall systems, starting with the basic theoretical concepts and progressing to practical implementation methods. We began by introducing the Harper-Hofstadter model and discussing its single-particle solutions, which helped us understand the behavior of these systems without inter-particle interactions. We then explored how to implement this model in cold atom systems by creating artificial gauge fields. Finally, we outlined our approach to generating artificial magnetic fields and quantum Hall states through stimulated Raman transitions. This chapter provides a clear path from theoretical understanding to practical realization of quantum Hall states, paving the way for the following chapters.

4 Preparation and Implementation of Quantum Hall Ladders

Building on the theoretical framework established in the previous chapter, which explored the realization of quantum Hall states in quantum gases, this chapter focuses on their practical implementation and preparation. For this crucial step in exploring topological phases of matter, we detail the experimental setup, preparation techniques, and primary measurements required to observe and characterize these states. Sec. 4.1 begins with the technical implementation, including an overview of the Raman Laser System. We discuss our design considerations and the selected parameter space with a focus on the measurement possibilities, which are necessary for achieving the desired quantum control. In Sec. 4.2, we address the eigenstate preparation for the Hamiltonian. Starting with our applied technique: the adiabatic passage and then discuss other approaches. Sec. 4.3 covers primary measurements to verify the successful creation of these states. We examine Raman resonances, Raman-Rabi oscillations and chiral edge currents, which directly indicate the topological nature of the quantum Hall effect. Lastly, Sec. 4.4 addresses various methods for optimizing the experimental data, including improvements in the spin detection, imaging, eigenstate preparation and data analysis. This chapter provides a concise guide to the experimental procedures necessary for studying quantum Hall ladder systems, laying the groundwork for further exploration of their unique properties.

The planning and design of the Raman laser system in Sec. 4.1 was mainly done by the author and supervised by C. Becker. The building and characterization of the laser system described in Sec. 4.1.1 was mainly done by N. Pintul (see Ref. [155] for details) under supervision of B. Abeln and the author, with small alterations done by the author at a later stage. The analysis of the eigenstate preparation in Sec. 4.2 and 4.4.3 was primarily conducted by the author, with initial analysis provided by L. Hilbig under the author's supervision (see Ref. [116] for details). All computations were performed by the author and are partially based on code developed by L. Hilbig. The primary measurements and those for the optimization methods presented in Sec. 4.3 and 4.4 were conducted by the author with the assistance of T. Petersen. All measurements were planned and analyzed by the author.

4.1 Technical Preparation

4.1.1 Raman Laser System

After the theoretical description of stimulated Raman transitions in the previous chapter, we discuss the implementation of a Raman laser system in our experiment in the following. This laser system is used to realize a synthetic dimension (see Sec. 3.2.1) and explore the physics described in this chapter and chapters 3 and 5. First, we describe the chosen transition and the laser. Second, we present advantages and disadvantages of two design options and discuss our design decision. Third, the whole laser system is presented. At last, we introduce the application possibilities. Further details on the Raman laser system, such as the custom-made attachments and a characterization of the beam quality can be found in Ref. [155].

Table 4.1: Comparison of Raman Laser Setup Options. The table lists advantages and disadvantages of two implementation options for the Raman laser setup described in the main text.

	Option 1: Raman beams split in front of fiber	**Option 2: Raman beams split behind fiber**
Advantages	• less space needed in the vicinity of the atoms • better beam profile • simpler to change angle between Raman beams	• Raman beams are completely separated
Disadvantages	• possible decoherence caused by insufficient splitting of Raman beams	• more space needed in the vicinity of the atoms • worse beam profile • more difficult to change angle between Raman beams

For the stimulated Raman transitions, we choose to work with green laser light of 556 nm, which addresses the intercombination transition $^1S_0 \rightarrow {}^3P_1$. This transition features a broad hyperfine splitting, which can be exploited to reach high ratios of the Raman coupling strengths over the total scattering rate of the Raman beams Ω_R/Γ_R. As this ratio can limit the coherence time of the quantum Hall system, high values are desired. This transition was also addressed in Ref. [3, 7, 71] to successfully implement Raman transitions in ytterbium for synthetic dimensions. To generate the Raman beams, we use a single laser exclusively. Since the laser is not used for any other applications, its operating frequency can be chosen as desired (in the limits of the laser capabilities). The laser is not frequency stabilized, but free running. This is sufficient, because the laser's frequency walk-off is not a problem for the Raman transitions described in this thesis. We observe the walk-off with a wavemeter to be in the order of ≤ 20 MHz per day. The frequency of the laser translates directly to a change of the single-photon detuning Δ_R for the Raman transition as defined in Sec. 3.2.2. We operate the Raman beams at a single-photon detuning of 2.44 GHz and 3.25 GHz above the transition $^1S_0 \rightarrow {}^3P_1(F' = 1/2)$ and $^1S_0 \rightarrow {}^3P_1(F' = 7/2)$ for ^{171}Yb and ^{173}Yb, respectively. The largest influence of the frequency walk-off is on the Raman coupling strength Ω^{Raman}. There, the uncertainty caused by a 20 MHz change can be estimated to be approximately 0.3 % and 1.2 % (for details see Sec. 4.1.2). Hence, this effect can be neglected, as other imperfections, such as the stability of the beam intensity or the uncertainty in the determination of Ω^{Raman}, are dominating the atomic behavior and total measurement uncertainty.

The first design consideration for the implementation of a Raman laser system at our quantum gas machine is the placement of the optical components. Since there is not enough space to build a whole laser system in free space at the optical table of the ytterbium atoms, some parts of the system need to be placed on a separate optical table and the laser beams must propagate to the atoms through a fiber at some point. There are two options to implement this with low differential phase noise. Low differential phase noise is crucial for the coherence of Raman transitions, whereas common phase noise cancels out for the two-photon transition, as the phase relation between the beams stays stable. The first implementation option is, that both laser beams are coupled into the same polarization-maintaining fiber, one on the fast and one on the slow axis. This was realized for example in Ref. [3]. The second option is, that the laser beam is split into the two Raman beam branches after it is brought to the vicinity of the atoms

and the Raman beams stay in free space until they hit the atoms.

Advantages of option one are, that only little space is needed in the vicinity of the glass cell and that it is simpler to change the beam paths of the Raman beams, if needed, for example for changing the transferred momentum on the atoms (see Sec. 4.1.2). Moreover, the laser beam profiles are usually closer to a Gaussian profile than for option two. However, with this option, it is crucial, that the beams are very well separated behind the fiber to avoid decoherence. This requires, that the coupling into the fiber is very accurate along the respective propagation axis and that the splitting of the two polarizations behind the fiber is very clean. Remaining fractions of light with the frequency of the other Raman beam destroy coherence. This is not necessarily the case for the Raman transition itself, but for the realization of an artificial gauge field with it, as the gauge field requires the momentum transfer to be clearly directed.

Disadvantages of option two are, that the frequency changes via AOM to the two Raman beams have to be made in the vicinity of the glass cell. This requires more space and makes a fast adjustment of the beam paths more difficult. Furthermore, the beam profile of light, which propagated through an AOM, differs usually from a Gaussian profile, which can affect the coherence of the atomic sample. However, a great advantage of this option is, that the two Raman beams are completely separated. For an overview of the advantages and disadvantages of the two options see Table 4.1. We decided to use option two for the implementation at our experiment. To prevent alterations in the beam profiles to affect the coherence of the transition, we choose the waists of the Raman beams with approximately 0.6 mm large enough, such that only the centers of the beams hit the atomic cloud, which is expanded over a few μm. In addition, this strategy has the benefit, that the intensity of the beams is more homogeneous for the atoms than for smaller beam diameters. Moreover, the alignment of the beams on the atoms is more robust and an estimation of the beam intensity at the position of the atoms is typically more accurate.

The setup of the Raman beam paths is as follows. The used laser provides approximately 105 mW of laser radiation at 556 nm. Behind the laser output, there is a half-waveplate and a polarizing beam splitter (PBS) to regulate the transmitted laser power, which goes to the Raman branch. Unwanted power in the laser beam, which is not needed for the Raman transition, can be dumped in the reflection of the PBS. Behind the PBS, the beam propagates through an AOM, which is operated in double passage. On the one hand, this AOM is used to regulate the power of the Raman beams from cycle to cycle. On the other hand, it is used to switch the Raman beams on and off. After passing through the AOM, the laser beam is coupled into a polarization-maintaining fiber, which directs it to a breadboard, where additional optical elements manipulate the laser beam further. We refer to this breadboard as the Raman breadboard.

The realized Raman breadboard can be seen in Fig. 4.1. The starting point on the Raman board is a fiber coupler, which emits the linearly polarized 556 nm light from the polarization-maintaining fiber mentioned above. The fiber coupler has an adjustable lens included, which can be used for a fast tuning of the beam waists. The board is designed to be used with a beam diameter of approximately 1.2 mm. This beam diameter results in a Rayleigh length of approximately 2.0 m, which means, that the beam diameter can be assumed to be stable over the whole beam path through the Raman board up to the atoms in the glass cell, which is a total length of approximately 80 cm. Behind the fiber coupler, there is a half-waveplate and a PBS. The waveplate can be used to alter the branching ratio at the beam splitter and the beam splitter divides the beam into the two Raman beams. The fiber to the Raman board is polarization-maintaining to keep the polarization and, therefore, the relative powers of the two Raman beams stable. In both paths, behind the beam splitter, there is an AOM to change the frequency of each beam individually. The frequencies applied to the AOMs are used to realize a detuning between the two Raman beams. The AOMs on the Raman board are switched on, for most of the time of the experimental

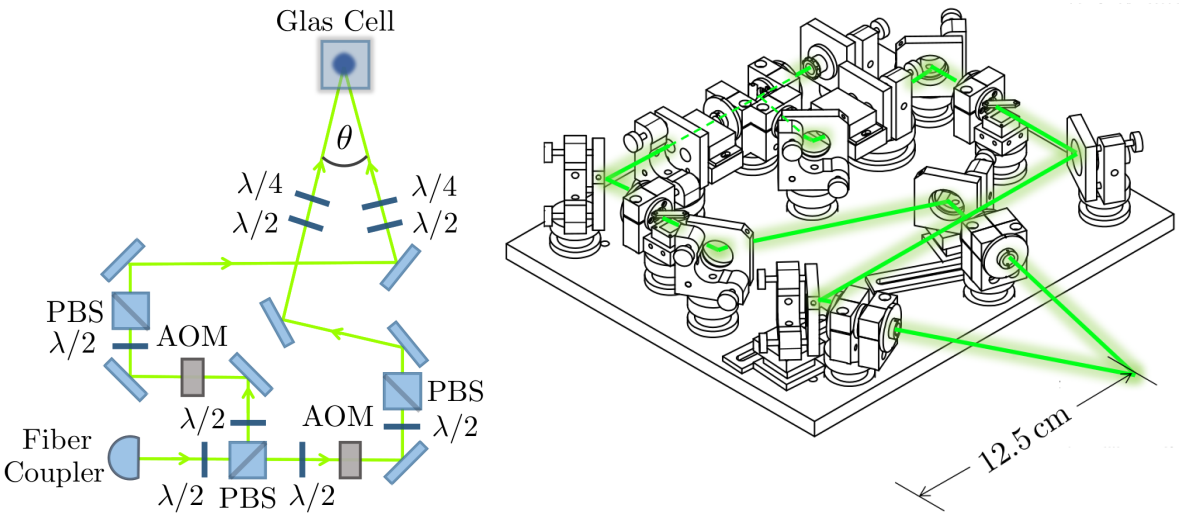

Figure 4.1: Raman breadboard setup. The figures show the setup of the optical elements of the Raman breadboard as a schematic on the left and as a computer assisted drawing on the right. The drawing on the right is true-to-scale. Laser beams are illustrated as green lines. A detailed description of all optical elements and their function can be found in the main text. Taken from [155].

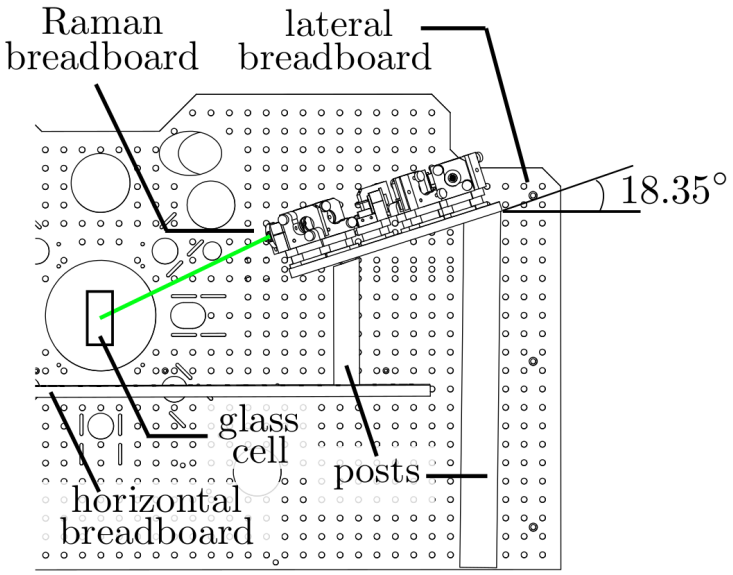

Figure 4.2: Raman breadboard implementation. The figure illustrates the implementation of the Raman breadboard in the experimental setup. The breadboard is connected to two posts and a lateral breadboard. The breadboard is implemented under an angle of approximately $18.35°$ with respect to the horizontal axis. Taken from [155].

cycle. This keeps the AOMs at operating temperature and inhibits thermal walk-offs of the laser pointing during measurements. In front of each AOM, there is another half-waveplate to rotate the polarization for an optimum AOM efficiency. Light in undesired orders of the AOMs is blocked. Behind the AOMs, there are three mirrors in each beam path in total. The first two mirrors can be used to align the beams in all degrees of freedom on the last mirror. The last mirror is used to align the beams on the atoms in the glass cell. In addition, in each beam path behind the AOMs, there are a pair of half- and quarter-waveplates to change the final polarization of the Raman beams as desired. The Raman breadboard is placed at the experimental setup under an angle of approximately 18.35° with respect to the horizontal plane. The implementation is shown in Fig. 4.2. To check and monitor the polarization of the Raman beams, we additionally installed a PBS in each Raman beam path, after they propagated through the glass cell. When the beam splitters are combined with a power meter or photodiode behind it, changes of the polarization can be seen. In our measurements, we could not detect a difference between the beam polarization in front of and behind the glass cell. Thus, we assume, that the polarization behind the glass cell is very similar to the polarization at the position of the atoms.

The Raman board is designed, such that the angle between the Raman beams can be changed by translating the last mirror in front of the glass cell for each beam. The minimal angle is limited by the dimensions of the mounts for the last mirrors and the distance between the last mirrors and the glass cell. The maximal angle is limited by the space between the Helmholtz coils of the 3D MOT. The possible angle range is $\theta \in [5°, 24°]$. This corresponds to a magnetic flux range of $\phi \in [0.12\pi, 0.57\pi]$, if implemented with an optical lattice at the magic wavelength of 759 nm (for details see Sec. 4.1.2). Using a state-dependent lattice at a wavelength of 660 nm, which is also already implemented at the experiment (see Ref. [100]), the possible magnetic flux range would be $\phi \in [0.10\pi, 0.49\pi]$.

4.1.2 Applied Raman Transitions

In this section, we provide a detailed description of the applied Raman transitions, focusing on the specific parameters used in our setup. We begin by examining the polarization of the Raman beams for ^{171}Yb and ^{173}Yb. Next, we discuss how we select the single-photon detuning and the momentum transfer. Finally, we present the simplified Raman Hamiltonians for both isotopes, tailored to the parameters we have chosen.

We use stimulated Raman transitions to couple two m_F states of the ground state manifold. We use only two states for both isotopes, because there are only two states available for ^{171}Yb with $F = 1/2$ and we want both systems to be as similar as possible. Hence, we couple also only two states, when working with ^{173}Yb. How we achieve this for the six different spin states of ^{173}Yb ($F = 5/2$) is discussed below. Independently of which states are coupled for ^{173}Yb, the two coupled states can be treated as a pseudo spin up $|\uparrow\rangle$ and pseudo spin down state $|\downarrow\rangle$ [156]. The applied Raman couplings for both isotopes are illustrated in Fig. 4.3. In the following, we discuss the polarizations of the Raman beams for the implementation of the shown coupling.

For the $m_F = -1/2$ and $m_F = 1/2$ state of ^{171}Yb the transition polarizations need to be σ in one beam and π in the other. For the realization of the Peierls phase, it is important, that the momentum transfer of the Raman beams to the atoms has an unambiguous direction. Consequently, the virtual absorption process must always be from one beam and the virtual stimulated emission process from the other. To realize this, the quantization axis of the atoms is chosen to be normal to the plane, which is spanned by the propagation directions of the Raman beams. In this configuration, one beam can be purely π polarized

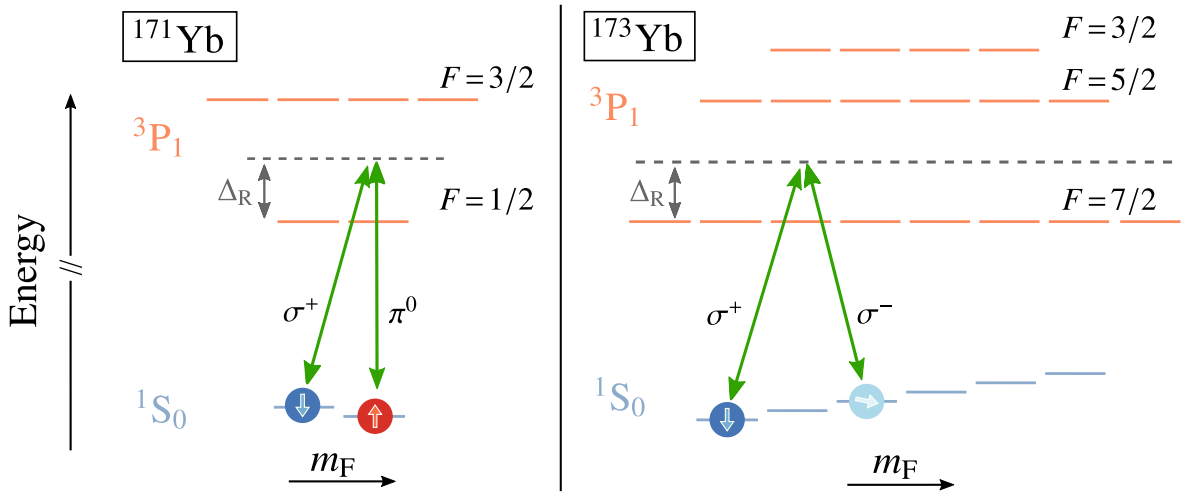

Figure 4.3: Scheme of the Raman couplings in ^{171}Yb and ^{173}Yb. The figure depicts a scheme for the implemented Raman couplings in the two fermionic isotopes ^{171}Yb and ^{173}Yb. The Raman beams are operated in between the hyperfine splitting of the $^1S_0 \rightarrow {}^3P_1$ transitions with a single-photon detuning Δ_R to the lowest hyperfine state. There, the ratio of Raman coupling strength over scattering rate Ω_R/Γ_R is the highest. We use a σ-π transition for ^{171}Yb and a σ-σ transition for 173Yb to couple two spin states in each case. The displayed energies along the vertical axis are scaled. The hyperfine splittings of the $^3P_1$ states and the detunings Δ_R are on the order of GHz, while the depicted Zeeman splittings in the ground states are on the order of kHz. This representation highlights that the single-photon detunings are robust against external magnetic field changes, whereas the two-photon detunings strongly depend on the magnetic field.

(linearly polarized along the quantization axis), whereas the other can be a combination of σ^- and σ^+ polarization (linearly polarized perpendicular to the quantization axis). In addition, for a clear direction of the momentum transfer, it is important, that the states have an energy difference greater than the power broadened linewidth. Then, only one of the two processes, σ^+ absorption paired with π emission or π absorption paired with σ^- emission, is resonant with the two-photon transition. The energy difference between the states is a combination of the Zeeman splitting and a spin-dependent dipole potential induced by the Raman beams. This is further discussed in Sec. 4.3.1.

For ^{173}Yb, there are more possibilities to choose the beam polarizations. As mentioned above, we want to realize a system for ^{173}Yb, which is similar to the scenario of the ^{171}Yb case. This means, we want to couple only two different spin states, thereby forming a two-leg ladder. For the same beam polarizations as for ^{171}Yb, several spin states of ^{173}Yb would automatically be coupled. There are two reasons for that. First, the Zeeman splitting is linear. This means, it does not affect the individual two-photon resonances between different states, as long as the spin difference Δm_F between the states is equal. Second, for these beam polarizations, the spin-dependent dipole potentials are very similar, which makes it difficult to shift spin states out of resonance. Hence, it is unfavorable to use the same polarization for ^{173}Yb as for ^{171}Yb. Instead, we use $\sigma\,\sigma$ transitions for ^{173}Yb. This already reduces possible unwanted transitions from four to only one with respect to $\sigma\,\pi$ transitions. The spin-dependent dipole potentials have the largest difference for the case, in which both beams are linearly polarized orthogonal to the quantization axis, i.e. they are an equal combination of σ^- and σ^+ polarization. This is the optimal configuration, if only two Raman beams with single frequencies are considered. However, the unwanted coupling to the third state does not completely vanish. This is further discussed below and in Sec. 4.3 (see also Ref. [116] for additional computations).

The exact polarizations of the Raman beams differ slightly from the ideal cases described above, because of the choice of the external magnetic field direction. The magnetic field, and consequently the quantization axis, is aligned along the 1D lattice direction using our 3D-MOT coils. This alignment is essential for spin-selective imaging with blast pulses (see Sec. 1.5.2) and a rapid rotation of the magnetic field could influence the data. This leads to a small angle between the quantization axis and the linearly polarized light, which would be ideally along the quantization axis for π transitions. The σ transitions are not influenced, since the polarization is still perpendicular on the quantization axis. This small angle is half the angle between the Raman beams: $\theta/2 = 9.95(45)^\circ$. The linearly polarized light is then composed of 97.3 % π-polarized light for the atoms. This has no effect on the measurements described in this thesis, except for a small relative energy shift on the order of 10×10^{-5} of the Raman resonance for ^{171}Yb.

The single-photon detuning of the Raman transition should be chosen mainly such, that the ratio of Raman coupling strength over scattering rate Ω_R/Γ_R is at its maximum. This maximum provides the longest coherence times for the system. Additionally, at this maximum, the slope of the coupling strength over scattering rate is zero and, thus, changes in the laser frequency during a measurement have minimal effect. If necessary, one could make a trade-off of stronger coupling against shorter coherence times, but this was not needed for the measurements presented in this thesis. As mentioned in subsection 4.1.1, the base frequency of the Raman beams can be chosen freely as the laser is free running and not used for other applications. Therefore, we operate the laser such, that the single-photon detuning is exactly at the maximum of the ratio Ω_R/Γ_R for both isotopes ^{171}Yb and ^{173}Yb. Concretely, the detunings are 2.440 GHz and 3.255 GHz above the transitions $^1S_0 \rightarrow {}^3P_1(F' = 1/2)$ and $^1S_0 \rightarrow {}^3P_1(F' = 7/2)$ for ^{171}Yb and ^{173}Yb, respectively. Details for the calculation of the ratio Ω_R/Γ_R can be found in Ref. [116, 155]. At the chosen detunings, they are 11.54×10^3 and 3.983×10^3, respectively. This means, that the expected coherence lifetimes are on the order of $10^3/\,\Omega$. This is much longer than the timescales of the measurements, which are $< 10 \cdot 2\pi/\Omega$. Therefore, the scattering rates can be neglected for the measurements presented in this thesis.

The magnetic flux of the system is determined by the angle θ between the Raman beams (see Eq. 3.26). For the purposes of this work, which is to probe interaction effects in a quantum Hall ladder, the exact value of the magnetic flux is of minor importance. It should only be chosen as such, that the chiral currents are very prominent. The currents vanish at $\phi = 0$ modulus π, because of the symmetry of the system [4]. Therefore, taking theoretical considerations and published experimental data from Ref. [4] into account, the range $\phi \in [0.2, 0.8]\pi$ modulus π is expected to be fine. The results in this thesis were taken at an angle $\theta = 19.9(9)^\circ$ and correspondingly at a magnetic flux of $\phi = 0.444(20)\,\pi$.

In the following, we derive simplified Raman Hamiltonians, which are specified to our selected parameters. As described in Sec. 3.2.2, the Raman transitions can be described by the effective Raman Hamiltonian in Eq. 3.20. We only consider the state coupling of the synthetic dimension. For this purpose, we disregard the kinetic energy term $p^2/(2m)$ and the phase factor $\exp(i(\vec{k}_2 - \vec{k}_1) \cdot \vec{r})$ in the Raman Hamiltonian. We present the coupling Hamiltonians for both isotopes and denote them in matrix notation in the basis of (possibly) coupled m_F states, i.e. $|m_{171} = -1/2\rangle, |+1/2\rangle$ and $|m_{173} = -5/2\rangle, |-1/2\rangle, |+3/2\rangle$ for ^{171}Yb and ^{173}Yb, respectively. For ^{171}Yb, we obtain

$$\frac{\mathcal{H}_{171}}{\hbar} = \begin{pmatrix} {}^{171}V_{-1/2} & {}^{171}\Omega_{12}/2 \\ {}^{171}\Omega_{12}/2 & {}^{171}V_{+1/2} - {}^{171}\Delta\omega \end{pmatrix} \tag{4.1}$$

and for ^{173}Yb, we get

$$\frac{\mathcal{H}_{173}}{\hbar} = \begin{pmatrix} {}^{173}V_{-5/2} & {}^{173}\Omega_{12}/2 & 0 \\ {}^{173}\Omega_{12}/2 & {}^{173}V_{-1/2} - {}^{173}\Delta\omega & {}^{173}\Omega_{23}/2 \\ 0 & {}^{173}\Omega_{23}/2 & {}^{173}V_{+3/2} - 2\,{}^{173}\Delta\omega \end{pmatrix}. \tag{4.2}$$

We further simplify $\mathcal{H}_{173}$ for our parameters. For the fixed single-photon detuning $^{173}\Delta_R$ and polarizations of the Raman beams in the ^{173}Yb case, the coupling $^{173}\Omega_{23}$ can be expressed by $^{173}\Omega_{12}$. We obtain $^{173}\Omega_{23} = 1.339 \cdot {}^{173}\Omega_{12}$. Moreover, with the chosen beam polarizations, we find $^{173}V_{+3/2} - 2\,{}^{173}\Delta\omega = {}^{173}V_{-5/2} + 2.65 \cdot {}^{173}\Omega_{12}$. We consider this energy difference to be large enough to neglect the effect of the coupling in our model and for most measurements. The Hamiltonian $\mathcal{H}_{173}$ takes the following form

$$\frac{\mathcal{H}_{173}}{\hbar} = \begin{pmatrix} {}^{173}V_{-5/2} & {}^{173}\Omega_{12}/2 & 0 \\ {}^{173}\Omega_{12}/2 & {}^{173}V_{-5/2} & 1.339 \cdot {}^{173}\Omega_{12}/2 \\ 0 & 1.339 \cdot {}^{173}\Omega_{12}/2 & {}^{173}V_{-5/2} + 2.65 \cdot {}^{173}\Omega_{12} \end{pmatrix}. \tag{4.3}$$

This section has detailed the technical groundwork necessary for implementing stimulated Raman transitions to explore synthetic dimensions in quantum gases. We designed a laser system that maintains coherence while minimizing spatial constraints. Furthermore, we carefully selected transition parameters to ensure accurate measurements.

4.2 Eigenstate Preparation

With the detailed description of the laser system and the specific Raman transitions, we only need one more step to carry out the planned measurements on the influence of interactions in quantum Hall systems: the preparation of single eigenstates of the Harper-Hofstadter Hamiltonian. This ensures clear and unambiguous measurement results and enables the isolated analysis of physical phenomena. In this section, we describe the technical aspects of the preparation in detail. Following that, we will discuss potential optimizations of the preparation. We will sometimes refer to the eigenstates as the dressed states, as the eigenstates are the bare atomic states dressed with the Raman laser light.

4.2.1 Adiabatic Passage

For the preparation of an eigenstate, we use an adiabatic passage. An adiabatic passage is a very common approach to transfer atoms from one quantum state to another. It is described in detail in Ref. [117] for example. In this method, the change in the Hamiltonian is performed slowly with respect to the energy difference between the eigenenergies of the initial and final Hamiltonian. This is done in such a way, that the state follows an avoided crossing to always stay in an eigenstate of the current Hamiltonian.

Initially, we assume that all atoms are in the lowest Bloch band. This can be confirmed experimentally by performing a bandmapping technique (see Sec. 1.5.1). We aim to transfer all atoms to the same eigenstate band of the Harper-Hofstadter Hamiltonian. For this purpose, the Raman beams are switched on at the desired power of the final system with a large two-photon detuning δ_R, such that the coupling is very weak (see details below). For the adiabatic passage, we ramp the detuning to zero, such that the atoms can follow the time evolution of the state and always stay in the current eigenstate of the

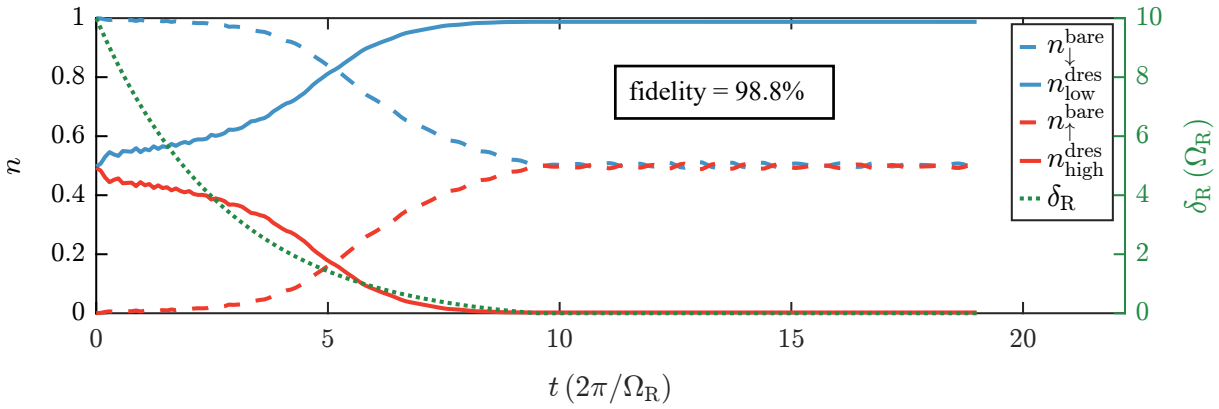

Figure 4.4: Adiabatic passage. The figure displays state transfer for an adiabatic passage. For this purpose, we present several quantities as a function of the ramp time t. On the left vertical axis, we depict, on the one hand, the relative population $n_{\uparrow/\downarrow}$ of the pseudo spin states $|\uparrow\rangle$ and $|\downarrow\rangle$ for the bare states (dashed lines). On the other hand, we depict the population $n_{\text{low/high}}^{\text{dres}}$ of the lowest and higher (second lowest) dressed band (solid lines). On the right vertical axis, we show the two-photon detuning δ_R (dotted line) in units of the Raman coupling strength Ω_R. The illustrated adiabatic passage reaches a fidelity of 98.8 %.

system. For this ramp, we choose an initial detuning, as small as possible, while large enough, that the coupling of the Raman transition is negligible. This is equivalent to the statement, that the amplitude of the induced Raman-Rabi oscillations is negligible for the chosen detuning. The amplitude can be calculated as [157]

$$A_R = \frac{\Omega_R^2}{\Omega_R^2 + \delta_R^2}. \tag{4.4}$$

We choose to work with $\delta_{ini} = 10 \cdot \Omega_R$, for which $A_{R,\,max} = 1/101 \approx 1.0\ \%$.

For the shape of the ramp, we choose an exponential-like shape, as it shortens the preparation duration for the same preparation fidelity with respect to a linear or s-shaped ramp. This does not necessarily mean, that an exponential shape is the best ramp shape to avoid the observed decay of the chiral currents, but it gives a shorter upper limit on the duration of the decay, which makes it easier for first investigations. The exponential-like experimental ramp has the form:

$$\begin{aligned} \delta_R(t) &= A(t) \exp\left(-\frac{t}{\tau}\right) + B(t), \\ A(t) &= \frac{\delta_{fin} - \delta_{ini}}{\exp\left(-\frac{T}{\tau}\right) - 1}, \\ B(t) &= \delta_{ini} - A(t), \end{aligned} \tag{4.5}$$

where δ_{ini} is the initial detuning, δ_{fin} is the final detuning, τ is the exponential time constant and T is the total time of the ramp. This ramp has the advantage with respect to a pure exponential, that the final detuning is reached in the finite time T.

We calculate the preparation behavior during and after the adiabatic passage for different parameters by numerically solving the time-dependent Schrödinger equation

$$i\hbar \frac{\partial}{\partial t} |\Psi(t)\rangle = \mathcal{H}(k) |\Psi(t)\rangle . \tag{4.6}$$

For details on these calculations see Ref. [116]. A typical example of such a calculation is shown in Fig. 4.4. We observe in the displayed case, that all atoms are initially in the $|\downarrow\rangle$ state. During the adiabatic ramp half the population smoothly transfers into the $|\uparrow\rangle$ state and the lowest dressed band is prepared with a fidelity of 98.8 %. If the ramp parameters are expressed in units of Ω_R and the ratio Ω_R/t_x stays the same, the preparation dynamics are equal for different values of t_x.

For the adiabatic passage, we want to realize the avoided crossing only for the targeted transfer. This means, there must not be other state crossings during the detuning ramp. Other crossings could be higher Bloch bands, if the ramp starts blue-detuned and the initially populated bare state is energetically higher (in the rotating frame) than the unpopulated bare state. Further crossings could be unwanted Raman resonances to other m_F states. This would be the case, for example, if the initial state is $|^1S_0,\ m_F = 5/2\rangle$ for ^{173}Yb and one ramps red-detuned to zero. The wanted Raman coupling would be of $m_F = 5/2 \rightarrow m_F = 1/2$, but there is the resonance $m_F = 5/2 \rightarrow m_F = -3/2$ energetically in between (for the chosen Raman beam polarizations). Therefore, we choose to work with a spin-polarized sample in $|^1S_0,\ -5/2\rangle$ for ^{173}Yb. Furthermore, there are Raman resonances to other m_F states such as $m_F = -5/2 \rightarrow m_F = -3/2$ for ^{173}Yb (even though this transition is only possible by residual parts of incorrect polarization), which could be crossed by the ramp. To avoid this, we apply a high enough external magnetic field, such that the other resonances are pushed further away in frequency than the initial detuning $\delta_{ini} = 10\Omega_R$ and that also for the initial detuning the coupling to other m_F states is negligible.

4.2.2 Other Approaches

In Ref. [5, 6], it is described, that the chiral edge currents in a very similar system seem to decay much faster than the theoretically expected coherence time. The measured decay constants were in the order of $2/\Omega_R$ or $1/(2t)$ for systems with $\Omega_R/t_x = 3.7$, whereas the scattering rates of the Raman beams were only in the order of $10^{-3}\Omega_R$ [154]. This decay happened on the same timescale as typical adiabatic preparations used in the references. Hence, the decay could have already influenced the measured chiral currents. This issue motivated us, to explore alternative methods for eigenstate preparation. In the following, we review common approaches and argue, that the adiabatic passage is the most suitable option for our purposes. The investigated methods are a fast non-adiabatic method (colloquially often called **Bang-Bang method**) and stimulated Raman adiabatic passage (**STIRAP**).

One possibility would be to use a fast non-adiabatic method. With this method, some physical systems can be brought into the eigenstate of a new Hamiltonian. The basic idea is to quench between the initial Hamiltonian and the final one [158, 159]. When the system is not in an eigenstate of the final Hamiltonian, it experiences a time evolution, which can bring the system closer to the desired eigenstate. By quenching back to the initial Hamiltonian the time evolution is changed and another quench to the desired Hamiltonian can now bring the system closer to the eigenstate than a single quench could have done it. With a sequence of different time evolutions, it has been demonstrated, that a BEC can be prepared from a weak harmonic confinement into Bloch bands of an optical lattice [158, 159]. This method is very useful in cases, where an adiabatic loading is not possible or unfavored. In addition, it can be much faster than an adiabatic preparation. In our case, a quench between the Fermi-Hubbard and Harper-Hofstadter Hamiltonian can be accomplished by switching the Raman beams on with the desired power at a two-photon detuning $\delta_R = 0$. Unfortunately, this method cannot be used to prepare our system. As discussed in detail in Ref. [116], the largest problem is, that to every momentum state k with a certain time evolution under quench, there exists a momentum state k' in the system, for which

the time evolution is exactly reversed with respect to the lowest and second lowest eigenstate. This means, that, if a quench dynamic is optimized to prepare an atom in state k in the lowest eigenstate of the Harper-Hofstadter Hamiltonian, an atom in state k' will be prepared in the second lowest eigenstate. Therefore, not all momentum states can be prepared in the same eigenstate. In total, this would lead to the preparation of a mixed state instead of a pure eigenstate for typical momentum state occupations. For initial states, which occupy less than half of the Brillouin zone, this technique might be applicable, but this is not our desired case. Hence, this approach is not suited for our purposes.

The next possibility would be a stimulated Raman adiabatic passage (STIRAP), which is a common method to transfer particles from one quantum state to another [160]. In this method, the detuning of the Raman beams would be fixed on resonance, and instead, the two beams are independently ramped in their intensity. This approach would have the advantage, that the atoms remain in a dark state during the preparation. Details of the investigation can be found in Ref. [116]. It turns out, that the system cannot be prepared in the lowest eigenstate for all momentum classes. However, it is possible to prepare nearly all atoms in the second lowest eigenstate for sufficient large ratios of $\Omega_R/t_x > 2$. Close to this lower boundary, the preparation works only well for preparation times longer than the adiabatic preparation in Ref. [5, 6]. For the desired preparation times of this thesis, the ratio should rather be $\Omega_R/t_x \geq 3$. However, this parameter regime is unfavored for our measurements, where we want to work at a ratio of $\Omega_R/t_x = 2$. Thus, also this approach is not suited for our measurements. Instead, to reduce the possible influence of the decay on the data, we perform the adiabatic passage as rapidly as possible in our measurements. This matter is discussed in detail in Sec. 4.4.3.

4.3 Primary Measurements

With all the components in place to prepare a quantum Hall ladder system, we now conduct primary measurements to characterize and probe the system. For this purpose, we first characterize the Raman transition by measuring Raman resonances and Raman-Rabi oscillations for both fermionic isotopes, ^{171}Yb and ^{173}Yb. Subsequently, we demonstrate the successful preparation of a Harper-Hofstadter eigenstate and explain, how we extract the chiral edge currents in the system. The measurements are discussed in detail for single examples in this section. In following sections, only their outcomes will be presented.

4.3.1 Raman Resonances

For the characterization of the Raman transitions and the eigenstate preparation, it is crucial to know the exact resonance position of the Raman transition. With the Raman transition, we want to couple two ytterbium states of the ground state manifold. These states have an energy difference ΔE_{tot}. The Raman resonance detuning $\Delta\omega_{res}$ is the frequency detuning $\Delta\omega$, which matches this energy difference: $\Delta\omega_{res} = \Delta E_{tot}/\hbar$. The energy difference ΔE_{tot} is dictated by the Zeeman shift ΔE_{Zeeman} and all state-dependent AC Stark shifts ΔE_{Stark}: $\Delta E_{tot} = \Delta E_{Zeeman} + \Delta E_{Stark}$. The state-dependent AC Stark shifts are caused by the Raman beams themselves (see Eq. 3.24). The optical lattice beams are so far detuned from any dipole transitions, that the induced AC Stark shifts are equal for all m_F states, whereas the single-photon detuning of the Raman beams Δ_R is on the order of the hyperfine splitting and close enough to resonances to induce different potentials for different m_F states.

In order to measure the Raman resonance, we prepare a spin-polarized sample of quantum degenerate Fermions in the $m_F = -1/2$ ($m_F = -5/2$) state for ^{171}Yb (^{173}Yb). We load the atoms in a deep three dimensional optical lattice to make the Bloch bands flat for the resolution of the spectroscopy measurement. The lattice depths are $s_{1D} = 30\,E_{rec}$ for the 1D-lattice and $s_{2D} = 15\,E_{rec}$ for the triangular 2D-lattice. Moreover, we set an external magnetic field of about 19 Gauss to separate the different m_F states using the Zeeman effect. The corresponding Zeeman splittings are $-14.2\,\mathrm{kHz}\cdot m_F$ and $3.90\,\mathrm{kHz}\cdot m_F$ for ^{171}Yb and ^{173}Yb, respectively. On the one hand, the magnetic field must be strong enough to separate the m_F states (including the contribution of the AC Stark shifts), such that the adiabatic passage (see Sec. 4.2.1) is unperturbed. On the other hand, we choose the magnetic field to be weak enough to enable spin-selective imaging with blast pulses (see Sec. 1.5.2), where the frequency range of a double-pass AOM limits the possible splitting of the resonances. We do not alter the magnetic field between the imaging and the prepared eigenstate of the Harper-Hofstadter Hamiltonian to avoid any disturbances of the data. For the measurement, we estimate the duration t_{pulse} of a π-pulse on resonance. The π-pulse time can be calculated with [117]

$$t_\pi = \pi/\Omega_R. \tag{4.7}$$

Ω_R, in turn, is estimated by using Eq. 3.23 and calculating the Rabi frequencies of the single Raman beams. For this purpose, we measure the power of the single Raman beams in front of the glass cell and take their waists, the single-photon detuning Δ_R (see Sec. 4.1.2) and the Clebsch-Gordan coefficients into account (for details see Ref. [116]). Subsequently, we apply the estimated π-pulse using the Raman beams and take an OSG image to distinguish between atom population in different m_F states (see Sec. 1.5.2). The spin state populations are used to calculate the population fraction n_{m_F} for all relevant spin states. We define it as

$$n_{m_F} := \frac{N_{m_F}}{\sum_{m_F} N_{m_F}}, \tag{4.8}$$

where N_{m_F} is the number of atoms in the corresponding m_F state. The summation goes over all relevant m_F states, i.e. $m_F = \{-\frac{1}{2}, +\frac{1}{2}\}$ ($m_F = \{-\frac{5}{2}, -\frac{1}{2}, +\frac{3}{2}\}$) for ^{171}Yb (^{173}Yb). To form a spectrum, we record data for a variation of $\Delta\omega$ in a range of approximately two to three expected full width at half maximum (FWHM) around the expected resonance frequency.

To visualize the Raman resonances, we plot n_{m_F} as a function of $\Delta\omega$ for both isotopes in Fig. 4.5. The error bars reflect the uncertainty in the determination of the atom number after the separation by the OSG. To determine the atom numbers in the different spin states, the optical density in the OSG images is integrated along the direction, which is (nearly) orthogonal to the separation direction. The integrated signal of each atomic cloud is fitted with a Gaussian profile to extract the number of atoms and the fit uncertainty is used as the uncertainty of the atom number. We fit a numerical solution for the time evolution of the density matrix to the plotted data. The fit allows us to extract key system parameters and confirms the validity of our applied model. Taking the Hamiltonian of the Raman transitions for ^{171}Yb and ^{173}Yb from Eq. 4.1 and 4.3, we can calculate the time evolution of an arbitrary density matrix using the Von-Neumann equation [161]

$$\partial_t \rho(t) = -\frac{i}{\hbar}[\mathcal{H}, \rho(t)]. \tag{4.9}$$

The fit parameters are Ω_R, the energy differences ΔE_{m_F} between different m_F states, the state populations at time $t = 0$ in the density matrix $\rho^{ini}_{m_F}$, and the evolution time t_{pulse}. The shaded areas around the lines in Fig. 4.5 mark the 95 % confidence interval of the fit. The fit results are listed in Table 4.2.

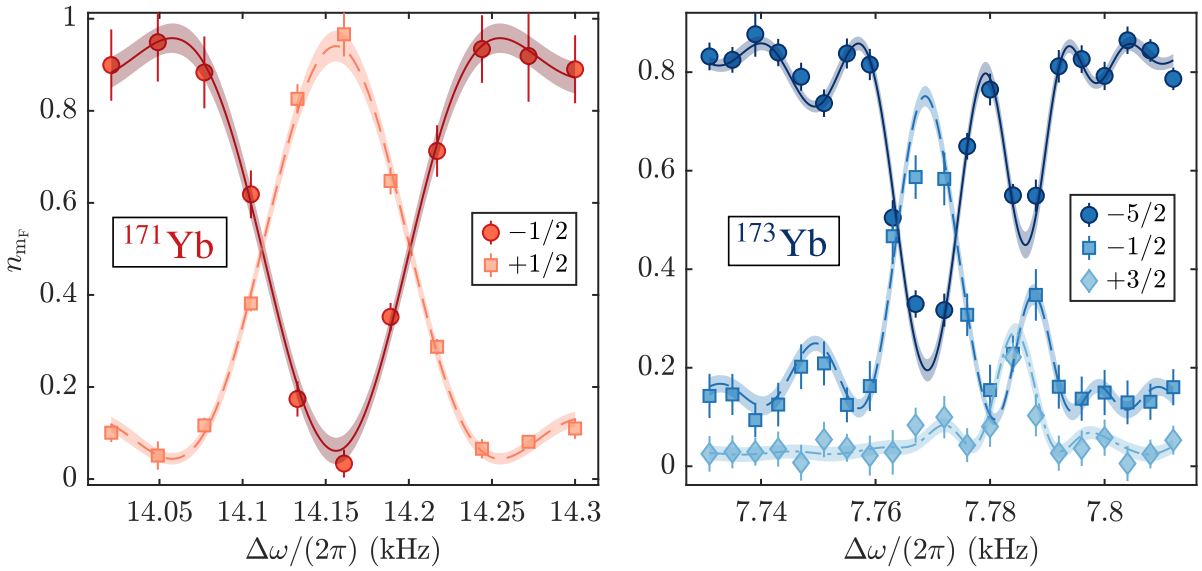

Figure 4.5: Typical Raman resonances for ^{171}Yb (left) and ^{173}Yb (right). The Figure displays the population fraction n_{m_F} as a function of the Raman frequency difference $\Delta\omega$. The system starts in a spin-polarized state in a deep optical lattice ($s_{1D} = 30\,E_{rec}$ and $s_{2D} = 15\,E_{rec}$). The data points show n_{m_F} after an estimated π-pulse of the desired transitions for the relevant m_F states. The error bars illustrate the uncertainty in the determination of the atom number. The lines display a fit of numerically solving the time evolution of the density matrix (see main text for details). The shaded areas around the lines show the 95 % confidence interval of the fit. The fit results are listed in Table 4.2.

Table 4.2: Fit results for Fig. 4.5. The table lists the fit results for the time evolution of the density matrix.

Parameter	^{171}Yb fit	^{173}Yb fit
Ω_R	$2\pi \times 50.5(21)$ Hz	$2\pi \times 9.58(19)$ Hz
$\Delta E_{-1/2}/h$	-	7.770 28(16) kHz
$\Delta E_{+1/2}/h$	14.156 22(56) kHz	-
$\Delta E_{+3/2}/h$	-	7.784 22(21) kHz
$\rho^{ini}_{-5/2}$	-	85.86(71) %
$\rho^{ini}_{-1/2}$	95.8(16) %	12.45(99) % [1]
$\rho^{ini}_{+1/2}$	4.40(63) %	-
$\rho^{ini}_{+3/2}$	-	2.36(75) %
t_{pulse}	9.02(10) ms	64.37(92) ms

The measured data can be well described with the fit model. The fit results agree with theoretical expectations within experimental limitations. We determine the center of the resonance from the fit parameter $\Delta E_{+1/2}$ ($\Delta E_{-1/2}$) for ^{171}Yb (^{173}Yb). The value of $\Delta E_{+1/2}$ for ^{171}Yb is recorded in several measurements and used to precisely measure the applied magnetic field at the position of the atoms. The magnetic field is found to be $|B| = \left|\Delta E^{171}_{\text{Zeeman}} / (-752.6\,\text{Hz/G})\right| = 18.808(1)\,\text{G}$. For this magnetic field strength and the measured Ω_R in the ^{173}Yb case, we expect the energy differences between the states to be $\Delta E_{-1/2} = 7.780$ kHz and $\Delta E_{+3/2} = 7.792$ kHz. However, if the magnetic field slightly changed within the 19 days between the two measurements by about 20 mG, the corresponding Zeeman shift would be $\Delta E_{-1/2} = 7.770$ kHz and $\Delta E_{+3/2} = 7.782$ kHz. The slightly larger splitting measured between the two resonances suggests a larger $\Omega_\text{R} \approx 2\pi \times 11$ Hz.

For the ^{173}Yb isotope, we have a second resonance slightly overlapping with the desired resonance $m_\text{F} = -5/2 \rightarrow m'_\text{F} = -1/2$. This means, that there is a residual coupling to another state, which is unwanted. This additional resonance comes from the Raman transition $m_\text{F} = -1/2 \rightarrow m'_\text{F} = +3/2$. For our single-photon detuning Δ_R, the coupling strength of this transition is 1.339 times stronger than Ω_{12} because of the Clebsch-Gordan coefficients (see Sec. 4.1.2). For our polarization, the separation of the two resonances is already maximized, if only one frequency per Raman beam is used. For multiple frequencies in a single Raman beam, it is possible to achieve an additional differential light shift, which increases the separation of the two resonances. This could be a next step for future measurements. However, for our work, this is not necessary, as other influences dominate the data quality. Furthermore, not introducing additional frequencies has the benefit of keeping the system simpler and reducing potential sources of discrepancies. This is particularly important in our case, as an unexpected behavior in the data, described below in Sec. 4.4 and chapter 5, prompted a search for possible issues in the measurements. The coupling to $m_\text{F} = +3/2$ can also be seen in the Raman-Rabi oscillations, which are presented below.

4.3.2 Raman-Rabi Oscillations

With the knowledge of the Raman resonances, we know the exact energy difference between the states and can perform Raman-Rabi oscillations. The Raman-Rabi oscillations let us precisely measure Ω_R and test the coherence of our system. With a Raman transition one can drive Raman-Rabi oscillations analogously to Rabi oscillations.

For recording Raman-Rabi oscillations, a spin-polarized degenerate Fermi gas is loaded into a deep optical lattice as in the previous section. For the measurement, we set the magnetic field again to 19 Gauss and the two-photon detuning δ_R to zero (according to the Raman resonance measurement in Sec. 4.3.1). We use square pulses with a rise and fall time of about 1 µs and take an OSG image directly after the end of the pulse. We evaluate the OSG images and extract the number of atoms in the different spin states N_{m_F}. We plot the relative population of the spin states n_{m_F} as a function of time t in Fig. 4.6. The error bars show the uncertainty in the determination of the atom number in the same way as in Fig. 4.5. We fit a numerical solution for the time evolution of the density matrix to this data, analogous to how we fit the Raman resonances. Only the fit parameters change to a single one: Ω_R. The shaded areas around

[1] The initial population of the $-1/2$ spin state $\rho^{\text{ini}}_{-1/2}$ is measured to be unexpectedly large with about 12.5 %, we attribute this result to the method of determining the relative populations (see 1.5.2). We expect the residual population of the $-1/2$ state to be below 10 % after our spin polarization procedure (see 1.3.2).

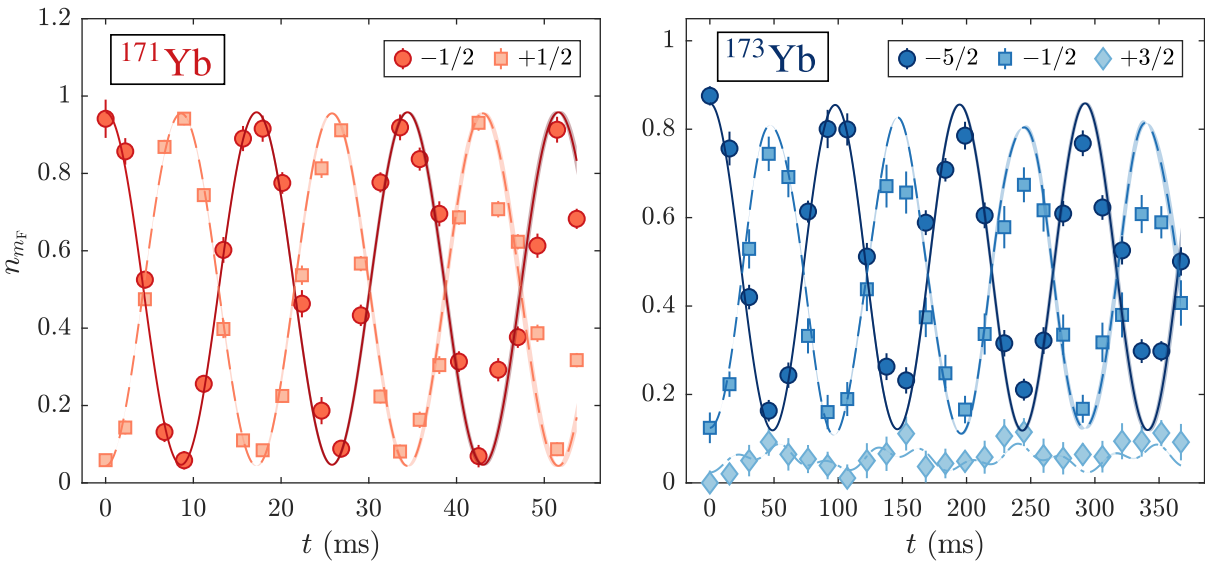

Figure 4.6: Typical Raman-Rabi oscillations for ^{171}Yb (left) and ^{173}Yb (right). The figure displays the population fraction n_{m_F} as a function of the evolution time t. The system starts in a spin-polarized state in a deep lattice. The data points show n_{m_F} for the relevant m_F states, while the Raman frequency difference $\Delta\omega$ is set on resonance. The error bars mark the uncertainty in the determination of the atom number. The lines present a fit of numerically solving the time evolution of the density matrix (see main text for details). The shaded areas around the lines mark the 95 % confidence interval of the fit. Fit results and parameters of the measurements are listed in Table 4.3.

Table 4.3: Fit results and parameters for Fig. 4.6. The table lists fit results and parameters for the time evolution of the density matrix.

Parameter	^{171}Yb fit	^{173}Yb fit
Ω_R	$2\pi \times 58.03(17)$ Hz	$2\pi \times 10.534(30)$ Hz
$\Delta\omega$	$2\pi \times 14.153$ kHz	$2\pi \times 7.769$ kHz

the lines in Fig. 4.6 mark the 95 % confidence interval of the fit. The fit results can be seen in Table 4.3.

The measured data can be well described with the fit model and the uncertainties show a precise measurement of Ω_R. For longer oscillation times - in particular for the data with ^{173}Yb - the amplitude of the oscillations decreases. However, the data displayed here shows high amplitudes for up to 200 ms, which is longer than all chiral edge current measurements performed in this thesis. In addition, with $\Omega_R \approx 2\pi \times 11$ Hz the displayed data resembles a more critical scenario than all chiral current data with $\Omega_R \geq 2\pi \times 49$ Hz. One could capture the decoherence in the oscillations with additional terms in the Hamiltonian (see for example Ref. [162, 163]), but this goes beyond the scope of these calibration measurements. As already discussed above for the Raman resonances, there is a coupling to the $m_F = +3/2$ state for ^{173}Yb. The population of the state stays below 10 % for the relevant timescales of the experiment. This can be used to deduce an upper limit on expected influences.

4.3.3 Chiral Edge Currents

After we characterized the system for a specific parameter set, we can use the information of the exact position of the Raman resonance and the coupling strength given by the Raman-Rabi oscillation frequency, to realize the Harper-Hofstadter model by preparing an eigenstate. Subsequently, we want to investigate the system and characterize it further. For us, the most interesting property are the chiral currents - despite the basic characteristics of magnetic flux and tunneling amplitudes along the real and synthetic dimension, which we already know. Here, we describe and discuss our measuring process and present a typical data set.

The chiral currents are a consequence of the topologically non-trivial system. They are a remarkable property of quantum Hall systems, as they are protected by the bulk-boundary correspondence and robust against impurities. The net current along one leg of our ladder system, would manifest itself as an imbalance in the quasi-momentum distribution of the (effectively) charge carrying particles. Therefore, in order to measure the currents, we need the quasi-momentum information of the atoms. Furthermore, as the currents are chiral and have opposite signs along the two legs of our ladder system, it is important to only measure the currents for one leg at a time. Otherwise, the absolute value of the currents may be reduced or even zero, for a fully occupied dressed band. In the following, we demonstrate how we extract this information from the system. In contrast to the Raman resonance and oscillation measurements described above, for these measurements, the optical 1D-lattice is shallow (tunneling in the order of Ω_R) and not deep, such that a system as illustrated in Fig. 3.5 is realized. Furthermore, the 2D-lattice depth is reduced to $s_{2D} = 9E_{rec}$, which reduces the harmonic confinement along the 1D-lattice, while it is still deep enough to inhibit transverse tunneling. We assume a system where the Fermi energy lies between the lowest two Bloch bands of the 1D lattice, and initially, only one spin state is occupied. Unless explicitly stated otherwise, this is our intended filling factor. After loading the atoms into the three-dimensional lattice, all dipole traps are ramped down, leaving only the lattice beams to support the atoms against gravity. The system is then allowed to relax for 300 ms. Following this relaxation period, we begin the adiabatic passage (see Sec. 4.2.1) to prepare the atoms in an eigenstate of the Harper-Hofstadter Hamiltonian. Immediately after the preparation of the eigenstate, we perform a bandmapping technique along the shallow one-dimensional optical lattice. Subsequently, the deep optical 2D-lattice in the transverse directions is switched off abruptly without any bandmapping to avoid influences on the data. Possible influences of the bandmapping and countermeasures are discussed in Sec. 4.4.2. In the 1D-lattice direction, the quasi-momentum of the atoms is transferred into momentum in free space and after a time of flight, it is mapped to a position in space (see Sec. 1.5.1). In addition to the quasi-momentum imaging, we include a spin-selective imaging to only image one spin state and, thus, only one leg at a time. For this purpose, we blast away all atoms in other spin states with short resonant light pulses during TOF (see Sec. 1.5.2). We do not use the spin-selective imaging method with OSG, which in principle could detect atoms in both legs individually, as it may influence the momentum information (see Sec. 1.5.2).

To demonstrate the agreement between the measurements and the theoretical model, we prepare the two isotopes in two different eigenstate bands. ^{173}Yb is prepared in the lowest dressed band, whereas ^{171}Yb is prepared in the second lowest. According to Fig. 3.6, we anticipate complementary spin state populations for the different bands. For the measurements, we average five data images and rotate the spin-selective images, such that the shallow lattice direction is exactly along our horizontal axis. Typical examples of these rotated images can be seen in Fig. 4.7. We extract the chiral current information from the images analogously as in Ref. [3, 4]. For this purpose, we compute the integral along the vertical

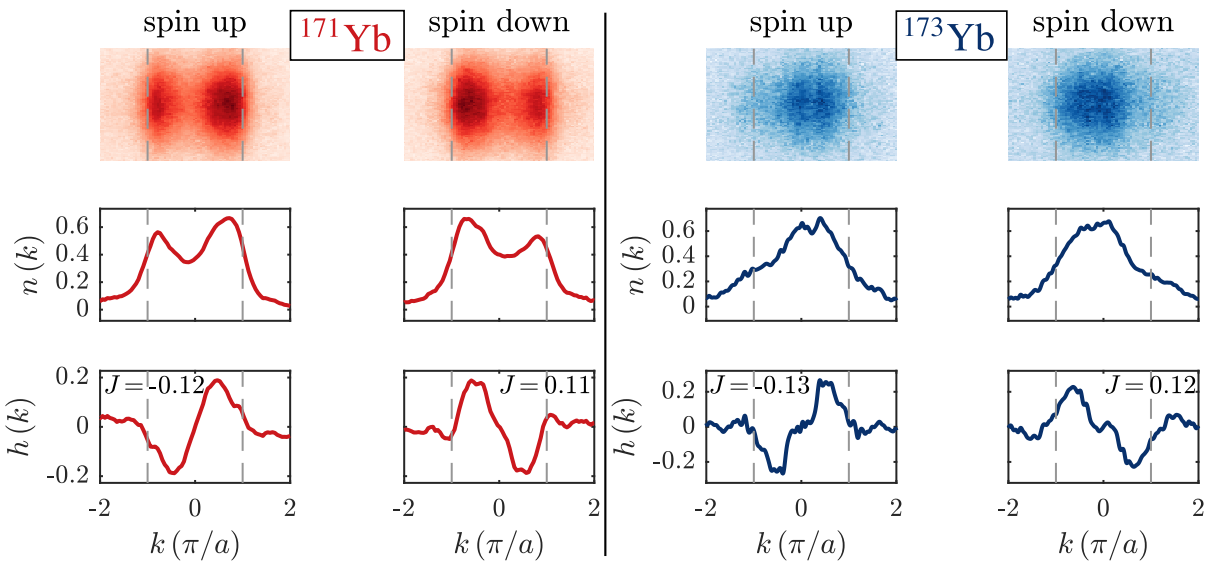

Figure 4.7: Typical chiral current data. The figure presents typical data for the calculation of chiral currents. Data on the left in red is taken with ^{171}Yb and illustrates the second lowest eigenstate of the Harper-Hofstadter Hamiltonian, whereas data on the right in blue is taken with ^{173}Yb and illustrates the lowest eigenstate. The top row shows atoms of a single spin state, i.e. of a single leg of the ladder system. The images are averages of five data images. The middle row shows the atom density $n(k)$ as a function of the momentum k. The normalization of $n(k)$ is defined in Eq. 4.10. The bottom row shows the asymmetry function $h(k)$ (defined in Eq. 4.11) as a function of k. Furthermore, the values of J (equation 4.12) are displayed for the corresponding data. The gray vertical dashed lines mark the boundaries of the first Brillouin zone.

axis and normalize the atom density $n(k)$ such that

$$\int_{-\pi/a}^{\pi/a} n(k)\,dk = 1, \tag{4.10}$$

where the integral goes over the first Brillouin zone. Then, we compute the asymmetry function defined as

$$h(k) := n(k) - n(-k). \tag{4.11}$$

Finally, the chiral current J is calculated as

$$J = -\int_{0}^{\pi/a} h(k)\,dk. \tag{4.12}$$

$n(k)$ and $h(k)$ are plotted as a function of the lattice momentum k in Fig. 4.7 for the first and second Brillouin zone for typical data. Also, the values of J for this data can be seen in the figure. The chiral edge currents of the two distinct eigenstate bands have the same sign for the same pseudo-spin state. The reason for that is, that the isotopes are not only prepared in different bands, but additionally, we inverted the direction of the momentum transfer and, consequently, the sign of the magnetic flux. Hence, the chiral currents for both isotopes are expected to have the same direction and magnitude, if interactions are neglected.

For the correct calculation of h and J, the exact position of the Brillouin zone center is crucial. We determine the center from a reference image in auxiliary measurements, which we take additionally for

all data. The reference images display atoms in the initially prepared spin state loaded into the same lattice as the data images. They are taken with the same procedure as the data images, but without the Raman beams. To minimize differences to the data, we also use the spin-selective imaging. The Brillouin zone center is identified using a Gaussian fit to the reference data. While the actual line profile generally deviates from a perfect Gaussian shape, our deliberately incomplete bandmapping (see Sec. 4.4.2) results in a line profile that closely approximates a Gaussian. Consequently, this fitting method provides an accurate determination of the center. To not be limited to a discrete pixel of the camera for the Brillouin zone center, we interpolate the data. This reduces the uncertainty in the chiral current value. The typical measurements of the chiral currents confirm that our system behaves as a synthetic ladder system under the influence of an artificial magnetic field. It demonstrates directly the underlying spin-orbit coupling. As predicted, the lowest and second-lowest eigenstate exhibit complementary atom distributions in momentum space.

In this section, we have presented the primary measurements that lay the groundwork for characterizing the quantum Hall ladder system. By recording the Raman resonances and Raman-Rabi oscillations, we have shown how to obtain the essential information about the Raman transitions needed to realize the quantum Hall ladder states. Additionally, the successful preparation of Harper-Hofstadter eigenstates has been demonstrated, and the method for extracting chiral edge currents has been outlined. These foundational measurements provide a detailed understanding of the system, which will serve as the basis for the results presented in chapter 5.

4.4 Methods for Data Optimization

With the ability to create quantum Hall ladders and to measure the intriguing chiral edge currents, we are ready to explore interaction effects in these systems. However, before we begin, we detail different methods for data optimization in this section. This is particularly important in our case, as we encountered some unexpected results in the data, which are described in Chapter 5. We provide a comprehensive overview of our methods for acquiring data on interaction effects, detailing countermeasures and remaining influences. Specifically, we address the following aspects:

- Sec. 4.4.1: The impact and management of imperfect spin manipulation and detection.
- Sec. 4.4.2: Detailed analysis of the imaging stage components.
- Sec. 4.4.3: The effects of eigenstate preparation.
- Sec. 4.4.4: Potential optimizations in data analysis.

By systematically addressing these areas, we aim to enhance the accuracy and reliability of our data before proceeding with the study of interaction effects.

4.4.1 Imperfect Spin Manipulation and Detection

The starting point of our measurements for the chiral currents of the quantum Hall ladder is a spin-polarized Fermi gas. For the spin-polarization, atoms are optically pumped into a single spin state, but this process does not work perfectly. This can be seen, for example, in the data of the typical Raman resonances in Fig. 4.5 and their fit results in Table 4.2. Therefore, we want to explore the influence of

atoms in unwanted spin states on the chiral current data. For this purpose, we consider, what happens to the atoms in the incorrect spin state. In the case of ^{171}Yb, there is only one other spin state available, which is the $m_F = 1/2$ state. During the eigenstate preparation, atoms in this state will be prepared in the other dressed band of the two available bands shown in Fig. 3.1 and 3.6. This means, if the atoms in $m_F = -1/2$ are prepared in the lowest dressed band, then, atoms in $m_F = 1/2$ are prepared in the second lowest dressed band and vice versa. The reason for this is, that, in the rotating frame and at the beginning of the adiabatic passage, the atoms in $m_F = -1/2$ start, for example, in a state lower than the other spin state, whereas atoms in $m_F = 1/2$ start in the higher spin state. During the eigenstate preparation, the atoms perform an avoided crossing and remain in the lower or higher available state, respectively. Thus, the atoms in the undesired spin state of the imperfect spin-polarized Fermi gas are prepared in the opposite dressed band. The opposite dressed band also exhibits chiral currents. The exact value of these undesired currents is unclear, as it is hard to predict the currents at the particular reduced filling factor. However, it is known from Ref. [85], that the atoms show a chiral current in the *opposite* direction of the correct data. This is true, if all atoms remain in the opposite dressed band, which is the case for our available parameter regimes of $\Omega_R/t_x = 2.06(15)$ and filling factors equal or below the ones of the correct data. Thus, we treat this influence of the imperfect spin-polarization as an additional uncertainty on the chiral current data. Therefore, we add the relative population in the unwanted spin state as a relative uncertainty to the standard deviation of the statistical uncertainty on the chiral current data. The added uncertainty has only a component along the direction of the chiral currents, i.e. in positive direction for positive currents and in negative direction for negative currents.

In the case of ^{173}Yb, there are more spin states available than for ^{171}Yb. All spin states, which have a negligible Raman coupling to the two states, which form the legs of the quantum Hall ladder, can be neglected, as they can be expected to not affect the system. This means, only the $m_F = 3/2$ state needs to be considered, since it has a residual population after the optical pumping for the spin-polarization process and which is slightly coupled to the two relevant spin states, as described in Sec. 4.3. However, the off-resonant Raman coupling to this spin state results in a very weak alteration of the band's spin composition in the dressed frame. Thus, atoms in this spin state populate a dressed state, which features chiral currents, that are at least one order of magnitude smaller than the currents of the other dressed bands. In addition, the residual population of this state with respect to the desired state is at least one order of magnitude smaller, so the total influence of the state population on the measured chiral currents can be neglected. Hence, we can treat the data for ^{173}Yb analogously to the ^{171}Yb data and only need to consider the residual population in $m_F = -1/2$.

In addition to the imperfect spin manipulation, there are also imperfections in our spin state detection methods, which influence our measurement data. As extensively discussed in Ref. [95, 97, 100], for the OSG method in our setup (see Sec. 1.5.2), there is finite scattering of atoms by the OSG beam. Since this scattering varies in strength for the respective spin states, the atom numbers of different spins are also influenced and distorted to a different extent. As a result, the relative occupancies of spin states in the OSG images are not accurately represented. We observe this very clearly, for example, when imaging a Fermi gas, which should feature uniform occupancy of all spins. We assume that this is the case, when we do not perform any optical pumping for the following reasoning. After the MOT stage, where not all spin states can be trapped [94, 115], there is an experimental stage, where the external magnetic field from an Anti-Helmholtz configuration is switched off and there is no defined quantization axis. Afterwards, a quantization axis is reintroduced by an external magnetic field from a Helmholtz configuration. Therefore, we expect a homogeneous spin distribution at this stage and the distribution is also not changed during evaporative cooling, because the inter-particle interactions are SU($\mathcal{N}$) symmetric

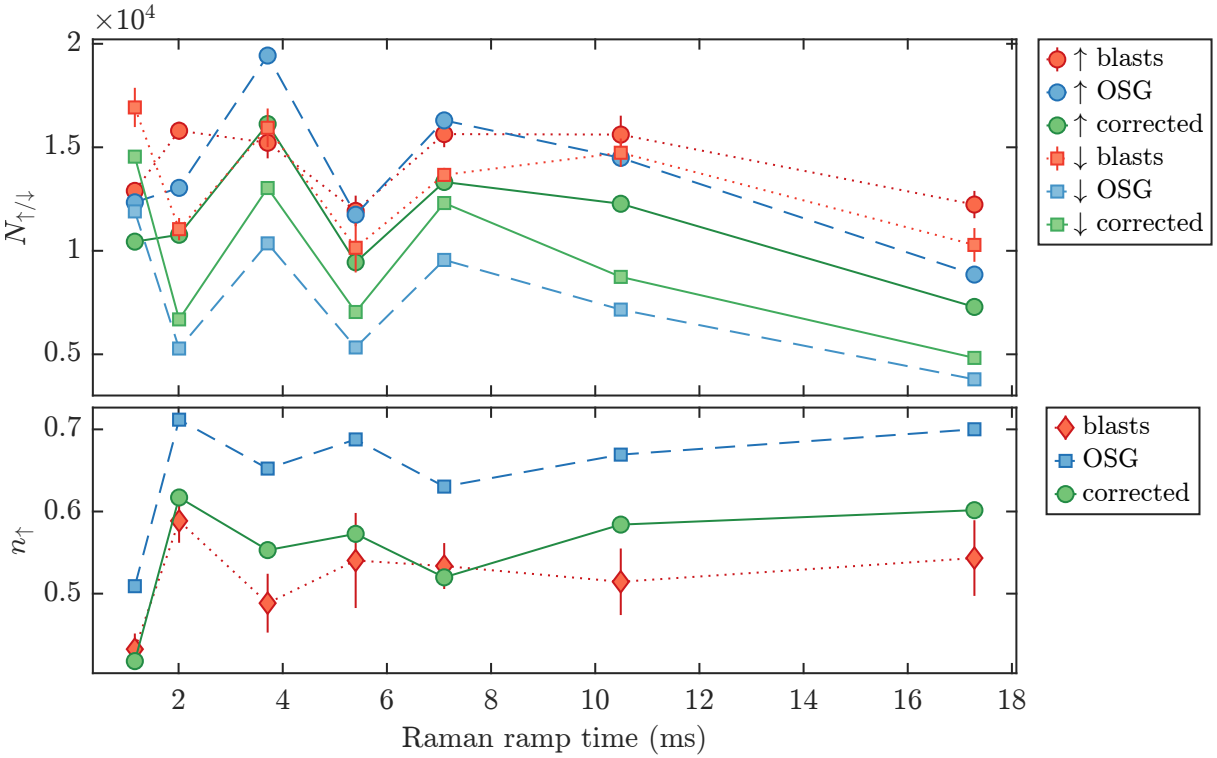

Figure 4.8: Comparison of spin state detection methods. The upper subfigure displays the atom numbers in the $m_F = +1/2$ and $m_F = -1/2$ state for ^{171}Yb determined with three different methods. The atom numbers are presented for separate measurements, which are distinguished by different Raman preparation ramp times and plotted as such to make the connection to other data presented below in Fig. 4.11 clearer. The exact meaning of this parameter is explained below in Sec. 4.4.3. We determine the atom numbers with the uncorrected OSG method (labeled as "OSG"), with the correction described in the main text (labeled as "corrected") and with our other spin-selective imaging method (labeled as "blasts"), which uses blast pulses (see Sec. 1.5.2). In the lower subfigure, the relative occupancy $n_\uparrow$ of the $|\uparrow\rangle$ state is shown, which is calculated from the data in the upper subfigure. As displayed in the legend, markers indicate different spin states, while colors indicate the detection method. Data from the OSG methods are single-shot data, while the data from the blast pulses method are averaged five times and the error bars to these data points show the standard deviation.

(see Sec. 1.1). Thus, we would expect, that, when imaging such a gas with OSG, an equal number of atoms would be measured in each spin state, but this is not the case.

To partially compensate for this imperfection of the OSG method in our measurements, we perform auxiliary measurements, where we image a spin-balanced Fermi gas and use it as a reference for the imaging efficiency of individual spin states. We obtain a corrected number of atoms in a spin state $N_{m_F}^{cor}$, by adjusting the measured atom number in a spin state $N_{m_F}^{OSG}$ according to the following equation

$$N_{m_F}^{cor} = \frac{N_{m_F}^{OSG}}{Z \cdot n_{m_F}^{ref}}, \tag{4.13}$$

where Z is the number of available spin states for each isotope, i.e. 2 for ^{171}Yb and 6 for ^{173}Yb, and $n_{m_F}^{ref}$ is the relative spin state population measured in the auxiliary measurements of the spin-balanced sample. To verify, whether this correction indeed reflects the occupation of spin states better, we compare atom numbers between three different methods in Fig. 4.8. We determine the atom number with the uncorrected OSG method, with the correction described above and with our other spin-selective imaging method, which uses blast pulses (see Sec. 1.5.2). We present data with ^{171}Yb and for several separate measurements. In the upper subfigure, we display the absolute atom numbers, while in the lower subfigure, the relative occupancy $n_{1/2}$ of the spin $m_F = +1/2$ state is shown. In the absolute numbers, we observe, that the atom numbers for the blast pulse method are generally higher than for the OSG methods. There are several possible reasons for this. First, it could be that not all atoms in other spin states are blasted away in the blast pulse method. Second, despite the wrong spin state classification, the scattering of atoms by the OSG beam can lead to atom losses. Third, there could also be a systematic error, since the atom numbers in the OSG images are determined with a Gaussian profile fit, while for the blast pulse method, the atom number is determined directly through the optical density. We do not fit the images of the blast pulse method, as they are additionally used for further analysis purposes and, thus, generally do not exhibit a simple line profile and cannot easily be fitted. However, the exact details and clarification of the discrepancy is of minor importance to us for our measurements and further investigations go beyond the scope of this thesis.

In the relative occupancy shown in the lower subfigure, it can be seen, that the OSG data with correction matches the blast method data much better than the OSG data without correction. From this, we conclude, that our compensation method reflects the genuine spin state occupation better. Hence, we use it for all data extracted from OSG images. This means, among others, in the measurements of the Raman resonances, the Raman-Rabi oscillations and in the auxiliary measurements for the chiral edge currents.

4.4.2 Imaging

To extract the chiral currents information from the physical system, the atoms need to be imaged spin-selectively in their quasimomentum state. For this purpose, there are several steps included in the imaging procedure: switching off the Raman beams, bandmapping, TOF and spin-selective imaging. In the following, we shortly discuss the possible influences on the chiral current data from the individual stages. The first step of the imaging is to switch off the Raman beams before the bandmapping. This step ensures, that the spin state composition of the atoms is locked before the tunneling amplitude t is changed during bandmapping. Hence, the atoms cannot change their spin state composition, which is necessary as a change in Ω_R/t_x generally influences the composition. We do not expect a further influence on the chiral

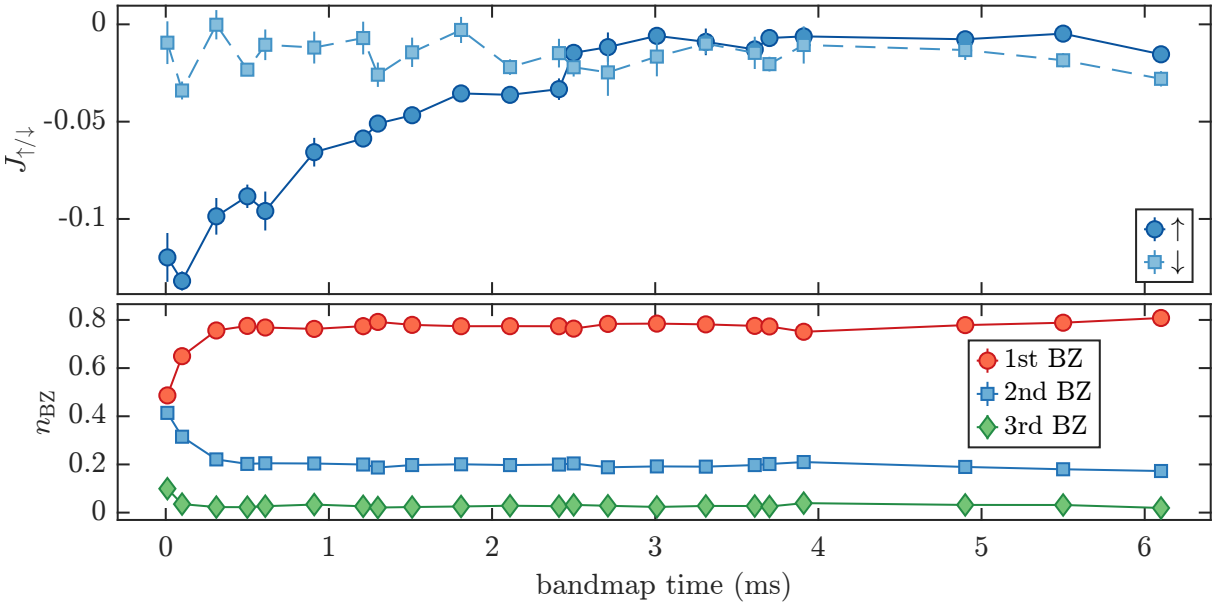

Figure 4.9: Influence of bandmapping time. The figure displays data with ^{173}Yb atoms, $\Omega_R/t_x = 2.06(15)$ and $s_{1D} = 12E_{rec}$ for various times of the quasi-exponential bandmapping ramp of the 1D-lattice. The 2D-lattice is switched off abruptly at the beginning of the ramp. The different ramp times are plotted on the horizontal axis and labeled as "bandmap time". The upper figure presents the chiral currents J for the two legs of the quantum Hall ladder, denoted by their pseudospin $|\uparrow\rangle$ and $|\downarrow\rangle$. The lower figure presents the atom number fraction in the first three Brillouin zones, defined as $n_i = N_i/(N_{1\text{st BZ}} + N_{2\text{nd BZ}} + N_{3\text{rd BZ}})$, $i \in$ {1st BZ, 2nd BZ, 3rd BZ} for the same data as in the upper figure. Data points are averaged at least five times and error bars denote the standard deviation. In the lower figure, error bars are typically smaller than the data point markers.

current data by the missing Raman beams. The next imaging step is the bandmapping, which we discuss in detail below. We first discuss the other stages briefly. During TOF, the atoms evolve according to their initial momentum state. This is a well established process for momentum imaging and its imperfection in the mapping from momentum space to position space is negligible compared to other uncertainties for the chiral currents determination. The last imaging stage is the spin-selective imaging. We expect the uncertainty on the chiral currents caused by this technique to be negligible, as there are indications, that the process works very well. The first indication is, that the atom numbers in the initially prepared spin-polarized state equals the sum of the atom numbers in the two spin states of the quantum Hall ladder. These atom numbers are displayed below in Fig. 4.11. The second indication is, that the found relative atom numbers of the individual spin states of the dressed state are confirmed in the auxiliary measurements where the dressed state is imaged with the OSG technique. This data is presented in Fig. 4.8.

In the following, we discuss the influences of the bandmapping technique. First, we discuss the transverse lattice direction, which means the triangular 2D-lattice. In this direction, the beams are switched off abruptly to avoid any corruption of the data. This quench has the effect, that the quasimomentum of the atoms is not mapped onto a single real space momentum. Instead, the quasimomentum q will evolve according to its momentum distribution, expanding as a superposition of plane waves with momenta $p_n = \hbar q \pm n\hbar G$, where n is an arbitrary integer and G is the reciprocal-lattice vector [151]. Since we integrate the optical density in this direction for the calculation of the chiral currents, the mapping into other Brillouin zones does not affect the data. Along the 1D lattice direction, the influence of the

bandmapping is explored by measurements displayed in Fig. 4.9. The figure depicts data with ^{173}Yb atoms, $\Omega_R/t_x = 2.06(15)$ and $s_{1D} = 12E_{rec}$ for various times of the quasi-exponential bandmapping ramp of the 1D-lattice. The upper figure displays the chiral currents J for the two legs of the quantum Hall ladder, denoted by their pseudospin $|\uparrow\rangle$ and $|\downarrow\rangle$. The lower figure presents the atom number fraction in the first three Brillouin zones for the same data as in the upper figure. The atom number fractions n_i are defined as

$$n_i = N_i/(N_{1\text{st BZ}} + N_{2\text{nd BZ}} + N_{3\text{rd BZ}}), \tag{4.14}$$

where $i \in \{1\text{st BZ}, 2\text{nd BZ}, 3\text{rd BZ}\}$. In the upper figure, we observe, that the chiral current of $|\uparrow\rangle$ decreases in its absolute value, i.e. increases from a negative value towards zero, for longer bandmap times. At a bandmap time of about 3 ms, the current has nearly reached zero and stays in the regime up to the longest measured bandmap times. The chiral current of $|\downarrow\rangle$ is close to zero for all bandmap times and fluctuates, but does not show a clear behavior trend as a function of the bandmap time. We attribute the strong asymmetric chiral currents for the two pseudospin states for the shortest bandmap times to the influence of the eigenstate preparation, which is discussed in detail below in Sec. 4.4.3. In the lower figure, we observe, that the atom number fractions in the first three Brillouin zones starts at a nearly equal occupation of 45 % in the first and second Brillouin zone and about 10 % in the third Brillouin zone for the shortest bandmap time of 10 µs. For longer bandmap times, the atom number fraction in the first Brillouin zone increases, as the fraction in the second and third Brillouin zone decreases monotonically until a bandmap time of about 0.5 ms. For this and longer bandmap times, the fractions stay constant within experimental accuracy at about 80 % in the first Brillouin zone, 20 % in the second Brillouin zone and 0 % in the third Brillouin zone. The behavior of the atom number fractions is as expected. The fidelity of the bandmapping increases for longer bandmap times up to a saturation time. The remaining occupancy in the second Brillouin zone for long bandmap times is higher than expected, but not further investigated in this thesis due to minor importance for our measurements. By comparing the upper and lower figure, we observe, that the bandmapping and, thus, the correct Brillouin zone projection of the atoms, saturates already at a bandmap time of about 0.5 ms, whereas the decrease in $|J_\uparrow|$ continues up to bandmap times of about 3 ms. This means, that the influence of the bandmap time on the chiral current value cannot be reduced to an imperfect bandmapping. In addition, we see that, if we perform a projection of atoms from higher Brillouin zones into the first, which is described in detail below in Sec. 4.4.4, we still observe the same qualitative behavior of the chiral currents in the upper figure.

Therefore, we observe a strong dependence of the alleged currents on the bandmap time. This seems to be a corruption of the data. We choose to present only data for the deepest 1D-lattice depth, with which we work in this chapter, as it is expected to be the most critical scenario. We recorded also data for shallower lattice depths, which are not presented here, but also show a dependency on the bandmap time with a smaller magnitude. In some of this data, the chiral currents are not decreased, but increased in their absolute value. We conclude, that data with long bandmapping times cannot be trusted. As a countermeasure, it would be good to eliminate the bandmapping, while still being able to extract the quasimomentum information of the atoms along the 1D lattice. This could be realized by switching off the 1D lattice beam abruptly like the 2D lattice beams and, subsequently, project all atoms from higher Brillouin zones to the first one in the data analysis. This method would require, that only the first Brillouin zone is occupied by the atoms, which is in general the case for our parameter regimes to a great extent. However, as evident from the data (displayed in Fig. 4.9), for very short bandmap times, the chiral currents are only slightly affected, while the bandmapping fidelity can already increase. As a compromise between avoiding the influence of the bandmapping and to reduce possible additional uncertainties in the data analysis, we decide to work with a very fast, non-optimal bandmapping ramp

time of 300 µs for all following chiral current measurements. As the deepest 1D-lattice depth requires the longest bandmap time to achieve a high fidelity, we anticipate that this ramp time will even work better for shallower lattice depths.

To further understand, what happens to the data during bandmapping, one could investigate the timescales, on which these dynamics take place for different parameter regimes. Another strategy to understand this better, would be to take images also during the bandmapping ramp and not only after it. In this way, one could follow the actual dynamics also during bandmapping. However, such investigations are not the main purpose of our measurements and go beyond the scope of this thesis.

4.4.3 Eigenstate Preparation

After the discussion of optimizations for the imaging above, we consider optimizations for the eigenstate preparation in this section. As described in Sec. 4.2.1, we use an adiabatic ramp of the two-photon Raman detuning δ_R to prepare an eigenstate of the Harper-Hofstadter Hamiltonian. Here, we investigate the preparation further in their influence on the measured chiral currents.

As mentioned in Sec. 4.1, there are indications of a much faster decay of the chiral currents than theoretically expected in Ref. [5, 6] and the observed decay rates are in the order of the eigenstate preparation time. Therefore, an optimized preparation of the eigenstate would be one, which prepares the eigenstate well and at the same time is fast enough to avoid any decay of the currents. To get a good estimation of the fastest well-working preparation times, we simulate the adiabatic passage of the eigenstate preparation and try to find a good parameter regime. For a fixed ratio of Ω_R/t_x and a fixed value of ϕ, the time evolution of the adiabatic passage is independent of the individual values of Ω_R and t_x, if all parameters are expressed in values of Ω_R. This means, we can find universal ramp parameters for the measurements of various lattice depths with fixed Ω_R/t_x. Thereby, we neglect interaction effects, which may cause the optimal parameters to change slightly.

We find a fast preparation with a theoretical fidelity of 97.9 % for the following parameters:

$$\begin{aligned} \delta_{\text{ini}} &= 10\Omega_R \\ T_{\text{ramp}} &= \frac{75}{2\pi} \cdot \frac{1}{\Omega_R} \\ \tau_{\text{ramp}} &= 0.3 T_{\text{ramp}}. \end{aligned} \tag{4.15}$$

The exact form of the exponential-like ramp can be found in Eq. 4.5. In addition, we simulate the adiabatic passage for various ramp times $A \cdot T_{\text{ramp}}$ around the found value to get insights into the dependence on the ramp duration. The simulations are displayed in Fig. 4.10, where the additional factor A is monotonically increasing from top to bottom and takes the values: 0.25, 0.5, 1 and 5. This means, the third simulation displays the simulation for the parameters listed above, whereas the first two simulations show faster ramps and the fourth ramp is slower. In the simulations, we observe, that the fidelity does only marginally increase for ramp times longer than the found parameters, whereas for faster ramp times the fidelity decreases significantly to values, where it can be expected, that the insufficient eigenstate preparation has a major influence on the behavior of the system.

For these simulated adiabatic passages and additionally for $A = 1.5,\ 2$ and 3, we take experimental data with the weakly interacting ^{171}Yb. We use a fixed parameter set of $\Omega_R/t_x = 2.06(15)$ and $\phi = 0.444(20)\pi$

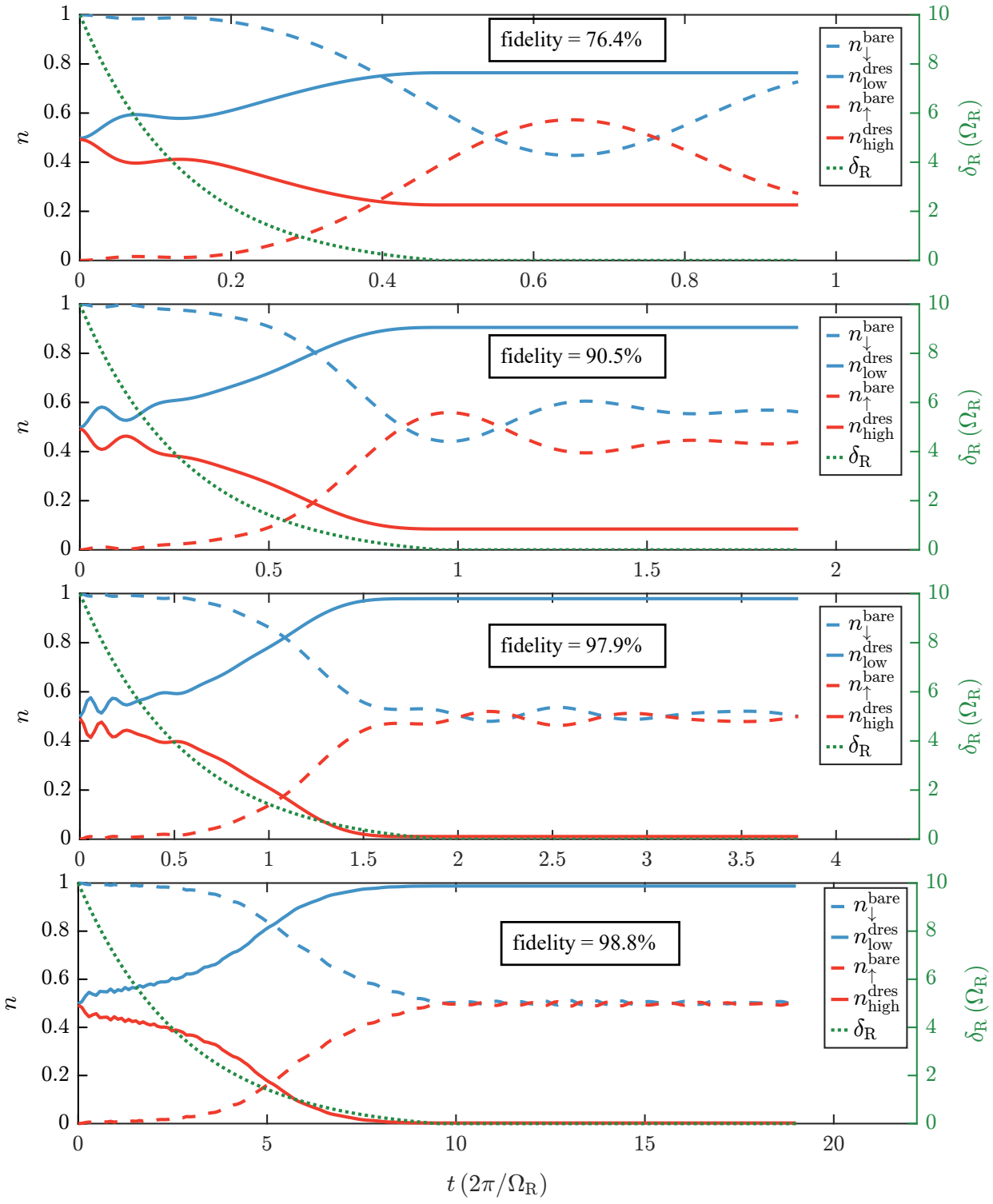

Figure 4.10: Comparison of preparation ramp times. The figures display the state transfer for adiabatic passages with various ramp times. For this purpose, we present several quantities as a function of the ramp time t in each subfigure. On the left vertical axis, we depict the relative population n of different states. On the one hand, the population $n_{\uparrow/\downarrow}^{\text{bare}}$ of the pseudo spin states $|\uparrow\rangle$ and $|\downarrow\rangle$ in the bare states is plotted (dashed lines). On the other hand, we present the population $n_{\text{low/high}}^{\text{dres}}$ of the lowest and higher (second lowest) dressed band (solid lines). On the right vertical axis, we show the two-photon detuning δ_R (dotted line) in units of the Raman coupling strength Ω_R. From top to bottom the displayed ramp times of the adiabatic passages increase. The ramp times are $A \cdot T_{\text{ramp}} = A \cdot 75/(2\pi\Omega_R)$, where the additional factor A takes the values from top to bottom: 0.25, 0.5, 1 and 5.

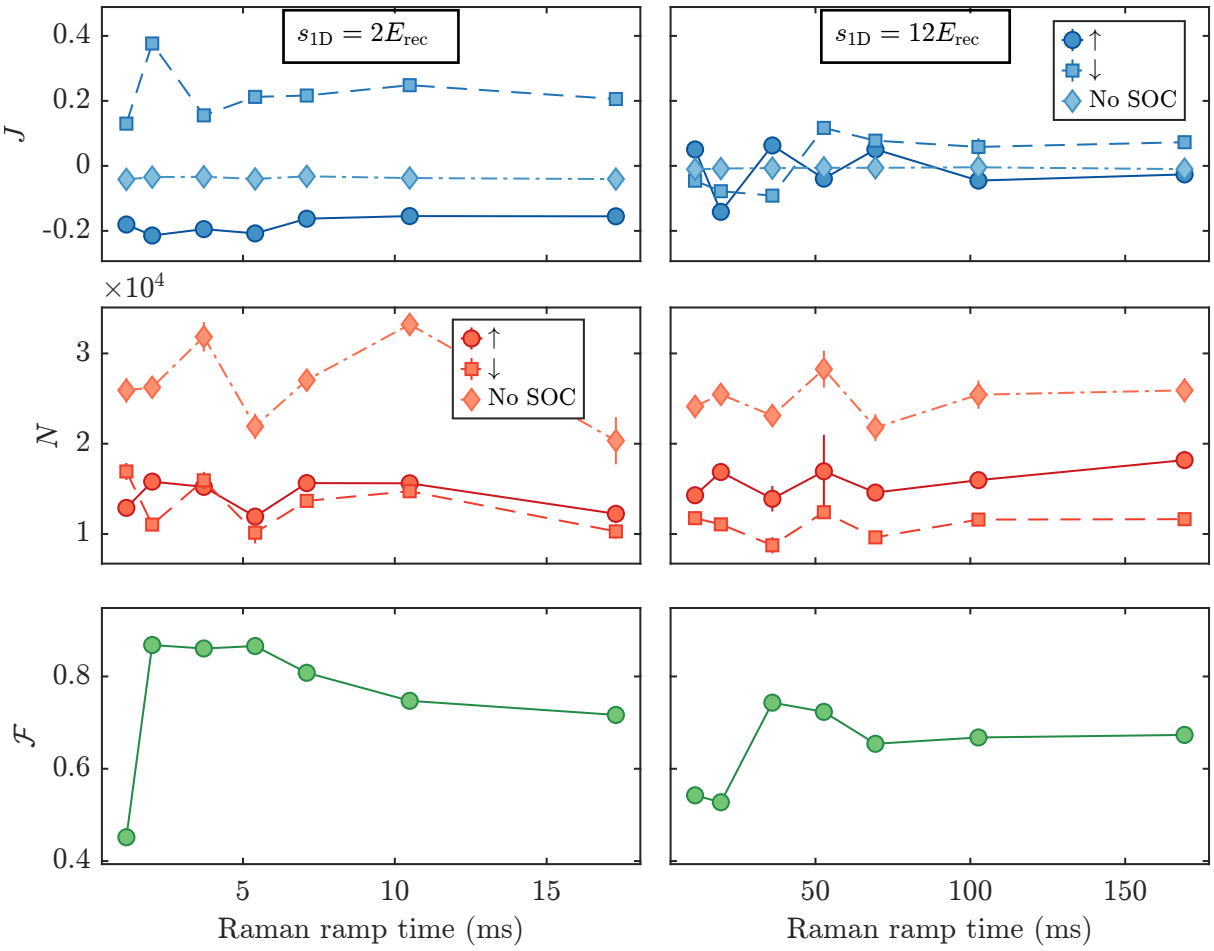

Figure 4.11: Influence of preparation ramp times. The figure displays various quantities recorded with ^{171}Yb as a function of the Raman ramp time. The parameters are set to $\Omega_R/t_x = 2.06(15)$ and $\phi = 0.444(20)\pi$. The left column presents data for the shallowest 1D lattice depth, $s_{1D} = 2\,E_{rec}$, while the right column presents data for the deepest 1D lattice depth, $s_{1D} = 12\,E_{rec}$. The figures in the top row show the measured chiral currents J for the spin states $|\uparrow\rangle$ and $|\downarrow\rangle$ and the reference case without spin-orbit coupling (SOC) labeled as "No SOC". The figures in the middle row display the number of atoms N for the three different cases of the top figures. The bottom figures exhibit the fidelity $\mathcal{F}$ for the preparation of the eigenstate. The data in the top and middle row is averaged five times and the error bars indicate the standard deviations, which are often smaller than the data point markers. The fidelity data is extracted from a single-shot measurement.

and measure the chiral currents. In auxiliary measurements, we additionally track data to evaluate the fidelity of the preparation. The results are presented as a function of the Raman ramp time in Fig. 4.11 for a 1D lattice depth of $s_{1D} = 2E_{rec}$ on the left and $s_{1D} = 12E_{rec}$ on the right. The top row of the figure exhibits the chiral currents for $|\uparrow\rangle$, $|\downarrow\rangle$ and reference data without spin-orbit coupling (SOC) labeled "No SOC". For the reference data, the measurement cycle is equal to the one, which records the chiral currents in the (pseudo)spin states, but without the Raman beams. To minimize differences to the data, we also use the spin-selective imaging in these measurements. In the middle row of the figure, we depict the atom numbers N for the same data as in the top row. These subfigures are used to verify, that the system behaves as expected and to rule out large particle losses during the eigenstate preparation. We observe in the different atom numbers, that the total number of atoms before and after the ramp are equal for all preparation times within experimental accuracy, i.e. $N_{\mathrm{No\,SOC}} = N_\uparrow + N_\downarrow$. This means, that the scattering of photons by the Raman beams can be neglected as expected from theory. An additional observation is, that, after the preparation ramp, the atoms are distributed over the two spin states to roughly equal amounts, which is expected for the dressed state. The population of the dressed state in our Harper-Hofstadter model for fully occupied band would theoretically consist of 50 % in one spin state and 50 % in the other spin state. However, some effects can influence this ratio in our experimental system. First, if the two-photon detuning δ_R is not exactly zero (this can be caused by an imperfect measurement of the Raman resonance). Second, due to the small coupling to the third spin state for data with ^{173}Yb (which is not the case of the chosen data). Third, because of the harmonic confinement, which couples the quasimomentum and position of the atoms and leads to an inhomogeneous momentum distribution for the initial spin-polarized state (see Ref. [116]), which is further described below. Because of these influences, it is hard to define an optimal population ratio of the spin states for a perfect eigenstate preparation. Thus, we do not use it to evaluate the fidelity of the eigenstate preparation. We only take this measurement into account as an additional check, that a population transfer occurred.

To evaluate the fidelity of an eigenstate preparation, we make another auxiliary measurement, where we perform the preparation ramp and immediately afterwards perform an additional inverse preparation ramp. After this inverse ramp, we measure the relative number of atoms n_{m_F} as defined in Eq. 4.8 in the two spin states, which constitute the synthetic dimension. After the inverse ramp, we expect all atoms to be transferred back to the initially prepared spin state. With this data, we determine the fidelity $\mathcal{F}$ of the eigenstate preparation as

$$\mathcal{F} = n_{m_F,\mathrm{ini}}, \tag{4.16}$$

where $n_{m_F,\mathrm{ini}}$ denotes the relative population in the initially prepared spin state after the inverse ramp. Using this measurement to assess the fidelity of the eigenstate preparation is not entirely precise, as the atoms, for instance, pass through two Raman ramps instead of just one. However, it provides a reasonable estimate. The calculated fidelity of the eigenstate preparation is plotted in the bottom row of Fig. 4.11. For the case of $s_{1D} = 2E_{rec}$, we observe, that the fastest ramp time reveals only a fidelity below 50 %, whereas for the other ramp times, the fidelity is above 70 %. For the second to fourth fastest ramp times the fidelity is the highest and for longer ramp times the fidelity decreases monotonically. This behavior is qualitatively as expected by the theory, for too fast preparations the fidelity is bad, then it reaches a maximum and at some point for slower preparations, it gradually decreases, which is most likely caused by the limited coherence time of the system. For the case of $s_{1D} = 12E_{rec}$, we observe, a similar behavior. Differences are, that the two fastest preparation ramps exhibit bad fidelity values instead of only the fastest and the maximum values for the fidelity are lower than for the case of the shallower lattice depth.

For the data at $s_{1D} = 2E_{rec}$, we observe prominent chiral currents, which feature values higher than

in comparable experimental studies (see Ref. [3–7]). In all quantities of the auxiliary measurements, we observe a behavior consistent with the theory. However, even though, we only observe a small decoherence in the fidelity for the displayed preparation times, the chiral currents strongly depend on the preparation time in the case of $s_{1D} = 12E_{rec}$. The currents even change sign. This behavior cannot be explained by the observed decoherence in the fidelity measurements and is unexpected. Despite the dependency on the preparation ramp time, we observe two other behaviors, which are unexpected from the theoretical model. First, for some ramp times with a good eigenstate preparation fidelity, the $s_{1D} = 12E_{rec}$ data displays strongly asymmetric chiral currents. Second, the chiral currents for $s_{1D} = 12E_{rec}$ are generally smaller in their amplitude than for $s_{1D} = 2E_{rec}$. Instead, the predictions from the model are, that the chiral currents are the same for all lattice depths and that the currents are equally strong for both spin states but in opposite directions. We discuss the implications of these findings after making further data optimizations in the next section.

4.4.4 Data Analysis

The work in this section so far concentrated on the possibilities to optimize the chiral current data acquisition by varying parameters for the measurements. In this subsection, we continue with optimizations in the analysis of the data. First, we try to reconstruct the data of a perfect bandmapping by projecting atoms to the first Brillouin zone. Second, we account for the initial quasimomentum distribution caused by the harmonic confinement.

Brillouin Zone Projection

As mentioned in the previous subsection, the bandmapping affects the chiral current data, which is, why we record all data with a very fast ramp of the lattice, instead of a well-working bandmap time. Therefore, the bandmapping works only up to a certain extent, and some quasimomenta from the lowest Bloch band are not exclusively transferred into the first Brillouin zone, but also into higher Brillouin zones. Here, we describe our approach to handling this influence in our data analysis. We first calculate the Brillouin zone size $2\pi/a$ on our images in pixels using the following relation:

$$\frac{2\pi}{a} = \frac{2\hbar k_{lat} t_{TOF}}{m_{Yb}} \cdot \frac{M}{d_{px}} \quad \text{Pixels}, \tag{4.17}$$

where t_{TOF} is the time of flight, m_{Yb} is the mass of an ytterbium atom (with small differences between the isotopes), M is the magnification of the imaging, d_{px} is the pixel size. In addition, the center of the Brillouin zone is determined as for the extraction of the chiral currents. Then, we project atoms from higher Brillouin zones into the first by transferring them by multiples of the lattice vector $\vec{G}$. We perform this projection, before we normalize the atom density according to Eq. 4.10. Hence, for some momenta the atom density in the first Brillouin zone is reduced, even though atoms are exclusively added by the projection.

Fig. 4.12 shows an example of the Brillouin zone projection, using data from auxiliary measurements to determine the initial quasimomentum distribution $n_{ini}(k)$ of the spin-polarized Fermi gas in our setup. This is the same data, which we used for the determination of the atom number before the eigenstate preparation (see Sec. 4.4.3). The figure presents $n_{ini}(k)$ for the shallowest ($s_{1D} = 2$) and deepest ($s_{1D} = 12$) 1D lattice depths of our measurements. In each subfigure, the momentum distribution is displayed for three different scenarios. First, it is shown without any projection of atoms. Second, the momentum

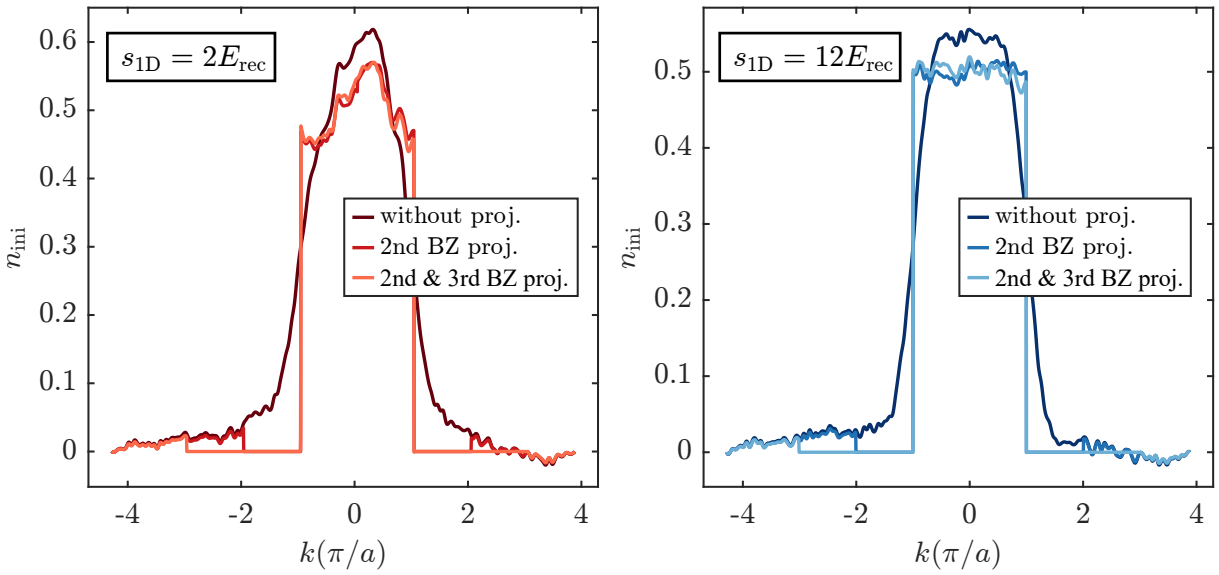

Figure 4.12: Typical initial momentum distributions with and without Brillouin zone projections. The figure presents typical initial momentum distribution $n_{ini}(k)$ for the shallowest ($s_{1D} = 2$ on the left side) and deepest ($s_{1D} = 12$ on the right side) 1D lattice depths of our measurements. In each subfigure, the momentum distribution is displayed as a function of the quasimomentum k of the 1D lattice and for three different scenarios. First, it is shown without any projection of atoms from higher Brillouin zones into the first one (labeled as "without proj."). Second, the momentum distribution is shown with a projection of atoms from the second to the first Brillouin zone (labeled as "2nd BZ proj."). Third, the momentum distribution is shown with a projection of atoms from the second and third Brillouin zone into the first Brillouin zone (labeled as "2nd & 3rd BZ proj.").

distribution is shown with a projection of atoms from the second to the first Brillouin zone. Third, the momentum distribution is shown with a projection of atoms from the second and third Brillouin zone into the first Brillouin zone.

In both lattice depth cases, we observe, that the difference between the data with only the second Brillouin zone projected in comparison to the data with the second and third Brillouin zone projected is marginal. Hence, the influence of higher Brillouin zones than the third can be neglected. For our parameters and a lattice depth of $s_{1D} = 12E_{rec}$, we expect for a Fermi energy between the lowest two Bloch bands, that the initial momentum distribution is approximately homogeneous. This can in fact be observed in the data with projections, which suggests, that the Brillouin zone projection works correctly and that the quasimomenta are represented more realistically with such a projection. Furthermore, this supports the assumption, that there are only negligible occupancies in higher Bloch bands (than the lowest one), because of the following reasoning. The data shows, that the second Bloch band is at least not fully occupied. If it were partially occupied (because of the Fermi energy lying in the band and not by thermal excitations), the momentum distribution at the edges of the Brillouin zone would be higher than in the center. This would be a consequence of the shape of the second Bloch band, which has lower energy states at the Brillouin zone edges than in the center. This reasoning is at least valid, when the effect of the harmonic confinement on the initial quasimomentum distribution is disregarded, which is reasonable for this lattice depth.

Initial Quasimomentum Distribution

Since the initial quasimomentum distribution is not homogeneous for shallow lattice depths, we explore in the following, how we can consider its influence. This is another option to optimize the data analysis, besides the Brillouin zone projection. Without harmonic confinement, the quasimomentum distribution of the prepared spin-polarized Fermi gas would be homogeneous over the first Brillouin zone for a Fermi energy between the lowest two Bloch bands. This means, that the probability to find an atom in a certain quasimomentum state would be equal for all quasimomenta in the first Brillouin zone. However, in our system, we have a finite harmonic confinement induced by the beam profiles of our lattice beams. The harmonic confinement is not diagonal in quasi-momentum space, and therefore it couples different quasimomentum states. As a result, the quasimomentum distribution changes and is in general not homogeneous. One consequence of the inhomogeneous distribution is, that the chiral currents along the two legs are not necessarily equal in their absolute value with opposite sign. Instead, the currents can be very different and can even have the same sign (see Ref. [116] for details). The reason for this unbalanced influence is, that the distribution is different for both spin states, because of the momentum transfer, which the atoms experience, when they change the spin state.

The data in Fig. 4.12 already allows for a preliminary assessment of the influence of the initial quasimomentum distribution on the edge current data. First, it tends to be stronger for shallower lattices than for deeper ones. Second, if the Brillouin zone projection is additionally performed, the influence of considering the initial distribution is weaker, such that for example the influence for $s_{1D} = 12E_{rec}$ with Brillouin zone projection can be neglected. Moreover, if we consider the initial distribution for the chiral currents, we expect, that the effect of the imperfect bandmapping is partially compensated, if the Brillouin zone projection is not performed. The reason for this is, that the initial distribution is also affected by the imperfect bandmapping and has a lower occupancy at the Brillouin zone edges, as it would be expected for a perfect bandmapping.

We aim to reconstruct the momentum distribution, $n^{\downarrow/\uparrow}_{\mathrm{hom}}(k)$, that would result from an initially homogeneous distribution. This allows us to better compare the data with the ideal case in our theoretical model, enabling more accurate interpretations. We achieve this by dividing the measured momentum distributions $n^{\downarrow/\uparrow}(k)$ by the initial momentum distribution $n_{\mathrm{ini}}(k)$. For the spin-up case, we further account for the momentum kick induced by the Raman transition by dividing by $n_{\mathrm{ini}}(k-\phi/a)$. The following calculations outline this process:

$$n^{\downarrow}_{\mathrm{hom}}(k) = \frac{n^{\downarrow}(k)}{n_{\mathrm{ini}}(k)} \qquad \text{and} \tag{4.18}$$

$$n^{\uparrow}_{\mathrm{hom}}(k) = \frac{n^{\uparrow}(k)}{n_{\mathrm{ini}}(k-\phi/a)}. \tag{4.19}$$

Comparison of Different Analysis Options

We compare the consideration of the initial momentum distribution with the effect of the Brillouin zone projections on the chiral currents, by presenting the momentum distribution for a single parameter set and four analysis options and compare them with the theoretical expectation. Fig. 4.13 displays the momentum distribution of the spin-down state on the left and of the spin-up state on the right. The displayed data corresponds to chiral currents for a 1D-lattice depth of 4 E_{rec} and a Raman ramp time of 9.2 ms (i.e. $A \cdot T_{ramp} = 1.5 \cdot 75/(2\pi\Omega_R)$). We choose this parameter set, because at this lattice depth and ramp time, the influence of the undesired dynamics is minimal, while at the same time, the tight-binding approximation is well satisfied. The analysis options are – despite the raw data without further analysis

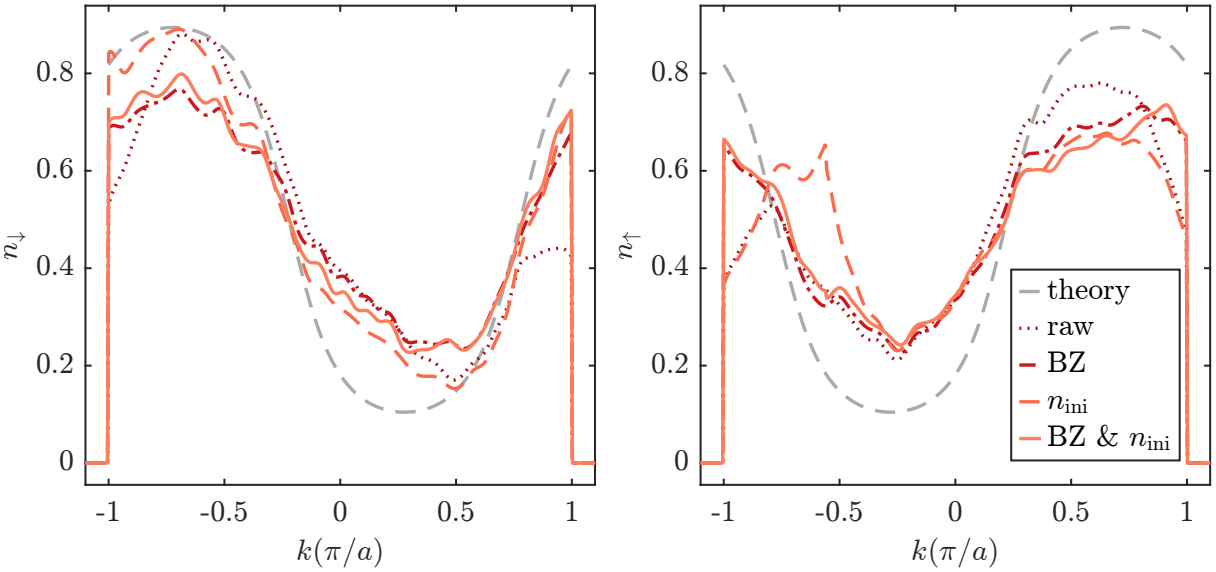

Figure 4.13: Momentum distribution for different analysis options. The figure displays the momentum distribution of the spin down state on the left and of the spin up state on the right for different analysis options. The displayed data corresponds to the chiral currents shown in Fig. 4.14 for a 1D-lattice depth of 4 E_{rec} and a Raman ramp time of 9.2 ms. The colors of the data indicate the four different analysis options as labeled in the legend (for a detailed description see Fig. 4.14). In addition, the expected distribution from the theoretical model is plotted.

(labeled "raw") – data with the projection of atoms from higher Brillouin zones to the first zone labeled as "BZ", data with the consideration of the initial momentum distribution labeled as n_{ini} and data as a combination of both additional options. This means, with the Brillouin zone projections and with the consideration of $n_{\mathrm{ini}}(k)$ labeled as "BZ & n_{ini}". The analysis options are indicated by the color of the data as illustrated in the legend.

We observe that the data, compared to the theoretical curve, aligns particularly well, when there is a balanced occupancy (i.e. $n = 0.5$). The higher values are undershot by the experimental data, while the lower values are exceeded. It appears as though there is a redistribution in the occupancy towards an equal distribution throughout the Brillouin zone. In the figure on the right, there's a visible effect resulting from imperfect bandmapping. If only the initial population is considered, the atoms located at the edges of the Brillouin zone are not properly captured. For this spin state, there is the peculiarity that the initial distribution is shifted by ϕ/a. However, if the Brillouin zone projection is not performed, the atoms at the edge of the Brillouin zone are underrepresented and, for this spin state, are not located at the edge but at $k = \pi/a - \phi/a \bmod 2\pi/a$. The unusual peak indicates that the atoms are not being correctly mapped. This shows that the BZ projection is quite important for accurately representing the data. The BZ projection better approximates the momentum distribution to the theoretical model, especially near the BZ edges. Overall, the trend looks similar to the theoretical curve, but the asymmetry is less pronounced in the data compared to the theory. Otherwise, we observe similar patterns as mentioned for the analysis of the chiral currents.

In addition to the momentum distribution, we present chiral current data in Fig. 4.14 for the same analysis options, but for different Raman ramp times and 1D lattice depths. The used raw data is the same as in Fig. 4.11 with additional data for $s_{\mathrm{1D}} = 8E_{\mathrm{rec}}$. Both additional analysis options seem to improve the data quality in the sense, that the momentum distribution is closer to the expected behavior of the theory.

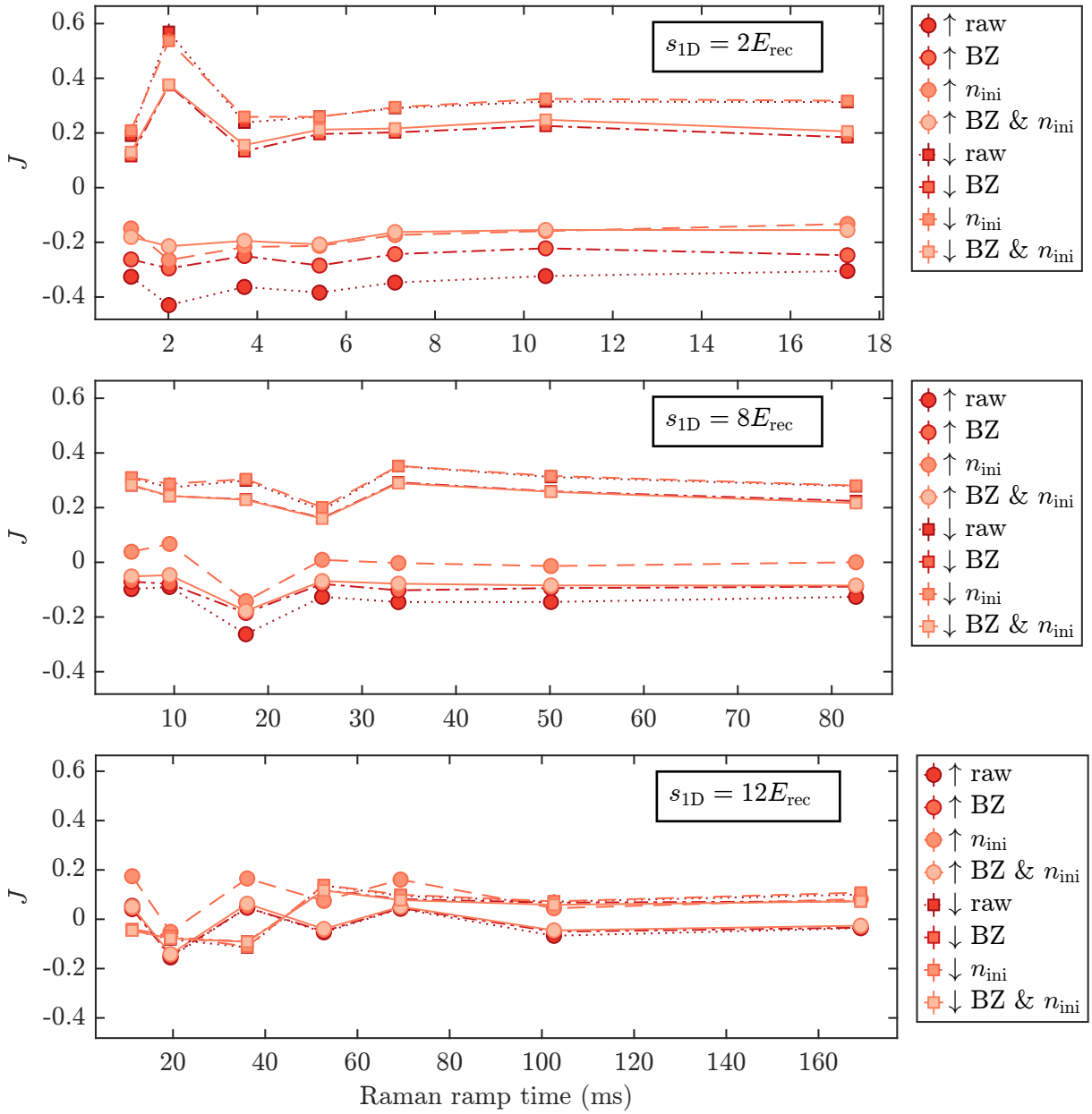

Figure 4.14: Chiral currents for different analysis options. The figure displays chiral current data for different analysis options and different lattice depths. From top to bottom, the subfigures present data for the 1D lattice depths $s_{1D} = 2E_{rec}$, $s_{1D} = 8E_{rec}$ and $s_{1D} = 12E_{rec}$. In each subfigure, the chiral currents are presented as a function of the Raman ramp time in the same way as in Fig. 4.11. The data point markers indicate the state of the data as the chiral current along the pseudo spin up state $|\uparrow\rangle$ or pseudo spin down down state $|\downarrow\rangle$. For clarity the reference data without SOC is omitted. The different analysis options do not change the reference data significantly. The colors of the data indicate the four different analysis options as labeled in the legend. The first option is the data without any further analysis, which means the same data as in Fig. 4.11, which is labeled as "raw". The second option is the data with the projection of atoms from higher Brillouin zones to the first zone, which is labeled as "BZ". The third option is the data with the consideration of the initial momentum distribution $n_{ini}(k)$, which is labeled as "n_{ini}". The fourth option is the data as a combination of the second and third option. This means, with the Brillouin zone projections and with the consideration of $n_{ini}(k)$. This option is labeled as "BZ & n_{ini}".

Especially, the Brillouin zone projection is reasonable, as we perform a very fast lattice power ramp instead of a proper bandmapping. However, the main issues of the chiral current data, which were evident for the raw data without further analysis, remain: The deeper the lattice, the more the data shows an unstable behavior for different preparation times, even though these preparations feature a very similar fidelity. In addition, the amplitude of the chiral currents decreases on average for deeper lattices, even though the particles are nearly non-interacting. These For this behavior of the chiral current data, we rule out any perturbation, that would destroy the coherence of the system, since the fidelity of the preparations suggests, that the system is coherent. Furthermore, we exclude, that the preparation is too fast for all preparation times in the measurement. The first reason for that is again, that the system behaves coherent in the fidelity measurements. The second reason is, that these preparation ramps feature a very high fidelity of 97.9 % and higher, according to the theoretical calculations in Fig. 4.10. The calculations do not include interaction effects, but for the ^{171}Yb data, interactions can be neglected, as they are much weaker than other system parameters.

We conclude, that an additional dynamic must occur, which is not accounted for in the theoretical model and which does not reduce the system's coherence. We suspect, that the harmonic confinement along the 1D-lattice is the cause of these dynamics. Ref. [164] demonstrates, that the coupling between (quasi)momentum states, induced by harmonic confinement, can generate non-linear pendulum dynamics in the (quasi)momentum distribution. Consequently, we expect dynamic behavior in the system, if the momentum distribution differs from the distribution, which is favored by the harmonic confinement. This situation generally arises in the presence of chiral currents. Thus, this effect appears to be the most plausible explanation for the observed behavior. However, quantifying these dynamics is challenging, and our data suggests no dependencies on either relative or absolute time scales. A complete understanding of these dynamics will require further investigation, which lies beyond the scope of this thesis.

One possibility to understand the dynamics further would be to take images also during the preparation ramp and not only after it. In this way, one could try to understand, what happens already over the course of the preparation. In addition, one could perform theoretical simulations for the expected pendulum dynamics and compare them with the data. By doing so, it might be possible to reconstruct the initial chiral current data to some extent. As an alternative strategy, it is possible to implement countermeasures for the harmonic confinement induced by the lattice beams. This was for example implemented for a similar system in Ref. [165] with an additional laser beam, which creates a double-well potential at an anti-trapping frequency (1112 nm). The laser beam is shone onto the atoms from a direction perpendicular to the shallow lattice, such that the atoms are between the double-well potential. In this reference, the harmonic confinement could be compensated to a residual value of $0.01t_x$ along the legs of the quantum Hall ladder. Unfortunately, it is not possible for us to get rid of the harmonic confinement in our current setup. We can only reduce it as much as possible. However, this is already the case, as the harmonic confinement is only caused by the lattice beams and the transverse lattice depth cannot be reduced further, as otherwise motion in a transverse direction is not inhibited. The optimization methods in this section are already aimed at getting data, which is as little influenced by this effect as possible.

In this section, we discussed and implemented methods to improve the quality and accuracy of the chiral current data. We examined unreported dynamics that occur during the bandmapping and eigenstate preparation stages, analyzing their impact on the measured momentum distribution and, consequently, on the chiral current data. To reduce these effects, we implemented targeted strategies, focusing mainly on utilizing a fast 1D lattice ramp and shortening the eigenstate preparation time.

In this chapter, we have outlined the critical steps involved in the preparation and implementation of

quantum Hall ladders at our quantum gas machine. Beginning with the technical setup, we detailed the design and operation of the Raman Laser System and the applied Raman transitions. We then discussed the preparation of eigenstates, where we described the performed adiabatic passage in detail. Through the primary measurements of Raman resonances, Raman-Rabi oscillations, and chiral edge currents, we verified the successful realization of the quantum Hall effect in our experimental setup. Lastly, we addressed various methods for optimizing the experimental data, including improvements in the spin detection, imaging, eigenstate preparation and data analysis. We observed prominent chiral currents, which feature values higher than in comparable experimental studies (see Ref. [3–7]) and which exhibit momentum distributions very close to theoretical expectations. This chapter lays a solid groundwork for further exploration of quantum Hall ladder systems and their topological properties in quantum gases, providing valuable insights into both the practical challenges and the strategies to overcome them.

5 Interactions in Quantum Hall Ladders

With the groundwork covered in the previous two chapters, we now present our findings on interaction effects in quantum Hall ladders. In general interactions in synthetic dimensions can be very diverse. Ref. [166] lists various implementations of synthetic dimensions, which yield different forms of inter-particle interactions. For example, in synthetic directions constituted by harmonic oscillator eigenstates, interactions decay algebraically [78], whereas in photonic frequency modes [167, 168], interactions preserve the total synthetic positions of colliding particles. Furthermore, momentum states as synthetic dimensions in ultracold gases [77] result in effective locally attractive interactions in momentum states, which have been experimentally explored regarding localization transitions [169, 170]. Theoretical studies examined dipolar interactions when synthetic dimensions are defined by the rotational states of polar molecules, revealing phase transitions to intriguing states localized along the synthetic dimension [171, 172]. Moreover, a proposed synthetic dimension based on the angular coordinate of a photonic ring resonator can have local interactions within the resonator, which would translate to local interactions along the synthetic dimension [173].

In our system, we investigate how inter-particle interactions, which are infinitely long-ranged along the synthetic dimension and localized to a single lattice site along a shallow optical lattice, affect the topologically protected chiral edge currents. It is an open question, what happens to the system, if interactions come into play. First, we examine the quantum Hall ladder system with vanishing interactions using ^{171}Yb. Second, we compare the data for the non-interacting case with those obtained with repulsive interactions using ^{173}Yb, in order to extract the effects of the interactions. The measurements in this chapter were planned, conducted and analyzed by the author under the project administration and supervision of C. Becker and K. Sengstock.

To investigate the influence of interaction effects on chiral edge currents in a quantum Hall ladder, we measure the chiral currents as a function of the 1D lattice depth, while holding the ratio Ω_R/t_x constant. We do this for the nearly non-interacting isotope ^{171}Yb ($a_{scat} = -3(4)a_0$) and the repulsive interacting isotope ^{173}Yb ($a_{scat} = 199(2)a_0$). By comparing the two data sets, we extract the effect of interactions, as we treat the ^{171}Yb data as non-interacting reference data. We prepare the quantum Hall ladder system with an adiabatic passage and measure the chiral currents directly afterwards. After the preparation, we first switch off the Raman beams and then at the same time switch off the transverse lattice beams and perform a very fast bandmapping in the 1D lattice direction to avoid additional dynamics during this stage, which we observed for longer bandmapping times (see Sec. 4.4.2). Finally, we analyze the absorption images as described in Sec. 4.3.3 to calculate the chiral currents. For the chiral current data presented in this chapter, we averaged over several preparation ramp times. For this, we use data of all preparation ramp times, which exhibit a high fidelity for the preparation of the eigenstates in the theoretical calculations and in the auxiliary measurements, namely for $T_{ramp} \geq 75/(2\pi \cdot \Omega_R)$. We choose this averaging, as it captures the uncertainty in the chiral currents caused by the undesired dynamics discussed in Sec. 4.4. With more insight into the exact behavior of these dynamics, one could possibly find a more accurate approach to represent the unperturbed currents and reduce uncertainties. However, given our current level of understanding, this would be speculative and lies beyond the scope of this thesis.

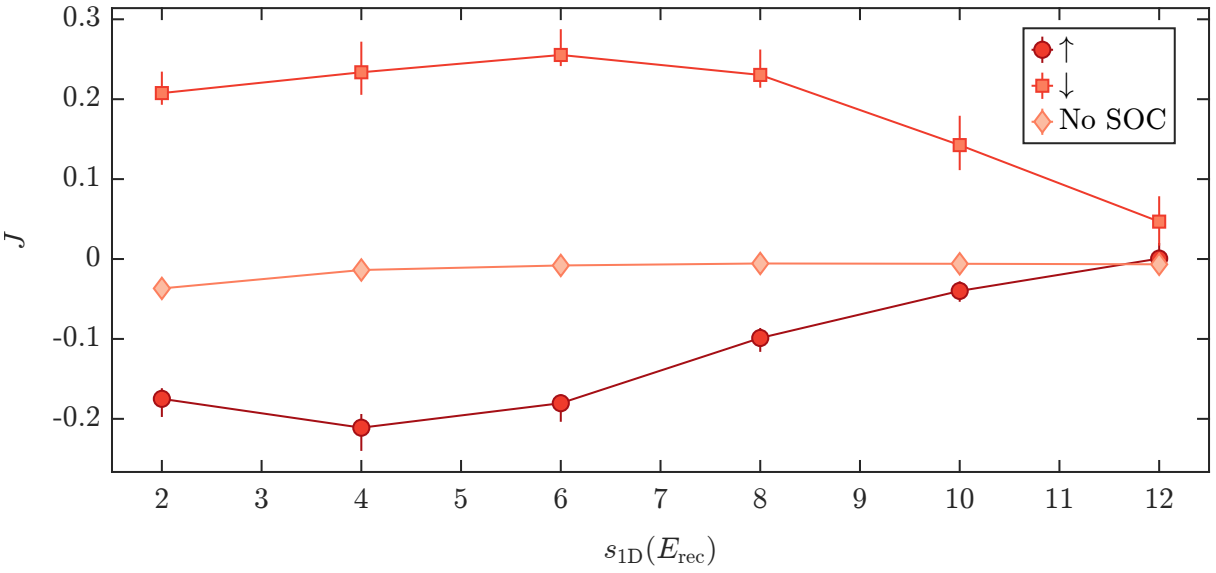

Figure 5.1: Chiral currents for various lattice depths without interactions. The figure presents the measured chiral edge currents J of a two-leg quantum Hall ladder as a function of lattice depth along the legs. The currents are displayed for the spin states $|\uparrow\rangle$ and $|\downarrow\rangle$ and the reference case without spin-orbit coupling (SOC) labeled as "No SOC". This data is recorded with ^{171}Yb atoms, which exhibit vanishing interactions of $-3(4)\,a_0$. The magnetic flux is $\phi = 0.444(20)\pi$ and the ratio of synthetic and real tunneling is kept constant at $\Omega_R/t_x = 2.06(15)$. Chiral currents are averaged for various preparation ramp times with $T_{ramp} \geq 75/(2\pi \cdot \Omega_R)$ (see Sec. 4.4.3 for details). Error bars represent the uncertainties calculated through error propagation.

5.1 Vanishing Interactions

First, we present data for the case of vanishing interactions of $-3(4)\,a_0$. This data is recorded with the isotope ^{171}Yb. We measure the chiral currents of both spin states (synthetic lattice sites) for different 1D lattice depths at a constant ratio of $\Omega_R/t_x == 2.06(15)$. The data is displayed in Fig. 5.1. In particular for data at shallow lattice depths, we observe prominent chiral currents, which feature values higher than in comparable experimental studies (see Ref. [3–7]). Moreover, the amplitude of the chiral currents decreases for deeper lattices. We attribute this to the observed dynamics for different preparation times, which become worse for deeper lattices as it is discussed in Sec. 4.4.3. Additionally, an increasing number of atoms may become trapped in localized states as the lattice depth grows. These localized atoms would not contribute to the current, thereby reducing the measured values. Without the knowledge about the observed dynamics, which are most likely caused by the harmonic confinement, we would have expected that the data of the chiral currents as a function of the 1D-lattice depth is constant for the weakly interacting isotope ^{171}Yb, as we keep ϕ and Ω_R/t_x constant. In particular, the data for $s_{1D} = 10$ and $12\,E_{rec}$ behaves very different from theoretical expectations in the momentum distribution and in the value of the currents. Furthermore, we notice asymmetries in the absolute values of the currents for opposite legs of the quantum Hall ladder. Since we already consider the initial momentum distribution n_{ini}, which can cause asymmetries, we do not know the origin of this effect. However, as the dynamics during the preparation are asymmetric as well, we assume that the two effects are related. Another observation on the data is, that the first data point with $2\,E_{rec}$ features slightly lower chiral currents than the data for $s_{1D} = 4$ and $6\,E_{rec}$. This might be caused by the tight-binding approximation breaking down, as this lattice is already such shallow, that the requirement of atoms localized at a single lattice site is not perfectly met. Moreover, the data without spin-orbit coupling (No SOC) is expected to be symmetric

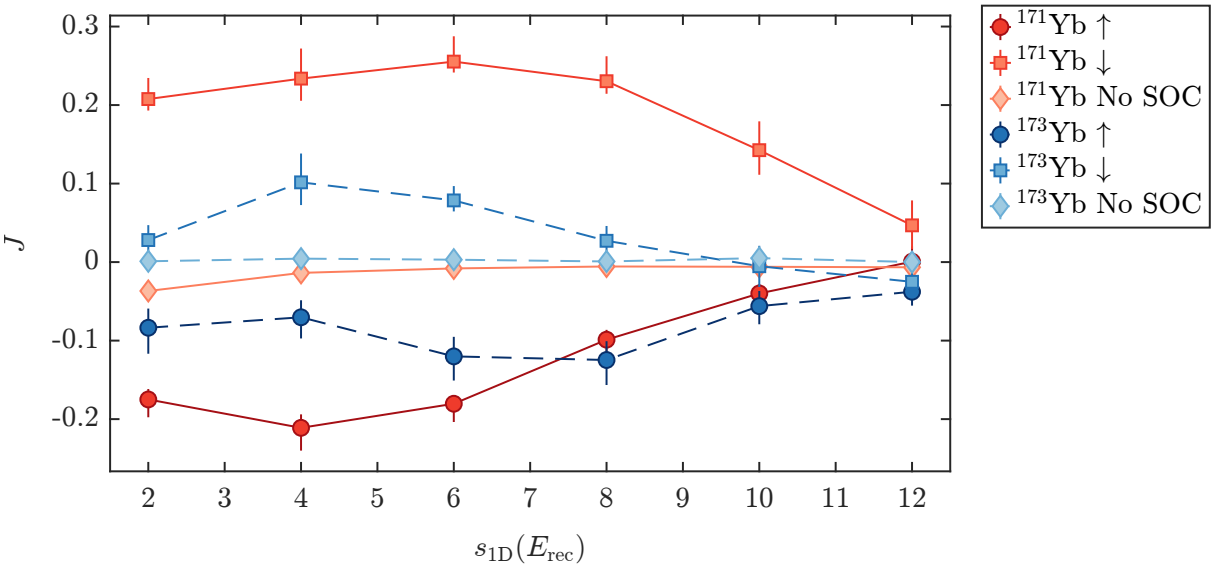

Figure 5.2: Comparison of chiral currents with vanishing and repulsive interactions. The figure displays the data of Fig. 5.1 for vanishing interactions (in red with solid lines) in comparison to analogous data with repulsive interactions (in blue with dashed lines). Measured chiral edge currents J of a two-leg quantum Hall ladder are presented as a function of lattice depth along the legs. Data for vanishing interactions ($a_{\text{scat}} = -3(4)a_0$) is recorded with ^{171}Yb atoms, whereas repulsive interaction data ($a_{\text{scat}} = 199(2)a_0$) is recorded with ^{173}Yb atoms. The magnetic flux is $\phi = 0.444(20)\pi$ and the ratio of synthetic and real tunneling is kept constant at $\Omega_R/t_x = 2.06(15)$. Chiral currents are averaged for various preparation ramp times with $T_{\text{ramp}} \geq 75/(2\pi \cdot \Omega_R)$ (see Sec. 4.4.3 for details). Error bars represent the uncertainties calculated through error propagation.

within the Brillouin zone, which would result in $J = 0$. However, we observe a significant deviation for the two shallowest lattice depths, $s_{1D} = 2$ and $4\,E_{\text{rec}}$. While the origin of this discrepancy is unclear, it appears to be present only in the non-interacting case (compare Fig. 5.2). Although further investigation into its cause could be of general interest, this issue is of secondary importance for the scope of our study and is not further explored. Despite the deviation from an ideal system without harmonic confinement, we use this data as a reference and compare it with data from interacting particles. This comparison can still provide insights into the interaction dynamics, assuming the interacting particles are influenced by the dynamics in a similar manner.

5.2 Repulsive Interactions

In this section, we present the effect of repulsive interactions on the chiral edge currents of a quantum Hall system. For this purpose, we record the same data displayed in Fig. 5.1 with ^{173}Yb. We plot the data sets of both isotopes in Fig. 5.2. The figure displays the case of vanishing interactions in red with solid lines in comparison to analogous data with repulsive interactions in blue with dashed lines. For the interacting isotope ^{173}Yb, we expect that the chiral currents data as a function of the lattice depth shows a different behavior than the ^{171}Yb data. The difference in the behavior would than be due to interactions as all other parameters are the same. We observe for the ^{173}Yb isotope, that the amplitude of the chiral currents is significantly smaller for most data. The exceptions are on the spin up side for the data at $s_{1D} = 8$ and $10E_{\text{rec}}$, where the current is equal within the uncertainties and for $s_{1D} = 12E_{\text{rec}}$, where the current for ^{173}Yb is stronger in the negative direction than for ^{171}Yb. Further observations for the ^{173}Yb

isotope are, that the chiral current for the spin down data first increases from $s_{1D} = 2$ to $4E_{rec}$ and then monotonically decreases for deeper lattices until they are even negative for $s_{1D} = 12E_{rec}$. For the spin up data, we observe, that the chiral current is similar for the two most shallow lattice depths, then decreases for $s_{1D} = 6$ to $8E_{rec}$ and finally increases to the highest values for $s_{1D} = 10$ to $12E_{rec}$. Moreover, for the data without SOC, we observe that in the case of ^{173}Yb, the measured chiral currents are consistent with zero, as expected. As discussed above, for ^{171}Yb, the data without SOC differs significantly from zero for the two shallowest lattice depths, $s_{1D} = 2$ and $4E_{rec}$.

The data of ^{173}Yb has in common with the non-interacting data, that the currents of the two legs are asymmetric. The asymmetries make it harder to compare the data of the two isotopes, while at the same time, they are not the main focus of our studies. It is rather the difference of the currents for the two legs of the quantum Hall ladder, which represent the non-triviality of the system's topology. Hence, to neglect the asymmetries, we additionally present the chiral current difference ΔJ of the two legs for the same data. We define it as

$$\Delta J := J_\downarrow - J_\uparrow. \tag{5.1}$$

In the current difference ΔJ, the asymmetries of the two legs do not play a role anymore and possible dynamics, which affect both current values in the same way are averaged out. We present ΔJ as a function of the lattice depth s_{1D} at the top of Fig. 5.3. As a consequence of this representation, the following similarities in the data of ^{171}Yb and ^{173}Yb become more evident. For both isotopes, the first data point at $s_{1D} = 2E_{rec}$ exhibits lower absolute values than the currents for $s_{1D} = 4$ and $6E_{rec}$. Moreover, except for the first data point, the currents tend to decrease for deeper lattices. Especially for $s_{1D} = 10$ and $12E_{rec}$, the absolute values of the currents are much lower than for the other lattice depths. Despite the similarities, we observe that the chiral current difference for the interacting particles $\left(^{173}\text{Yb}\right)$ is generally smaller than for the non-interacting case. This indicates a suppression of the chiral currents due to the interactions.

We present two additional visualizations to compare the interacting and non-interacting chiral currents, utilizing different representations of the non-interacting data as a reference. In the first case, we visualize the absolute (differential) change induced by interactions, while in the second, we examine the proportional (relative) change. To illustrate these two potential descriptions, we present, on one hand, the difference $\Delta J_{173} - \Delta J_{171}$, and on the other hand, the ratio $\Delta J_{173}/\Delta J_{171}$, shown in the middle and bottom panels of Fig. 5.3. For the difference in the currents, we observe, that it is equal for $s_{1D} = 2$ and $4\,E_{rec}$. For deeper lattice depths, it monotonically increases with increasing lattice depth, which means, that the absolute difference between the currents decreases until they are nearly equal for $s_{1D} = 12\,E_{rec}$. For the chiral current ratio, we observe a rather constant behavior within the experimental uncertainties. While for s_{1D} in the range of 2 to $6\,E_{rec}$, the uncertainties in the data, which are calculated through error propagation, are rather constant, the uncertainties increase for deeper lattice depths. For $s_{1D} = 12\,E_{rec}$, the uncertainties even include a negative ratio, which would mean an enhancement of chiral currents for strong repulsive inter-particle interactions.

To trace the differences between the data of the two isotopes back to variations in the interaction strength, we present the same data as a function of U_{int}/t_x in Fig. 5.4. We calculate U_{int} by determining the Wannier functions and using Eq. 1.7. As the ^{171}Yb isotope has nearly vanishing interactions ($-3(4)a_0$), all its data is close to $U_{int}/t_x = 0$, whereas the ^{173}Yb data is spread over the range [1.45, 36.30]. The specific values according to the different 1D lattice depths from shallowest to deepest are: $U_{int}/t_x \in \{1.45, 3.22, 6.50, 12.17, 21.50, 36.30\}$. For the differential data in the second row, we now observe a

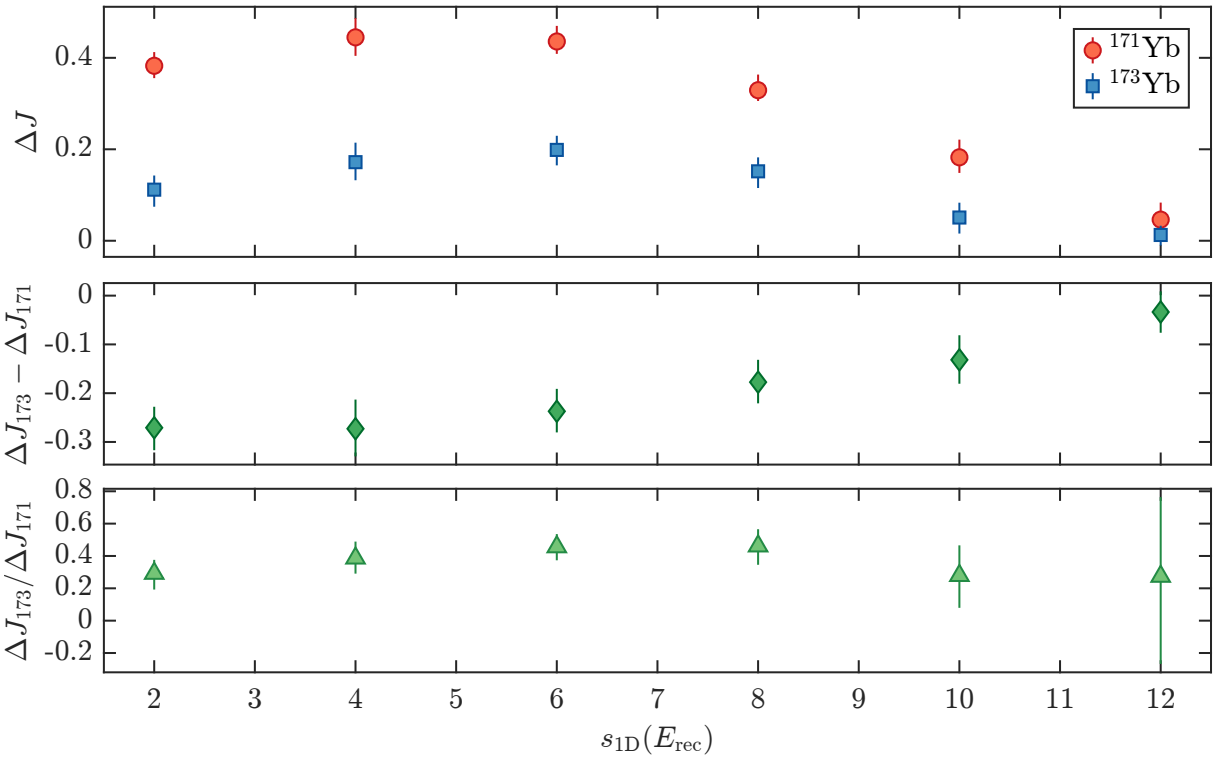

Figure 5.3: Different representations of chiral current data. The figure depicts the chiral current data of Fig. 5.2 in different representations as a function of the lattice depth s_{1D}. The top figure displays the chiral current difference $\Delta J = J_\downarrow - J_\uparrow$ for both isotopes, the middle figure displays the differential of the chiral currents with interactions and without $\Delta J_{173} - \Delta J_{171}$ and the bottom figure displays the ratio of the chiral currents $\Delta J_{173}/\Delta J_{171}$. Error bars represent the uncertainties calculated through error propagation.

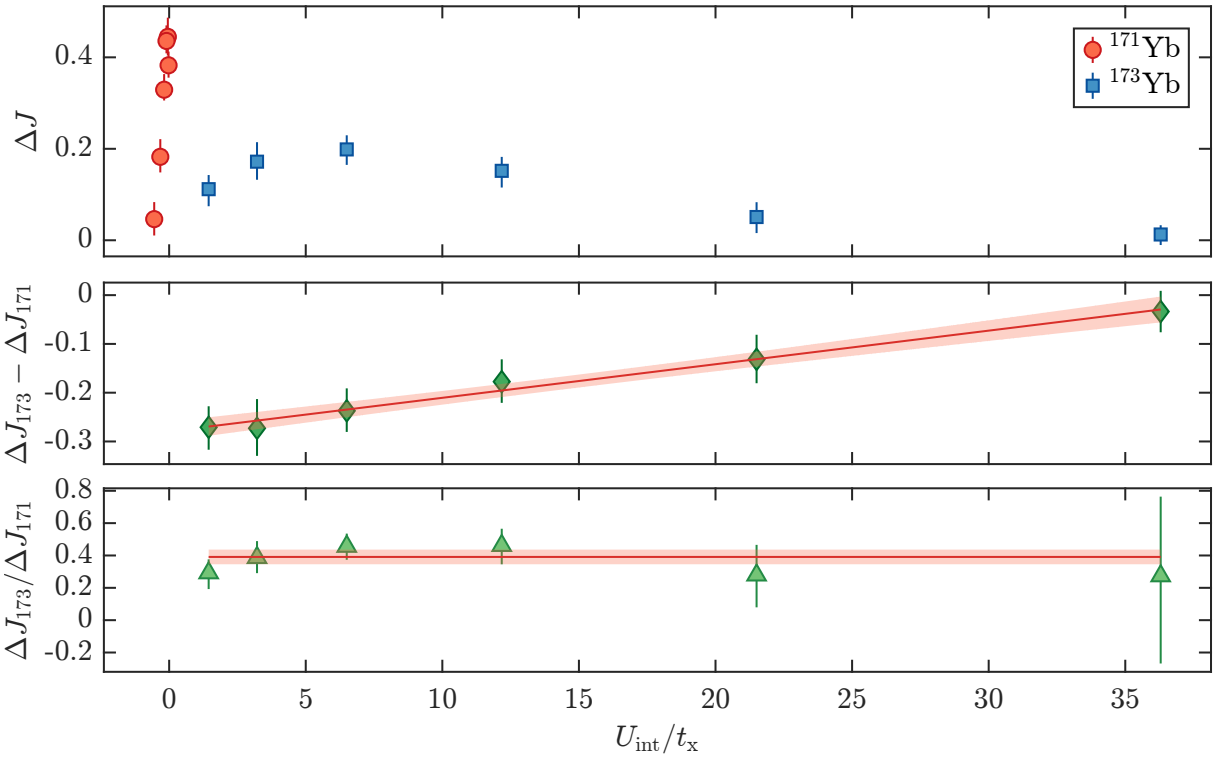

Figure 5.4: Chiral current data as a function of the interaction strength $U_{\mathrm{int}}/t_{\mathrm{x}}$. The figure shows the same data as in Fig. 5.3, but plotted as a function of the interaction strength $U_{\mathrm{int}}/t_{\mathrm{x}}$ instead of the lattice depth. In the middle panel, a linear fit is applied to the differential data, described by the function $(-0.279 \pm 0.010) + (0.00689 \pm 0.00053) \cdot U_{\mathrm{int}}/t_{\mathrm{x}}$. The shaded region around the fit represents the 95 % confidence interval. In the bottom panel, the weighted mean (solid line) and weighted uncertainty (shaded area) of the ratio data are included, with the value: $\overline{\Delta J_{173}/\Delta J_{171}} = 0.391 \pm 0.045$. Error bars represent the uncertainties calculated through error propagation.

linear behavior as a function of $U_{\mathrm{int}}/t_{\mathrm{x}}$. We fit this data with a linear function and obtain

$$(-0.279 \pm 0.010) + (0.00689 \pm 0.00053) \cdot U_{\mathrm{int}}/t_{\mathrm{x}}. \tag{5.2}$$

For the relative data of the ratio $\Delta J_{173}/\Delta J_{171}$, we still observe a constant behavior as a function of $U_{\mathrm{int}}/t_{\mathrm{x}}$. We determine the weighted mean and weighted uncertainties of the ratios and plot it with the data. The result is

$$\overline{\Delta J_{173}/\Delta J_{171}} = 0.391 \pm 0.045. \tag{5.3}$$

This data should be treated with caution, as it may not be fully reliable, given the observed dependence of the chiral currents on the preparation of the eigenstate. The averaging over different preparation velocities might also be suboptimal, potentially influencing the results. Nonetheless, the data exhibits a systematic trend within the measured range, and we explore potential consequences with caution and a critical perspective.

5.2.1 Possible interpretations

As a final step, we want to visualize our results in a way, that makes it easier to compare with future studies and show what the data might look like without the dynamics during the eigenstate preparation (i.e., likely without harmonic confinement). As discussed above, we assume, that the dynamics during the preparation are caused by the harmonic confinement and are the reason for the non-constant behavior of the chiral currents as a function of the lattice depth for the nearly non-interacting case $\left({}^{171}\mathrm{Yb}\right)$. Next, we illustrate our data under the assumption of constant chiral currents in the non-interacting scenario. Our best estimate for the undisturbed chiral currents, $\Delta J_{171}^{\mathrm{assumed}}$, is the average of the values for the lattice depths $s_{1\mathrm{D}} = 4\,E_{\mathrm{rec}}$ and $6\,E_{\mathrm{rec}}$:

$$\Delta J_{171}^{\mathrm{assumed}} = \frac{\Delta J_{171}^{4\,E_{\mathrm{rec}}} + \Delta J_{171}^{6\,E_{\mathrm{rec}}}}{2}. \tag{5.4}$$

At these lattice depths, the conditions for the tight-binding approximation are well satisfied, and the differences in the currents for varying preparation velocities are minimal. We then assume that these currents would be observed across all lattice depths if our measurements were conducted in a system without harmonic confinement. Based on this assumption, we hypothesize how the chiral current behavior might appear as a function of $U_{\mathrm{int}}/t_{\mathrm{x}}$. We adjust our data for the two investigated cases – differential and relative effects – according to the newly assumed constant currents, $\Delta J_{171}^{\mathrm{assumed}}$. For visualizing the differential effect, ΔJ_{diff}, we start with the assumed constant chiral current of the non-interacting case, $\Delta J_{171}^{\mathrm{assumed}}$, and add the current difference $\Delta J_{173} - \Delta J_{171}$, as observed in Fig. 5.3 and 5.4. This gives:

$$\Delta J_{\mathrm{diff}} = \Delta J_{171}^{\mathrm{assumed}} + (\Delta J_{173} - \Delta J_{171})\,. \tag{5.5}$$

For visualizing the relative effect, ΔJ_{rel}, we multiply the assumed constant currents, $\Delta J_{171}^{\mathrm{assumed}}$, by the ratios $\Delta J_{173}/\Delta J_{171}$, as shown in Fig. 5.3 and 5.4, resulting in:

$$\Delta J_{\mathrm{rel}} = \Delta J_{171}^{\mathrm{assumed}} \cdot \frac{\Delta J_{173}}{\Delta J_{171}}. \tag{5.6}$$

The results for both ΔJ_{diff} and ΔJ_{rel} are presented as a function of $U_{\mathrm{int}}/t_{\mathrm{x}}$ in Fig. 5.5. These visualizations represent two potential scenarios of how the data might appear in the absence of the dynamics during the eigenstate preparation (i.e., likely without harmonic confinement).

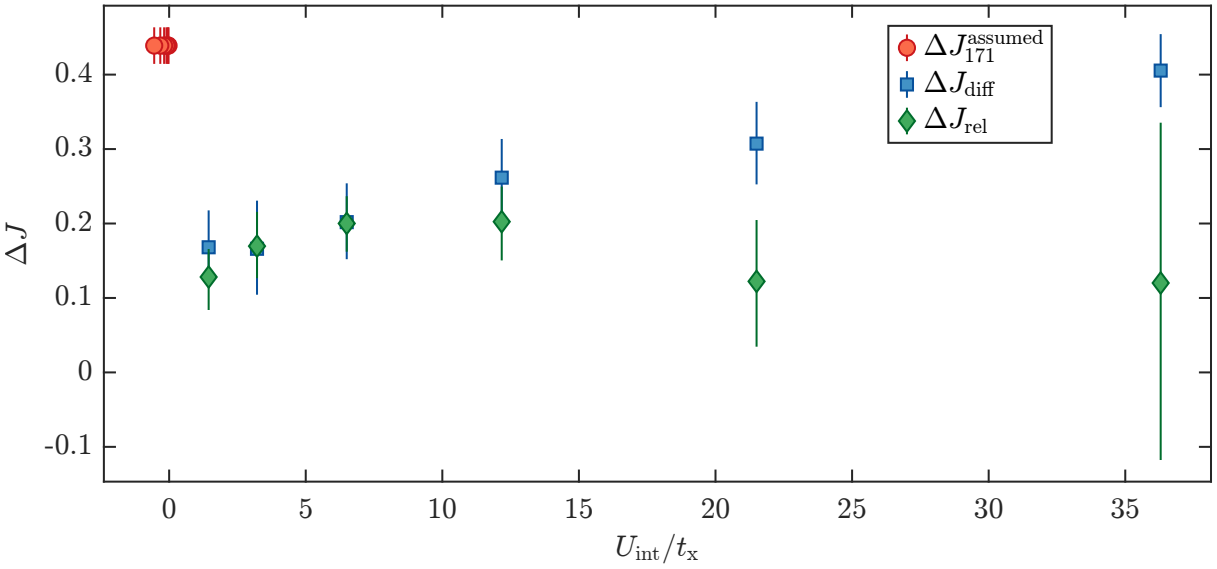

Figure 5.5: Possible interpretations for the interaction behavior of chiral edge currents in quantum Hall ladders. The figure illustrates two possible interpretations of the interaction behavior of chiral edge currents in quantum Hall ladders within the explored parameter regime. Assuming constant chiral currents $\Delta J_{171}^{\text{assumed}}$ in the non-interacting case (red data), we present two scenarios: a differential effect ΔJ_{diff} (blue data) and a relative effect ΔJ_{rel} (green data). Error bars represent the uncertainties calculated through error propagation. Details are provided in the main text.

For $U_{\text{int}}/t_{\text{x}} \in \{3.22, 6.50\}$, the currents in both interpretation scenarios are nearly congruent. For the remaining data points, the differential currents are larger than the relative currents. The data at $U_{\text{int}}/t_{\text{x}} \in \{1.45, 12.17\}$ only differs by about one sigma of their uncertainties for the two scenarios. The largest discrepancies between the two scenarios occur at $U_{\text{int}}/t_{\text{x}} \in \{21.50, 36.30\}$, suggesting that significantly different conclusions can be drawn for large interaction strengths. However, the uncertainties for the relative data, particularly at $U_{\text{int}}/t_{\text{x}} = 36.30$, are that large, that predictions based on these data have a wide range, potentially even including the differential data point at the same interaction strength.

In addition to the behavior observed for ΔJ_{diff} and ΔJ_{rel}, we note a significant difference between $\Delta J_{171}^{\text{assumed}}$ and the data with the weakest repulsive interactions. The transition between these data sets remains unclear. Given the substantial discrepancy in the edge current values on both sides, we expect that the system's behavior is strongly influenced. The weakest interaction point for ΔJ_{diff} and ΔJ_{rel} occurs at $U_{\text{int}}/t_{\text{x}} = 1.45$, placing it in a regime where interactions begin to dominate the tunneling rate and are close to Ω_{R} ($U_{\text{int}}/\Omega_{\text{R}} = 0.725$). This suggests that significant interaction effects are already present. However, we cannot completely rule out systematic differences between measurements with the two ytterbium isotopes, despite our efforts to make the systems as similar as possible. In our current setup, it is not possible to probe the transition in the regime of weakly repulsive interactions, as our parameters are already optimized for the weakest repulsive interactions achievable with ^{173}Yb. At the shallowest lattice depth of $s_{\text{1D}} = 2, E_{\text{rec}}$, the validity of the tight-binding approximation becomes already questionable.

In the following, we discuss our findings in relation to the existing literature on interactions in quantum Hall systems and compare our system and our results to a selection of similar works. The interactions in our ladder geometry are infinite-ranged along the synthetic dimension with special unitary group (SU($\mathcal{N}$)) symmetry. The effect of these interactions has been actively studied in several works. For fermions, intriguing gapped states have been proposed in the presence of magnetic flux, featuring

fractional filling and charge and/or spin order [9]. Additionally, edge physics [8, 85, 174], fractional pumping [11, 175], Creutz–Hubbard models [176], and exotic bound states [177, 178] have also been studied. For bosons, charge density wave states, 1D Haldane phases, and other exotic phases have been identified [179–183]. However, these works still lack experimental evidence in various scenarios.

In Ref. [184] the authors investigate the dynamics of interacting fermions under spin-orbit coupling with an optical lattice clock. While their system is similar to ours, there are several key distinctions. For example, they do not work in a three-dimensional lattice, thus, allowing transverse motion. Consequently, the atoms in their system experience p-wave interactions and are not limited to s-wave interactions. Furthermore, the authors do not work with a degenerate Fermi gas and do not prepare an eigenstate of the Harper-Hofstadter Hamiltonian. Due to these differences, a direct comparison of our data with the results in this reference is not possible.

In Ref. [185], the authors explored the Hall effect in quantum Hall ladders for both fermionic and bosonic cases with attractive and repulsive interactions. They identified an extensive parameter regime, in which the Hall imbalance exhibits universal behavior. This universality was experimentally confirmed in Ref. [165] for strongly repulsive interactions between fermions. However, a direct comparison between the results in these references and our results is not feasible, as their studies utilized a tilted ladder to measure the Hall imbalance, while our work is conducted without a tilt and relies on different observables.

In Ref. [186], the authors investigate resonant dynamics in strongly interacting SU(N) fermions in a synthetic flux ladder. They identify that the chiral currents in our system exhibit point symmetry with respect to the reversal of the coupling strength Ω_R, specifically $J(-\Omega_R/t_x) = -J(\Omega_R/t_x)$. The authors claim that under strong interactions, this symmetry is shifted from $\Omega_R/t_x = 0$ to $\Omega_R/t_x = U_{int}/t_x$. Additionally, they observe smaller resonances at fractions of U, such as $\Omega_R = U_{int}/2$, $U_{int}/3$, and so on. This behavior is explained by the fact, that the energy U_{int} required to create doublons can be derived from the energy difference Ω_R between the two dressed state bands, allowing for tunneling that is otherwise suppressed by U_{int}. The additional resonances are attributed to higher order (at least three-body) processes. If we derive predictions for our data based on the calculations presented in the referenced paper, we find the following. For the nearly non-interacting case $\left({}^{171}\mathrm{Yb}\right)$, we expect $\Delta J_{171} \approx 0.41$ at our ratio of $\Omega_R/t_x = 2.06(15)$, which agrees very well with our data for shallow lattice depths. For the interacting case, if $U_{int}/t_x > \Omega_R/t_x = 2$, the system should shift to the left of the original resonance. This shift would suggest a negative ΔJ_{173} that increases towards zero with increasing interaction strength. This is not consistent with our data. Furthermore, for the shallowest lattice depth at $U_{int}/t_x = 1.45$, we expect to remain on the right of the resonance, transitioning to the left as the interaction strength increases. This transition would imply a remarkable difference in the chiral current, including a sign reversal. However, this sign reversal is not observed in our measurements.

Our work is based on the scheme proposed in Ref. [85]. In this study, the authors employ DMRG simulations to analyze the impact of repulsive interactions on the emergence of chiral currents in a hybrid two- and three-leg Hall ribbon, similar to the one described in this thesis. The general result presented in the reference indicates that repulsive interactions are expected to significantly enhance the chiral currents for the filling factors considered in our experiments (i.e., less than one atom per lattice site and negligible population in the higher dressed band). However, the reference does not account for the influence of harmonic trapping confinement and finite-temperature effects. In addition, the authors of this reference calculated the behavior for a similar system, where they considered the effect of the harmonic confinement. In that case, they predict an approximately linear decrease in the chiral currents for increasing lattice depths [5, 6]. Our results show a suppression of the chiral currents for interactions in

comparison with the case of vanishingly small attractive interactions. However, an almost linear decrease is inconsistent with our findings.

In this chapter, we investigated how inter-particle interactions influence the formation of chiral edge currents in quantum Hall systems. We observed pronounced chiral currents that surpass those reported in comparable experimental studies (see Ref. [3–7]). In the regime of strong interactions, we observed a suppression of chiral currents and our data is consistent with two distinct interaction behaviors: a linear differential response and a constant relative suppression of the currents within the observed interaction regime. Additionally, our results hint at the potential existence of a dynamic region in the weakly repulsive regime.

To better understand and further study the interaction effects, it is crucial to eliminate or significantly reduce the harmonic confinement, as we observed its strong influence, which limits the reliability of our results. In the absence of harmonic confinement, it would be possible to gather similar data that could potentially lead to more conclusive findings. One approach to achieve this was demonstrated in Ref. [165], where the authors implemented an additional laser beam to create a double-well potential at an anti-trapping frequency of 1112 nm. The laser beam was directed perpendicular to the shallow lattice, placing the atoms between the double-well potential. In this setup, the harmonic confinement was reduced to a residual value of $0.01 t_x$ along the legs of the quantum Hall ladder.

In principle, interaction effects could also be investigated with an alkaline element, which has a magnetic Feshbach resonance to tune the interaction strength. The coherence time would not be as long as for alkaline earth (like) elements, but this might not be a limiting factor. However, the interactions would be different as they would not be SU(N) symmetric and spin-changing collisions are possible. These might also occur to "lost" spin states, which are not included in the synthetic dimension, if not all spin states are coupled in the quantum Hall ladder system.

Conclusion and Outlook

This thesis contributes to the field of quantum simulation by improving our understanding of interactions and topological properties in cold atom systems. The findings provide valuable insights into interactions in different scenarios and could aid in the investigation of *fractional* quantum Hall states [8–13]. In this context, gaining a deeper understanding of interactions may support the development of robust quantum information protocols [14].

We investigated how inter-particle interactions influence the formation of topologically protected chiral edge currents in quantum Hall ladder systems. The interactions are infinitely long-ranged along a synthetic dimension and confined to individual lattice sites along a shallow optical lattice. We observed pronounced chiral currents that surpass those reported in comparable experimental studies (see Ref. [3–7]) and closely match theoretical predictions in their momentum distributions. In the regime of strong interactions, we observed a suppression of chiral currents. Our data is consistent with two distinct interaction behaviors: a linear differential response and a constant relative suppression of the currents within the explored interaction regime. Additionally, our results hint at the potential existence of a dynamic region in the weakly repulsive regime.

We provided a comprehensive overview of the experimental realization of a quantum Hall ladder system, starting with the theoretical framework of the Harper-Hofstadter model and its implementation in cold atom systems using artificial gauge fields. We outlined the key steps for preparing and implementing quantum Hall ladders, confirming the system's successful realization through precise measurements of chiral edge currents. Additionally, this work offered valuable insights into practical challenges and strategies for improving experimental techniques, including advancements in spin detection, imaging, eigenstate preparation, and data analysis. During bandmapping and the eigenstate preparation, we observed previously unreported dynamics, which had a significant impact on the measurement of chiral currents. To gain deeper insights into these dynamics, a promising approach would be to capture images at various stages of the preparation ramp, rather than solely at its conclusion. This could reveal, what happens already over the course of the preparation. In addition, theoretical simulations of the expected pendulum dynamics could be computed and compared with the experimental data. This might enable a partial reconstruction of the initial chiral currents. As an alternative strategy, it would be possible to implement countermeasures for the harmonic confinement induced by the lattice beams. This was for example implemented for a similar system in Ref. [165] with an additional laser beam, which creates a double-well potential at an anti-trapping wavelength of (1112 nm). The laser beam is shone onto the atoms from a direction perpendicular to the shallow lattice, such that the atoms are between the double-well potential. In this reference, the harmonic confinement along the quantum Hall ladder's legs could be compensated to a residual value of $0.01t_x$.

Moreover, we measured interactions in ytterbium Fermi gases using clock spectroscopy. On the one hand, we examined interisotope interorbital interactions in mixtures of ^{171}Yb and ^{173}Yb, and, on the other hand, spin-exchange interactions of ^{171}Yb. We determined the elastic scattering lengths as ${}^{171}_{173}a_{\mathrm{eg}} = 497.4(8)a_0$ and ${}^{171}_{173}a_{\mathrm{ge}} = 482(1)a_0$ and proofed their SU(2) $\otimes$ SU(6) symmetry. While these values are similar, their significant difference offers a fascinating subject for theoretical studies, as it cannot be attributed to mass scaling. Despite the similarity of the elastic interactions, measurements of the inelastic decay coefficients showed strong contrasts, with ${}^{171}_{173}\beta_{\mathrm{eg}}$ being roughly 400 times stronger than ${}^{171}_{173}\beta_{\mathrm{ge}}$. This suggests that mixtures of $^{171}\mathrm{Yb_g}$ and $^{173}\mathrm{Yb_e}$ are more promising for quantum simulations. For the

spin-exchange interactions of ^{171}Yb, we determined scattering lengths of $a_{\mathrm{eg}^+} = 203(5)a_0$ and $a_{\mathrm{eg}^-} = 308(6)a_0$. These interorbital spin-exchange interactions in ^{171}Yb were also analyzed in Ref. [58, 59]. All three sets of measurements indicate an antiferromagnetic spin-exchange interaction with $V_{\mathrm{ex}} < 0$ and are showing qualitative agreement as the values are within the same order of magnitude. Quantitatively, however, the results differ significantly. The cause of the discrepancies between the results remains uncertain. The observed moderate antiferromagnetic spin-exchange interactions, combined with the very weak ground-state interactions, position ^{171}Yb as a strong candidate for simulating the Kondo lattice model [1, 2]. Moreover, our precise clock spectroscopy of interorbital interactions in ^{171}Yb gases and ^{171}Yb-^{173}Yb mixtures deepens our understanding of interorbital scattering behavior and lays a foundation for future research.

Bibliography

[1] A. V. Gorshkov, M. Hermele, V. Gurarie, C. Xu, P. S. Julienne, J. Ye, P. Zoller, E. Demler, M. D. Lukin, and A. M. Rey. "Two-orbital S U(N) magnetism with ultracold alkaline-earth atoms". In: *Nature Physics* 6 (4 Apr. 2010), pp. 289–295. ISSN: 1745-2473. DOI: 10.1038/nphys1535 (cit. on pp. iii, v, 2, 6, 28, 34, 96).

[2] M. Foss-Feig, M. Hermele, and A. M. Rey. "Probing the Kondo lattice model with alkaline-earth-metal atoms". In: *Physical Review A* 81 (5 May 2010), p. 051603. ISSN: 1050-2947. DOI: 10.1103/PhysRevA.81.051603 (cit. on pp. iii, v, 2, 28, 34, 96).

[3] M Mancini, G Pagano, G Cappellini, L Livi, M Rider, J Catani, C Sias, P Zoller, M Inguscio, M Dalmonte, and L Fallani. "Observation of chiral edge states with neutral fermions in synthetic Hall ribbons". In: *Science* 349 (6255 Sept. 2015), pp. 1510–1513. ISSN: 0036-8075. DOI: 10.1126/science.aaa8736 (cit. on pp. iii, v, 2, 35, 43, 47, 52, 66, 78, 84, 86, 94, 95).

[4] L. Livi, G. Cappellini, M. Diem, L. Franchi, C. Clivati, M. Frittelli, F. Levi, D. Calonico, J. Catani, M. Inguscio, and L. Fallani. "Synthetic Dimensions and Spin-Orbit Coupling with an Optical Clock Transition". In: *Physical Review Letters* 117 (22 Nov. 2016), p. 220401. ISSN: 0031-9007. DOI: 10.1103/PhysRevLett.117.220401 (cit. on pp. iii, v, 2, 35, 43, 44, 47, 57, 66, 78, 84, 86, 94, 95).

[5] L. F. Livi. "New quantum simulations with ultracold Ytterbium gases". In: *PhD thesis* (2017) (cit. on pp. iii, v, 38, 45, 60, 61, 74, 78, 84, 86, 93–95).

[6] M. Diem. "Synthetic Gauge Field and Spin-Orbit Coupling Studies with Ytterbium Atoms". In: *Master thesis* (2017) (cit. on pp. iii, v, 60, 61, 74, 78, 84, 86, 93–95).

[7] J. H. Kang, J. H. Han, and Y Shin. "Realization of a Cross-Linked Chiral Ladder with Neutral Fermions in a 1D Optical Lattice by Orbital-Momentum Coupling". In: *Physical Review Letters* 121 (15 2018), p. 150403. ISSN: 1079-7114. DOI: 10.1103/PhysRevLett.121.150403 (cit. on pp. iii, v, 2, 35, 43, 47, 52, 78, 84, 86, 94, 95).

[8] E. Cornfeld and E. Sela. "Chiral currents in one-dimensional fractional quantum Hall states". In: *Physical Review B* 92 (11 Sept. 2015), p. 115446. ISSN: 1098-0121. DOI: 10.1103/PhysRevB.92.115446 (cit. on pp. iii, v, 37, 93, 95).

[9] S. Barbarino, L. Taddia, D. Rossini, R. Fazio, and L. Mazza. "Magnetic crystals and helical liquids in alkaline-earth fermionic gases". In: *Nat. Commun.* 6 (2015), pp. 1–9. ISSN: 2041-1723. DOI: 10.1038/ncomms9134 (cit. on pp. iii, v, 37, 93, 95).

[10] M. C. Strinati, E. Cornfeld, D. Rossini, S. Barbarino, M. Dalmonte, R. Fazio, E. Sela, and L. Mazza. "Laughlin-like States in Bosonic and Fermionic Atomic Synthetic Ladders". In: *Physical Review X* 7 (2 June 2017), p. 021033. ISSN: 2160-3308. DOI: 10.1103/PhysRevX.7.021033 (cit. on pp. iii, v, 37, 95).

[11] L. Taddia, E. Cornfeld, D. Rossini, L. Mazza, E. Sela, and R. Fazio. "Topological Fractional Pumping with Alkaline-Earth-Like Atoms in Synthetic Lattices". In: *Physical Review Letters* 118 (23 June 2017), p. 230402. ISSN: 0031-9007. DOI: 10.1103/PhysRevLett.118.230402 (cit. on pp. iii, v, 37, 93, 95).

[12] A. Petrescu and K. L. Hur. "Chiral Mott insulators, Meissner effect, and Laughlin states in quantum ladders". In: *Physical Review B* 91 (5 Feb. 2015), p. 054520. ISSN: 1098-0121. DOI: 10.1103/PhysRevB.91.054520 (cit. on pp. iii, v, 37, 95).

[13] F. Grusdt and M. Höning. "Realization of fractional Chern insulators in the thin-torus limit with ultracold bosons". In: *Physical Review A* 90 (5 Nov. 2014), p. 053623. ISSN: 1050-2947. DOI: 10.1103/PhysRevA.90.053623 (cit. on pp. iii, v, 37, 95).

[14] C. Nayak, S. H. Simon, A. Stern, M. Freedman, and S. D. Sarma. "Non-Abelian anyons and topological quantum computation". In: *Reviews of Modern Physics* 80 (3 Sept. 2008), pp. 1083–1159. ISSN: 0034-6861. DOI: 10.1103/RevModPhys.80.1083 (cit. on pp. iii, v, 36, 37, 95).

[15] K. Sponselee, L. Freystatzky, B. Abeln, M. Diem, B. Hundt, A. Kochanke, T. Ponath, B. Santra, L. Mathey, K. Sengstock, and C. Becker. "Dynamics of ultracold quantum gases in the dissipative Fermi-Hubbard model". In: *Quantum Science and Technology* 4 (1 Jan. 2019). ISSN: 20589565. DOI: 10.1088/2058-9565/aadccd (cit. on pp. vi, 2).

[16] B. Abeln, K. Sponselee, M. Diem, N. Pintul, K. Sengstock, and C. Becker. "Interorbital interactions in an SU(2) - SU(6) -symmetric Fermi-Fermi mixture". In: *Physical Review A* 103 (3 2021), pp. 1–8. ISSN: 24699934. DOI: 10.1103/PhysRevA.103.033315 (cit. on pp. vi, 2, 19, 20, 22–25, 27, 30, 32–34).

[17] E. Altman et al. "Quantum Simulators: Architectures and Opportunities". In: *PRX Quantum* 2 (1 Jan. 2021). ISSN: 26913399. DOI: 10.1103/PRXQuantum.2.017003 (cit. on p. 1).

[18] *Nobelprize.org*. URL: https://www.nobelprize.org/, accessed on 08/08/2024. (Cit. on pp. 1, 36, 37).

[19] M. H. Anderson, J. R. Ensher, M. R. Matthews, C. E. Wieman, and E. A. Cornell. "Observation of Bose-Einstein Condensation in a Dilute Atomic Vapor". In: *Science* 269 (5221 July 1995), pp. 198–201. ISSN: 0036-8075. DOI: 10.1126/science.269.5221.198 (cit. on p. 1).

[20] K. B. Davis, M. O. Mewes, M. R. Andrews, N. J. V. Druten, D. S. Durfee, D. M. Kurn, and W. Ketterle. "Bose-Einstein condensation in a gas of sodium atoms". In: *Physical Review Letters* 75 (22 1995), pp. 3969–3973. ISSN: 00319007. DOI: 10.1103/PhysRevLett.75.3969 (cit. on p. 1).

[21] B. DeMarco and D. S. Jin. "Onset of Fermi Degeneracy in a Trapped Atomic Gas". In: *Science* 285 (5434 1999), pp. 1703–1706. ISSN: 00368075. DOI: 10.1126/science.285.5434.1703 (cit. on p. 1).

[22] A Görlitz, J. M. Vogels, A. E. Leanhardt, C Raman, T. L. Gustavson, J. R. Abo-Shaeer, A. P. Chikkatur, S Gupta, S Inouye, T Rosenband, and W Ketterle. "Realization of Bose-Einstein Condensates in Lower Dimensions". In: *Physical Review Letters* 87 (13 Sept. 2001), p. 130402. ISSN: 0031-9007. DOI: 10.1103/PhysRevLett.87.130402 (cit. on p. 1).

[23] C. Chin, R. Grimm, P. Julienne, and E. Tiesinga. "Feshbach resonances in ultracold gases". In: *Reviews of Modern Physics* 82 (2 Apr. 2010), pp. 1225–1286. ISSN: 0034-6861. DOI: 10.1103/RevModPhys.82.1225 (cit. on p. 1).

[24] M. P. A. Fisher, P. B. Weichman, G. Grinstein, and D. S. Fisher. "Boson localization and the superfluid-insulator transition". In: *Physical Review B* 40 (1 1989), pp. 546–570. ISSN: 01631829. DOI: 10.1103/PhysRevB.40.546 (cit. on p. 1).

[25] D Jaksch, C Bruder, J. I. Cirac, C. W. Gardiner, and P Zoller. "Cold bosonic atoms in optical lattices". In: *Physical Review Letters* 81 (15 1998), pp. 3108–3111. ISSN: 0031-9007. DOI: 10.1103/PhysRevLett.81.3108 (cit. on p. 1).

[26] M. Greiner, O. Mandel, T. Esslinger, T. W. Hänsch, and I. Bloch. "Quantum phase transition from a superfluid to a Mott insulator in a gas of ultracold atoms". In: *Nature* 415 (6867 2002), pp. 39–44. ISSN: 00280836. DOI: 10.1038/415039a (cit. on p. 1).

[27] M Bartenstein, A Altmeyer, S Riedl, S Jochim, C Chin, J. H. Denschlag, and R Grimm. "Crossover from a molecular Bose-Einstein condensate to a degenerate Fermi gas". In: *Physical Review Letters* 92 (12 2004), pp. 120401–1. ISSN: 00319007. DOI: 10.1103/PhysRevLett.92.120401 (cit. on p. 1).

[28] T Bourdel, L Khaykovich, J Cubizolles, J Zhang, F Chevy, M Teichmann, L Tarruell, S. J. J. M. F. Kokkelmans, and C Salomon. "Experimental study of the BEC-BCS crossover region in lithium 6". In: *Physical Review Letters* 93 (5 2004), pp. 3–6. ISSN: 00319007. DOI: 10.1103/PhysRevLett.93.050401 (cit. on p. 1).

[29] M. Greiner, C. A. Regal, and D. S. Jin. "Emergence of a molecular Bose–Einstein condensate from a Fermi gas". In: *Nature* 426 (6966 2003), pp. 537–540. ISSN: 0028-0836. DOI: 10.1038/nature02199 (cit. on p. 1).

[30] J Kinast, S. L. Hemmer, M. E. Gehm, A Turlapov, and J. E. Thomas. "Evidence for Superfluidity in a Resonantly Interacting Fermi Gas". In: *Physical Review Letters* 92 (15 Apr. 2004), p. 150402. ISSN: 0031-9007. DOI: 10.1103/PhysRevLett.92.150402 (cit. on p. 1).

[31] M. W. Zwierlein, C. A. Stan, C. H. Schunck, S. M. F. Raupach, A. J. Kerman, and W Ketterle. "Condensation of pairs of fermionic atoms near a Feshbach resonance". In: *Physical Review Letters* 92 (12 2004), pp. 120403–1. ISSN: 00319007. DOI: 10.1103/PhysRevLett.92.120403 (cit. on p. 1).

[32] D. Jaksch and P. Zoller. "Creation of effective magnetic fields in optical lattices: The Hofstadter butterfly for cold neutral atoms". In: *New Journal of Physics* 5 (2003). ISSN: 13672630. DOI: 10.1088/1367-2630/5/1/356 (cit. on pp. 1, 43).

[33] G. Juzeliūnas, J. Ruseckas, P. Öhberg, and M. Fleischhauer. "Light-induced effective magnetic fields for ultracold atoms in planar geometries". In: *Physical Review A* 73 (2 Feb. 2006), p. 025602. ISSN: 1050-2947. DOI: 10.1103/PhysRevA.73.025602 (cit. on p. 1).

[34] J. Dalibard, F. Gerbier, G. Juzeliunas, and P. Öhberg. "Colloquium: Artificial gauge potentials for neutral atoms". In: *Reviews of Modern Physics* 83 (4 2011), pp. 1523–1543. ISSN: 00346861. DOI: 10.1103/RevModPhys.83.1523 (cit. on pp. 1, 37–40, 43).

[35] Y.-J. Lin, R. L. Compton, K Jiménez-García, J. V. Porto, and I. B. Spielman. "Synthetic magnetic fields for ultracold neutral atoms." In: *Nature* 462 (7273 2009), pp. 628–32. ISSN: 1476-4687. DOI: 10.1038/nature08609 (cit. on p. 1).

[36] H. Miyake, G. A. Siviloglou, C. J. Kennedy, W. C. Burton, and W. Ketterle. "Realizing the harper hamiltonian with laser-assisted tunneling in optical lattices". In: *Physical Review Letters* 111 (18 2013), pp. 1–5. ISSN: 00319007. DOI: 10.1103/PhysRevLett.111.185302 (cit. on pp. 1, 2, 35, 43).

[37] A. R. Kolovsky. "Creating artificial magnetic fields for cold atoms by photon-assisted tunneling". In: *EPL (Europhysics Letters)* 93 (2 Jan. 2011), p. 20003. ISSN: 0295-5075. DOI: 10.1209/0295-5075/93/20003 (cit. on pp. 1, 2, 43).

[38] A. Eckardt, P. Hauke, P. Soltan-Panahi, C. Becker, K. Sengstock, and M. Lewenstein. "Frustrated quantum antiferromagnetism with ultracold bosons in a triangular lattice". In: *EPL (Europhysics Letters)* 89 (1 Jan. 2010), p. 10010. ISSN: 0295-5075. DOI: 10.1209/0295-5075/89/10010 (cit. on pp. 1, 2, 43).

[39] A. Hemmerich. "Effective time-independent description of optical lattices with periodic driving". In: *Physical Review A* 81 (6 June 2010), p. 063626. ISSN: 1050-2947. DOI: 10.1103/PhysRevA.81.063626 (cit. on pp. 1, 2, 43).

[40] J. Struck, C. Ölschläger, M. Weinberg, P. Hauke, J. Simonet, A. Eckardt, M. Lewenstein, K. Sengstock, and P. Windpassinger. "Tunable Gauge Potential for Neutral and Spinless Particles in Driven Optical Lattices". In: *Physical Review Letters* 108 (22 May 2012), p. 225304. ISSN: 0031-9007. DOI: 10.1103/PhysRevLett.108.225304 (cit. on pp. 1, 2, 43).

[41] J. Struck, M. Weinberg, C. Ölschläger, P. Windpassinger, J. Simonet, K. Sengstock, R. Höppner, P. Hauke, a. Eckardt, M. Lewenstein, and L. Mathey. "Engineering Ising-XY spin-models in a triangular lattice using tunable artificial gauge fields". In: *Nature Physics* 9 (September 2013), pp. 738–743. ISSN: 1745-2473. DOI: 10.1038/nphys2750 (cit. on pp. 1, 2, 43).

[42] A. Mazurenko, C. S. Chiu, G. Ji, M. F. Parsons, M. Kanász-Nagy, R. Schmidt, F. Grusdt, E. Demler, D. Greif, and M. Greiner. "A cold-atom Fermi-Hubbard antiferromagnet". In: *Nature* 545 (7655 May 2017), pp. 462–466. ISSN: 14764687. DOI: 10.1038/nature22362 (cit. on p. 1).

[43] L. Asteria, H. P. Zahn, M. N. Kosch, K. Sengstock, and C. Weitenberg. "Quantum gas magnifier for sub-lattice-resolved imaging of 3D quantum systems". In: *Nature* 599 (7886 Nov. 2021), pp. 571–575. ISSN: 14764687. DOI: 10.1038/s41586-021-04011-2 (cit. on p. 1).

[44] M. Endres, H. Bernien, A. Keesling, H. Levine, E. R. Anschuetz, A. Krajenbrink, C. Senko, V. Vuletic, M. Greiner, and M. D. Lukin. "Atom-by-atom assembly of defect-free one-dimensional cold atom arrays". In: *Science* 354 (6315 Nov. 2016), pp. 1024–1027. ISSN: 0036-8075. DOI: 10.1126/science.aah3752 (cit. on p. 1).

[45] D. Barredo, S. D. Léséleuc, V. Lienhard, T. Lahaye, and A. Browaeys. "An atom-by-atom assembler of defect-free arbitrary two-dimensional atomic arrays". In: *Science* 354 (6315 Nov. 2016), pp. 1021–1023. ISSN: 10959203. DOI: 10.1126/science.aah3778 (cit. on p. 1).

[46] A. Omran, H. Levine, A. Keesling, G. Semeghini, T. T. Wang, S. Ebadi, H. Bernien, A. S. Zibrov, H. Pichler, S. Choi, J. Cui, M. Rossignolo, P. Rembold, S. Montangero, T. Calarco, M. Endres, M. Greiner, V. Vuletić, and M. D. Lukin. "Generation and manipulation of Schrödinger cat states in Rydberg atom arrays". In: *Science* 365 (6453 Aug. 2019), pp. 570–574. ISSN: 0036-8075. DOI: 10.1126/science.aax9743 (cit. on p. 1).

[47] S. de Léséleuc, V. Lienhard, P. Scholl, D. Barredo, S. Weber, N. Lang, H. P. Büchler, T. Lahaye, and A. Browaeys. "Observation of a symmetry-protected topological phase of interacting bosons with Rydberg atoms". In: *Science* 365 (6455 Aug. 2019), pp. 775–780. ISSN: 0036-8075. DOI: 10.1126/science.aav9105 (cit. on p. 1).

[48] G. Semeghini, H. Levine, A. Keesling, S. Ebadi, T. T. Wang, D. Bluvstein, R. Verresen, H. Pichler, M. Kalinowski, R. Samajdar, A. Omran, S. Sachdev, A. Vishwanath, M. Greiner, V. Vuletić, and M. D. Lukin. "Probing topological spin liquids on a programmable quantum simulator". In: *Science* 374 (6572 Dec. 2021), pp. 1242–1247. ISSN: 0036-8075. DOI: 10.1126/science.abi8794 (cit. on p. 1).

[49] S. G. Porsev and A. Derevianko. "Hyperfine quenching of the metastable3P0,2 states in divalent atoms". In: *Physical Review A - Atomic, Molecular, and Optical Physics* 69 (4 2004), pp. 042506–1. ISSN: 10502947. DOI: 10.1103/PhysRevA.69.042506 (cit. on p. 2).

[50] A. D. Ludlow, M. M. Boyd, J. Ye, E. Peik, and P. O. Schmidt. "Optical atomic clocks". In: *Reviews of Modern Physics* 87 (2 June 2015). ISSN: 15390756. DOI: 10.1103/RevModPhys.87.637 (cit. on p. 2).

[51] N Hinkley, J. A. Sherman, N. B. Phillips, M Schioppo, N. D. Lemke, K Beloy, M Pizzocaro, C. W. Oates, and A. D. Ludlow. "An Atomic Clock with 10–18 Instability". In: *Science* 341 (6151 2013), pp. 1215–1218. ISSN: 0036-8075. DOI: 10.1126/science.1240420 (cit. on pp. 2, 6).

[52] B. J. Bloom, T. L. Nicholson, J. R. Williams, S. L. Campbell, M. Bishof, X. Zhang, W. Zhang, S. L. Bromley, and J. Ye. "An optical lattice clock with accuracy and stability at the 10-18 level". In: *Nature* 506 (7486 2014), pp. 71–75. ISSN: 00280836. DOI: 10.1038/nature12941 (cit. on p. 2).

[53] F Scazza, C Hofrichter, M Höfer, P. C. D. Groot, I. Bloch, and S. Fölling. "Observation of two-orbital spin-exchange interactions with ultracold SU(N)-symmetric fermions". In: *Nature Physics* 10 (10 2014), pp. 779–784. ISSN: 1745-2473. DOI: 10.1038/nphys3061 (cit. on pp. 2, 19, 28).

[54] G. Cappellini, M. Mancini, G. Pagano, P. Lombardi, L. Livi, M. S. D. Cumis, P. Cancio, M. Pizzocaro, D. Calonico, F. Levi, C. Sias, J. Catani, M. Inguscio, and L. Fallani. "Direct observation of coherent interorbital spin-exchange dynamics". In: *Physical Review Letters* 113 (12 2014), pp. 1–5. ISSN: 10797114. DOI: 10.1103/PhysRevLett.113.120402 (cit. on pp. 2, 19, 28).

[55] X. Zhang, M. Bishof, S. L. Bromley, C. V. Kraus, M. S. Safronova, P. Zoller, A. M. Rey, and J. Ye. "Spectroscopic observation of SU(N)-symmetric interactions in Sr orbital magnetism". In: *Science* 345 (6203 Sept. 2014), pp. 1467–1473. ISSN: 0036-8075. DOI: 10.1126/science.1254978 (cit. on pp. 2, 19, 28).

[56] R Bouganne, M. B. Aguilera, A Dareau, E Soave, J Beugnon, and F Gerbier. "Clock spectroscopy of interacting bosons in deep optical lattices". In: *New Journal of Physics* 19 (11 Nov. 2017), p. 113006. ISSN: 1367-2630. DOI: 10.1088/1367-2630/aa8c45 (cit. on pp. 2, 19).

[57] A. Goban, R. B. Hutson, G. E. Marti, S. L. Campbell, M. A. Perlin, P. S. Julienne, J. P. D'Incao, A. M. Rey, and J. Ye. "Emergence of multi-body interactions in a fermionic lattice clock". In: *Nature* 563 (7731 Nov. 2018), pp. 369–373. ISSN: 0028-0836. DOI: 10.1038/s41586-018-0661-6 (cit. on pp. 2, 19, 24, 25).

[58] K. Ono, J. Kobayashi, Y. Amano, K. Sato, and Y. Takahashi. "Antiferromagnetic interorbital spin-exchange interaction of 171Yb". In: *Physical Review A* 99 (3 Mar. 2019), p. 032707. ISSN: 2469-9926. DOI: 10.1103/PhysRevA.99.032707 (cit. on pp. 2, 19, 28, 32, 34, 96).

[59] O. Bettermann, N. D. Oppong, G. Pasqualetti, L. Riegger, I. Bloch, and S. Fölling. "Clock-line photoassociation of strongly bound dimers in a magic-wavelength lattice". In: *arXiv preprint* (Mar. 2020). DOI: 10.48550/arXiv.2003.10599 (cit. on pp. 2, 19, 28, 31, 32, 34, 96).

[60] L Franchi, L. F. Livi, G Cappellini, G Binella, M Inguscio, J Catani, and L Fallani. "State-dependent interactions in ultracold". In: *New J. Phys* 19 (2017), p. 103037. URL: http://iopscience.iop.org/article/10.1088/1367-2630/aa8fb4/pdf, accessed on 08/08/2024. (Cit. on pp. 2, 19).

[61] T. Tomita, S. Nakajima, Y. Takasu, and Y. Takahashi. "Dissipative Bose-Hubbard system with intrinsic two-body loss". In: *Physical Review A* 99 (3 Mar. 2019), p. 031601. ISSN: 2469-9926. DOI: 10.1103/PhysRevA.99.031601 (cit. on p. 2).

[62] M. Foss-Feig, A. J. Daley, J. K. Thompson, and A. M. Rey. "Steady-state many-body entanglement of hot reactive fermions". In: *Physical Review Letters* 109 (23 2012), pp. 1–5. ISSN: 00319007. DOI: 10.1103/PhysRevLett.109.230501 (cit. on p. 2).

[63] A. Eckardt, C. Weiss, and M. Holthaus. "Superfluid-insulator transition in a periodically driven optical lattice". In: *Physical Review Letters* 95 (26 2005). ISSN: 00319007. DOI: 10.1103/PhysRevLett.95.260404 (cit. on pp. 2, 43).

[64] J Struck, J Simonet, and K Sengstock. "Spin-orbit coupling in periodically driven optical lattices". In: *Physical Review A* 90 (3 Sept. 2014), p. 031601. ISSN: 1050-2947. DOI: 10.1103/PhysRevA.90.031601 (cit. on pp. 2, 43).

[65] O. Boada, A. Celi, J. I. Latorre, and M. Lewenstein. "Quantum simulation of an extra dimension". In: *Physical Review Letters* 108 (13 2012), pp. 2–7. ISSN: 00319007. DOI: 10.1103/PhysRevLett.108.133001 (cit. on pp. 2, 43).

[66] B. K. Stuhl, H. I Lu, L. M. Aycock, D. Genkina, and I. B. Spielman. "Visualizing edge states with an atomic Bose gas in the quantum Hall regime". In: *Science* 349 (6255 Sept. 2015), pp. 1514–1518. ISSN: 0036-8075. DOI: 10.1126/science.aaa8515 (cit. on pp. 2, 35, 43).

[67] S. Kolkowitz, S. L. Bromley, T. Bothwell, M. L. Wall, G. E. Marti, A. P. Koller, X. Zhang, A. M. Rey, and J. Ye. "Spin–orbit-coupled fermions in an optical lattice clock". In: *Nature* 542 (7639 Feb. 2017), pp. 66–70. ISSN: 0028-0836. DOI: 10.1038/nature20811 (cit. on pp. 2, 35, 43, 44).

[68] M. Aidelsburger, M. Atala, M. Lohse, J. T. Barreiro, B. Paredes, and I. Bloch. "Realization of the hofstadter hamiltonian with ultracold atoms in optical lattices". In: *Physical Review Letters* 111 (18 2013), pp. 1–5. ISSN: 00319007. DOI: 10.1103/PhysRevLett.111.185301 (cit. on pp. 2, 35).

[69] T. Chalopin, T. Satoor, A. Evrard, V. Makhalov, J. Dalibard, R. Lopes, and S. Nascimbene. "Probing chiral edge dynamics and bulk topology of a synthetic Hall system". In: *Nature Physics* 16 (10 Oct. 2020), pp. 1017–1021. ISSN: 17452481. DOI: 10.1038/s41567-020-0942-5 (cit. on pp. 2, 35, 44).

[70] J.-B. Bouhiron, A. Fabre, Q. Liu, Q. Redon, N. Mittal, T. Satoor, R. Lopes, and S. Nascimbene. "Realization of an atomic quantum Hall system in four dimensions". In: *Science* 384 (6692 Apr. 2024), pp. 223–227. ISSN: 0036-8075. DOI: 10.1126/science.adf8459 (cit. on pp. 2, 35).

[71] J. H. Han, J. H. Kang, and Y. Shin. "Band Gap Closing in a Synthetic Hall Tube of Neutral Fermions". In: *Physical Review Letters* 122 (6 Feb. 2019), p. 065303. ISSN: 0031-9007. DOI: 10.1103/PhysRevLett.122.065303 (cit. on pp. 2, 35, 52).

[72] P. W. Anderson. *Basic Notions of Condensed Matter Physics*. Westview Press, 1997. ISBN: 0201328305, 9780201328301 (cit. on pp. 2, 36).

[73] N. Goldman, J. C. Budich, and P. Zoller. "Topological quantum matter with ultracold gases in optical lattices". In: *Nature Physics* 12 (7 2016), pp. 639–645. ISSN: 1745-2473. DOI: 10.1038/nphys3803 (cit. on p. 2).

[74] C. L. Kane and E. J. Mele. "Z2 topological order and the quantum spin hall effect". In: *Physical Review Letters* 95 (14 2005). ISSN: 00319007. DOI: 10.1103/PhysRevLett.95.146802 (cit. on pp. 2, 35).

[75] M. Z. Hasan and C. L. Kane. "Colloquium: Topological insulators". In: *Reviews of Modern Physics* 82 (4 2010), pp. 3045–3067. ISSN: 00346861. DOI: 10.1103/RevModPhys.82.3045 (cit. on pp. 2, 35, 40, 45).

[76] J. E. Moore. "The birth of topological insulators." In: *Nature* 464 (7286 2010), pp. 194–8. ISSN: 1476-4687. DOI: 10.1038/nature08916 (cit. on p. 2).

[77] B. Gadway. "Atom-optics approach to studying transport phenomena". In: *Physical Review A - Atomic, Molecular, and Optical Physics* 92 (4 2015), pp. 1–9. ISSN: 10941622. DOI: 10.1103/PhysRevA.92.043606 (cit. on pp. 2, 43, 85).

[78] H. M. Price, T. Ozawa, and N. Goldman. "Synthetic dimensions for cold atoms from shaking a harmonic trap". In: 023607 (2017), pp. 1–17. DOI: 10.1103/PhysRevA.95.023607 (cit. on pp. 2, 43, 85).

[79] X. Li, E. Zhao, and W. V. Liu. "Topological states in a ladder-like optical lattice containing ultracold atoms in higher orbital bands". In: *Nature Communications* 4 (1 Feb. 2013), p. 1523. ISSN: 2041-1723. DOI: 10.1038/ncomms2523 (cit. on pp. 2, 43).

[80] S.-L. Zhang and Q. Zhou. "Shaping topological properties of the band structures in a shaken optical lattice". In: *Physical Review A* 90 (5 Nov. 2014), p. 051601. ISSN: 1050-2947. DOI: 10.1103/PhysRevA.90.051601 (cit. on pp. 2, 43).

[81] M. A. Khamehchi, C. Qu, M. E. Mossman, C. Zhang, and P. Engels. "Spin-momentum coupled Bose-Einstein condensates with lattice band pseudospins". In: *Nature Communications* 7 (1 Feb. 2016), p. 10867. ISSN: 2041-1723. DOI: 10.1038/ncomms10867 (cit. on pp. 2, 43).

[82] M. L. Wall, A. P. Koller, S. Li, X. Zhang, N. R. Cooper, J. Ye, and A. M. Rey. "Synthetic Spin-Orbit Coupling in an Optical Lattice Clock". In: *Physical Review Letters* 116 (3 2016), pp. 1–6. ISSN: 10797114. DOI: 10.1103/PhysRevLett.116.035301 (cit. on pp. 2, 43).

[83] O. Boada, A. Celi, J. Rodríguez-Laguna, J. I. Latorre, and M. Lewenstein. "Quantum simulation of non-trivial topology". In: *New Journal of Physics* 17 (4 Apr. 2015), p. 045007. ISSN: 1367-2630. DOI: 10.1088/1367-2630/17/4/045007 (cit. on p. 2).

[84] H. M. Price, O. Zilberberg, T. Ozawa, I. Carusotto, and N. Goldman. "Four-Dimensional Quantum Hall Effect with Ultracold Atoms". In: *Physical Review Letters* 115 (19 2015), pp. 1–6. ISSN: 10797114. DOI: 10.1103/PhysRevLett.115.195303 (cit. on p. 2).

[85] S. Barbarino, L. Taddia, D. Rossini, L. Mazza, and R. Fazio. "Synthetic gauge fields in synthetic dimensions: interactions and chiral edge modes". In: *New Journal of Physics* 18 (3 Mar. 2016), p. 035010. ISSN: 1367-2630. DOI: 10.1088/1367-2630/18/3/035010 (cit. on pp. 2, 69, 93).

[86] K.-K. Ni, S. Ospelkaus, M. H. G. de Miranda, A. Pe'er, B. Neyenhuis, J. J. Zirbel, S. Kotochigova, P. S. Julienne, D. S. Jin, and J. Ye. "A High Phase-Space-Density Gas of Polar Molecules". In: *Science* 322 (5899 Oct. 2008), pp. 231–235. ISSN: 0036-8075. DOI: 10.1126/science.1163861 (cit. on p. 2).

[87] A. Griesmaier, J. Werner, S. Hensler, J. Stuhler, and T. Pfau. "Bose-Einstein condensation of chromium". In: *Physical Review Letters* 94 (16 Apr. 2005). ISSN: 00319007. DOI: 10.1103/PhysRevLett.94.160401 (cit. on p. 2).

[88] M. Lu, N. Q. Burdick, S. H. Youn, and B. L. Lev. "Strongly dipolar Bose-Einstein condensate of dysprosium". In: *Physical Review Letters* 107 (19 Oct. 2011). ISSN: 00319007. DOI: 10.1103/PhysRevLett.107.190401 (cit. on p. 2).

[89] K. Aikawa, A. Frisch, M. Mark, S. Baier, A. Rietzler, R. Grimm, and F. Ferlaino. "Bose-Einstein condensation of erbium". In: *Physical Review Letters* 108 (21 May 2012). ISSN: 00319007. DOI: 10.1103/PhysRevLett.108.210401 (cit. on p. 2).

[90] H. Metcalf and P. V. der Straten. *Laser Cooling and Trapping*. Springer Science & Business Media, 1999 (cit. on pp. 5, 12).

[91] P. V. der Straten and H. Metcalf. *Atoms and Molecules Interacting with Light: Atomic Physics for the Laser Era*. Cambridge University Press, 2016. ISBN: 978-1-107-09014-9 (cit. on pp. 5, 8–10, 45, 46).

[92] W. Ketterle, D. S. Durfee, and D. M. Stamper-Kurn. "Making, probing and understanding Bose-Einstein condensates". In: *arXiv preprint* (1999). DOI: 10.48550/arXiv.cond-mat/9904034 (cit. on pp. 5, 15).

[93] N. W. Ashcroft and N. D. Mermin. *Solid State Physics*. Saunders College, 1976 (cit. on pp. 5, 13, 14).

[94] S. E. Dörscher. "Creation of ytterbium quantum gases with a compact 2D-/3D-MOT setup". In: *PhD thesis* (2013) (cit. on pp. 5, 7, 10, 69).

[95] A. Thobe. "Ultracold Yb Gases with Control over Spin and Orbital Degrees of Freedom". In: *PhD thesis* (2014) (cit. on pp. 5, 7, 12, 16, 28, 69).

[96] B. Hundt. "Optical Potentials for the Realization of Dissipative Fermi-Hubbard Models with Ultracold Ytterbium Atoms". In: *PhD thesis* (2016) (cit. on pp. 5, 7).

[97] A. Kochanke. "Towards Quantum Simulation of the Kondo-Lattice-Model Dissertation". In: *PhD thesis* (2017) (cit. on pp. 5, 7, 16, 17, 69).

[98] T. Ponath. "Probing Ytterbium Quantum Gases in an Optical Lattice using the Clock Transition". In: *PhD thesis* (2018). URL: http://ediss.sub.uni-hamburg.de/volltexte/2018/9242/pdf/Dissertation.pdf, accessed on 08/08/2024. (Cit. on pp. 5, 7, 12).

[99] K. C. Sponselee. "Lattice Clock Experiments with Interacting Fermionic Quantum Gases". In: *PhD thesis* (2021) (cit. on pp. 5, 8, 19, 26, 32).

[100] B. Abeln. "Probing Interactions in Ytterbium Fermi Gases and Mixtures Using the Optical Clock Transition". In: *PhD thesis* (2021) (cit. on pp. 5, 6, 8, 9, 12, 13, 15, 17, 19, 21, 28–30, 32, 55, 69).

[101] J. Meija, T. B. Coplen, M. Berglund, W. A. Brand, P. D. Bièvre, M. Gröning, N. E. Holden, J. Irrgeher, R. D. Loss, T. Walczyk, and T. Prohaska. "Isotopic compositions of the elements 2013 (IUPAC Technical Report)". In: *Pure and Applied Chemistry* 88 (3 Mar. 2016), pp. 293–306. ISSN: 1365-3075. DOI: 10.1515/pac-2015-0503 (cit. on p. 5).

[102] M. M. Boyd, T. Zelevinsky, A. D. Ludlow, S. Blatt, T. Zanon-Willette, S. M. Foreman, and J. Ye. "Nuclear spin effects in optical lattice clocks". In: *Physical Review A* 76 (022510 2007). ISSN: 10502947. DOI: 10.1103/PhysRevA.76.022510 (cit. on p. 6).

[103] C. W. Hoyt, Z. W. Barber, C. W. Oates, T. M. Fortier, S. A. Diddams, and L. Hollberg. "Observation and absolute frequency measurements of the S01-P03 optical clock transition in neutral ytterbium". In: *Physical Review Letters* 95 (8 2005), pp. 1–4. ISSN: 00319007. DOI: 10.1103/PhysRevLett.95.083003 (cit. on p. 6).

[104] M. Inguscio and L. Fallani. *Atomic Physics: Precise Measurements and Ultracold Matter*. 2013, p. 349. ISBN: 9780198525844. DOI: 10.1080/00107514.2014.910274 (cit. on pp. 6, 14).

[105] M. Kitagawa, K. Enomoto, K. Kasa, Y. Takahashi, R. Ciuryło, P. Naidon, and P. S. Julienne. "Two-color photoassociation spectroscopy of ytterbium atoms and the precise determinations of s -wave scattering lengths". In: *Physical Review A - Atomic, Molecular, and Optical Physics* 77 (1 2008), pp. 1–8. ISSN: 10502947. DOI: 10.1103/PhysRevA.77.012719 (cit. on pp. 7, 26, 28, 32).

[106] M. A. Cazalilla and A. M. Rey. "Ultracold fermi gases with emergent SU(N) symmetry". In: *Reports on Progress in Physics* 77 (12 2014). ISSN: 00344885. DOI: 10.1088/0034-4885/77/12/124401 (cit. on p. 6).

[107] M. A. Cazalilla, A. F. Ho, and M. Ueda. "Ultracold gases of ytterbium: Ferromagnetism and Mott states in an SU(6) Fermi system". In: *New Journal of Physics* 11 (Oct. 2009). ISSN: 13672630. DOI: 10.1088/1367-2630/11/10/103033 (cit. on p. 6).

[108] R. Zhang, Y. Cheng, H. Zhai, and P. Zhang. "Orbital Feshbach Resonance in Alkali-Earth Atoms". In: *Physical Review Letters* 115 (13 Sept. 2015), p. 135301. ISSN: 0031-9007. DOI: 10.1103/PhysRevLett.115.135301 (cit. on p. 7).

[109] M. Höfer, L. Riegger, F. Scazza, C. Hofrichter, D. Fernandes, M. Parish, J. Levinsen, I. Bloch, and S. Fölling. "Observation of an Orbital Interaction-Induced Feshbach Resonance in 173Yb". In: *Physical Review Letters* 115 (26 Dec. 2015), p. 265302. ISSN: 0031-9007. DOI: 10.1103/PhysRevLett.115.265302 (cit. on p. 7).

[110] G. Pagano, M. Mancini, G. Cappellini, L. Livi, C. Sias, J. Catani, M. Inguscio, and L. Fallani. "Strongly Interacting Gas of Two-Electron Fermions at an Orbital Feshbach Resonance". In: *Physical Review Letters* 115 (26 Dec. 2015), p. 265301. ISSN: 0031-9007. DOI: 10.1103/PhysRevLett.115.265301 (cit. on p. 7).

[111] E. D. Black. "An introduction to Pound–Drever–Hall laser frequency stabilization". In: *American Journal of Physics* 69 (1 2001), p. 79. ISSN: 00029505. DOI: 10.1119/1.1286663 (cit. on p. 9).

[112] J. Appel, A. MacRae, and A. I. Lvovsky. "A versatile digital GHz phase lock for external cavity diode lasers". In: *Measurement Science and Technology* 20 (5 May 2009), p. 055302. ISSN: 0957-0233. DOI: 10.1088/0957-0233/20/5/055302 (cit. on p. 9).

[113] U. Schünemann, H. Engler, R. Grimm, M. Weidemüller, and M. Zielonkowski. "Simple scheme for tunable frequency offset locking of two lasers". In: *Review of Scientific Instruments* 70 (1 Jan. 1999), pp. 242–243. ISSN: 0034-6748. DOI: 10.1063/1.1149573 (cit. on p. 9).

[114] B. Abeln. "Design, Implementation and Characterization of a new Laser System for Mixtures of Ytterbium Quantum Gases". In: *Master thesis* (November 2016) (cit. on pp. 10, 16, 17).

[115] F. Scazza. "Probing SU(N)-symmetric orbital interactions with ytterbium Fermi gases in optical lattices". In: *PhD thesis* (2015). URL: https://edoc.ub.uni-muenchen.de/18159/1/Scazza_Francesco.pdf, accessed on 08/08/2024. (Cit. on pp. 10, 11, 21, 28, 30, 69).

[116] L. Hilbig. "Artificial Gauge Fields and Synthetic Dimensions". In: *Master thesis* (2019) (cit. on pp. 11, 35, 38–42, 49, 51, 56, 57, 60–62, 77, 80).

[117] D. A. Steck. "Quantum and Atom Optics". In: *Book* (2007), p. 932. URL: http://steck.us/academic.html\nhttp://atomoptics.uoregon.edu/~dsteck/teaching/, accessed on 08/08/2024. (Cit. on pp. 12, 45, 46, 58, 62).

[118] S. G. Porsev, A. Derevianko, and E. N. Fortson. "Possibility of an optical clock using the [Formula Presented] transition in [Formula Presented] atoms held in an optical lattice". In: *Physical Review A - Atomic, Molecular, and Optical Physics* 69 (2 2004), p. 4. ISSN: 10941622. DOI: 10.1103/PhysRevA.69.021403 (cit. on p. 12).

[119] H. Katori, M. Takamoto, V. G. Pal'chikov, and V. D. Ovsiannikov. "Ultrastable Optical Clock with Neutral Atoms in an Engineered Light Shift Trap". In: *Physical Review Letters* 91 (17 Oct. 2003), p. 173005. ISSN: 0031-9007. DOI: 10.1103/PhysRevLett.91.173005 (cit. on pp. 12, 13).

[120] D. Wineland, C. Monroe, W. Itano, D. Leibfried, B. King, and D. Meekhof. "Experimental issues in coherent quantum-state manipulation of trapped atomic ions". In: *Journal of Research of the National Institute of Standards and Technology* 103 (3 May 1998), p. 259. ISSN: 1044677X. DOI: 10.6028/jres.103.019 (cit. on p. 12).

[121] D. Jaksch and P. Zoller. "The cold atom Hubbard toolbox". In: *Annals of Physics* 315 (1 Jan. 2005), pp. 52–79. ISSN: 0003-4916. DOI: 10.1016/J.AOP.2004.09.010 (cit. on pp. 13, 14).

[122] C. Becker. "Multi component Bose-Einstein condensates". In: *PhD thesis* (2008) (cit. on p. 13).

[123] W Kohn. *Analytic Properties of Bloch Waves and Wannier Functions**. Tech. rep. 1959 (cit. on p. 14).

[124] J. Hubbard. "Electron Correlations in Narrow Energy Bands". In: *Proceedings of the Royal Society A: Mathematical, Physical and Engineering Sciences* 276 (1365 Nov. 1963), pp. 238–257. ISSN: 1364-5021. DOI: 10.1098/rspa.1963.0204 (cit. on p. 14).

[125] T. Sobottke. "Design and realisation of a high-resolution imaging system for Ytterbium quantum gases". In: *Bachelor thesis* (2014) (cit. on p. 15).

[126] J. Heinze, S. Götze, J. S. Krauser, B. Hundt, N. Fläschner, D. S. Lühmann, C. Becker, and K. Sengstock. "Multiband spectroscopy of ultracold fermions: Observation of reduced tunneling in attractive Bose-Fermi mixtures". In: *Physical Review Letters* 107 (13 2011), pp. 21–25. ISSN: 00319007. DOI: 10.1103/PhysRevLett.107.135303 (cit. on pp. 15, 21).

[127] M. Greiner, I. Bloch, O. Mandel, T. W. Hänsch, and T. Esslinger. "Exploring Phase Coherence in a 2D Lattice of Bose-Einstein Condensates". In: *Physical Review Letters* 87 (16 Oct. 2001), p. 160405. ISSN: 0031-9007. DOI: 10.1103/PhysRevLett.87.160405 (cit. on p. 15).

[128] T. Sleator, T. Pfau, V. Balykin, O. Carnal, and J. Mlynek. "Experimental demonstration of the optical Stern-Gerlach effect". In: *Physical Review Letters* 68 (13 Mar. 1992), pp. 1996–1999. ISSN: 0031-9007. DOI: 10.1103/PhysRevLett.68.1996 (cit. on p. 15).

[129] S. Stellmer, R. Grimm, and F. Schreck. "Detection and manipulation of nuclear spin states in fermionic strontium". In: *Physical Review A* 84 (4 Oct. 2011), p. 043611. ISSN: 1050-2947. DOI: 10.1103/PhysRevA.84.043611 (cit. on p. 15).

[130] N. Pintul. "Ytterbium Fermi-Fermi Mixtures in Optical Lattices". In: *Master thesis* (2020) (cit. on p. 17).

[131] L. Lepori, A. Trombettoni, and W. Vinci. "Simulation of two-flavor symmetry-locking phases in ultracold fermionic mixtures". In: *EPL (Europhysics Letters)* 109 (5 Mar. 2015), p. 50002. ISSN: 0295-5075. DOI: 10.1209/0295-5075/109/50002 (cit. on p. 19).

[132] J. C. P. Barros, L. Lepori, and A. Trombettoni. "Phase diagram and non-Abelian symmetry locking for fermionic mixtures with unequal interactions". In: *Physical Review A* 96 (1 July 2017), p. 013603. ISSN: 2469-9926. DOI: 10.1103/PhysRevA.96.013603 (cit. on p. 19).

[133] N. D. Lemke, A. D. Ludlow, Z. W. Barber, T. M. Fortier, S. A. Diddams, Y. Jiang, S. R. Jefferts, T. P. Heavner, T. E. Parker, and C. W. Oates. "Spin-1/2 optical lattice clock". In: *Physical Review Letters* 103 (6 2009), pp. 10–13. ISSN: 00319007. DOI: 10.1103/PhysRevLett.103.063001 (cit. on p. 21).

[134] C. L. Kane and E. J. Mele. "Quantum Spin Hall Effect in Graphene". In: *Physical Review Letters* 95 (22 Nov. 2005), p. 226801. ISSN: 0031-9007. DOI: 10.1103/PhysRevLett.95.226801 (cit. on p. 35).

[135] J. Avron, D. Osadchy, and R. Seiler. "A topological look at the quantum Hall effect". In: *Physics today* 56 (8 2003), p. 38. ISSN: 00319228. DOI: 10.1063/1.1611351 (cit. on pp. 35, 37).

[136] X. L. Qi and S. C. Zhang. "Topological insulators and superconductors". In: *Reviews of Modern Physics* 83 (4 2011). ISSN: 00346861. DOI: 10.1103/RevModPhys.83.1057 (cit. on pp. 35, 36).

[137] K. v. Klitzing, G. Dorda, and M. Pepper. "New Method for High-Accuracy Determination of the Fine-Structure Constant Based on Quantized Hall Resistance". In: *Physical Review Letters* 45 (6 Aug. 1980), pp. 494–497. ISSN: 0031-9007. DOI: 10.1103/PhysRevLett.45.494 (cit. on p. 35).

[138] N. R. Cooper, J. Dalibard, and I. B. Spielman. "Topological bands for ultracold atoms". In: *Reviews of Modern Physics* 91 (1 2019), p. 15005. ISSN: 15390756. DOI: 10.1103/RevModPhys.91.015005 (cit. on pp. 36, 38).

[139] V. Galitski and I. B. Spielman. "Spin–orbit coupling in quantum gases". In: *Nature* 494 (7435 Feb. 2013), pp. 49–54. ISSN: 0028-0836. DOI: 10.1038/nature11841 (cit. on pp. 36, 45).

[140] Y. Aharonov and D. Bohm. "Significance of Electromagnetic Potentials in the Quantum Theory". In: *Physical Review* 115 (3 Aug. 1959), pp. 485–491. ISSN: 0031-899X. DOI: 10.1103/PhysRev.115.485 (cit. on pp. 37, 38).

[141] R. Peierls. "Zur Theorie des Diamagnetismus von Leitungselektronen". In: *Zeitschrift für Physik* 80 (11-12 1933), pp. 763–791. ISSN: 14346001. DOI: 10.1007/BF01342591 (cit. on p. 37).

[142] M. Aidelsburger. "Artificial gauge fields with ultracold atoms in optical lattices". In: *PhD thesis* (2015). DOI: 10.1007/978-3-319-25829-4 (cit. on pp. 37, 38).

[143] N. Goldman, G. Juzeliunas, P. Öhberg, and I. B. Spielman. "Light-induced gauge fields for ultracold atoms". In: *Reports on Progress in Physics* 77 (12 2014). ISSN: 00344885. DOI: 10.1088/0034-4885/77/12/126401 (cit. on pp. 38, 42, 43, 45).

[144] P. G. Harper. "The General Motion of Conduction Electrons in a Uniform Magnetic Field, with Application to the Diamagnetism of Metals". In: *Proceedings of the Physical Society. Section A* 68 (10 Oct. 1955), pp. 879–892. ISSN: 0370-1298. DOI: 10.1088/0370-1298/68/10/305 (cit. on p. 38).

[145] D. R. Hofstadter. "Energy levels and wave functions of Bloch electrons in rational and irrational magnetic fields". In: *Physical Review B* 14 (6 Sept. 1976), pp. 2239–2249. ISSN: 0556-2805. DOI: 10.1103/PhysRevB.14.2239 (cit. on pp. 38, 39).

[146] D. Hügel and B. Paredes. "Chiral ladders and the edges of quantum Hall insulators". In: *Physical Review A* 89 (2 Feb. 2014), p. 023619. ISSN: 1050-2947. DOI: 10.1103/PhysRevA.89.023619 (cit. on p. 40).

[147] F. Gerbier and J. Dalibard. "Gauge fields for ultracold atoms in optical superlattices". In: *New Journal of Physics* 12 (2010). ISSN: 13672630. DOI: 10.1088/1367-2630/12/3/033007 (cit. on p. 43).

[148] E. J. Mueller. “Artificial electromagnetism for neutral atoms: Escher staircase and Laughlin liquids”. In: *Physical Review A - Atomic, Molecular, and Optical Physics* 70 (4 2004). ISSN: 10502947. DOI: 10.1103/PhysRevA.70.041603 (cit. on p. 43).

[149] K. Osterloh, M. Baig, L. Santos, P. Zoller, and M. Lewenstein. “Cold atoms in non-abelian gauge potentials: From the hofstadter "moth" to lattice gauge theory”. In: *Physical Review Letters* 95 (1 2005). ISSN: 00319007. DOI: 10.1103/PhysRevLett.95.010403 (cit. on p. 43).

[150] J. Ruostekoski, G. V. Dunne, and J. Javanainen. “Particle Number Fractionalization of an Atomic Fermi-Dirac Gas in an Optical Lattice”. In: *Physical Review Letters* 88 (18 2002), p. 180401. ISSN: 0031-9007. DOI: 10.1103/PhysRevLett.88.180401 (cit. on p. 43).

[151] I. Bloch, J. Dalibard, and W. Zwerger. “Many-body physics with ultracold gases”. In: *Reviews of Modern Physics* 80 (3 July 2008), pp. 885–964. ISSN: 0034-6861. DOI: 10.1103/RevModPhys.80.885 (cit. on pp. 43, 72).

[152] M. Lewenstein, A. Sanpera, V. Ahufinger, B. Damski, A. Sen(De), and U. Sen. “Ultracold atomic gases in optical lattices: mimicking condensed matter physics and beyond”. In: *Advances in Physics* 56 (2 Mar. 2007), pp. 243–379. ISSN: 0001-8732. DOI: 10.1080/00018730701223200 (cit. on p. 43).

[153] M. Aidelsburger, M. Atala, S. Nascimbène, S. Trotzky, Y. a. Chen, and I. Bloch. “Experimental Realization of Strong Effective Magnetic Fields in an Optical Lattice”. In: *Physical Review Letters* 107 (25 2011), pp. 1–5. ISSN: 0031-9007. DOI: 10.1103/PhysRevLett.107.255301 (cit. on p. 43).

[154] M. Mancini. “Quantum Simulation with Ytterbium Atoms in Synthetic Dimensions”. In: *PhD thesis* (2015) (cit. on pp. 45, 60).

[155] N. Pintul. “Towards the Creation of Artificial Gauge Fields in Synthetic Dimensions for Fermionic Ytterbium”. In: *Bachelor thesis* (November 1996 2018) (cit. on pp. 51, 54, 57).

[156] A. Celi, P. Massignan, J. Ruseckas, N. Goldman, I. B. Spielman, G. Juzeliunas, and M. Lewenstein. “Synthetic gauge fields in synthetic dimensions”. In: *Physical Review Letters* 112 (4 2014), pp. 1–6. ISSN: 00319007. DOI: 10.1103/PhysRevLett.112.043001 (cit. on p. 55).

[157] W. Demtröder. *Laser Spectroscopy*. Springer Berlin Heidelberg, 2003. ISBN: 978-3-662-05157-3. DOI: 10.1007/978-3-662-05155-9 (cit. on p. 59).

[158] X. Liu, X. Zhou, W. Xiong, T. Vogt, and X. Chen. “Rapid nonadiabatic loading in an optical lattice”. In: *Physical Review A* 83 (6 June 2011), p. 063402. ISSN: 1050-2947. DOI: 10.1103/PhysRevA.83.063402 (cit. on p. 60).

[159] X. Zhou, S. Jin, and J. Schmiedmayer. “Shortcut loading a Bose–Einstein condensate into an optical lattice”. In: *New Journal of Physics* 20 (5 May 2018), p. 055005. ISSN: 1367-2630. DOI: 10.1088/1367-2630/aac11b (cit. on p. 60).

[160] B. W. Shore. “Picturing stimulated Raman adiabatic passage: a STIRAP tutorial”. In: *Advances in Optics and Photonics* 9 (3 2017), p. 563. DOI: 10.1364/aop.9.000563 (cit. on p. 61).

[161] J. J. Sakurai. *Modern Quantum Mechanics*. Ed. by S. F. Tuan. 1994. ISBN: 0201539292 (cit. on p. 62).

[162] N. Kosugi, S. Matsuo, K. Konno, and N. Hatakenaka. “Theory of damped Rabi oscillations”. In: *Physical Review B* 72 (17 Nov. 2005), p. 172509. ISSN: 1098-0121. DOI: 10.1103/PhysRevB.72.172509 (cit. on p. 65).

[163] S. Matsuo, T. Fujii, N. Kosugi, and N. Hatakenaka. "Theory of damped Rabi oscillations at finite temperatures". In: *Journal of Physics: Conference Series* 150 (2 Feb. 2009), p. 022056. ISSN: 1742-6596. DOI: 10.1088/1742-6596/150/2/022056 (cit. on p. 65).

[164] J. Heinze, J. Krauser, N. Fläschner, B. Hundt, S. Götze, A. P. Itin, L. Mathey, K. Sengstock, and C. Becker. "Intrinsic Photoconductivity of Ultracold Fermions in Optical Lattices". In: *Physical Review Letters* 110 (8 Feb. 2013), p. 085302. ISSN: 0031-9007. DOI: 10.1103/PhysRevLett.110.085302 (cit. on p. 83).

[165] T.-W. Zhou, G. Cappellini, D. Tusi, L. Franchi, J. Parravicini, C. Repellin, S. Greschner, M. Inguscio, T. Giamarchi, M. Filippone, J. Catani, and L. Fallani. "Observation of universal Hall response in strongly interacting Fermions". In: *Science* 381 (6656 July 2023), pp. 427–430. ISSN: 0036-8075. DOI: 10.1126/science.add1969 (cit. on pp. 83, 93–95).

[166] T. Ozawa and H. M. Price. "Topological quantum matter in synthetic dimensions". In: *Nature Reviews Physics* 1 (5 2019), pp. 349–357. DOI: 10.1038/s42254-019-0045-3 (cit. on p. 85).

[167] T. Ozawa, H. M. Price, N. Goldman, O. Zilberberg, and I. Carusotto. "Synthetic dimensions in integrated photonics: From optical isolation to four-dimensional quantum Hall physics". In: 043827 (2016), pp. 1–17. DOI: 10.1103/PhysRevA.93.043827 (cit. on p. 85).

[168] L. Yuan, Y. Shi, and S. Fan. "Photonic gauge potential in a system with a synthetic frequency dimension". In: *Optics Letters* 41 (4 Feb. 2016), p. 741. ISSN: 0146-9592. DOI: 10.1364/OL.41.000741 (cit. on p. 85).

[169] F. A. An, E. J. Meier, J. Ang, and B. Gadway. "Correlated Dynamics in a Synthetic Lattice of Momentum States". In: *Physical Review Letters* 120 (4 2018), p. 40407. ISSN: 1079-7114. DOI: 10.1103/PhysRevLett.120.040407 (cit. on p. 85).

[170] F. A. An, E. J. Meier, and B. Gadway. "Engineering a Flux-Dependent Mobility Edge in Disordered Zigzag Chains". In: *Physical Review X* 8 (2018). DOI: 10.1103/PhysRevX.8.031045 (cit. on p. 85).

[171] B. Sundar, B. Gadway, and K. R. Hazzard. "Synthetic dimensions in ultracold polar molecules". In: *Scientific Reports* 8 (1 Dec. 2018). ISSN: 20452322. DOI: 10.1038/s41598-018-21699-x (cit. on p. 85).

[172] B. Sundar, M. Thibodeau, Z. Wang, B. Gadway, and K. R. Hazzard. "Strings of ultracold molecules in a synthetic dimension". In: *Physical Review A* 99 (1 Jan. 2019). ISSN: 24699934. DOI: 10.1103/PhysRevA.99.013624 (cit. on p. 85).

[173] T. Ozawa and I. Carusotto. "Synthetic Dimensions with Magnetic Fields and Local Interactions in Photonic Lattices". In: *Physical Review Letters* 118 (1 Jan. 2017). ISSN: 10797114. DOI: 10.1103/PhysRevLett.118.013601 (cit. on p. 85).

[174] Z. Yan, S. Wan, and Z. Wang. "Topological Superfluid and Majorana Zero Modes in Synthetic Dimension". In: *Nature Publishing Group* (2015), pp. 1–7. DOI: 10.1038/srep15927 (cit. on p. 93).

[175] T.-S. Zeng, C. Wang, and H. Zhai. "Charge Pumping of Interacting Fermion Atoms in the Synthetic Dimension". In: *Physical Review Letters* 115 (9 Aug. 2015), p. 095302. ISSN: 0031-9007. DOI: 10.1103/PhysRevLett.115.095302 (cit. on p. 93).

[176] J. Jünemann, A. Piga, S. J. Ran, M. Lewenstein, M. Rizzi, and A. Bermudez. "Exploring interacting topological insulators with ultracold atoms: The synthetic creutz-hubbard model". In: *Physical Review X* 7 (3 2017), pp. 1–25. ISSN: 21603308. DOI: 10.1103/PhysRevX.7.031057 (cit. on p. 93).

[177] S. K. Ghosh, U. K. Yadav, and V. B. Shenoy. "Baryon squishing in synthetic dimensions by effective SU(M) gauge fields". In: *Physical Review A* 92 (5 Nov. 2015), p. 051602. ISSN: 1050-2947. DOI: 10.1103/PhysRevA.92.051602 (cit. on p. 93).

[178] S. K. Ghosh, S. Greschner, U. K. Yadav, T. Mishra, M. Rizzi, and V. B. Shenoy. "Unconventional phases of attractive Fermi gases in synthetic Hall ribbons". In: *Physical Review A* 95 (6 June 2017), p. 063612. ISSN: 2469-9926. DOI: 10.1103/PhysRevA.95.063612 (cit. on p. 93).

[179] E. Anisimovas, M. Račiunas, C. Sträter, A. Eckardt, I. B. Spielman, and G. Juzeliunas. "Semisynthetic zigzag optical lattice for ultracold bosons". In: *Physical Review A* 94 (6 2016), pp. 1–8. ISSN: 24699934. DOI: 10.1103/PhysRevA.94.063632 (cit. on p. 93).

[180] J. Xu, Q. Gu, and E. J. Mueller. "Realizing the Haldane Phase with Bosons in Optical Lattices". In: *Physical Review Letters* 120 (8 Feb. 2018). ISSN: 10797114. DOI: 10.1103/PhysRevLett.120.085301 (cit. on p. 93).

[181] S. Greschner, M. Piraud, F. Heidrich-Meisner, I. P. McCulloch, U. Schollwöck, and T. Vekua. "Symmetry-broken states in a system of interacting bosons on a two-leg ladder with a uniform Abelian gauge field". In: *Physical Review A* 94 (6 Dec. 2016). ISSN: 24699934. DOI: 10.1103/PhysRevA.94.063628 (cit. on p. 93).

[182] S. Greschner and T. Vekua. "Vortex-Hole Duality: A Unified Picture of Weak- and Strong-Coupling Regimes of Bosonic Ladders with Flux". In: *Physical Review Letters* 119 (7 Aug. 2017). ISSN: 10797114. DOI: 10.1103/PhysRevLett.119.073401 (cit. on p. 93).

[183] T. Bilitewski and N. R. Cooper. "Synthetic dimensions in the strong-coupling limit: Supersolids and pair superfluids". In: *Physical Review A* 94 (2 Aug. 2016), p. 023630. ISSN: 2469-9926. DOI: 10.1103/PhysRevA.94.023630 (cit. on p. 93).

[184] S. L. Bromley, S. Kolkowitz, T. Bothwell, D. Kedar, A. Safavi-Naini, M. L. Wall, C. Salomon, A. M. Rey, and J. Ye. "Dynamics of interacting fermions under spin–orbit coupling in an optical lattice clock". In: *Nature Physics* 14 (4 Apr. 2018), pp. 399–404. ISSN: 1745-2473. DOI: 10.1038/s41567-017-0029-0 (cit. on p. 93).

[185] S. Greschner, M. Filippone, and T. Giamarchi. "Universal Hall Response in Interacting Quantum Systems". In: *Physical Review Letters* 122 (8 Feb. 2019). ISSN: 10797114. DOI: 10.1103/PhysRevLett.122.083402 (cit. on p. 93).

[186] M. Mamaev, T. Bilitewski, B. Sundar, and A. M. Rey. "Resonant Dynamics of Strongly Interacting SU(n) Fermionic Atoms in a Synthetic Flux Ladder". In: *PRX Quantum* 3 (3 Aug. 2022), p. 030328. ISSN: 2691-3399. DOI: 10.1103/PRXQuantum.3.030328 (cit. on p. 93).

Danksagung

Diese Arbeit wäre ohne die Hilfe und Unterstützung vieler Menschen nicht möglich gewesen, denen ich an dieser Stelle meinen tiefen Dank aussprechen möchte.

Als erstes möchte ich Prof. Dr. Klaus Sengstock meinen tiefen Dank dafür aussprechen, dass er mich in seine Arbeitsgruppe aufgenommen hat. Vom Beginn meiner Tätigkeit als Hilfswissenschaftler über die Mitbetreuung meiner Masterarbeit in Florenz bis hin zu meiner Doktorarbeit hat er mich stets unterstützt und gefördert. Seine wertvollen Anregungen und sein Vertrauen haben maßgeblich zum Gelingen dieser Arbeit beigetragen.

Prof. Dr. Henning Moritz danke ich für die Übernahme des Zweitgutachtens und die damit verbundene Unterstützung.

Ein besonderer Dank gilt Dr. Christoph Becker, der mich in den letzten Jahren als Betreuer begleitet hat. Er war immer für mich erreichbar, hat mir bei Fragen und Problemen geholfen und war stets offen, physikalische Themen mit mir zu diskutieren. Er ermutigte mich oft in schwierigen Phasen und seine Unterstützung war für den Erfolg dieser Arbeit von zentraler Bedeutung.

Mein Dank gilt auch der Ytterbium-Gruppe. Bei meinen beiden Mitdoktoranden Benjamin Abeln und Koen Sponselee bedanke ich mich für die gemeinsame Zeit und die gute Zusammenarbeit. Zudem möchte ich insbesondere Nejira Pintul für den Aufbau des Raman-Lasersystems und Lars Hilbig für die Entwicklung des Simulationscodes danken. Für die Unterstützung bei den Messungen aus Kapitel 4 danke ich Tobias Petersen herzlich für seine technische und moralische Hilfe sowie dafür, dass ich in dieser Zeit nicht immer allein im Labor arbeiten musste.

Darüber hinaus möchte ich der gesamten Arbeitsgruppe Sengstock für die hervorragende Arbeitsatmosphäre und die außergewöhnliche Hilfsbereitschaft danken. Mein Dank gilt explizit Dr. Ortwin Hellmig für seine schnelle und kompetente Unterstützung in Laser- und Optik-Krisen. Ebenso möchte ich Mathis Fischer und Justus Brüggenjürgen danken, sowohl für ihre Beratung bei technischen Fragen als auch für dem kurzfristigen Aushelfen mit Laborequipment.

Für die Unterstützung bei allen haustechnischen Angelegenheiten, wie der Klimaanlage, der Wasserkühlung und der schnellen sowie zuverlässigen Reparatur elektrischer Geräte, danke ich Reinhard Mielck herzlich. Deine Tipps, basierend auf deiner langjährigen Erfahrung, waren oft unbezahlbar.

Ein weiterer Dank gilt Ellen Gloy und Janina Neubert, die mir stets bei organisatorischen und bürokratischen Fragen zur Seite standen und mir Aufgaben in diesem Bereich erheblich erleichtert haben.

Mein tiefster und herzlichster Dank geht an meine Frau Anja, meine Eltern Angelika und Richard, meine Schwester Jennifer sowie an meinen engsten Freund Christian. Ohne euren positiven Einfluss, eure stete Begleitung während dieses Prozesses und eure unermüdliche Unterstützung hätte ich mir diese Doktorarbeit nicht vorstellen können. Vielen Dank für alles!

Eidesstattliche Versicherung

Hiermit versichere ich an Eides statt, die vorliegende Dissertationsschrift selbst verfasst und keine anderen als die angegebenen Hilfsmittel und Quellen benutzt zu haben.

Sofern im Zuge der Erstellung der vorliegenden Dissertationsschrift generative Künstliche Intelligenz (gKI) basierte elektronische Hilfsmittel verwendet wurden, versichere ich, dass meine eigene Leistung im Vordergrund stand und dass eine vollständige Dokumentation aller verwendeten Hilfsmittel gemäß der Guten wissenschaftlichen Praxis vorliegt. Ich trage die Verantwortung für eventuell durch die gKI generierte fehlerhafte oder verzerrte Inhalte, fehlerhafte Referenzen, Verstöße gegen das Datenschutz- und Urheberrecht oder Plagiate.

Lüneburg, den 12.12.2024

Marcel Diem